ABSTRACT

Title of Dissertation: TOWARD PHOTONIC ORBITAL ANGULAR MOMENTUM AS A REMOTE SENSING MODALITY THROUGH RANDOM MEDIA

Nathaniel A. Ferlic
Doctor of Philosophy, 2022

Dissertation directed by: Professor Christopher C. Davis
Electrical and Computer Engineering &
co-directed by Dr. Miranda van Iersel
Electrical and Computer Engineering

Within the last few decades, the spatial degree of freedom of light has gained significant attention in the form of photonic orbital angular momentum (OAM). The use of OAM for remote sensing has been of significant interest due to its inherent orthogonality that can be used for spatial frequency filtering, coherence filtering, and as both an active or passive sensing modality. Beams with OAM also contain interesting propagation properties that have potential to be more robust than non-OAM counterparts. One application of remote sensing is using OAM to measure the strength of optical phase distortions through random media that can contain turbulence or particulate matter. There has been significant work done on the subject, but there have been difficulties at creating an applicable OAM based sensing technique employed for use in an outdoor environment. This work develops an active OAM sensing modality denoted as Optical Heterodyne Detection of Orthogonal OAM Modes (OHDOOM) to reduce the optical receiver hardware based on a beatnote signal for the first time. The beatnote signal is then hypothesized to return information about the propagation environment by measuring the crosstalk between OAM modes due to channel perturbations.

OHDOOM results through an emulated turbulent medium show that our method is highly sensitive to weak and strong turbulence depending on the transmitted OAM mode. Within a turbid medium, OHDOOM is believed to be sensitive to particles larger than the wavelength and insensitive to smaller particles. Experimental results agree well with simulated environmental conditions using wave optic simulations (WOS) implementing phase screens. A WOS for a turbulent medium is derived from turbulent phase statistics based on refractive index fluctuations. However, for the first time, a turbid medium's phase statistics are derived from a solution to the radiative transfer equation within the paraxial approximation.

Toward Photonic Orbital Angular Momentum as a Remote Sensing Modality through Random Media

by

Nathaniel A. Ferlic

Dissertation submitted to the Faculty of the Graduate School of the
University of Maryland, College Park, in partial fulfillment
of the requirements for the degree of
Doctor of Philosophy
2022

Advisory Committee:
Professor Christopher C. Davis, Chair
Professor Christopher P. Cadou, Dean's Representative
Professor Julius Goldhar
Professor Thomas E. Murphy
Dr. Miranda van Iersel, University of Dayton
Dr. Linda J. Mullen, U.S. Navy

Dedication

To my parents to whom I owe all.

Acknowledgments

There isn't really a way I can truly thank all of those who've supported me throughout my schooling, but this is the least I can do. There isn't a particular order, but I would like to start first by saying thank you to my adviser Dr. Christopher Davis. You peaked by interest in optics and gave me a chance to start my research career in the Maryland Optics Group (MOG) after being introduced to optics in your design course. You provided guidance and feedback on my quest to find knowledge. A big thanks to the MOG including Dr. Daniel Paulson, Dr. John Rzasa, and Dr. Chensheng Wu for helpful conversations, advice, and support while at University of Maryland.

Miranda, my co-adviser, thank for your unwavering support and believing in me throughout my schooling. I was able to meet you a couple months after you started in MOG and since then we have been able to accomplish many things together. Its hard to put into words all your support. I would also like to say congratulations on your new faculty position and I wish you all the best on your future endeavours! I will never forget that first field test in Florida at the Kennedy Space Center in 2018, the burnt mallet from the car fire will be cherished for years to come.

Thank you to the entire A-LiST team at Patuxent River. None of this could have been done without your endless support. Alan, thank you for all your advice and teaching me much of the experimental knowledge I know today. Brandon, thank you for your support, enthusiasm, and endless positivity throughout the experiments and writing. Linda, I can't really begin to describe the support you've provided me through the endless PowerPoint presentations, fruitful conversations to drive many of these results forward, and motivation to keep myself going. Thank you!

Lastly, I am indebted to all my friends and family who supported me and understood my constant absences within, especially, the last few months and years. I could not have done any of this without your support. Especially the undying love and support of my dad Ken. Mom would be proud. Thank you for always being there with the tireless pep talks and relentless questioning that forced me to dig deep by questioning myself and methods to pave the path to finishing this work.

Publication list

1 N. A. Ferlic, M. van Iersel, and C. C. Davis, "Devising a lab-built point visibility meter," in Laser Communication and Propagation through the Atmosphere and Oceans VIII, Sep. 2019, vol. 11133, p. 111330B.

2 C. Wu, D. A. Paulson, M. van Iersel, J. R. Rzasa, N. A. Ferlic, and C. C. Davis, "Observing single and multiple laser glints through anisotropic turbulence with a plenoptic sensor," Sep. 2019, vol. 11133.

3 M. van Iersel, J. R. Rzasa, D. A. Paulson, N. A. Ferlic, C. C. Davis, J. Spychalsky, J. T. Coffaro, F. Titus, R. F. Crabbs, "Comparing measurements of RTD probe systems and sonic anemometers," in Imaging and Applied Optics 2019 (COSI, IS, MATH, pcAOP) (2019), Jun. 2019.

4 M. van Iersel, D. A. Paulson, C. Wu, N. A. Ferlic, J. R. Rzasa, C. C. Davis, M. Walker, M. Bowden, J. Spychalsky, F. Titus, "Measuring the turbulence profile in the lower atmospheric boundary layer," Appl. Opt., vol. 58, no. 25, pp. 6934–6941, Sep. 2019.

5 M. van Iersel, D. A. Paulson, N. A. Ferlic, J. Ko, C. Wu, J. R. Rzasa, C. C. Davis, "Characterization and compensation of atmospheric effects on laser beams," Oct. 2019, vol. 11161.

6 N. A. Ferlic, A. Jantzi, A. E. Laux, L. J. Mullen, and B. M. Cochenour, "Volume scattering of particles by beams carrying orbital angular momentum," in Ocean Sensing and Monitoring XII, Apr. 2020, vol. 11420, p. 114200H.

7 N. A. Ferlic, M. van Iersel, D. A. Paulson, and C. C. Davis, "Propagation of Laguerre-Gaussian and Im-Bessel beams through atmospheric turbulence: A computational study," in Laser Communication and Propagation through the Atmosphere and Oceans IX, Aug. 2020, vol. 11506, p. 115060H.

8 N. A. Ferlic, M. van Iersel, and C. C. Davis, "Measurement of the orbital angular momentum spectrum of light through artificial turbulence by interferometry," in Laser Communication and Propagation through the Atmosphere and Oceans IX, Aug. 2020, vol. 11506, p. 115060I.

9 N. A. Ferlic, A. E. Laux, M. van Iersel, C. C. Davis, L. J. Mullen, and B. M. Cochenour, "Measurement of the orbital angular momentum spectrum of light through turbid water using modal decomposition," in Laser Communication and Propagation through the Atmosphere and Oceans IX, Aug. 2020, vol. 11506, p. 1150609.

10 N. A. Ferlic, M. van Iersel, and C. C. Davis, "Weak turbulence effects on different beams carrying orbital angular momentum," JOSA A, vol. 38, no. 10, pp. 1423–1437, Oct. 2021.

11 N. A. Ferlic, C. O'Donnell, M. van Iersel, and C. C. Davis, "The azimuthal spectrum of common transmittance functions and random media," in Laser Communication and Propagation through the Atmosphere and Oceans X, Aug. 2021, vol. 11834, pp. 145–159.

12 N. A. Ferlic, M. van Iersel, and C. C. Davis, “Simulation of Im-Bessel beam propagation through time-correlated atmospheric turbulence,” in Laser Communication and Propagation through the Atmosphere and Oceans X, Aug. 2021, vol. 11834, pp. 160–177.

13 N.A. Ferlic, A.E. Laux, B. M. Cochenour, L.J. Mullen, M. van Iersel, and C. C. Davis, "Optical Heterodyne Detection of Orthogonal Orbital Angular Momentum modes", Applied Optics, (In Progress)

14 N.A. Ferlic, A.E. Laux, B. M. Cochenour, L.J. Mullen, M. van Iersel, and C. C. Davis, " Optical Heterodyne Detection of Orthogonal Orbital Angular Momentum Modes for Sensing through Turbid Media", in Ocean Sensing and Monitoring XIII, Apr. 2022, (Soon to be Published)

15 N.A. Ferlic, M. van Iersel, and C. C. Davis, "Estimating Optical Turbulence Parameters using an Optical Vortex," in Imaging and Applied Optics (2022), Jul. 2022 (In Progress).

16 N. A. Ferlic, M. van Iersel, and C. C. Davis, “Simulation of Vortex Beam Intensity Metrics through Atmospheric Turbulence,” Photonics, [Special Issue], 2022 (In Progress)

Table of Contents

List of Tables

List of Figures

List of Abbreviations

Name	**Description**
ACF	Angular Coherence Function
AOM	Acoustic Optic Modulator
ATD	A4-course Test Dust
BG	Bessel-Gaussian
CCD	Charge Coupled Device
CSD	Cross Spectral Density
DMD	Deformable Micromirror Device
DOC	Degree of Coherence
DPB	Dual Probe Beam
EHFP	Extended Huygens-Fresnel principle
FOV	Field of View
HWP	Half Waveplate
HyGG	Hypergeometric Gaussian
IOP	Inherent Optical Property
LCSLM	Liquid Crystal Spatial Light Modulator
LG	Laguerre-Gaussian
LIDAR	Light Detection and Ranging
MA	Modified Atmospheric Spectrum
MCF	Mutual Coherence Function
MTF	Modulation Transfer Function
MVK	Modified von Kármán Spectrum
OAM	Orbital Angular Momentum
OD	Optical Depth
OHDOOM	Optical Heterodyne Detection of Orthogonal OAM Modes
OSP	Optical Signal Processing
OTF	Optical Transfer Function
PSD	Power Spectral Density
PSF	Point Spread Function
RGD	Rayleigh-Gans-Debye Approximation
RTE	Radiative Transfer Equation
SAA	Small-Angle Approximation
SAM	Spin Angular Momentum
SCR	Spatial Coherence Radius
SDM	Spatial Division Multiplexing
SPP	Spiral Phase Plate
VSF	Volume Scattering Function
WFI	Wavefront Folding Interferometer
WSF	Wave Structure Function

List of Mathematical Symbols

Symbol	Description	Units
k	Optical wavenumber	[m^{-1}]
λ	Optical wavelength	[m]
n_0	Mean refractive index	[-]
$n_1(r)$	Varying refractive index	[-]
a	Particle radius	[m]
σ_{ext}	Extinction coefficient	[m^{-1}]
σ_{sca}	Scattering coefficient	[m^{-1}]
σ_{abs}	Absorption coefficient	[m^{-1}]
C_{sca}	Scattering cross section	[m^2]
C_{abs}	Absorption cross section	[m^2]
N_d	Particle number density	[m^{-3}]
$\beta(\theta,\varphi)$	Volume scattering function	[$m^{-1}sr^{-1}$]
$\sigma_V(\theta,\varphi)$	Phase function	[sr^{-1}]
θ	Spherical polar angle	[rad]
φ	Spherical azimuth angle	[rad]
$D_n(r)$	Refractive index structure function	[-]
$B_n(r)$	Refractive index autocorrelation	[-]
$\Phi_{n,d}(\kappa)$	Refractive index power spectral density	[m^d]
C_n^2	Refractive index structure parameter	[$m^{-2/3}$]
L_0	Turbulence outer scale	[m]
l_0	Turbulence inner scale	[m]
L	Total propagation length	[m]
z_0	Observation plane coordinate	[m]
z_s	Source plane coordinate	[m]
$I(...)$	Optical intensity	[Wm^{-2}]
$U(...)$	Spatial optical field profile	[Vm^{-1}]
$E(...,t)$	Electric field profile	[Vm^{-1}]
f	Optical frequency	[s^{-1}]
f_b	Beatnote frequency	[s^{-1}]
κ	Radial spatial wavenumber	[rad m^{-1}]
κ_x, κ_y	Cartesian spatial wavenumber	[rad m^{-1}]
r, ϕ	Cylindrical coordinates	[m],[rad]
x, y	Cartesian coordinates	[m],[m]
θ, φ	Spherical Coordinate Angles	[rad],[rad]
$\sigma_{T_{sca}}$	Turbulence scattering coefficient	[m^{-1}]
$D_S(r)$	Phase structure function	[rad^2]
$B_S(r)$	Phase autocorrelation function	[rad^2]
$\Phi_{S,d}$	Phase power spectral density	[m^d]
$\theta_{T(x,y)}$	Random phase perturbation field	[rad]
$\Gamma(...)$	Mutual coherence function	[-]

$\Gamma_B(...)$	Inital source MCF	[-]
r_0	Fried parameter	[m]
ρ_0	Spatial coherence radius	[m]
σ_R^2	Rytov variance	[-]
w_0	Inital beam waist	[m]
l	OAM mode index	[-]
z	Propagation variable	[m]
$\alpha_m(z)$	Fraction of OAM power	[-]
$c_{ln}(z)$	OAM coefficient	[-]
$\mathscr{R}$	Responsivity	[AW^{-1}]
$\mathscr{I}$	Photocurrent	[A]
t	Time variable	[s]
$t(...)$	Transmittance function	[-]
$h(...)$	Amplitude spread function	[-]
$H(...)$	Amplitude transfer function	[-]
$\mathscr{H}(...)$	Optical transfer fuction	[-]
$\mathscr{F}_2$	2D Fourier transform	[-]
V_{DC}	DC photovoltage	[V]
V_{AC}	Ac photovoltage	[V]
$\Psi(...)$	Random amplitude perturbation	[-]
$\chi(...)$	Log-amplitude perturbation	[-]
$S(...)$	Phase perturbation	[-]

Chapter 1: Introduction

Over the last few decades, significant effort has been dedicated to understanding the applications and practicality of structured laser light. "Structured light" refers to the spatial shape of a laser beam, represented mathematically as a complex field $U(x,y,z) = A(x,y,z)\exp(ikW(x,y,z))$, where $A(x,y,z)$ is a real amplitude, $k = 2\pi/\lambda$ is the optical wavenumber, and λ is the optical wavelength, whose amplitude and phase can be used to encode information. The optical wavefront, $W(x,y,z)$, is the spatial distribution of the optical phase shifts across a laser beam that is extremely sensitive to changes in the propagation environment. These "changes" are inhomogeneities of the medium's refractive index. These refractive index fluctuations can change the direction of the incident radiation, called scattering, that create random amplitude and phase fluctuations. For optical application such as imaging, communications, or Light Detection and Ranging (LIDAR), the light of interest is susceptible to these random scattering event. Random scattering events lead to image blurring, increase in communication error rates or incorrect ranging estimates for the aforementioned applications.

Being able to quantify the amplitude and phase perturbations present are of utmost importance to understand how well optical applications will perform. Optical remote sensing can be used as a method to return an estimate of the environmental parameters

present to predict system performance. The goal is how to extract information about the optical phase perturbations by exploiting laser light scattering in a random medium. Leveraging phase perturbations and scattering the incident beam can lead to a wealth of knowledge about the state of the propagation environment at any given time. Scattering can be exploited by laser light that contains various degrees each of which can be exploited to return information about the environment, such as intensity modulation, polarization, optical wavelength, and spatial phase structure. This work will focus on the spatial degree of freedom due to its high sensitivity to phase perturbations, unique propagation properties, and fruitful research directions. The spatial structure is connected to the phase perturbations that reduce spatial coherence, therefore, distorting the spatial information it carries.

The spatial coherence of a laser beam is terminology to describe the relationship between points along a laser's wavefronts in space and time. Spatially coherent light maintains a fixed relationship between multiple spatial points at a fixed time, whereas temporally coherent light maintains a fixed relationship at a single spatial point while it varies in time [1]. By studying spatially encoded light, coherence theory is implicitly involved to explain its propagation and interaction as the quality of the structured light depends on the laser beam source spatial coherence [2], [3]. This is because a laser beam's wavefront, containing high spatial and temporal coherence, can undergo controlled phase or amplitude modulation that induces deterministic interference. This ability to interfere is reduced if the wavefront contains random phase perturbations or reduced spatial coherence and temporal coherence.

Using the combination of coherence theory and spatially structured light, the goal of

this work is to understand how environmental information can be interpreted from quantifying structured laser beams propagation through an inhomogeneous medium or random medium. As coherence can be easily changed depending on the laser source chosen, the spatial structure of the light is the free parameter to use for environmental sensing. One form of structured light with notable interest contains orbital angular momentum (OAM) described by a helical wavefront with the form $\exp(il\phi)$, where ϕ is the cylindrical coordinate [4]. A beam containing OAM is denoted by l, which quantifies the number of 2π phase rotations within one wavelength along the azimuthal direction of a wavefront. The number of phase rotations is denoted as the beam order, mode, topological charge, or simply charge. The sign of l denotes the chirality, or vorticity, as either right or left handed. Beams containing OAM have a signature on-axis intensity null (see Fig. 1.1(a)) due to destructive inference created by the presence of a phase singularity (see Fig. 1.1(b)). The term "optical vortex" is often use to describe OAM beams due to the helix shape of the wavefront as the beam propagates as illustrated in Fig. 1.1(c-d) and on-axis intensity null.

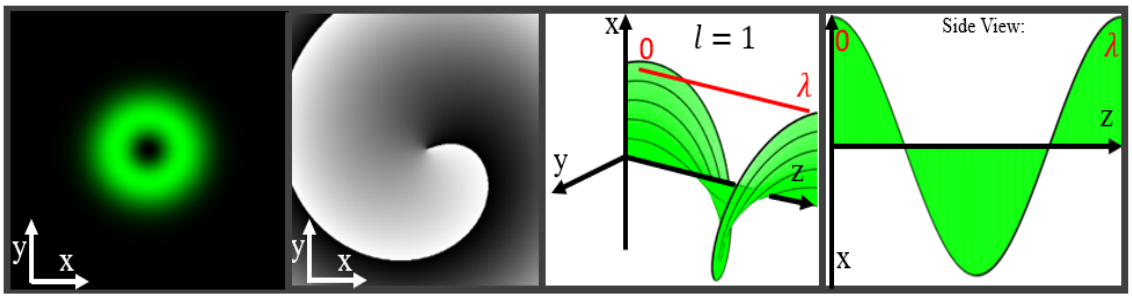

Figure 1.1: (a) Vortex beam containing an intensity null on-axis. (b) Phase of the previous beam with an optical vortex at the center. (c) Helical wavefront as a function of x, y, and z. (d) Side view of the helix showing a sinusoidal dependence in space.

The OAM of light is not a new phenomenon as Poynting [5], [6] predicted that circularly polarized light could carry an angular momentum, which was not confirmed until much later by Beth [7]. This angular momentum refers to spin angular momentum (SAM) of light with a value of $s\hbar$, where $s = \pm 1$. Our current understanding of photonic OAM was predicted later by Darwin who considered angular momentum transfer with values greater than simply $\hbar$ [8]. OAM and SAM are two separate phenomena and are not to be thought of analogs of each other. The connection between a helical wavefront and OAM was not made until 1992 using cylindrical lenses to reverse the vorticity of the phase profile [4]. OAM relies on the phase profile to contain a phase singularity, but phase singularities do not necessarily infer OAM. This is why many previous studies that focused on the phase singularity itself did not notice the evidence of OAM as it is the light around the phase singularity that contains OAM [9], [10].

The phenomenon of OAM itself is an intriguing field with many questions that are left unanswered, but this work focuses on its application for remote sensing in a random medium. OAM's practical appeal is due to its inherent orthogonality that implies OAM states are separable and can propagate in free-space without interaction. OAM beams also, as implied by the terminology, carry a rotational force that can impart torque on small particles. This force is generally not strong enough to exert the same effect on macroscopic particles. Light containing OAM has been applied to numerous applications such as: free-space spatial division multiplexed (SDM) optical communications [11]–[15], optical trapping [16], [17], polarization state shaping [18]–[20], spatial filtering [21]–[24], microscopy [25], and sensing [26]–[33]

1.1 OAM as a Sensing Modality

The focus of this work will be on the application of OAM for sensing within a random environment using a highly directional coherent light source. "Sensing" in this work refers to obtaining information about the environment using laser beams carrying OAM. OAM remote sensing methods can be grouped into three general categories: passive OAM sensing, active OAM sensing, and OAM based filters. The propagation environment in question contains optical inhomogeneities, mainly refractive index variations, that manifest themselves as phase distortions along the laser beam's wavefront. These distortions can either be removed or leveraged depending on the OAM sensing technique implemented. Figure 1.2 summarizes how OAM can be viewed to sense the environmental distortion. Each measurement method leads to different ways of how OAM is applied to the remote sensing problem.

Passive OAM sensing refers to detecting changes of OAM created in-situ without injecting extrinsic OAM [34]–[36]. In contrast, active OAM sensing which refers to injecting OAM into an environment and detecting how the input OAM changes due to the environment [26], [28], [30]–[32], [37]–[39]. Active OAM sensing has been seen to measure rotational Doppler shifts [32], [40]–[46], linear object speed and size [30], [31], and surface roughness [28], [47]. The last OAM based sensing method is called optical signal processing (OSP) [21]–[23], [26]. OAM based OSP techniques are used to distinguish between coherent and incoherent light components of a laser to improve light detection and ranging (LIDAR) efficacy [21], [26], [48], [49] or as a spatial frequency filter for imaging [22], [23], [25].

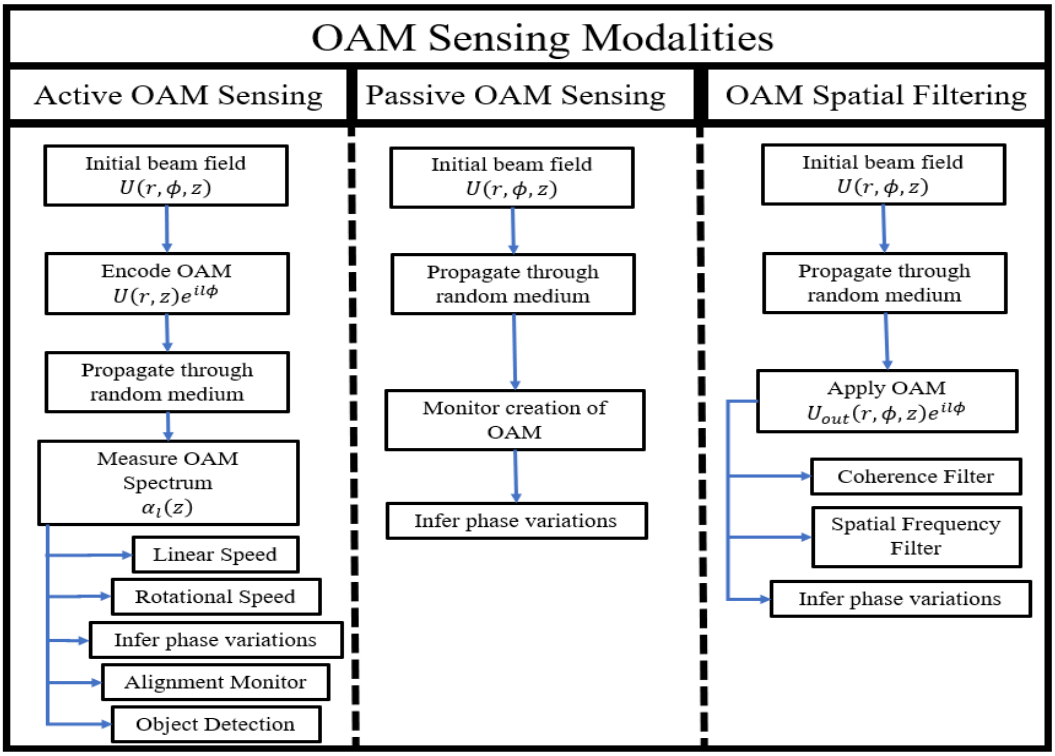

Figure 1.2: Illustration of the various methods to measure and apply OAM properties to the remote sensing problem.

OAM, as an active sensing modality, has spurred significant interest due to its spatial interaction with random media. A random medium can scatter the incident OAM mode into higher or lower value OAM modes that can be used to sense the strength of the random medium variations. The benefit of an active method is that one has knowledge of the input OAM state, whose perturbations upon propagation can be quantified to characterize environmental parameters. However, implementing active OAM sensing methods proves to be quite challenging due to the need for complex optical systems, which can limit practical implementation.

1.2 Dissertation Research Goals

The goal of this dissertation is to present work towards developing an active OAM based sensing modality that can quantify the optical effects of a random environment. To address practical limitations of active OAM sensing, a method called Optical Heterodyne Detection of Orthogonal OAM Modes (OHDOOM) is developed to reduce the optical receiver hardware.

To explore the effects of a random medium on an OAM beam, this work is segmented into a simulation and experimental based approach that studies the propagation and detection of OAM. The simulations aim to show how various metrics and degrees of freedom of OAM beams are affected by a random medium, which are then translated to developing the OHDOOM detection scheme. Properties of the laser beam specifically explored are laser beam size, OAM charge, and source coherence.

Along with the main goal of developing an active OAM sensing modality, the dissertation is written to also address secondary objectives that quantify effects of a random medium on OAM beam propagation. The first subgoal is to develop a theoretical foundation that outlines the similarities and differences between refractive index variations of scales smaller than the optical wavelength and those comparable to the optical wavelength. This will be done by discussing the radiative transfer equation under the small-angle approximation and its relationship to traditional treatment of the stochastic Helmholtz equation. The second subgoal is how to fairly compare OAM beam propagation to standard laser beams used in today's LIDAR systems.

1.3 Dissertation Organization

This dissertation is organized such that the reader has the necessary background to understand remote sensing using OAM. This includes background information on the necessary mathematical foundation to describe laser beam propagation through a random medium in Chapters 2 and 3, respectively. The theory places an emphasis on how the coherence of the main laser beam is affected by the medium within the context of image formation. This chapter will also address the similarities and differences between optical turbulence and particulate matter, as experimental results are presented for both cases.

The core of OAM sensing is presented in Chapter 4 using the foundations of Chapters 2 and 3 to predict how OAM changes in a random medium. Chapter 5 will discuss beam propagation simulations through turbulent and turbid media. The subgoal of comparing OAM beam propagation to a standard laser beam will be discussed in this chapter. Chapter 6 will give an overview of two experiments that were performed to explore OAM as a sensing modality and the knowledge gained. Chapter 7 introduces OHDOOM as a new active remote sensing modality using the knowledge gained from the previous chapters. Chapter 8 will summarize the findings of this work along with discussion of future direction of this work. Appendices A - F offer insight to the simulation and theoretical methods used throughout this thesis.

1.4 Summary of Forthcoming Contributions

Results of this dissertation research provide a unique perspective on laser scattering in a turbid and turbulent medium while connecting it to the effects on light's OAM. This contribution summary is meant to describe the key findings of this work that are most relevant to those studying the following topics: laser light propagation through a random medium, OAM beam propagation in random media, coherence, OAM based sensing, and random media effects on optical imaging. Each contribution is discussed in great detail in the specified chapter.

- Determined properties of random media that affect OAM through a simulated trade-off study determining most important dimensionless ratios for each medium.
- Turbid media is discussed in the language of turbulent media to provide a clear comparison of the effects of optical wave propagation.
- Created simulations of a turbid medium that can be easily combined with simulations of a turbulent medium.
- Acquired experiment mode spreading results using a different interferometric technique and mode projection.
- Developed an original OAM based sensing technique - OHDOOM. Its uniqueness falls with its inherent low frequency noise rejection, simplification of hardware and data processing, and inherent phase information.

- Demonstrated OHDOOM's response to a turbulent and turbid media with simulations and theory. Results are confirmed through experimentation.

Chapter 2: Review of Laser Beam Propagation through a Random Medium

2.1 Introduction

To thoroughly appreciate how an active OAM sensing method works, it is of necessity to introduce quantitative methods of laser beam propagation through a random medium. The theory of concern describes the evolution of a laser beam's spatial coherence in the presence of random phase perturbations. OAM beam propagation can be treated similarly to a Gaussian beam, without OAM, if it maintains a low divergence. The coherence properties of a random medium can be studied independently of the beam shape and spatial properties. However, when the effects on a finite beam are considered the random variations are dependent on the initial beam's coherence properties, wavefront curvature, spot size, and wave function shape. Effects of a random medium on a laser beam manifest itself as phase variations on the optical wavefront that lead to a coupling between phase and amplitude variations due to interference.

Before introducing further consequences of a random medium on beam propagation (Chapter 3), a short background on notation and functions of a random medium are introduced in Section 2.2 followed by the definitions of a random medium's inherent optical properties in Section 2.3.

2.2 Mathematical Formalism of a Random Medium

As a laser beam, or more generally an optical wave, propagates through a random medium the amplitude and phase are subject to random fluctuations. The fluctuations are mainly due to random changes of the medium's refractive index, but their scale size compared to the laser wavelength can significantly alter results. Due to these random changes of the optical field, the optical wave must be treated as a random variable.

The optical field depends on space and time allowing for the treatment as a "random field", which is a stochastic process denoted as $x(\mathbf{r},t)$, where $\mathbf{r} = (x,y,z)$. Using a probabilistic point of view, it is most convenient to work with the statistical moments of the field as they are most practical for physical measurements. Within this mathematical framework, the time dependence of the random variables is suppressed since the time scales of the considered random media are much slower than the time it takes for light to travel through them. The discussion of when temporal variations of the medium must be considered will be discussed briefly in Section 4.1.3. For more information on the mathematics involved in a random medium, the reader is referred to Andrews and Phillips [50]. As the theory focuses on a statistical treatment it is useful to define the following functions: spatial autocorrelation, spatial power spectrum, and structure function.

2.2.1 Spatial Autocorrelation Function

Given a randomly varying spatial field $x(\mathbf{r})$, the second order moment or autocorrelation function can be defined as

$$B_x(\mathbf{r}_1, \mathbf{r}_2) = \langle x(\mathbf{r}_1) x^*(\mathbf{r}_2) \rangle, \tag{2.1}$$

where $\langle ... \rangle$ denotes an ensemble average and * denotes the complex conjugate. Within the random medium of interest, the statistics can be assumed homogeneous and isotropic. This assumption leads to the autocorrelation depending only on the distance between two points within the field rather than their absolute position leaving $B_x(r)$, where $r = |\mathbf{r}_2 - \mathbf{r}_1|$.

2.2.2 Spatial Power Spectrum

In order to compute the autocorrelation in equation 2.1, a useful quantity to derive is the spatial power spectrum using the Wiener-Khinchin theorem. Assuming that the field $x(\mathbf{r})$ is statistically homogeneous with zero mean, the field can be represented using the Riemann-Stieltjes integral [50]

$$x(\mathbf{r}) = \int_{-\infty}^{\infty} e^{i\boldsymbol{\kappa}\cdot\mathbf{r}} d\nu(\boldsymbol{\kappa}), \tag{2.2}$$

where $\boldsymbol{\kappa} = (\kappa_x, \kappa_y, \kappa_z)$ and $d\nu(\boldsymbol{\kappa})$ represents the random amplitude of $x(\mathbf{r})$. Using equation 2.1 and 2.2 the autocorrelation can be written as

$$B_x(\mathbf{r}_1, \mathbf{r}_2) = \iiiint\!\!\iint e^{i[\boldsymbol{\kappa}_1 \cdot \mathbf{r}_1 + \boldsymbol{\kappa}_2 \cdot \mathbf{r}_2]} \langle d\nu(\boldsymbol{\kappa}_1) d\nu(\boldsymbol{\kappa}_2)^* \rangle. \tag{2.3}$$

Upon using statistical homogeneity, $\langle d\nu(\boldsymbol{\kappa}_1) d\nu(\boldsymbol{\kappa}_2)^* \rangle = \delta(\boldsymbol{\kappa}_2 - \boldsymbol{\kappa}_1) \Phi_{x,3}(\boldsymbol{\kappa}) d^3\kappa_1 d^3\kappa_2$, where $\Phi_{x,3}(\boldsymbol{\kappa})$ is the three-dimensional spatial power spectral density (PSD). Equation 2.3 simplifies to

$$B_x(\mathbf{r}_1, \mathbf{r}_2) = \iiint \Phi_{x,3}(\boldsymbol{\kappa}_1) e^{i\boldsymbol{\kappa}_1 \cdot \mathbf{r}} d^3\boldsymbol{\kappa}_1. \tag{2.4}$$

The inverse Fourier relationship is given as

$$\Phi_{x,3}(\boldsymbol{\kappa}_1) = \frac{1}{(2\pi)^3} \iiint B_x(\mathbf{r}_1, \mathbf{r}_2) e^{-i\boldsymbol{\kappa}_1 \cdot \mathbf{r}} d^3\mathbf{r}. \tag{2.5}$$

These relationships can be simplified further, again under isotropic statistics, where the vectors $\mathbf{r}$ and $\boldsymbol{\kappa}_1$ can be replaced with their scalar quantities r and $\kappa = (\kappa_x + \kappa_y)^{1/2}$ respectively.

2.2.3 Structure Function

Another useful function to describe the statistics of a random medium is the structure function, which is used throughout most literature involving turbulence or rough surfaces [50]–[52]. Its usefulness appears due to random fields having a mean value that

varies over various points in space which breaks the assumption of statistical homogeneity. A structure function is invariant to this varying mean value as it depends on the statistical relationships between the difference of two points rather than their absolute position and value. As the mean value varies across the random medium, the difference between two points removes the mean and only the fluctuating part of the random field is said to be statistically homogeneous. The structure function can be related to a random field's autocorrelation and its power spectrum from the following relationships assuming statistical homogeneity and isotropy

$$\begin{aligned} D_x(r) &= \langle [x(r_i) - x(r_i + r)]^2 \rangle \\ &= 2[B_x(0) - B_x(r)] \\ &= 2 \iiint d^3\kappa \Phi_{x,3}(\kappa) \left(1 - \cos(\boldsymbol{\kappa} \cdot \mathbf{r})\right), \end{aligned} \tag{2.6}$$

where r_i is some initial point of origin. In this work r_i is typically taken as the origin of the field leaving $r = (x^2 + y^2)^{1/2}$.

2.3 Inherent Optical Properties of a Random Medium

Inherent optical properties (IOPs) of a random medium generally consist of absorption and scattering coefficients that degrade optical power transfer. However, in this work, the refractive index fluctuations properties are also considered as an IOP. Each of these properties exists in a propagation medium such as the atmosphere, ocean, or biological tissue, but the values, properties, and length scales of the IOPs can change.

To start the study of laser beam propagation, a medium can be assumed to be a slab

of randomly distributed particles, with length dz illustrated in Fig. 2.1, that can include particles of any diameter. The change in optical power lost to propagation through the medium, dP, is proportional to the incident optical power P_{in} and can be written as

$$dP = -\sigma P dz, \tag{2.7}$$

where σ [m^{-1}] is a proportionality constant. Integration of equation 2.7 yields

$$P(z) = P_{in} e^{-\int_{z_s}^{z_o} \sigma_{ext}(z) dz}, \tag{2.8}$$

where $P(z)$ [W] is the output power, P_{in} is the input power, $\sigma_{ext}(z)$ is the extinction coefficient, z_s is the source plane initial position, and z_o is the observation plane (position of power measurement). The extinction coefficient is the sum of the absorption and scattering coefficients that degrade optical power transmission:

$$\sigma_{ext}(z) = \sigma_{sca}(z) + \sigma_{abs}(z) = N_d(z)(C_{sca} + C_{abs}), \tag{2.9}$$

where N_d [m^{-3}] is the particle density, C_{sca} [m^2] is the scattering cross section, and C_{abs} [m^2] is the absorption cross section. The scattering and absorption cross sections are related to the particle sizes present within a turbid medium, which can be be analytically found for spherically shaped particles.

If the propagation medium is isotropic, assuming the density of the medium and the particulate matter present are the same, the dependence on the propagation distance, z, can be ignored. Using this slab model, both scattering and absorption contribute to

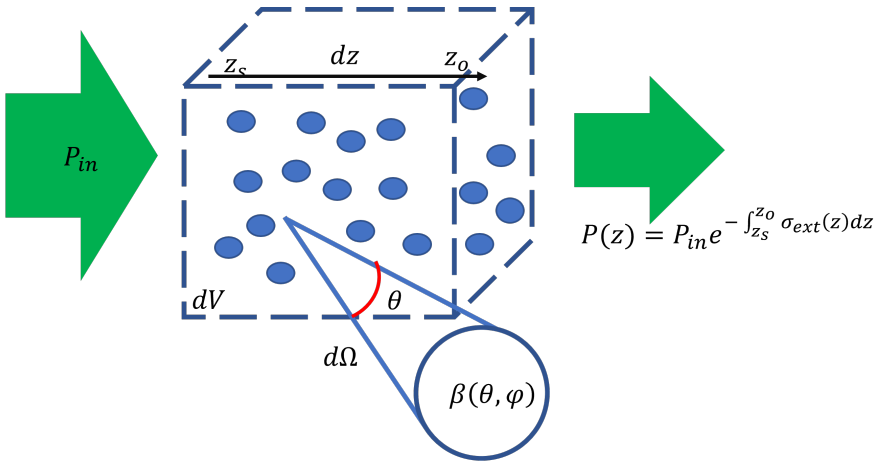

Figure 2.1: Geometry of the scattering volume consisting of a slab (of length dz) of a medium containing particles with diameters comparable to the laser wavelength.

an optical power attenuation factor. However, this total attenuation is only true for light that maintains its forward directionality. Scattering must be quantified by its strength and how it redirects the incident radiation upon interacting with particles or turbulence. Scattering phenomena can be generally broken down into three regions: molecular scattering, scattering by large particles, and turbulent scattering [53]. Each form of scattering phenomena will be discussed in this dissertation.

2.3.1 Absorption by Particles

Absorption is a wavelength dependent process where the laser light transfers electromagnetic energy to rotational, translational, vibrational, or electronic processes of a particle and the particle does not re-emit the same incident energy. In an atmospheric environment, the main aerosols that absorb light are water, carbon-based molecules, and ozone [50]. Due to the presence of different molecules some wavelengths propagate with small amounts of attenuation while others are quickly attenuated. This is because of dif-

ferent molecular absorption processes that are wavelength dependent. In the atmosphere there are many ranges of wavelengths that are least absorbed such as 785 nm or 1550 nm. This is not the case in the ocean where mainly blue/green wavelengths are absorbed the least.

2.3.2 Scattering by Particles

Scattering is the redirection of the incident laser radiation due to an interaction within the medium such as with particulate matter. In the atmospheric case, the main scatterer of radiation are aerosol particles of sizes comparable to the incident wavelength. For an oceanic environment scatterers are of a different nature, but the physics of scattering remains the same. These processes are highly dependent on the ratio of the particle radius, a, to the wavelength of light [54], [55]. Depending on the size of the particle various treatments can be applied as summarized in Table 2.1. "Particle size" throughout this paper means particle diameter unless otherwise specified.

Particle Type	Diameter [μm]	Scattering Process	a/λ
Molecules	0.00002	Rayleigh	$\ll 1$
Haze	0.02 - 2	Rayleigh - Mie	~ 1
Fog	2 - 40	Mie - Geometrical	> 1
Rain	200 - 20000	Mie - Geometrical	$\gg 1$
Snow	2000 - 10000	Geometrical	$\gg 1$
Hail	10000 - 100000	Geometrical	$\gg 1$

Table 2.1: Examples of particle sizes and the method to solve for the scattered light distribution [56].

The scattering of interest in this work is mainly due to particles comparable to the wavelength, which involves the electromagnetic interaction of the laser light with the particle. This interaction combines the effects of diffraction, refraction, and reflections

inside of the particle to dictate the scattering pattern of the incident light. To illustrate scattering, consider the illustration in Fig. 2.1 to describe the geometry of the scattering interaction.

Assume a collimated laser beam is incident on a thin slab of particles with length dz. Laser light scatters into a polar angle θ and spherical azimuth angle φ. At a distance away from the slab is a detector, with area A, viewing solid angle $d\Omega$ to measure the scattered intensity. The angular distribution of power incident on the detector can be written as

$$P(\theta,\varphi) = P_0\beta(\theta,\varphi)dzd\Omega \tag{2.10}$$

where $\beta(\theta,\varphi)$ [m^{-1} sr^{-1}] is the angular distribution of scattered light. The differential intensity is $dI(\theta,\varphi) = P(\theta,\varphi)/d\Omega$ [W sr^{-1}]. If the incident intensity falls on a detector with differential area dA, the incident irradiance is $E = P_0/dA$ [W m^{-2}]. If the beam illuminates a finite volume of particles $dV = dzdA$, equation 2.10 can then be rewritten as

$$\beta(\theta,\varphi) = \frac{1}{E}\frac{dI(\theta,\varphi)}{dV}. \tag{2.11}$$

Thus, $\beta(\theta,\varphi)$ defines the volume scattering function (VSF) describing the scattered intensity per unit input intensity per unit volume. The VSF is also known as the differential scattering cross section. Upon integration of the VSF over all solid angles, the scattering coefficient σ_{sca} (from equation 2.9) can be defined as

$$\sigma_{sca} = \int_0^{2\pi}\int_0^{\pi}\beta(\theta,\varphi)\sin(\theta)d\theta d\varphi = 2\pi\int_0^{2\pi}\beta(\theta)\sin(\theta)d\theta. \tag{2.12}$$

If the scattering is assumed homogeneous across the scattering volume and the VSF is symmetric across all azimuth angles, then the integral over φ results in 2π. Another function of interest is the normalized VSF

$$\sigma_V(\theta,\varphi) = \frac{\beta(\theta,\varphi)}{\sigma_{sca}}, \tag{2.13}$$

known as the phase function. The phase function is also known as the scattering indicatrix used in some literature cited in this work [57], [58]. The phase function has not to do with optical phase shifts, but rather an origination from the astronomical field to describe solar fluxes.

The phase function is a quantity that depends strongly on the ratio of the particle radius a to the optical wavelength λ. Alluded to in Table 2.1, Mie theory is an analytical approach used to predict the scattered light distribution for particles with $a \sim \lambda$. The scattering occurs due to the particles containing a different refractive index compared to the surrounding medium. This change in refractive index exists only within the particle, which size is on the order of a wavelength. This creates electromagnetic resonances that can only be predicted by solving Maxwell's equations. Larger particles can be treated in other manners such as geometrical optics [55].

Mie theory predicts light scattered from a spherical shaped particle, which can be used to estimate the effects of a random medium by incoherently summing together the phase functions of many different sized particles [59], [60]. In reality a random medium does not consist of spherically shaped particles, which limits the exactness of Mie theory.

2.3.2.1 Scattering by Small Particles

Small particle scattering, also known as molecular scattering, is due to molecular movement and density changes where the radii of these particles are generally much smaller than the optical wavelength, $a \ll \lambda$ known as Rayleigh scattering. Within this regime the phase function for unpolarized incident light is [61]

$$\sigma_V(\theta) = \frac{3}{16\pi}(1+\cos^2(\theta)). \tag{2.14}$$

This form of phase function is mostly isotropic across all scattering angles leaving no favorable direction of scattering. Rayleigh scattering is generally considered much weaker than that of larger particles and assumed negligible over short propagation paths. An atmosphere containing no aerosols or turbulence is then limited by molecular scattering, which is generally not the case. This work will ignore the effects of molecular particle scattering in later sections as it does not add to significant losses of coherence.

2.3.2.2 Scattering by Large Particles

Large particle scattering occurs when $a/\lambda \sim 1$ and $a/\lambda \gg 1$, which adds a significant amount of structure to the phase function. As the particle size increases more light is scattered in the forward direction leading to effects similar to diffraction from an increasingly large circular aperture. This treatment is known as anomalous diffraction where the diffraction from a circular aperture is similar to a particle of the same size, but mainly holds true for larger particles where $a/\lambda \gg 1$ [54], [55].

The phase function is proportional to the magnitude of the scattered field amplitude calculated directly from Mie theory. If the incident light is unpolarized, the phase function can be written as

$$\sigma_V(\theta,\varphi,a) = \frac{1}{2k^2 C_{sca}(a)}(|S_1(\theta,\varphi,a)|^2+|S_2(\theta,\varphi,a)|^2), \tag{2.15}$$

where $k = 2\pi n_0/\lambda$ is the optical wavenumber, and n_0 is the refractive index of the propagation medium. $S_1(\theta,\varphi,a)$ and $S_2(\theta,\varphi,a)$ are the scattering amplitudes for the perpendicular and parallel field components respectively. Calculations of $C_{sca}(a)$, $S_1(\theta,\varphi,a)$, and $S_2(\theta,\varphi,a)$ are provided in detail in Appendix A. Examples of the phase function for the particle sizes 0.05 μm, 0.5 μm, 5 μm, 50 μm, and 250 μm are shown in Fig. 2.2(a) for near forward scattering angles of $0^\circ - 3^\circ$.

As the particle size increases there is more significant structure of the phase function at near-forward scattering angles. The amplitude of the phase function also strongly peaks in the forward direction. This change in the amount of scattering at each angle will become significant in later sections.

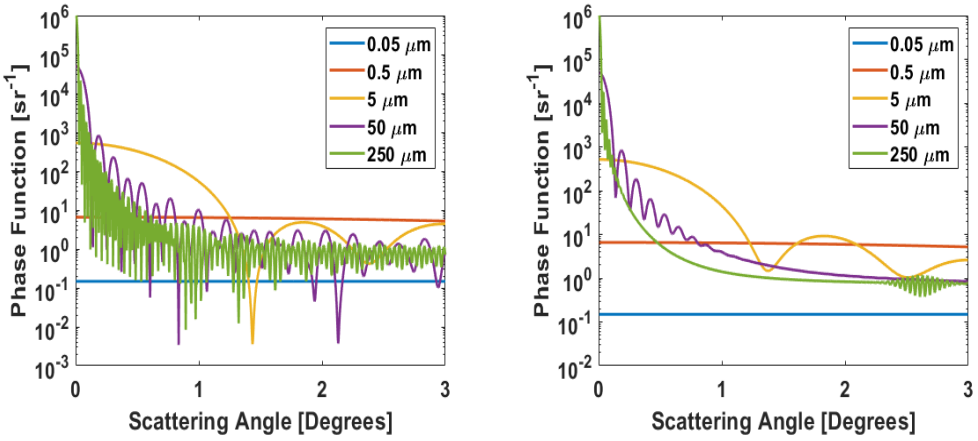

(a) (b)

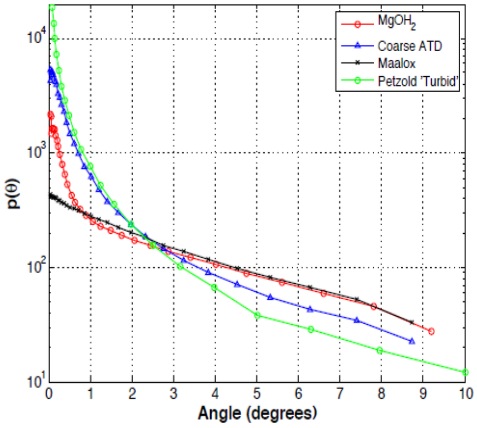

(c)

Figure 2.2: (a) Examples of single particle phase function for particle diameters 0.05 μm, 0.5 μm, 5 μm, 50 μm, and 250 μm as a function of polar scattering angle. (b) Examples of the phase functions for a Gaussian distribution of particle sizes with a standard deviation of 4.5 % of the mean value being 0.05 μm, 0.5 μm, 5 μm, 50 μm, and 250 μm. (c) Experimental phase function results for different polydisperse scattering media [62].

A feature of single particle scattering are the significant ripples that appear in the phase functions of larger particles as shown in Fig. 2.2(a). For a real medium, the scattering properties will depend not on a single particle, but on the particle distribution present. The scattering properties of the medium such as scattering coefficient, scattering cross section, and phase function depend on the particle distribution. The calculation of these

parameters is given in Appendix A to show how the equations change to become weighted averages over the particle distribution. The particle distributions used as an example are a Gaussian distribution with a mean value 0.05 μm, 0.5 μm, 5 μm, 50 μm, and 250 μm and standard deviation of 4.5 % of the mean value. Figure 2.2(b) shows how the phase function changes its forward scattering shape where the number of ripples are significantly reduced. Only at near forward scattering angles do ripples appear.

For a realistic volume of particles, a measurement of the phase function must be done to explicitly know how light will scatter. Figure 2.2(c) are measurements of the phase function for different scattering agents of $Mg(OH)_2$, A4-course test dust (ATD), Equate® (Maalox), and Petzold's oceanic measurements [63]. In comparison to a scattering medium containing a distribution of particles with smaller particle sizes, the phase function of realistic media are less forward peaked at near-forward scattering angles. The phase function values for Petzold turbid media decreases two orders of magnitude within the first three degrees whereas distribution seen to affect the beam fall up to three to five orders of magnitude within the first degree of scattering angle. This change in the phase function magnitude can have consequences on how it affects the coherence of laser light.

2.3.2.3 Quantification of Scattering Strength

Given a slab of particles of length dz, the phase function in equation 2.15 describes the scattering of light from the slab only in the "weak scattering" or "single scattering regime". This regime is dictated by the amount of scattering events that the incident light accumulates propagating through the medium. The number of scattering events is

described by the attenuation length or optical depth (OD) $\sigma_{ext}dz$ (assuming the extinction is isotropic along the slab).

The optical depth signifies the propagation length where the optical power, i.e. the squared magnitude of the field, decreases by a factor of $1/e$. If the extinction is mainly dominated by scattering ($\sigma_{ext} \sim \sigma_{sca}$), "single scattering" is satisfied when $\sigma_{sca}dz \ll 1$. If the medium contains a large optical depth then multiple scattering occurs where most forward coherence is lost and light scattering can be modeled using a Gaussian phase function [64], [65].

The optical depth is also related to the mean free path $l_s = 1/\sigma_{sca}$, which describes the distance an average number of photons travel before their direction is substantially altered due to multiple scattering events. Another interpretation of the optical depth is as a phase variance that dictates the strength of the phase fluctuations of the random medium [66].

A second form of "weak scattering" condition does not deal with the amount of scattering, but rather with the refractive index variation that initially causes phase delays resulting in scattered light. These limits are described by the Rayleigh-Gans-Debye (RGD) approximation [54], [55], [59]. This form of approximation perturbation method falls under a category that has been denoted as the Rytov method, Born approximation [50], Kirchhoff approximation [52], or phase screen approximation [67]. Each of them treat the phase variations, independent of the physical phenomena, as small perturbations to the incident field. This model can then be applied to an extended volume medium as an accumulation of weak scattering events [59].

The refractive index of a random medium $n(r) = n_0 + n_1(r)$ is described as the sum

of a mean value ($\langle n(r) \rangle = n_0$) and spatially varying component $n_1(r)$ with zero mean. For the weak scattering approximation to remain true two conditions must be satisfied:

$$\begin{aligned} \left| \frac{n_1(r)}{n_0} - 1 \right| &\ll 1 \\ 2ka \left| \frac{n_1(r)}{n_0} - 1 \right| &\ll 1 \end{aligned} \tag{2.16}$$

where a is the particle radius of interest, $n_1(r)$ is the spatially varying portion of the refractive index, and n_0 is the background index or mean value. The first condition means the phase delay created by the excess refractive index must be small to create no appreciable reflected light. The second condition, where most particle interactions break the weak scattering approximation, states that the incident wave must not undergo appreciable change in phase or amplitude upon entering the particle. Once the particle reaches the incident laser's wavelength or becomes larger than it, weak scattering cannot be met as the phase delay approaches multiple wavelengths [54], [55]. The effects of these two conditions will be made clear in the discussion of a turbulent medium in comparison to a turbid medium.

2.3.3 Turbulence Induced Refractive Index Variations

In contrast to the discussion in Section 2.3.2 that dealt with small scale refractive index variations created by particles, turbulence induced scattering occurs on larger length scales compared to the optical wavelength. Turbulent scattering is created by the medium's refractive index changes that is driven by temperature, pressure, humidity, density, or salinity gradients. As these variables are a randomly changing field in

three-dimensions a useful concept to use is that of velocity fluctuations. In a randomly changing velocity field dictated by flow it is the fluctuations in the velocity field not the mean value that are of concern. When a flow contains a uniform velocity it is called laminar otherwise, when a flow develops into a random state deemed "turbulent" due to larger fluctuations along the mean flow. A characteristic of turbulent flow are subfields known as turbulent eddies [50].

Eddies describe the scales of energy dissipation following from the energy cascade theory of turbulent flow. As energy randomly dissipates in the medium, a continuum of eddy sizes exists where kinetic energy is transferred from larger eddies to smaller eddies. This energy transfer depends on the viscosity of the medium's fluid that will eventually dissipate the energy as heat. Eddy sizes are limited based on the geometry of the location of energy dissipation where the largest eddy size is known as the outer scale, L_0, and the smallest size is known as the inner scale, l_0. Sizes of eddies between the inner and outer scale are known as the inertial subrange. Depending on the turbulence present, the inner scale notes the eddy scale size when energy is finally dissipated as heat that depends on the medium's viscosity.

Fluctuations of a medium's properties, mainly temperature gradients, drive the refractive index fluctuations that perturb optical wave propagation through the medium in question. Mathematically, this spatially varying refractive index is written as $n(\mathbf{r}) = n_0 + n_1(\mathbf{r})$, under the assumption that its time dependence is negligible. The medium's refractive index has a mean value $n_0 = \langle n(\mathbf{r}) \rangle$ and varying value $n_1(\mathbf{r})$ with zero mean statistics: $\langle n_1(\mathbf{r}) \rangle = 0$. This is due to the fluctuation time of the refractive index being slower than the time it takes the light to travel through the variation [50], [68].

As the refractive index variations $n(\mathbf{r})$ are a random field, the formalism in Sections 2.2.1 - 2.2.3 can be employed. The language of turbulence is typically written using structure functions as turbulence fluctuations are relationships among points in space rather than a field varying past a single point. Assuming the refractive index fluctuations are statistically homogeneous and isotropic, the refractive index structure function within the inertial subrange, $l_0 \ll r \ll L_0$, can be written as

$$D_n(r) = 2[B_n(0) - B_n(r)] = C_n^2 r^{2/3}, \tag{2.17}$$

where C_n^2 is known as the refractive-index structure constant. C_n^2 is connected physically to the strength of the fluctuations of the refractive index. Following from this structure function, for an idealized turbulence model, the refractive index power spectrum can be defined as

$$\Phi_{n,3}(\kappa) = 0.033 C_n^2 \kappa^{-11/3}. \tag{2.18}$$

This result is known as the Kolmogorov spectrum as it was first deduced by Andrey Kolmogorov in the 1940s to model eddy scales sizes in a three-dimensional volume. It remains valid only within the inertial subrange where $1/L_0 \ll \kappa \ll 1/l_0$ [69]. This result is not always physically accurate as there is sometimes a dissipation region where $\kappa \approx 1/l_0$. To account for these results, a simple analytic model with an outer and inner scale cutoff,

the modified von Kármán (MVK) spectrum, can be used, which is given by

$$\Phi_{n,3}(\kappa) = 0.033 C_n^2 \frac{e^{-(\kappa/\kappa_m)^2}}{(\kappa^2 + \kappa_0^2)^{11/6}}, \tag{2.19}$$

where $\kappa_0 = 2\pi/L_0$ and $\kappa_m = 5.92/l_0$. This model yields tractable analytic results for optical wave propagation, but experimental measurements by Hill *et al.* [70] showed that the atmosphere contains a dependence on the inner scale that results in a "bump" of the refractive index PSD due to a polynomial dependence on the inner scale. This empirical model is analytically fit by the modified atmospheric turbulence spectrum (MA)

$$\Phi_{n,3}(\kappa) = 0.033 C_n^2 \left[1 + 1.902 \left(\frac{\kappa}{\kappa_l}\right) - 0.254 \left(\frac{\kappa}{\kappa_l}\right)^{7/6}\right] \frac{e^{-(\kappa/\kappa_l)^2}}{(\kappa^2 + \kappa_0^2)^{11/6}}, \tag{2.20}$$

where $\kappa_l = 3.3/l_0$. This description of the refractive index fluctuations leads to the phase function of turbulent scattering to be written in terms of the refractive index PSD. Following from the Poynting vector, Tatarskii derived the turbulent phase function, assuming azimuth symmetry, to be [71]

$$\sigma_V(\kappa) = 2\pi k^4 \Phi_{n,3}(\kappa). \tag{2.21}$$

The phase function is written in terms of spatial wavenumber by using the relationship $\kappa = 2n_0 k \sin(\theta/2)$ [59], [71]–[73]. Examples of the previously mentioned refractive index PSDs are shown in Fig. 2.3(a) for an inner scale of 1 cm and outer scale of 10 m. The inner scale effects are related to the attenuation of large spatial frequencies whereas outer scale effects are reflected as the asymptote near small spatial frequencies.

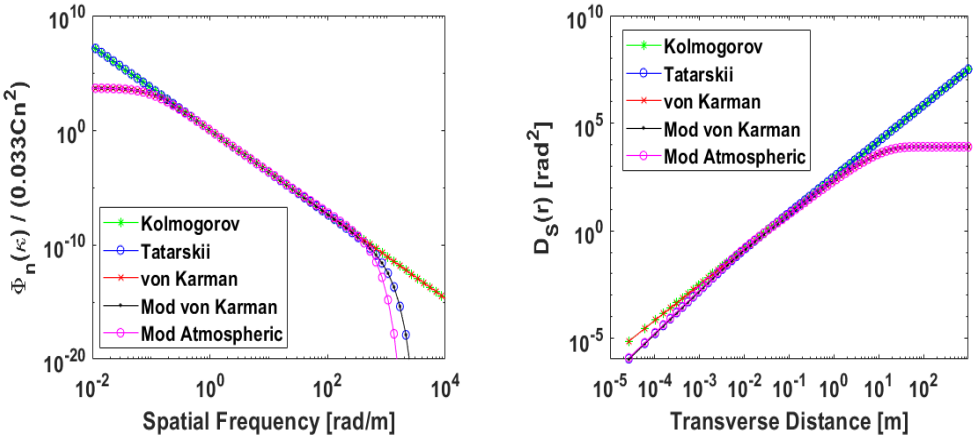

(a) (b)

Figure 2.3: (a) Various power spectra as a function of spatial wavenumber for $l_0 = 1$ cm, $L_0 = 10$ m, and $C_n^2 = 3.9 \times 10^{-16} \mathrm{m}^{-2/3}$. (b) Analytic structure function using various power spectra integrated from equation 2.6.

Figure 2.3(b) shows the refractive index structure function for each respective PSD calculated directly from equation 2.6. For spectra with a bounded outer scale, the effects are clearly seen for the MVK spectrum and MA spectrum in pink and red in Fig. 2.3(b) as the structure function reaches an asymptote. This will be used as a comparison point to a turbid medium in Section 3.6.2.

2.3.3.1 Quantification of Turbulence Strength

Depending on atmospheric conditions, PSD models for the refractive index fluctuations deal with eddy sizes that can vary in scale sizes between 1 mm and 100 m. These scale sizes, also known as scattering disks, are similar to particle sizes, therefore, the phase function will be strongly forward peaked similar to extremely large particles. Along with this analogy, the weak scattering assumptions in the conditions shown in equation 2.16 are both satisfied for turbulence perturbations. These are satisfied due to the scatter-

ing arising from variations in the atmosphere's molecular refractive index, meaning the size of the scattering particles are extremely small. Thus a small particle with a diameter on sub-micron scales will satisfy condition two in equation 2.16 and small refractive index fluctuations that induce less than a wavelength of phase delay which automatically satisfy condition one in equation 2.16.

In a similar manner to the mean free path of scattering through a medium containing particles, scattering by turbulent eddies has a similar parameter $\sigma_{T_{sca}}$ [51], [74], [75] for a bounded refractive index PSD with units of [m^{-1}] as

$$\sigma_{T_{sca}} = 4\pi^2 k^2 \int_0^{\infty} \Phi_{n,3}(\kappa)\kappa d\kappa = 1.3k^2 C_n^2 L_0^{5/3} U\left(1, \frac{1}{6}, \left(\frac{\kappa_0}{\kappa_m}\right)^2\right), \tag{2.22}$$

where $U(a,b,c)$ is a confluent hypergeometric function of the second kind. The equivalent "optical depth" for turbulence can then be thought of as $\sigma_{T_{sca}} dz$. This mean free path through turbulence is similar to the definition in equation 2.13 since equation 2.22 is an integral over the PSD rather than the particle phase function. It results in the same definition that the intensity of the laser drops by $1/e$ of its initial value upon propagation through this value. Notice that the PSD contains the turbulence strength depending on C_n^2 from the PSDs in the previous section.

This definition of the $1/e$ point of the field, is also equivalent to the spatial coherence radius as defined by Andrews and Phillips [50]. The dependence on propagation distance is included with the value of C_n^2 that is assumed to be isotropic across the propagation path. Although this is a useful factor for the comparison to particle scattering, turbulence strength on laser beam propagation typically is concerned with using image quality

based metrics. This definition of the mean free path is also hindered by the convergence of the PSD integral, which must be bounded using spectral models such as the MVK or MA. For the MVK spectrum, the mean free path is found to be $\sigma_{T_{sca}} = 0.39 C_n^2 k^2 L_0^{5/3}$. As most of this work used the Kolmogorov PSD for simplification of the turbulent fluctuations, a turbulence mean free path cannot be defined.

More popular definitions of turbulence scattering strengths are the spatial coherence radius (SCR), Fried parameter, and Rytov number. Each of their definitions and limitations are summarized in Table 2.2. Each of these parameters including the turbulence scattering length, $\sigma_{T_{sca}}$, are related to the $1/e$ point of the beam's electric field. The Fried parameter has a similar meaning and can be related to the SCR using $r_0 = 2.1\rho_0$. In contrast to the other two metrics, the Rytov number is rather a measurement of plane wave intensity fluctuations defining a region of weak $\sigma_R^2 < 0.1$, moderate $0.1 < \sigma_R^2 < 1$, and strong intensity fluctuations $\sigma_R^2 > 1$. The Rytov number is a non-dimensional parameter that can be used to quantify general regions rather than scale size. Each metric depends on the propagation distance of the wave from a source (z_s) point to observation point (z_o).

Parameter	Plane Wave	Spherical Wave
SCR (ρ_0)[m]	$\left(1.46k^2 \int_{z_s}^{z_o} C_n^2(z) dz\right)^{-3/5}$	$\left(1.46k^2 \int_{z_s}^{z_o} C_n^2(z) \left(\frac{z}{z_s - z_o}\right)^{5/3} dz\right)^{-3/5}$
Fried (r_0) [m]	$\left(0.423k^2 \int_{z_s}^{z_o} C_n^2(z) dz\right)^{-3/5}$	$\left(0.423k^2 \int_{z_s}^{z_o} C_n^2(z) \left(\frac{z}{z_s - z_o}\right)^{5/3} dz\right)^{-3/5}$
Rytov (σ_R^2) [a.u]	$1.23k^{7/6} C_n^2 (z_o - z_s)^{11/6}$	$0.5k^{7/6} C_n^2 (z_o - z_s)^{11/6}$

Table 2.2: Definitions of spatial coherence radius, Fried parameter, and Rytov number for plane wave and spherical wave propagation through a turbulent medium.

The main reason for defining these metrics instead of a single scattering length is the

ability to efficiently denote the cumulative effects of turbulence across some propagation distance. A scattering length quantifies the length until one scattering event and in the same process defines the length where the field reaches its $1/e$ point, but does not denote a strength of how the distortion affects spatial resolution. This is where the Fried parameter and SCR are useful as they can denote the limitations on the spatial resolution of an optical system, but not the distance at which this occurs like a mean scattering length.

2.4 Summary: Optical Properties of a Random Medium

In a random medium the scale size, correlation function, and strength of the refractive index fluctuations are the most important quantities to characterize to describe light scattering. A turbid medium is typically characterized with refractive index scale sizes comparable to the wavelength that induces scattering of light in all directions. The phase function contains the spatial information about the scattering whereas the optical depth determines the strength. In contrast, a turbulent medium contains scattering only in the near-forward direction as turbulent eddies are typically much larger than the wavelength. The refractive index PSD contains the spatial information about the scattering properties whereas the Rytov number, Fried parameter, or C_n^2 can quantify scattering strength in specific cases. Each of the scattering conditions and scattering strength metrics will be used throughout the rest of this work.

Chapter 3: Formalism of Beam Propagation using Statistical Optics

In most studies a distinction is made in terminology of a medium containing turbulence or particles. A turbulent medium contains only phase fluctuations created by turbulent refractive index variations, much larger than the wavelength such that light scattering is in the forward direction. However, a turbid medium contains particulate matter comparable to the wavelength that invokes an electromagnetic resonance that must be described using a full field treatment. Each random medium is considered "random" since the phase fluctuations of the optical wave are due to random changes in the refractive index.

In the turbid medium case, the directionality of light depends on the particles radius to wavelength ratio a/λ. When a/λ is small a turbid medium can strongly diffuse light into all angles $0^\circ - 180^\circ$. Quantification of laser scattering can be done using the radiative transfer equation (RTE) within the small-angle approximation (SAA) [57], [58], [76]–[79] also known as the paraxial approximation. In contrast, strong turbulent scattering does diffuse the incident beam into mostly forward scattering angles [67]. However, turbulent scattering is typically derived from the stochastic Helmholtz equation within the paraxial approximation that does not equate to the language of the RTE. Thus, approaching the scattering problem must be done using one of the two methods. In this work, the RTE

is chosen as the radiative transfer method has been seen as an equivalent derivation to the stochastic Helmholtz equation to describe near-forward scattering [80], [81]. The solution to the RTE is then connected to the solution of the stochastic Helmholtz equation to leverage traditional turbulent medium simulations for a turbid medium.

The goal is to maintain the greatest amount of generality between the two mediums to understand how both affect the coherence of a laser beam in a similar manner. This will make it possible to extrapolate the environmental effects directly to OAM carrying beams using Fourier optics. A general method to describe the coherence of a laser beam propagating through both a turbid and turbulent medium is the autocorrelation of the field known as the mutual coherence function (MCF). The MCF will be derived for both random media and then be connected with its optical transfer function (OTF) and transmittance function. Specifics of the transmittance function are discussed in Section 3.3 followed by the MCF in Section 3.4. Beam propagation through a turbulent and turbid medium will be discussed in Sections 3.5 and 3.6 by mirroring the derivation of the wave equation and spatial phase perturbations using the formalism of the wave structure function.

3.1 Radiative Transfer Equation

The RTE within the SAA that describes spatial dispersion of a monochromatic laser beam through a scattering layer is written as

$$\left(\frac{\partial}{\partial z}+\vec{n}_{\perp}\cdot\nabla_{\perp}+\sigma_{ext}(z)\right)I(r_{\perp},z,\vec{n}_{\perp})=\frac{\sigma_{sca}(z)}{4\pi}\iint d^{2}\vec{n}'_{\perp}p(|\vec{n}_{\perp}-\vec{n}'_{\perp}|,z)I(r_{\perp},z,\vec{n}_{\perp}). \tag{3.1}$$

The notation of the RTE follows from Zege *et al.* [58] and is related to that of Tatarskii [71] for convenience with the sections on turbulence is as follows: $\vec{n}_{\perp}\rightarrow(\hat{x},\hat{y})$, $\vec{n}'_{\perp}\rightarrow\vec{k}_{m}$, $r_{\perp}\rightarrow(x^{2}+y^{2})^{1/2}$, $p(|\vec{n}_{\perp}-\vec{n}'_{\perp}|,z)\rightarrow\sigma_{V}(\theta,\varphi)$, $\nabla_{\perp}=\partial/\partial x+\partial/\partial y$, and $I(r_{\perp},z,\vec{n}_{\perp})\rightarrow I(r,\phi,z)$ is the laser beam intensity distribution. The notation is used for turbulence in Section 3.2 when discussing the stochastic Helmholtz equation.

The RTE is difficult to solve by either numerical or analytical methods. However, the physical interpretation is more straightforward as the RTE describes how a laser's input intensity translates to the output intensity. The first two terms on the left hand side of equation 3.1 is the spatial change in intensity over a length. The third term is the total intensity loss due to attenuation and scattering. The right hand side, proportional to the phase function, describes the loss of intensity to scattering in all directions through space.

Two approximations of the RTE that lead to analytical solutions are the diffuse approximation and SAA. In this work the SAA will be the main simplifying assumption that limits the extent of the intensity to near-forward angles due to a laser's high directionality. The diffuse approximation is not used in this work as most scattering effects

of interest occur when coherence is maintained before the diffuse region. Otherwise if forward coherence is completely lost the use of the diffuse regime is appropriate.

3.1.1 Solution to the RTE within the SAA

The general solution to the integro-differential equation in equation 3.1 can be found using the spatial correlation function $\Gamma(...)$ discussed explicitly in Section 3.4. The general form is [57], [58]

$$\Gamma(r_1, r_2, z_o) = \Gamma_B(r_1, r_2, z_o) e^{-\int_{z_s}^{z_o} [\sigma_{ext}(z) - \sigma_{sca}(z)\sigma_V(|r_1 - r_2|, z)] dz} \tag{3.2}$$

where $\Gamma_B(...)$ is the source correlation function. The spatial correlation function is the 2D Fourier transform of the optical intensity $I(r', z)$

$$\Gamma(r_1, r_2, z_o) = \iint I(r', \kappa, z_o) e^{-ik\vec{r'}\cdot\vec{\kappa}} d^2\kappa. \tag{3.3}$$

The point made in this section is that solutions to the RTE can be found for specific forms of intensity distributions. However, this form of solution does not provide a connection to the spatial phase directly. The connection is made to the spatial correlation function instead. The relationship of the intensity to the MCF and thus the phase correlations will be made clear in Section 3.6 [57], [58], [80], [82].

3.2 Stochastic Helmholtz Method

For a turbulent medium the more common approach to describe laser propagation is done using the stochastic Helmholtz equation [50]. This method was first notably used by Tatarskii [71], [83] who used the first order Rytov approximation and independently by Yura [84]–[87] from the extended Huygens-Fresnel principle. These methods are equivalent to the derivation from transport theory and a method solving the Bethe-Salpeter equation summarized in Fante and Poirier [82]. The methods by Tatarskii [71] and Yura [84] are the most prominent and adopted by Andrews and Phillips [50]. The argument is briefly repeated here for comparison to transport theory to show how the stochastic Helmholtz equation does not take into account higher angle scattering from particle scattering. This method is only valid within the weak scattering limit of the RGD approximation where the refractive index PSD is proportional to the differential scattering cross section (or VSF) [59].

First, the stochastic Helmholtz equation is time independent leaving us with the scalar Helmholtz equation. It is deemed a scalar equation since the electric field profile of the beam, $E(\mathbf{r}) = U(\mathbf{r})e^{i\omega t}$, can be simplified into its vector components such that it describes the scalar field amplitude, $U(r,\phi,z)$. Under the assumption that polarization effects can be neglected, the wave equation through a turbulent medium is written as [50]

$$\nabla^2 U(r,\phi,z) + k^2 n^2(r) U(r,\phi,z) = 0, \tag{3.4}$$

where $\nabla^2 = \partial^2/\partial x^2 + \partial^2/\partial y^2 + \partial^2/\partial z^2$ is the Laplacian in Cartesian coordinates, $\omega =$

$2\pi f = kv$, v is speed of light in the medium, f is the optical frequency, $v = c/n_0$, c is the speed of light in vacuum. With the focus being on propagation of low-divergence coherent beams, the SAA can be applied to equation 3.4 resulting in the Fresnel approximation or parabolic wave equation

$$\nabla_{\perp}^2 U(r,\phi,z) + k^2 n^2(r) U(r,\phi,z) + 2ik\frac{\partial U(r,\phi,z)}{\partial z} = 0, \tag{3.5}$$

where $\nabla_{\perp}^2$ is the transverse Laplacian operator. The refractive index in equation 3.5 can be simplified for the atmospheric case using $n^2(r) \approx n_0 + 2n_1(r)$ with a mean index of 1 such that $n^2(r) \approx 1 + 2n_1(r)$.

3.2.1 Solution to Parabolic Wave Equation

The method of choice to solve equation 3.5 will be the Huygens-Fresnel integral due to its simpler analytic and numerical treatment of optical wave propagation. To generalize this solution to a random medium, the medium perturbations, $\psi(r,s)$, are included leading to the extended Huygens-Fresnel principle (EHFP) [50]. It is used to describe the relationship among the laser field U_s at the source plane and the field U_o at an observation plane located at propagation distances z_s and z_o, respectively. An illustration of the propagation geometry that satisfies the EHFP is shown in Fig. 3.1 with its quantitative definition in equation 3.6.

$$U_o(r,z_0) = \frac{-ike^{ikL}}{2\pi L}\iint d^2 s\, U_s(s,z_s) e^{\frac{ik|s-r|^2}{2L} + \psi(r,s)}. \tag{3.6}$$

Within the EHFP (equation 3.6) the propagation distance is $L = z_o - z_s$ with coordinates for the source plane being s and for the observation plane r. A discussion how to solve this equation numerically will be given in Chapter 5, but the reader is directed to Schmidt [88] and Fleck *et al.* [89], [90] for further clarification of numerical results.

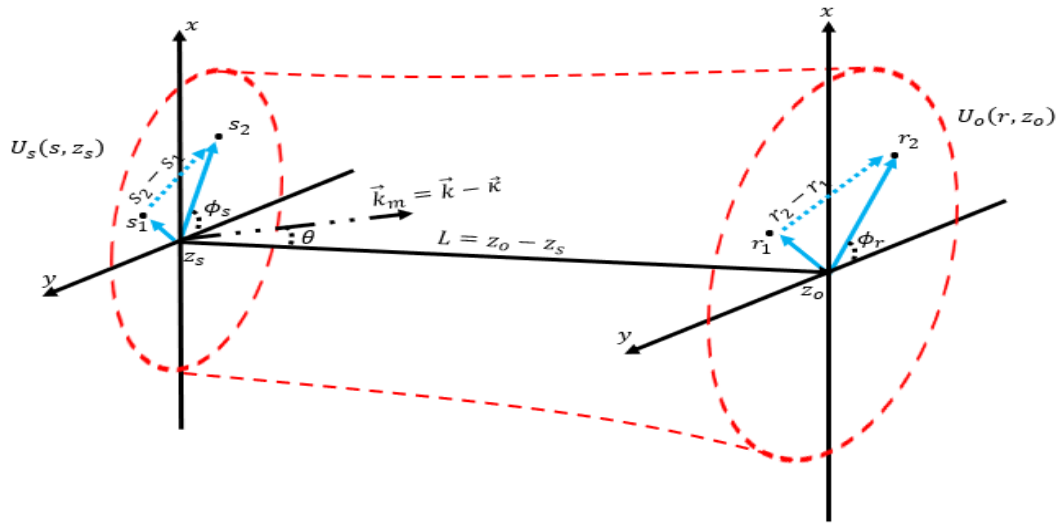

Figure 3.1: Coordinate geometry describing laser beam propagation using the Huygens-Fresnel principle and its coherence properties among two points in space used for the mutual coherence function. k_m is the scattering wave vector direction and κ is the spatial wavenumber in the far-field and $\vec{k}$ is the wave vector.

3.3 Transmittance Functions

In statistical optics, the transmittance function is a complex quantity that describes how an optical element, system, or random medium changes the spatial distribution of a laser beam's amplitude and phase [91]. A general transmittance function is defined, similar to a laser beam wavefront, as

$$t(x,y) = D(x,y)e^{ik\theta(x,y)}, \tag{3.7}$$

where $D(x,y)$ is the amplitude distribution and $\theta(x,y)$ is the spatial distribution of phase shifts. A transmittance function can be used to derive the OTF and PSF of an optical system. It will be used to simulate phase screens for a turbulent and turbid medium discussed in Sections 3.5.1 and 3.6.1. Their computational generation for a random medium is discussed in Appendix B. A phase screen is a transmittance function containing a varying phase distribution with unit amplitude, therefore, there are no amplitude variations. Amplitude variations occur upon propagation when the random phase shifts create interference.

Figure 3.2 visualizes the connection of the complex transmittance function to other optical system quantification metrics such as OTF, modulation transfer function (MTF), phase transfer function, and incoherent PSF. The main equality of interest is the autocorrelation of the transmittance function that can be equated to a scaled version of the OTF. This fact is used to extrapolate the phase screen autocorrelation function to describe how a random medium affects the frequency response of an optical system and OAM carrying beams.

3.4 Mutual Coherence Function

An important quantity to define is a laser beam's second order statistical moment, or autocorrelation function, known as the MCF or cross spectral density (CSD). The MCF is defined as

$$\Gamma_2(r_1, r_2, z) = \langle U(r_1, z) U^*(r_2, z) \rangle , \tag{3.8}$$

where $\langle ... \rangle$ denotes an ensemble average. An ensemble average is used assuming that the medium's statistics are ergodic, which allows a temporal average to be represented as the average of independent spatial realizations of the random medium [50]. The MCF describes the amount of correlation or similarity between spatial points along a beam's wavefront illustrated in Fig. 3.1. Note that this is directly calculated using a 2D convolution integral that can be done using Fourier transforms. A few important quantities that describe laser beam propagation can be derived from the MCF such as the OTF, average intensity, beam spread, degree of coherence, and beam wander [50].

Using the RTE within the SAA, the solution in Section 3.1.1 describes the intensity profile through a random medium, but not the optical field. Using the stochastic Helmholtz equation, the laser field is seen to satisfy a general wave equation, which the MCF also satisfies [92]. To relate the solution of a wave equation to the solution of the RTE, the Wiener-Khinchin theorem is used via equation 3.3. The MCF containing the relationship between the source and observation plane using the EHFP (equation 3.6) yields

$$\begin{aligned}\Gamma(r_1, r_2, z_o) &= \langle U(r_1, z_o) U^*(r_2, z_o) \rangle \\ &= \frac{k^2}{4\pi^2 L^2} \iiiint d^2 s_1 d^2 s_2 \langle U_s(s_1, z_s) U_s^*(s_2, z_s) e^{\frac{ik}{2L}\left(|s_1 - r_1|^2 + |s_2 - r_2|^2\right)} e^{\psi(s_1, r_1) + \psi^*(s_2, r_2)} \rangle .\end{aligned} \tag{3.9}$$

Equation 3.9 describes the full beam's coherence properties where the laser source MCF is contained in the first term $\Gamma_B(s_1, s_2, z_s) = U_s(s_1, z_s) U_s^*(s_2, z_s)$. This equation is a solution to both the radiative transfer equation with the SAA and the stochastic Helmholtz

equation. The analytical focus in this chapter is on coherent beam propagation, unless stated otherwise, that leads the ensemble average in equation 3.9 to only include the randomly fluctuating random medium complex perturbations $\psi(r,s) = \chi(s,r) + iS(s,r)$, where $\chi(s,r)$ is the log-amplitude and $S(s,r)$ is the phase. If a partially coherent beam is implemented the laser source MCF will fluctuate. This case is briefly discussed in Section 3.4.1.

The MCF can be used to study the spatial frequency response of an optical system to a random medium using the OTF, $\mathscr{H}(\kappa_x, \kappa_y)$. For coherent imaging, the properties of Fourier optics can be used to relate the MCF to the OTF of an optical system in equation 3.10 [91]. To illustrate these relationships Fig. 3.2 shows a flow chart illustrating mathematical relationships between functions used for coherent imaging. The spatial frequency response of the system is called the MTF or the magnitude of the OTF. By knowing the MTF, which is a function of the phase statistics, the complex transmittance function can be reconstructed. If the transmittance function of the medium can be created information about the statistical nature of the medium can be further studied.

$$\begin{aligned}
\mathscr{H}(\kappa_x, \kappa_y) &= \frac{\mathscr{F}_2\{|h(x,y)|^2\}}{\iint |h(u,v)|^2 du dv} \\
&= \frac{\iint H(p',q') H^*(p'-\kappa_x, q'-\kappa_y) dp' dq'}{\iint |H(p',q')|^2 dp' dq'} \\
&= \frac{\iint t(x,y) H^*(x-\kappa_x, y-\kappa_y) dx dy}{\iint |t(x,y)|^2 dx dy} \\
&= t(x_1,y_1) t^*(x_2,y_2)\big|_{x=\frac{f_i \kappa_x}{k}, y=\frac{f_i \kappa_y}{k}},
\end{aligned} \tag{3.10}$$

where $\mathscr{F}_2$ is the Fourier transform operator, $h(x,y)$ is the amplitude spread function and $H(\kappa_x, \kappa_y) = \mathscr{F}_2\{h(x,y)\}$ is the amplitude transfer function. From step 1 to 2 in equation

3.10 the Wiener-Khinchin theorem is used and from step 3 to 4 the following relationship between the ATF and transmittance function is applied

$$H(\kappa_x,\kappa_y)=\mathscr{F}_2\left\{\frac{k}{f_i}\mathscr{F}_2\{t(x,y)\}|_{\kappa_x=\frac{kx}{f_i},\kappa_y=\frac{ky}{f_i},}\right\} \quad =\frac{f_i}{k}t\left(\frac{f_i\kappa_x}{k},\frac{f_i\kappa_y}{k}\right). \tag{3.11}$$

The amplitude transfer function shows that the complex beam amplitude, optical system, and random medium all play a role in determining the bandlimit of the system. The transmittance function sets the passband to the diffraction limited spot size. In addition to the diffraction limit, the optical system may introduce lens aberrations that can be compounded by random medium distortions that limit the system further. The system MTF can be derived in terms of the separation distance r typically used in theoretical studies of a random medium. Equation 3.10 states that the OTF of an optical system is a rescaled form of the MCF, therefore, r can be replaced by $f_i\kappa/k$ to determine an optical system's spatial frequency [61]. The effective focal length of the optical system is f_i. This essentially leaves the OTF as a scaled version of the MCF.

Using the formalism of the MCF and OTF, a useful quantity referred to as the image quality or Strehl Ratio. It is defined as the ratio of the true system MTF over the diffraction limited MTF as given in equation 3.12. Typically it is measured at the on-axis ($\rho=0$) value of the MTF resulting in the exponential of equation 3.12 to vanish only leaving the MTF ratio.

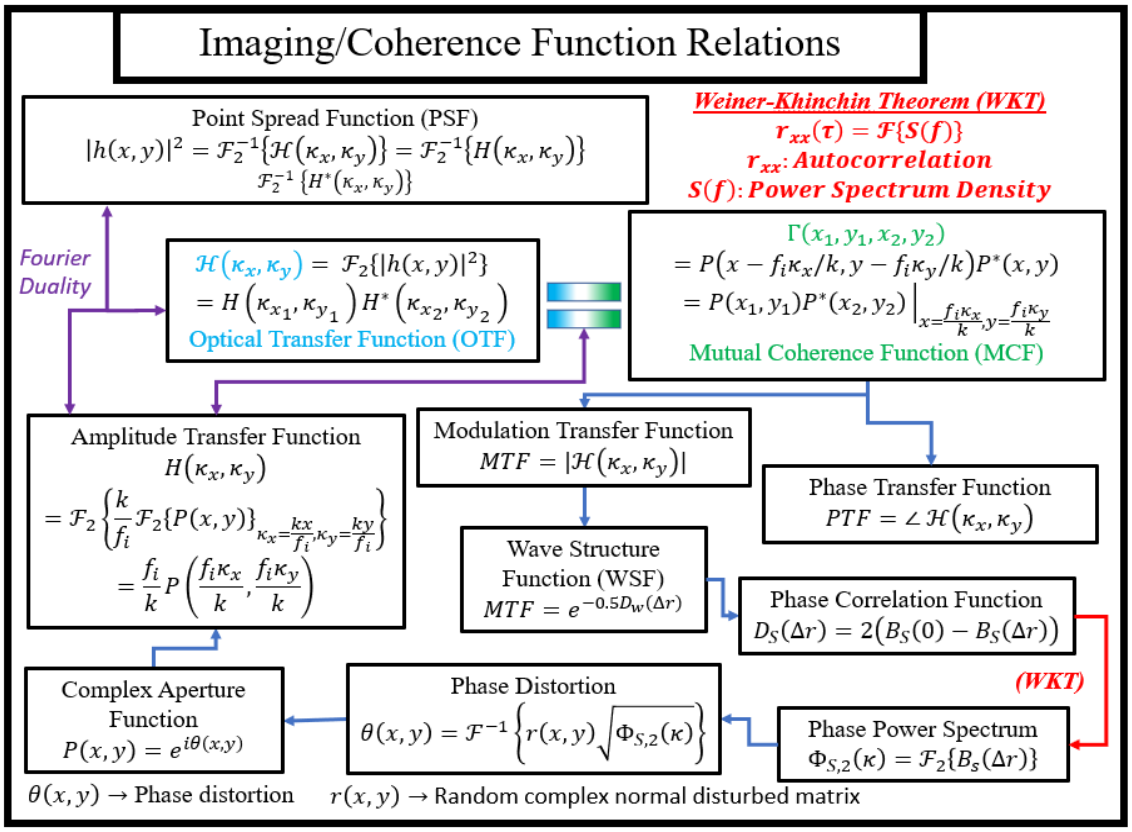

Figure 3.2: Flowchart describing the relationship between the MCF, OTF, PSF, WSF, and other optical system quantities of interest.

$$SR(\rho,\Theta) = \frac{\left|\int_0^\infty\int_0^{2\pi} P(r,\phi)e^{-i\frac{2\pi\rho r}{\lambda f}\cos(\Theta-\phi)}rdrd\phi\right|^2}{\left|\int_0^\infty\int_0^{2\pi} P_0(r,\phi)e^{-i\frac{2\pi\rho r}{\lambda f}\cos(\Theta-\phi)}rdrd\phi\right|^2}. \tag{3.12}$$

In equation 3.12, $P(r,\phi)$ is defined as the system pupil function, which is the product of the system transmittance function and the beam profile,

$$P(r,\phi,z) = t(r,\phi,z)U(r,\phi,z). \tag{3.13}$$

The pupil function for an ideal system is found by taking the transmittance function to be

of the system aperture denoted as $P_0(r,\phi,z)$. This pupil function is said to be diffraction limited as it depends only on the beam profile and size of the input aperture. The focus of the system may be limited by the size of the beam or aperture, but no other distortions play a role unless aberrations are present.

3.4.1 Impact of a Partially Coherent Laser Source

Partially coherent light is created from a source which contains limited spatial correlations meaning that a bandwidth is imposed on the MCF [92]. The normalized MCF, known as the complex degree of coherence (DOC), is used to quantify the coherence of the light source defined as

$$\mu(r_1,r_2,z) = \frac{|\Gamma(r_1,r_2,z)|}{(\Gamma(r_1,r_1,z)\Gamma(r_2,r_2,z))^{1/2}}. \tag{3.14}$$

When $\mu(r_1,r_2,z) = 1$ the light is coherent, if $\mu(r_1,r_2,z) = 0$ the light is incoherent, and when $0 < \mu(r_1,r_2,z) < 1$ the light is said to be partially coherent. Partially coherent light commonly is described by a DOC of a Gaussian form that depends on $|r_2 - r_1|$ that can be created by passing a laser beam through a ground glass diffuser.

In general, a notable effect of partially coherent light is that as $\mu(r_1,r_2,z)$ decreases, the laser loses its ability to create a high contrast interference pattern. This leads to two outcomes of interest: reduced intensity variance upon propagation through a random medium and the ability to be shaped into an OAM beam. This trade-off will briefly be explored in this thesis for an OAM based sensing modality in Section 5.2.4.

3.5 Wave Propagation through a Turbulent Medium

The full treatment of studying laser beam propagation pieces together the tools from the following sections. Propagation starts with a coherent laser beam travelling from a source plane to an observation plane, illustrated in Fig. 3.1, with turbulent phase perturbations $\psi(r,s)$ with an MCF given by equation 3.9. The focus will be on second order statistics and thus the MCF of the beam that contains the autocorrelation function of the phase perturbations. Using the discussion in Section 3.4 to relate the MCF to the OTF, the results can be extrapolated to determine the frequency response of an optical system. The MCF of a turbulent and turbid medium will be used to show the effects of a random medium on a laser carrying OAM in the next chapter.

3.5.1 Turbulent Medium MCF

Applying the EHFP to a coherent Gaussian beam propagating through a turbulent medium starting from the general form of the MCF in equation 3.9, the ensemble average over the random phase variations can be simplified as

$$\begin{aligned}
\left\langle e^{\psi(s_1,r_1)+\psi^*(s_2,r_2)}\right\rangle &= \left\langle e^{\chi(s_1,r_1)+\chi(s_2,r_2)+i(S(s_1,r_1)-S(s_2,r_2))}\right\rangle \\
&= \left\langle e^{\frac{1}{2}[\chi(s_1,r_1)-\chi(s_2,r_2)]^2-\frac{1}{2}[(S(s_1,r_1)-S(s_2,r_2))]^2}\right\rangle \\
&= e^{-\frac{1}{2}D_\chi(s_1,r_1,s_2,r_2)-\frac{1}{2}D_S(s_1,r_1,s_2,r_2))} \\
&= e^{-\frac{1}{2}D_w(s_1,r_1,s_2,r_2)},
\end{aligned} \tag{3.15}$$

where $D_w(s_1, r_1, s_2, r_2)$ is the wave structure function (WSF) assuming the perturbation statistics are Gaussian distributed with zero mean. The moment generating function is used $\langle e^{\alpha t} \rangle = e^{-\frac{1}{2}\alpha^2 \langle t^2 \rangle}$ from line one to two [93], [94]. This leaves

$$\Gamma(r_1, r_2, z_o) = \frac{k^2}{4\pi^2 L^2} \iiint d^2 s_1 d^2 s_2 \langle U_s(s_1, z_s) U_s^*(s_2, z_s) e^{\frac{ik}{2L}\left(|s_1 - r_1|^2 + |s_2 - r_2|^2\right)} e^{-\frac{1}{2} D_w(s_1, r_1, s_2, r_2)}, \tag{3.16}$$

as the general MCF in terms of WSF defined as $D_w = D_\chi + D_S$. D_χ and D_S are the the log-amplitude and phase structure functions. The WSF is typically assumed to be equal to the phase structure function when the scales across the wavefront are greater than the first Fresnel zone ($\sqrt{L/k}$) and less than the outer scale [50]. Using this assumption, the focus turns to only the phase structure function defined for the limiting cases of a plane wave and spherical wave as [51]

$$\begin{aligned} D_{S_{pw}}(r) &= 8\pi^2 k^2 L \int_0^\infty \kappa \Phi_{n,3}(\kappa)[1 - J_0(\kappa r)] d\kappa, \\ &= 2\sigma_{T_{sca}} L \left(1 - \frac{\int_0^\infty \Phi_{n,3}(\kappa) J_0(\kappa r) \kappa d\kappa}{\int_0^\infty \Phi_{n,3}(\kappa) \kappa d\kappa}\right) \end{aligned} \tag{3.17}$$

$$\begin{aligned} D_{S_{sw}}(r) &= 8\pi^2 k^2 L \int_0^1 \int_0^\infty \kappa \Phi_{n,3}(\kappa)[1 - J_0(\kappa r \eta)] d\kappa d\eta \\ &= 2\sigma_{T_{sca}} L \left(1 - \frac{\int_0^1 \int_0^\infty \Phi_{n,3}(\kappa) J_0(\kappa r \eta) \kappa d\kappa d\eta}{\int_0^\infty \Phi_{n,3}(\kappa) \kappa d\kappa}\right), \end{aligned} \tag{3.18}$$

each of which are derived using equations 2.5 and 2.6 where J_0 is a zeroth order Bessel function of the first kind. For more specific analytical treatments of beam propagation the reader is directed towards [50]. The spherical wave WSF contains an extra integration

variable that represents the divergence of the spherical wave from the source plane to observation plane [84]. For a Gaussian beam, the spherical wave structure function can be used or an explicit form of the Gaussian beam MCF [50]. Each WSF is written in terms of the turbulence mean scattering length ($\sigma_{T_{sca}}$) to show the similarity to the optical depth of a turbid medium in Section 3.6 only for bounded refractive index PSDs. Defining these metrics can now be used to predict average second order beam statistics.

3.5.2 Turbulent Medium Phase Power Spectrum

In order to find a single phase realization, the turbulent phase must be related to the refractive index power spectrum. This can be done by defining the phase power spectrum $\Phi_{S,m}(\kappa)$ that depends on the spatial wave number, which contains the same statistical properties and assumptions as equations 2.5 and 2.6. Another assumption to reduce the dimensionality of the phase PSD is using equation 2.2 that says the refractive index fluctuations are uncorrelated along the propagation direction using the Markov approximation

$$\begin{aligned} B_n(\mathbf{r},z) &= \frac{1}{2\pi^3}\iiint \Phi_{n,3}(\boldsymbol{\kappa},\kappa_z)e^{i(\boldsymbol{\kappa}\cdot\mathbf{r}+\kappa_z z)}d^2\boldsymbol{\kappa}d\kappa_z, \\ &= \frac{1}{2\pi^3}\int e^{i\kappa_z z}d\kappa_z \iint \Phi_{n,3}(\boldsymbol{\kappa},\kappa_z)e^{i\boldsymbol{\kappa}\cdot\mathbf{r}}d^2\boldsymbol{\kappa} \\ &= 2\pi B_n(\mathbf{r})\delta(z), \end{aligned} \tag{3.19}$$

where the phase PSD can be defined using the two-dimensional refractive index PSD, $\Phi_{n,2}(\kappa)$, as (chapter 6.2 of Tatarskii [71])

$$\Phi_{S,2}(\kappa) = 2\pi k^2 L\Phi_{n,2}(\kappa). \tag{3.20}$$

The two-dimensional PSD describes the strength of various spatial frequencies present in the phase perturbations of the optical medium. The spatial frequencies can also be related to the various lens aberrations by modeling turbulent phase perturbations using a series of Zernike polynomials [95].

For this work, the phase perturbations are modeled using the phase screen approximation. It assumes the phase shifts are sufficiently weak such that a three-dimensional volume can be compressed to a multiplicative transmittance function that models one statistical realization as $\exp(i\theta_T(x,y))$. The random phase shifts induced by turbulence $\theta_T(x,y)$ are assumed to be Fourier transformable such that

$$\theta_T(x,y) = \sum_{n=-\infty}^{\infty} \sum_{m=-\infty}^{\infty} \tilde{c}_{nm}(\kappa_x, \kappa_y) e^{i\left(x\kappa_x + y\kappa_y\right)}, \tag{3.21}$$

where κ_x and κ_y are the spatial frequency variables, n and m are the Fourier component indices, and $\tilde{c}$ are the randomly varying Fourier coefficients proportional to the phase PSD ,$\langle |c_{nm}|^2 \rangle \sim \Phi_S(\kappa)$. This representation of the phase fluctuations lends itself to a simple computational implementation using the fast Fourier transform (FFT) discussed in Appendix B.

Examples of the WSF and MCF for a plane wave following from a Kolmogorov refractive index power spectrum (equation 2.18) are shown in Fig. 3.3(a-b). The blue line represents the simulated data using the phase screen generation routine described in Appendix B and the red line is the theoretical value of the WSF from equation 3.16 and MCF from equation 3.15. Figure 3.3(a) shows three phase structure functions averaged

over 500 random realizations for three strengths of turbulence with Rytov numbers 0.1, 1, and 10. The main difference between these curves is the phase variance that dictates the magnitude of the WSF. The weakest turbulence strength MCF is represented by diamonds that can noticeably begin to deviate from theory at larger distances of r due to limitations of the low frequency components from a finite numerical grid. As the turbulence becomes more moderate (circles), the MCF fits theory well due to the large frequency distortions being suppressed due to decorrelation. The same effect occurs for the strongest turbulence case (squares) that contains the least amount of correlation represented by the small width of the MCF. The grid parameters contain a 512x512 grid with pixel pitch of 9.8 μm and a physical size of 5 mm.

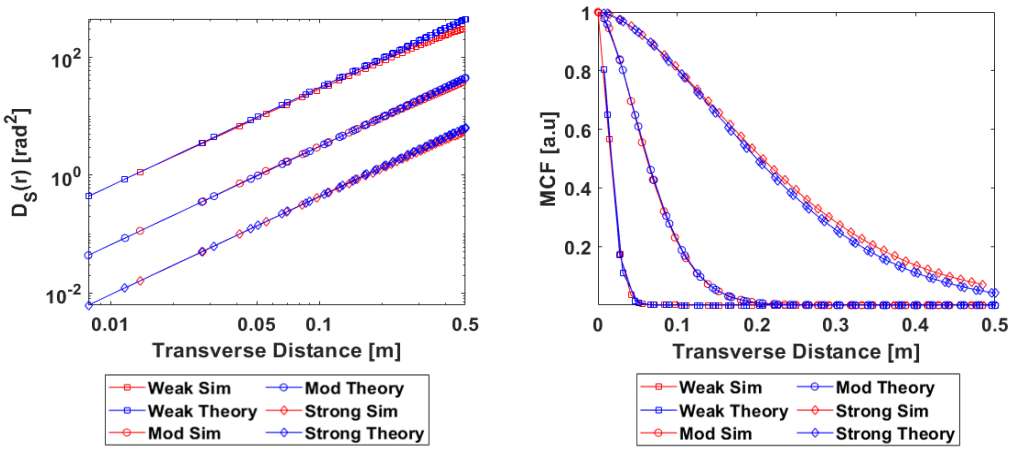

(a) (b)

Figure 3.3: (a) Examples of the plane wave WSF in a turbulent medium following a Kolmogorov PSD for the following Fried parameters of: 52 cm (squares), 16 cm (circles), and 4 cm (diamonds). (b) Plane wave MCF in a turbulent medium for the previous WSF for the same fried parameters. Analytic results are in blue from equation 3.17 whereas simulated are in red.

Figure 3.3(b) shows the respective MCF of the previous WSFs for three strengths of turbulence. The squares represent the weak regime where the simulated and theoretical

MCF deviate slightly due to the larger scale sizes introduced in the weaker turbulence leading to numerical errors. For moderate and stronger turbulence scales the MCF values fit well with theory. If the MCF is to be rescaled to determine a system OTF, the larger turbulence strength will act as a lowpass filter blurring any high spatial frequencies.

3.6 Wave Propagation through a Turbid Medium

For a turbid medium, the statistical treatment is similar to a turbulent medium with the starting point being the study of the MTF using the MCF [61], [79], [86], [96]–[98]. A new suggested treatment of the turbid medium MTF in this work can be used to describe the turbid phase PSD for adaptation to phase screen simulations. To the best of the knowledge of the author, this approach for simulation of a turbid medium has not been seen without the support of Monte Carlo ray tracing programs, finite element methods, or the assumption of a Gaussian phase function.

3.6.1 Turbid Medium MCF

The turbid medium MCF can be defined following from transfer theory as

$$\Gamma(r,z_o) = \iint d^2\kappa U(0,z_s)U^*(r,z_s)e^{i\boldsymbol{\kappa}\cdot\mathbf{r}}e^{-\int_{z_s}^{z_o}[\sigma_{ext}(z)+(B_S(0,z)-B_S(r,z))]dz}, \tag{3.22}$$

where $B_S(r)$ is the phase correlation function. Compared to a turbulent medium, whose language is written using structure functions, a turbid medium is typically not studied using this formalism unless spatial coherence is of concern. The phase correlation function

in terms of the phase function is given by

$$\begin{aligned} B_S(r) &= \iiint \beta(\theta,\varphi,a) e^{ik\mathbf{r}\cdot\mathbf{\Omega}} d^2\Omega da \\ &= \int_0^{\infty} \int_0^{\pi} n(a)\sigma_V(\theta,a) J_0(kr\sin(\theta))\sin(\theta) d\theta da. \end{aligned} \tag{3.23}$$

The MCF in equation 3.22 consists of the source MCF as defined in previous sections and the MCF due to particle scattering. Equation 3.23 describes the same PSD relationship used in equation 2.4 for the refractive index PSD and correlation function. The difference in notation follows from simplification using the polar scattering angle θ instead of spatial frequency κ. Using $\kappa = 2kn_0\sin(\theta/2)$ equation 3.23 can be rewritten in terms of spatial frequency and the same functional form is obtained as equation 3.17. Another main difference is the inclusion of the particle distribution $n(a)$ that occurs in a polydisperse turbid medium. Assuming an isotropic turbid medium, the turbid medium MCF can be rewritten as

$$\Gamma_{sca}(r,z_o) = e^{-\sigma_{ext}L}\left(e^{-\sigma_{sca}L} + e^{-\sigma_{sca}L}\left(e^{\sigma_{sca}LB_S(r,L)} - 1\right)\right), \tag{3.24}$$

where $L = z_o - z_s$. The first multiplicative term is described in Section 2.3 due to losses of higher angle scattering that falls outside of the detector field of view and particle absorption. The first term in the summation describes how the incident beam is perturbed by small-angle scattering that undergoes no appreciable phase shift due to the particles. The second term describes scattered light whose phase is determined by the medium's phase correlation function [65], [99], [100].

By comparing a turbid medium to a turbulent medium, the turbid medium WSF, for

a polarized laser beam, can be represented using a similar form to equations 3.17 and 3.18 as [61], [96]

$$\begin{aligned} D_{S_{pw}}(r) &= 2\left[\sigma_{ext}L+\sigma_{sca}L-\frac{N_dL}{k^2}\iint|S_p(\theta,\varphi,a)|^2J_0(kr\sin(\theta))\sin(\theta)d\theta da\right] \\ &= 2\sigma_{ext}L+2\sigma_{sca}L\left[1-\int_0^{\infty}\int_0^{\pi}n(a)\sigma_V(\theta,a)J_0(kr\sin(\theta))\sin(\theta)d\theta da\right], \end{aligned} \tag{3.25}$$

$$\begin{aligned} D_{S_{pw}}(r) &= 2\left[\sigma_{ext}L+\sigma_{sca}L-\frac{N_dL}{k^2}\iiint|S_p(\theta,\varphi,a)|^2J_0(kr\eta\sin(\theta))\sin(\theta)d\theta d\eta da\right] \\ &= 2\sigma_{ext}L+2\sigma_{sca}L\left[1-\int_0^{\infty}\int_0^{1}\int_0^{\pi}n(a)\sigma_V(\theta,a)J_0(kr\eta\sin(\theta))\sin(\theta)d\theta dad\eta\right], \end{aligned} \tag{3.26}$$

where $S_p(\theta,\varphi,a)$ are the scattering amplitudes and $p=1,2$ is the index for horizontal or vertical polarization. The phase correlation function in equation 3.25 is simplified using equation 2.12. The difference between equations 3.25 and 3.26 are the extra integral over η that includes the curvature of the spherical wavefront. Simplification and physical context of these equations follows from Section 3.1. However, another explanation is found from DeWolf [96] who derives equation 3.22 from coherence theory for a wave propagating through a slab of particles. Qualitative and quantitative results for a narrow and finite beam's MTF are seen to be in agreement with previous works [79], [101]–[110].

3.6.2 Turbid Medium Phase Power Spectrum

For a turbid layer transmittance function to represent a single realization of phase perturbations due to particle scattering, the two-dimensional turbid phase PSD must be

defined. The phase PSD is now given in terms of the spatial frequencies determined by the phase function and not the refractive index fluctuations PSD. Using the WSF relation for a plane wave in equation 3.25 and the Wiener-Khinchin theorem in equation 2.4 the phase PSD becomes the phase function. This has been pointed out as well by DeWolf [96] citing the RTE method by Fante [80].

Instead of the phase PSD representing the fluctuations of the refractive index due to turbulence, the phase PSD represents the spatial frequencies induced due to the light-particle interaction. When the weak scattering conditions (equations 2.16) are met, the excess change in refractive index can be used to predict the phase statistics in the case of turbulence using the RGD approximation. When the excess refractive index or particle size increases, the phase statistics rely on the electromagnetic resonance that imparts multiple wavelengths of phase shifts. These resonances directly impact the spatial frequencies as each particle, or particle distribution, presents results in a specific shape of the phase function. This can seen as the a/λ and n_1/n_0 ratios coupled with the particle distribution dictate the shapes of the phase function. In other words, for smaller particles the scattering angles are wide leaving only a few photons to reach the detector compared to larger particles where more photons reach the receiver leading to more intrusive phase distortions leading to loss of spatial resolution [101].

Examples of turbid medium plane wave WSFs and MCFs are shown in Fig. 3.4(a-b). The plane wave WSFs are calculated from equation 3.25 (red) and simulated by generating 500 random phase screen realizations following the phase PSD for 10 μm and 100 μm diameter particles with optical depths of 10 and 5. The corresponding MCF is calculated and shown in Fig. 3.4(b) for all the WSFs from Fig. 3.4(a). The grid

parameters contain a 512x512 grid with pixel pitch of 9.8 μm and a physical size of 5 mm.

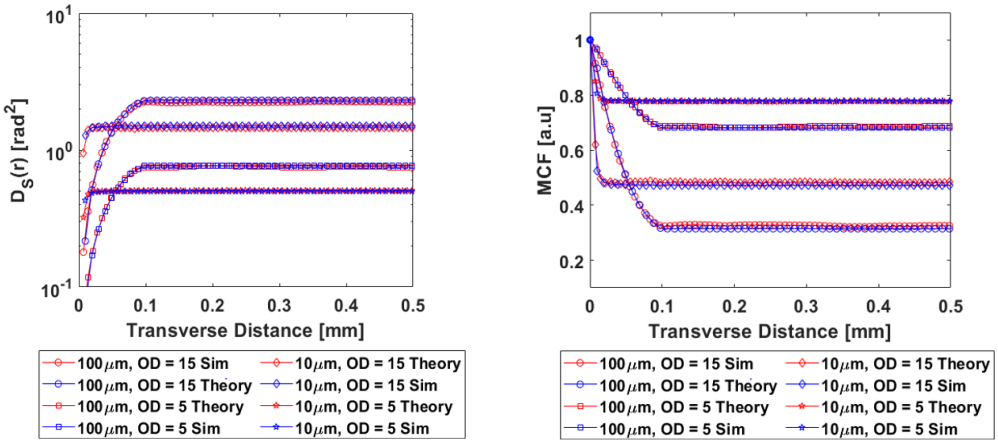

(a) (b)

Figure 3.4: (a) Examples of the plane wave WSF in a turbid medium for both analytic (red) using equation 3.25 and simulated (blue) for various particle sizes and optical depth. (b) Plane wave MCF in a turbid medium for the previous WSF for various particle sizes and optical depth.

The WSFs and MCFs for a turbid medium are significantly different than that of a turbulent medium mainly because a turbulent medium does not have a significant outer scale limitation. The theory that predicted each WSF and MCF also fits well with the simulated values from the turbid medium phase screen generation discussed in Appendix B. The MCFs of a turbulent medium also show a prominent cutoff frequency where the outer scale bound limits the value of the MCF. This effect was seen in MCFs/MTFs calculated by Bissonnette [101] for the case of fog and experimentally seen through aerosols [111]–[113]. In general, the form of the WSF and MCF of a turbid medium are quite different to those in a turbulent medium due to the presence of a small equivalent outer scale in a turbid medium. Using the simulation approach in Chapter 5, WOSs can be used to further understand the impacts of particulate matter on a laser wavefront in combination

with turbulence.

3.6.3 A scattering equivalent SCR/Fried Parameter

Up until this point wave propagation through both turbulent and turbid media have been discussed, but no parameter has been defined for a turbid medium similar to the Fried parameter or the SCR in a turbulent medium. The SCR is the distance to the $1/e$ point when the argument of the normalized degree of coherence,

$$\mu(r,L) = e^{-\frac{1}{2}D_S(r,L)}, \tag{3.27}$$

is $D_S(r,L) = 2$. For a turbulent medium, depending on the refractive index PSD, there are analytic results for the plane and spherical wave SCRs or equivalently the Fried parameter using $r_0 = 2.1\rho_{SCR}$ [50]. Using the definition of the WSFs from equations 3.25 and 3.26, the SCR is not clear to find due to the complex form of the phase function without approximation. The traditional approximations use the SAA, a Gaussian phase function [65], [66], [73], [78], [97], [107], [114]–[119], a Bessel phase function [96], or Henyey-Greenstein (HG) phase function [114], [120]. For a turbid medium there is no similar metric to the Fried parameter that is universal to define environmental resolution limitations. A turbid medium could be approximated with a Gaussian phase function with a single coherence length. This coherence length is then the equivalent to the SCR of of a turbulent medium, but this strictly approximates the shape of the phase function.

The Gaussian phase function assumes forward peaked scattering at near-forward scattering angles that is true for large particles, but does not incorporate the near-forward

scattering effects carried by more structured phase functions. It also approximates the effects of scattering within the multiple scattering regime, but is not true of the general case of scattering. The region before multiple scattering is where the beam retains the most coherence, which is of interest for OAM based work [64]. Larger particles contain significant near-forward scattering that is similar in nature to a circular aperture whose anisotropy can be modeled more accurately using a Bessel phase function or the HG phase function.

The main difference between a turbid medium and turbulent SCR is that for a turbid medium it is related to quantized particle sizes rather than a continuum of scale sizes. The comparison of the two media can be seen using the phase variance. The phase variance is deemed by the scaling constants, dependent on the medium's scattering strength, of the WSF. To explicitly show this scaling the plane wave WSF is used. The analytic plane wave WSF is found for turbulence following a Kolmogorov power-law as

$$D(r) = 6.88 \left(\frac{r}{r_0} \right)^{5/3}. \tag{3.28}$$

Kolmogorov turbulence ensures there is no inner or outer scale, leaving only the inertial subrange. Within this approximation the WSF becomes equation 3.28 which leaves the Fried parameter as an effective "phase variance" that dictates distortion strength. If the exact numerical result is considered, the phase variance depends on the propagation length, scaling of the refractive index PSD, and magnitude of the Hankel transform of the refractive index PSD. For more general WSFs the phase variance can be related to other power-law spectra or anisotropic turbulence [121].

For a turbid medium plane wave WSF (equation 3.25), the scaling similarly relies on σ_{sca}, propagation distance, and the magnitude of the Hankel transform of the phase function. If Mie theory is used to predict the phase function analytic results are difficult to reach. Figure 3.5 shows an empirical form of phase variance calculated from equation 3.25 for WSFs with varying particle size for a fixed optical depth of 1. The SCR of a turbid medium becomes roughly comparable to the particle diameter as the location of the asymptote of the WSF is located at the particle radius. The phase variance for a turbid medium couples both particle size and scattering strength, which is not the case for Kolmogorov turbulence containing no inner and outer scale. If turbulence contains a small inner and outer scale, then the phase variance is coupled to the scale sizes.

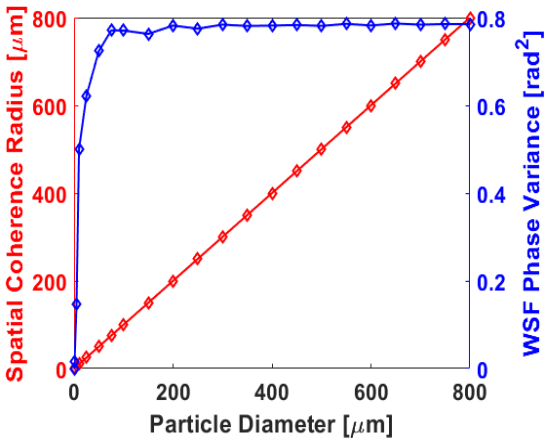

Figure 3.5: Spatial coherence radius (red) and phase variance (blue) for plane wave WSFs with varying particle diameter. The optical depth is held constant at 4.

Along with the phase variance, the scale sizes of the phase fluctuations also play a role in shaping the WSF. The turbid medium WSFs in Fig. 3.4 show an asymptote of the WSF for larger r that indicates an effective outer scale. The asymptote begins at the cusp of the WSF measured to be the particle radius, therefore, it can be inferred that the particle

size dictates the outer scale of a turbid medium. The inner scale of a turbid medium is assumed to always be zero as the WSF reaches the origin independent of particle size.

If a turbid medium analogy to the inertial subrange is made, not having to do with energy dissipation, it can be said that; as particle size increases the turbid "inertial subrange" expands (larger difference between inner and outer scale) leaving a larger continuum of phase perturbation scale sizes. When the difference between inner and outer scale is small, the effects of a turbulent medium are reduced. This is the same effect in a turbid medium when the particle diameter is small leading to molecular scattering. Results of varying the size of the turbulent inertial subrange are simulated in Chapter 5 with further discussion.

3.7 Effect of Phase Perturbation Scale Sizes

Both the laser beam shape/size and phase perturbations sizes/scales contribute to how the laser will propagate. This prompts the use of ratio between the system aperture diameter to Fried parameter ratio D/r_0. Typically this metric is introduced to describe how the diffraction limited spot size is increased due to atmospheric turbulence affecting astronomical telescopes. In this work, the beam size will be generally smaller than the telescope aperture, therefore, the beam size is the limiting aperture. To denote turbulence strength later on in this work the ratio of the beam waist (w_0) to r_0 is used: $2w_0/r_0$.

For a turbid medium, the SCR is deemed proportional to the particle diameter (see Fig. 3.5) leading to the ratio of the beam waist to particle radius a: w_0/a. This is different than the ratio a/λ that dictates the shape and size of the phase function, but also couples

to the strength of phase distortions.

3.8 Summary: Application to OAM Propagation

Within this chapter the theoretical foundation of optical wave scattering through a random medium has been discussed for both turbulent and turbid media. The parallels of the two mediums are apparent using the scattering length $1/\sigma_{sca}$ and turbulence length $1/\sigma_{T_{sca}}$. The main difference between the two mediums is that a turbid medium can contain refractive index variations sizes comparable to the wavelength that create electromagnetic resonances leading to large optical phase shifts. This interaction leads to the PSD of the phase fluctuations depending on the phase function rather than a refractive index PSD due to the weak scattering condition (equation 2.16) being broken.

The main take away from this chapter is the form of the WSFs that determine the MCF for both turbulent and turbid media. The parallels between the two random mediums becomes quite apparent due to the forms of equation 3.17 and 3.25 being exactly the same. However, the length scales and phase variance depend on different phase PSDs and IOPs of the medium. By deriving the phase PSDs of each medium it can be seen that different phase perturbation scales are introduced by each medium dictated by the strength of forward scattering. The continuum of length scales present described by the inertial subrange of each medium also affects how the optical phase will be perturbed. By understating the significance of the phase variance and length scales present an intuition can be developed on how the phase of a laser will be perturbed which will be used in the rest of this work. Using the plane wave MCF for a collimated laser a beam's OAM

statistics can be derived in Chapter 4.

The second main takeaway is the parameters that describe the effects on the MCF using the SCR, Fried parameter, extinction coefficient, scattering coefficient, optical depth, and turbulence length. Each parameter determines the strength of a turbulent or turbid medium. However, some of these metrics may be limited to specific approximations of the scattering strength. The magnitude of these metrics provide insight to the limit that coherent laser propagation will be practical for an active OAM based sensing modality.

Chapter 4: The Orbital Angular Momentum of Light

OAM beam propagation through a random medium has the potential for obtaining information about the environment itself. One of the ways environmental parameters appear is a beam's OAM spectrum upon propagation through the medium. This chapter will introduce the OAM spectrum and its use for remote sensing through turbulent and turbid mediums using the formalism developed in Chapters 2 and 3.

4.1 Creation of OAM

As OAM depends on a helical wavefront, the wavefront shape must be imprinted onto a laser beam from other means such as laser cavity design [122], optical elements [123]–[125], or environmental effects [34]–[36], as a few examples. The seminal work by Allen *et al.* [4] in 1992 led to the breakthrough that beams with a helical wavefront carry integer amounts of OAM of $l\hbar$ per photon along with the implications that OAM can be imprinted on a beam by simple means. This realization became paramount as light carrying vortices was not a new topic at the time [9], [124], [126]. It could then be concluded that phase singularities do not imply OAM, but rather that the light surrounding the phase singularity carries the OAM [8], [127].

4.1.1 Static Devices

There are many ingenious ways to impart a helical phasefront on a laser beam, but two ways have been found to be the most common. The first method uses static devices called spiral phase plates (SPP) that create a single OAM mode [123]. SPPs are a refractive element that relies on a helically shaped refractive index gradient that turns a non-helically phased beam, shown in Fig. 4.1(a-b), into a helically phased beam. Theoretically, the resulting beam profile is commonly modeled using the Laguerre-Gaussian (LG) beam, with the intensity and phase shown in Fig. 4.1(c-d). LG modes are typically

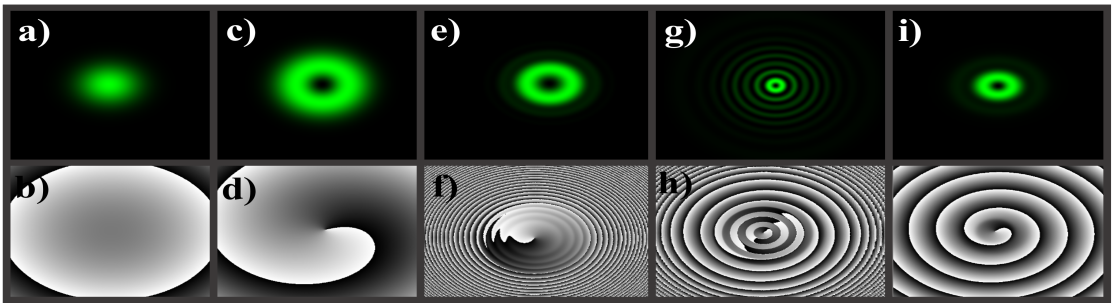

Figure 4.1: (a-b) Gaussian beam intensity and phase, (c-d) Laguerre-Gaussian intensity and phase, (e-f) Hyper-geometric beam intensity and phase, (g-h) Bessel-Gaussian beam intensity and phase, and (i-j) apertured Bessel beam intensity and phase. Each beam starts with an initial spot size of 5mm and $l = 1$ and is propagated 20 meters through air.

desired due to their ease of use in theoretical treatment, but SPPs do not shape the radial degree of freedom. This leads to a beam with a radial basis of hypergeometric functions rather than Laguerre polynomials. These forms of beam are called Hypergeometric Gaussian beams (HyGG) [128]. A HyGG beam is seen to behave quite differently compared to an LG beam as the intensity and phase in Fig. 4.1(e-f) are compared to 4.1(c-d). This leads to note there are many other forms of OAM beams such as Bessel, Bessel-Gaussian

(BG), and Mathieu beams to name a few [129]–[131]. The BG and Bessel beam behave quite different due to the radial basis function that lead to autofocusing effects (see Fig. 4.1(g-h) and 4.1(i-j)). Appendix C explicitly shows the wave function expressions for the Gaussian, HyGG, BG, and Bessel beam as they will be used in later chapters.

4.1.2 Dynamic Devices

The second method to create OAM uses a dynamic optical element, commonly a liquid crystal spatial light modulator (LCSLM) or deformable micromirror device (DMD), to switch between OAM modes [132]–[134]. LCSLMs are light shaping devices that use a liquid-crystal display to modulate the wavefront of the incident light by mapping optical phase shifts to the gray scale level, 0 to 255, of an 8 bit image. As this is a phase-only device, more specific techniques can be used to also modulate the laser beam's amplitude to create high fidelity OAM beams [135], [136]. DMDs use a 2D array of micromirrors that can either be turned on or off to manipulate the wavefront by inducing amplitude modulation through interference. The DMD also uses an 8 bit image, but instead of displaying the image all at once, each bit-plane is quickly cycled on the micro-mirror array leading to a minimum exposure time to experimentally see the beam of interest correctly. Both methods of generation will be used in the experimental portion of this work. For OAM beam generation using LCSLMs or DMDs, it is then necessary to introduce digital holography. The digital holograms of interest contain the interference pattern between a reference beam and some form of OAM carrying beam. The digital hologram contains a 2D phase profile of the OAM beam, which is then displayed on the LCSLM/DMD and

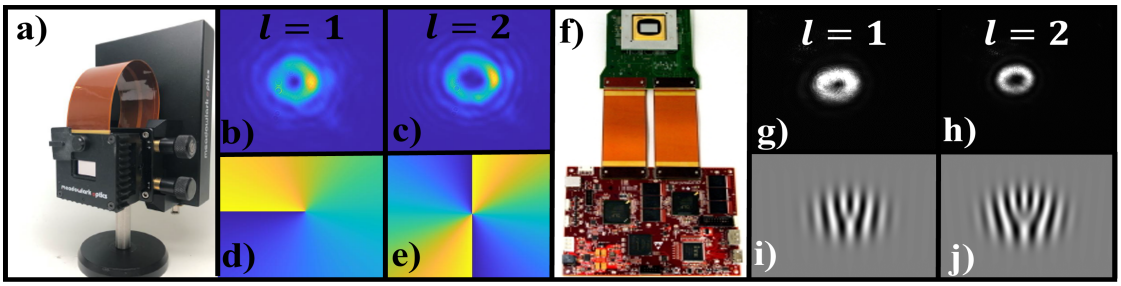

Figure 4.2: (a) Example of an LCSLM and experimentally created beams (b-c) with their respective digital hologram (d-e) used on the LCSLM. (f) Example of a DMD and experimentally created beams (g-h) with their respective digital holograms (i-j).

encodes the incident laser with the phase shifts necessary to create OAM. From section 3.3, the hologram is equivalent to the phase of a complex transmittance function [91]. Depending on the optical setup and device, the hologram may take the form of a spiral phase or forked diffraction grating. This distinction is important as the holograms behave quite differently, the spiral phase is imparted directly on the beam unlike the forked diffraction grating that creates higher diffracted orders. Forked gratings are more commonly used as they can be modified to create highly accurate transmittance functions [135], [136]. However, depending on the application a spiral phase hologram or SPP will suffice if only the OAM information is of interest. If the applications require a shaped radial basis as well a DMD or LCSLM will be necessary.

4.1.3 Impact of a Partially Coherent Source

Static and dynamic elements imparting OAM rely solely on the ability for light to interfere as it refracts or diffracts. Consequently, decreasing the coherence of the optical wavefront directly impacts its ability to interfere. This is seen for beams that follow a

Gaussian-Schell model MCF, which washes out the optical vortex shape as source coherence decreases [137]. Other forms of partially coherent sources can include OAM in the MCF such as I_m Bessel beams whose MCF contains well-defined OAM states discussed in Appendix D [138]–[140]. Partially coherent OAM beams of this form have been suggested to reduce the effects of a random medium by reducing intensity variations and their effects will be simulated in Chapter 5.

4.2 Detection of OAM

After OAM was first realized, the measurement of OAM soon followed starting with physically measuring the torque imparted on small particles [16] and moved to focusing on the phase structure of the laser by spiral fringe counting [141] or diffraction by apertures [142], [143]. Interferometric measurements of OAM lead to further interest in the phase, but with the added complexity of pattern recognition. For SDM communications the necessity to measure multiple OAM modes is highly sought after which lead to the development of systems to measure multiple OAM modes in a quick manner without complex image processing.

A first method to measure the OAM spectrum is based on dove prism rotation angles to measure more than one OAM mode at a time, but required a highly stable interferometer [144], [145]. The next methods to measure OAM can be classified as mode projectors (matched filter or correlator) that perform an optical phase cancellation to remove the helical phase [146]–[150]. This OAM information is quantified using the knowledge that helical wavefronts are orthogonal to each other allowing for any wavefront to be decom-

posed into a series of OAM basis functions as

$$U_l(r,\phi,z) = \sum_{n=-\infty}^{\infty} c_{ln}(z)\Psi_n(r,\phi,z)\,, \tag{4.1}$$

where $c_{ln}(z)$ are the weights of each OAM eigenfunction $\Psi_n(r,\phi,z)$ using some radial basis [146]. The weights, $c_{ln}(z)$, are collectively known as the OAM spectrum where each component can be found from the following inner product with the optical field of interest $U_l(r,\phi,z)$,

$$c_{ln}(z) = \int_0^{2\pi}\int_0^{\infty} U_l(r,\phi,z)\Psi_n^*(r,\phi,z)rdrd\phi\,. \tag{4.2}$$

The OAM spectrum of a beam quantifies only the azimuthal degree of freedom leaving the radial basis free. In this work radial basis information is not needed, but some imaging applications will find this information useful [151], [152].

Experimental implementation of mode projection requires a spatial light modulator, lens, and pinhole to measure the nth inner product in equation 4.2 and illustrated in Fig. 4.3. The OAM element can either be an SPP or LCSLM that displays a helical phase containing the information of the OAM eigenfunctions, $\Psi_n^*(r,\phi,z)$. After encoding the beam with the basis function, the beam is transmitted through a lens whose Fourier transforming properties perform a 2D Fourier transform that implements the inner product in equation 4.2. The on-axis intensity at the focus of the Fourier lens is selected using a pinhole and is proportional to $|c_{ln}(z)|^2$. Each $|c_{ln}(z)|^2$ represents the power of each OAM mode within the incident beam following a decomposition in equation 4.1. The power of

the OAM spectrum is normalized such that

$$\alpha_l(z) = \frac{|c_l(z)|^2}{\sum_{m=-\infty}^{\infty}|c_m(z)|^2}, \tag{4.3}$$

where $\alpha_l(z)$ represents the fraction of power in the l^{th} OAM mode of the beam. The phase angle of the coefficient, $\angle c_{ln}(z)$, can also be determined from a series of mode projection measurements [30]. Consequently this spatial orthogonality allows for efficient encoding or decoding with a first practical demonstration of an FSO SDM communication system by Graham *et al.* [153]. An inefficiency of mode projection is that it requires n measurements to measure n OAM coefficients with the loss of significant power due to the use of a pinhole.

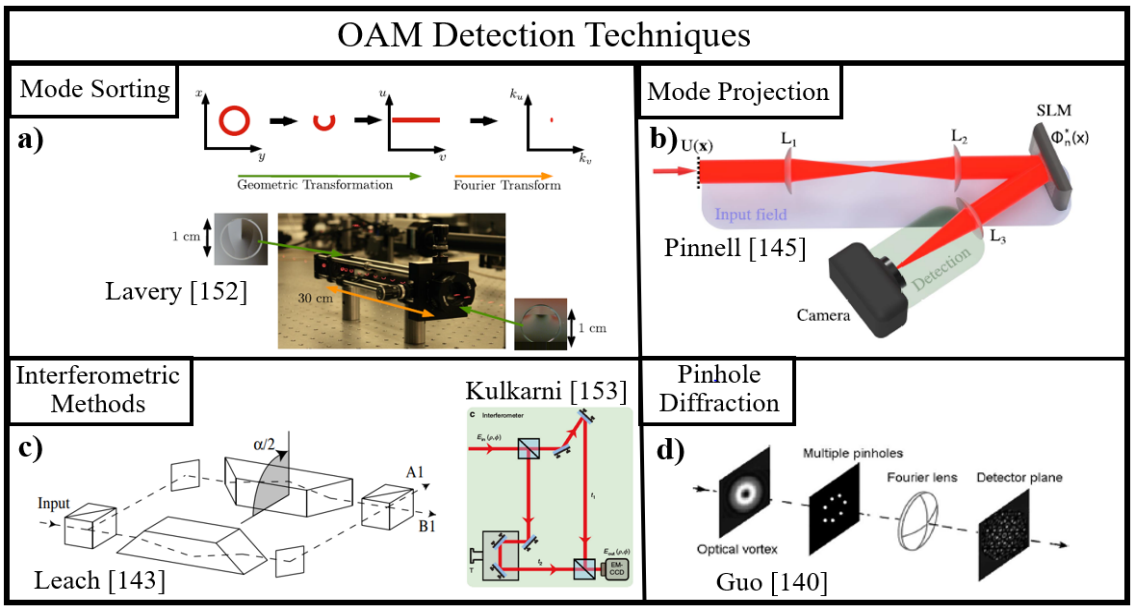

Figure 4.3: (a) Mode sorter showing the geometric transfer of an OAM beam to a transverse momentum state [154]. (b) Mode projection measurement setup using an LCSLM to rotate through the holograms displaying the phase of the conjugate basis mode [147]. (c) Two forms of interferometer measurements using dove prisms [145] and a wavefront folding interferometer [155]. (d) An example of pinhole diffraction that can be used to measure the OAM of an input laser [142].

Due to the lack of a power efficient, stable, and simple OAM spectrum measurement tool, the development of a highly efficient mode sorter by Lavery *et al.* to measure the OAM spectrum in a single shot with simple image processing was sought for [32], [154], [156]–[161]. Mode sorters rely on custom optical elements that perform a conformal mapping to convert the annular shape of an OAM beam to a line in space [157]. This method was then modified to measure the modal content of an OAM beam in real-time [162]. The mode sorter, illustrated in Fig. 4.3, is a widely accepted way to measure the modal content of an OAM beam in a single measurement where the collection of modes are known as the OAM spectrum.

OAM spectrum measurements have been further developed on a more situational basis depending on the optical system in question. For extremely sensitive measurements Kulkarni *et al.* [155], [163] developed a single-shot OAM spectrum technique using the angular correlation function for down converted light. Another method to measure the OAM spectrum is the use of a Shack-Hartmann wavefront sensor that can measure the curl of the optical phase and map it back to the OAM present [164]. There are also many other unmentioned ways to measure OAM depending on the application in question [144], [165]–[174].

If the optical channel contains environmental or systemic distortions, the incident OAM will be changed leading to the creation of extra OAM modes within the OAM spectrum. This creation of OAM modes is known as mode spreading, since the energy of the incident OAM mode is spread out among other neighboring OAM modes. If an optical channel's optical distortions are strong enough, the incident OAM information can be completely lost. The quantification of mode spreading through a random medium

is presented in the next section by determining how the OAM coefficients in equation 4.2 change.

4.3 Spreading of the OAM Spectrum

OAM mode spreading is the fundamental concept that drives an active OAM sensing modality in this work. To quantify the amount of mode spreading expected from the effects of a random medium, it must first be understood how a random medium affects the wavefront of a laser beam. The metric of utmost concern is the power within each OAM mode ($|c_{ln}(z)|^2$) as the OAM measurement techniques introduced measure the OAM spectral density rather than the amplitude itself. If the coefficient amplitude ($c_{ln}(z)$) is averaged over a zero-mean random medium, the result will be zero similar to the mean field [50].

As the nature of a random medium incites that the phase perturbations are random, this leads to a statistical approach to determine the mode spreading. Determining the average OAM power, $\langle|c_{ln}(z)|^2\rangle$, is the first step to quantify mode spreading through a random medium. It is worth noting the average OAM power can also be interpreted as the probability that the incident OAM mode will scatter into another OAM state [175]. Using definitions of the OAM spectrum and EHFP from equations 4.1, 4.2, and 2.8, the average

power of the OAM coefficients can be determined as

$$\begin{aligned}
\langle |c_n^2(z)| \rangle &= \iiint\!\!\int \langle U_o(r_1,\phi_1,z) U_o^*(r_2,\phi_2,z) \Psi(r_1,\phi_1,0) \Psi^*(r_2,\phi_2,0) \rangle r_1 dr_1 d\phi_1 r_2 dr_2 d\phi_2 \\
&= \iiint \langle U_o(r,\phi_1,z) U_o^*(r,\phi_2,z) \rangle e^{il(\phi_1-\phi_2)} r dr d\phi_1 d\phi_2, \\
&= \iiint U_{ov}(r,\phi_1,z) U_{ov}^*(r,\phi_2,z) e^{il(\phi_1-\phi_2)} e^{-\frac{1}{2}D_w(r,\phi_1,\phi_2)} r dr d\phi_1 d\phi_2. \\
&= \iint \Gamma_B(r,\Delta\phi) \Gamma_{RM}(r,\Delta\phi) \cos(l\Delta\phi) r dr d\Delta\phi \\
&= \int_0^{\infty} \int_0^{2\pi} |U(r,z)|^2 \Gamma_{RM}(r,\Delta\phi) \cos(l\Delta\phi) r dr d\Delta\phi
\end{aligned} \tag{4.4}$$

using an OAM basis function defined as $\Psi(r,\phi,z) = R(r,0)e^{il\phi}$ and the radial basis completeness $\sum_{p=0}^{\infty} R(r_1,z)R^*(r_2,z) = \delta(r_1,r_2)/r$ [175]. U_o is the field at the observation plane after propagation through the random medium and U_{ov} is the field propagation through vacuum. Notice that the random medium effects are included in the average coefficient power as a WSF similar to the MCF in equation 3.9. The last line in equation 4.4 represents the source MCF and random medium MCF ($\Gamma_{RM}(r,\Delta\phi) = e^{-\frac{1}{2}D_w r,\Delta\phi}$), where the variable substitution $\Delta\phi = \phi_1 - \phi_2$ is used following statistical isotropy.

Equation 4.4 can then be tuned using specific forms of the WSF for plane waves or spherical waves with the appropriate WSF that carries the IOPs of the random medium. It is also important to note that this average OAM power can also be normalized following equation 4.3 such that it represents the fraction of OAM power on average. The resulting WSF can be seen to degrade the OAM spectrum following as phase correlations decrease. Instead, the beam profile now also determines the OAM channel losses rather than the distortion alone. If the beam size becomes comparable to the coherence length of the

medium, then noticeable OAM mode spreading will begin [175], [176]. Conservation of energy is satisfied for each individual realization of turbulence as OAM is scattered between the various OAM states.

The one piece of information that is lost using this formalism is the phase information of the OAM coefficient. To find the phase component of the OAM coefficient, the focus turns to using a mean field approach of the phase perturbations rather than the MCF which quickly approaches zero due to the nature of the phase statistics having a zero mean [50]. Finding the phase component of the OAM coefficients can also be done by taking an azimuthal Fourier transform of the transmittance function for a single realization of a random medium [177], [178]. Unfortunately this phase information is typically hard to measure as it requires multiple modal projection measurements [30] or complex mode sorters [179]. The OAM phase is typically ignored due to its difficulty to measure, its unnecessary measurement for communication applications depending on only intensity measurements, and its zero-mean average. But for sensing this phase component may be useful for temporally correlated turbulence to measure its evolution as a function of time.

To show some examples of OAM mode spreading, the mode spreading due to optical system perturbations, turbulent, and turbid medium are shown as a function of their respective phase perturbation strengths. Each result is predicted by numerically solving equation 4.4 for each respective distortion.

4.3.1 Optical System Perturbations

Lens aberrations from an imperfect optical system, depending on their strength and symmetry, can also lead to OAM spreading. Azimuthally symmetric aberrations such as defocus or spherical aberrations will not lead to a change in the OAM spectrum, but rather a perturbation in the measurement technique. Depending on the measurement scheme there may be an optically induced background signal depending on the diffraction limit [157], [160], [161]. Fig 4.4 shows a few examples of optical aberrations and their respective OAM spectra with a plane wave incident on the aperture.

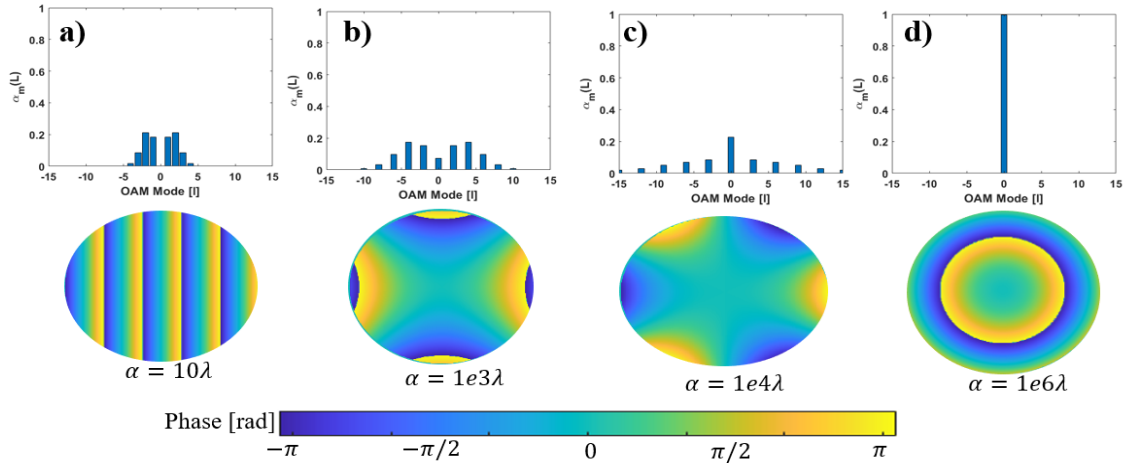

Figure 4.4: Plane wave OAM spectra upon incidence of a 25 mm aperture with the Lens aberrations of (a) tilt, (b) astigmatism, (c) trefoil, and (d) defocus with the following aberration coefficients respectively 10λ, $1 \times 10^3\lambda$, $1 \times 10^6\lambda$, $1 \times 10^4\lambda$.

For simple aberrations such as tilt (Fig. 4.4(a)) or coma (Fig. 4.4(b)), the optical axis slightly shifts which makes a large contribution to measuring the OAM spectrum incorrectly. Higher order aberrations such as trefoil (Fig. 4.4(c)), astigmatism , or quadrafoil do not perturb the OAM spectrum as greatly when the aberrations are weak.

Azimuthally symmetric aberrations such as defocus (Fig. 4.4(d)) add no contribution to the OAM spectrum as there is no perturbation of the azimuthal coordinate, but for systems that rely on measuring the OAM spectrum at the focus of a lens this will contribute to inaccurate OAM spectra measurements. A lens aberration is a transmittance function that has an analytic expression thus the average MCF can be substituted by calculating an azimuthal Fourier transform of the transmittance function of one realization instead of hundreds [178].

4.3.2 Random Medium Perturbations

Using the simplified version of equation 4.4, the OAM spectrum for a known WSF can be calculated. If the incident laser beam is assumed collimated, removing the spherical wavefront, the plane wave WSF can be used as a first approximation to calculate the OAM mode spreading [175], [180]–[182]. The effects of path length, beam size, and perturbation strength for a turbulent and turbid medium are both summarized in Fig. 4.5(a-d).

Within a turbulent medium the strength of turbulence is quantified using the ratio $2w_0/r_0$. The value of $2w_0/r_0$ can be used to infer information about the turbulence present: $2w_0/r_0 > 1$ is when the turbulence scales are small compared to w_0 and turbulence is considered strong; $2w_0/r_0 < 1$ contains turbulence scales larger than w_0 and is considered weak; and $2w_0/r_0 \sim 1$ is when the turbulence scale is on the same order as the beam size and considered moderate. Typically the input aperture diameter is used D/r_0, but the beam diameter in this work is the limiting "seeing" parameter to measure

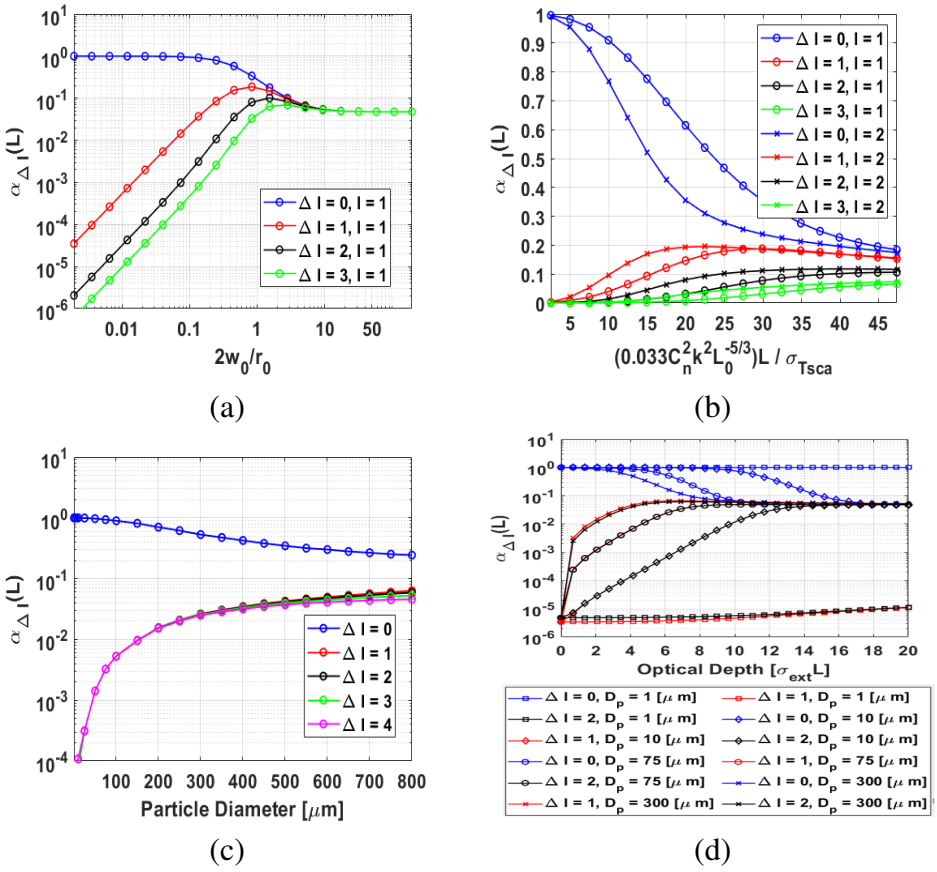

Figure 4.5: (a) Turbulent medium mode spreading, $\alpha_{\Delta l}(L)$ as a function of $2w_0/r_0$. (b) Turbulent medium mode spreading as a function of normalized scattering distance $0.033C_n^2k^2L_0^{-5/3}L/z_c$. (c) Turbid medium mode spreading as a function of particle diameter for a fixed optical depth of 4. (d) Turbid medium mode spreading as a function of optical depth at a fixed particle radius. Each plot is used with an incident LG beam with $l = 1$.

the turbulence rather than the receiver aperture.

As the turbulence scales reach the beam size, considerable mode spreading occurs as seen in Fig. 4.5(a). The mode spreading is measured by looking at the OAM coefficients at $\Delta l = |l - m|$ where l is the incident OAM order and m is the next closest mode. This transition between a pure OAM state and uniform OAM spectrum occurs quickly when $2w_0/r_0 \sim 1$. It depends on the initial beam size not the initial OAM mode as the OAM mode spreading is seen to be independent of OAM mode order [175], [176], [183].

OAM beams contain a spot size that is coupled to the OAM order, which leads to confusion as to what is an OAM effect versus beam size effects [184]. The OAM spectrum also decreases as a function of propagation distance through isotropic turbulence with a constant inner ($l_0 = 0$ m) and outer scale ($L_0 = 100$ m). In Fig. 4.5(b) the plots with circles represent a beam waist of 20 cm whereas the crosses are a beam size of 2 cm after propagating through a 1000 m turbulent channel. The propagation distance is normalized by $\sigma_{T_{sca}}$ and multiplied by a constant scaling factor $0.033C_n^2k^2L_0^{-5/4}$, which leaves a normalized scattering depth. As this normalized turbulence strength reaches ~ 15, the power in other OAM modes begins to significantly increase.

The next two figures are of OAM mode spreading in a turbid medium. Figure 4.5(c) shows mode spreading for an LG beam with $l = 1$ as a function of particle diameter at a fixed optical depth of 4. As the particle diameter increases, the amount of mode spreading also increases. A significant difference to a turbulent medium is the power distribution between side modes. Figure 4.5(c) shows that the power within modes greater than the incident OAM mode $l = 1$ (when $\Delta l > 0$) increase at a similar rate rather as a function of particle diameter. Also as particle diameter increases, the amount of phase distortion increases similar to a rise in turbulence strength. This same effect is seen as a function of particle diameter and optical depth in Fig. 4.5(d). However, the amount of power in the incident OAM mode $l = 1$ decreases quicker as a function of optical depth as the particle size increases. This is because larger particles contribute more near-forward scattered light unlike small particles.

Within a turbid medium, the parameters that dictate mode spreading are the OD, particle size, and beam size. OD ties in the amount of scattering per unit length, but not

the propagation distance and coherence effects. In contrast to a turbulent medium these turbid medium scenarios suggest that smaller beams are perturbed more significantly than larger beams. This is hypothesized to be due to the functional form of the phase PSD. In turbulence there is a small, or mostly no, ballistic component due to the light being scattered all in the forward direction. From a wave perspective, the ballistic component of the light can be explained by the distorted wavefront constructively interfering that results in a recombination of the main beam as it propagates. As the particle size increases, this region of recombination decreases due to the phase perturbation scales increasing. This is why in turbulence the beam is completely distorted with no clear ballistic component.

A significant portion of the motivation for this work is built from the simulations developed by Viola *et al.* [185] who simulated OAM beam propagation through a turbid medium by modeling it as a series of random circular apertures. Viola *et al.* saw that as the particle size increased the amount of mode spreading was also seen to increase. An experiment was also performed that also saw mode spreading along a 3 m, 12 m, and 20 m optical path for the scattering agents of Maalox (Equate) and corn starch with the same optical depth. It was not clear what the size of the beam was as the grid size implemented in simulation was roughly 1 mm x 1mm, which lends itself to a small beam. From this work it was shown that as the beam size approaches the size of the phase perturbations significant mode spreading is seen, but for larger beams this is not the case even over longer propagation paths.

4.4 Summary: OAM Spectrum as a Sensing Modality

For remote sensing the spreading of the OAM spectrum is the quantity of interest. Seen from section 4.3.2 as the turbulent or turbid medium changes, the OAM spectrum is also perturbed which can be used to infer information about the current environment. An active mode spreading technique has yet to be seen implemented practically compared to passive methods, the next chapters will address this implementation. Practical OAM spectrum measurements are difficult to implement due to optical system or data acquisition limitations. The OAM spectrum is chosen other than intensity only measurements due to its connection to optical phase perturbations. If only the OAM beam intensity is measured the connection to the phase distortions is not as apparent since OAM projections couple phase perturbations to intensity changes within the OAM coefficients. The other difference is that the OAM spectrum is related to second order field statistics rather than fourth order statistics for intensity measurements.

To practically implement OAM as an active sensing modality a compromise must be made between optical and measurement complexity. The first two methods of interest for this work are: Kulkarni *et al.*'s [155] method that requires high stability with less complexity and modal projections that requires less stability with more complexity. The simulation work is presented initially in context to understanding how OAM beams propagate, which will then be used to provide more insight to the experimental results in Chapters 5 and 6. The scattering portion of this theory will be developed further in Chapter 6 when examining experimental data.

Chapter 5: Simulation of OAM Beam Propagation through a Random Medium

5.1 Motivation for OAM Beam Simulations

In order to understand OAM beam propagation and predict the OAM spectrum's interaction within a random medium a series of simulation routines are developed [186]. This is done by implementing wave optic simulations (WOS) using the split-step method that solve the Huygens-Fresnel integral within the SAA or paraxial approximation [88]–[90]. The simulation method is verified by comparing the results to analytic theory for Gaussian beam propagation [50]. The simulations are then adapted for OAM beam propagation by changing the incident beam profiles to those of OAM beams given in Appendix C. To understand the simulation method used a brief explanation is provided here.

The numerical technique in this work states, with the Huygens-Fresnel integral in free-space as

$$U_o(\mathbf{r}_2,\phi,z_s+\Delta z) = \frac{1}{i\lambda\Delta z}\int_{\infty}^{\infty} U_s(\mathbf{r}_1,\phi,z_s)e^{i\frac{k}{2\Delta z}\left|\mathbf{r}_2-\mathbf{r}_1\right|^2}d\mathbf{r}_1, \tag{5.1}$$

the electric field at the source plane, $U_s(\mathbf{r}_1),\phi,z_s$, can be related to the field at the observation plane, $U_o(\mathbf{r}_2,\phi,z_o)$. Here Δz is the propagation step size to the next observation

plane and $\mathbf{r}_1 = (x_1, y_1)$ and $\mathbf{r}_2 = (x_2, y_2)$ are the source and observation plane spatial coordinates. A turbid medium undergoes a similar propagation equation as the beam also undergoes a series of effective phase shifts, but they are rather related to a different phase correlation function.

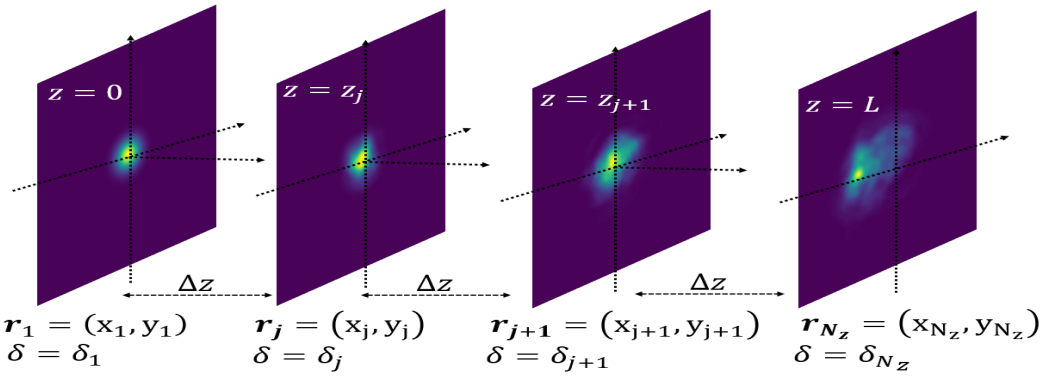

Figure 5.1: Beam propagation geometry of the split-step method using a multi-phase screen approach. Each picture of the beam represents the application of another phase screen.

The geometry of the split-step method is shown in Figure 5.1, using multiple propagation steps, where L is the total propagation distance, N_z is the number of propagation steps in increments of Δz, and δ_j and $\mathbf{r}_j = (x_j, y_j)$ are the grid spacing and spatial coordinate at the j^{th} propagation step. The accumulation of turbulent phase distortions can be seen as the Gaussian beam in Figure 5.1 begins to breakup along each propagation step.

For a single propagation step, from r_j to r_{j+1}, equation 5.1 can be written as

$$\begin{aligned} U(r_{j+1}) &= \frac{1}{i\lambda\Delta z}\int_{\infty}^{\infty} U(r_j) e^{\frac{ik}{2\Delta z}\left|r_{j+1}-r_j\right|^2} dr_j \\ &= \frac{e^{-\frac{ik}{2\Delta z}\frac{1-m_j}{m_j}r_{j+1}^2}}{i\lambda\Delta z}\int_{\infty}^{\infty} U(r_j) e^{\frac{ik}{2\Delta z}(1-m_j)r_j^2} e^{\frac{ikm_j}{2\Delta z}\left|\frac{r_{j+1}}{m_j}-r_j\right|^2} dr_j . \end{aligned} \tag{5.2}$$

A grid scaling factor, m_j, which accounts for converging or diverging beams, is introduced

(see Schmidt [88] for more detail). Equation 5.2 is then rewritten using the convolution theorem (see equation 5.3) and numerically implemented using the Fourier transform.

$$\begin{aligned} U(r_{j+1}) &= e^{-\frac{ik}{2\Delta z}\frac{1-m_j}{m_j}r_{j+1}^2}\mathscr{F}_2^{-1}\left[f_{j+1},\frac{r_{j+1}}{m_j}\right]e^{-\frac{i\pi\lambda\Delta z}{m_j}f_j^2} \\ &\quad\times\mathscr{F}_2[r_j,f_j]\left\{\frac{U(r_j)}{m_j}e^{\frac{ik}{2\Delta z}(1-m_j)r_j^2}\right\} \\ &= \mathscr{Q}_1\left[\frac{m_j-1}{m_j\Delta z},r_{j+1}\right]\mathscr{F}_2^{-1}\left[f_{j+1},\frac{r_{j+1}}{m_j}\right]\mathscr{Q}_2\left[-\frac{\Delta z}{m_j},f_j\right] \\ &\quad\times\mathscr{F}_2[r_j,f_j]\mathscr{Q}_1\left[\frac{1-m_j}{\Delta z},r_j\right]\left\{\frac{U(r_j)}{m_j}\right\}. \end{aligned} \tag{5.3}$$

Here the operator notation is introduced, where $\mathscr{F}_2$ is the 2D Fourier transform, $\mathscr{F}_2^{-1}$ is the inverse 2D Fourier transform, $f_j=\sqrt{f_x^2+f_y^2}$ is the Fourier domain radial coordinate, f_x and f_y are the Fourier grid coordinates, and $\mathscr{Q}_1$ and $\mathscr{Q}_2$ are operators representing quadratic phase terms from equation 5.2.

Equation 5.3 describes the simulation of a beam propagating through vacuum. To include phase distortions, the phase screen operator, $\mathscr{T}$, is introduced

$$\mathscr{T}(z_j,z_{j+1})=\exp\left(-i\theta_{rnd}(q\Delta x,p\Delta y)\right). \tag{5.4}$$

The accumulated random phase is $\theta_{rnd}(q\Delta x,p\Delta y)=k\int_{z_s}^{z_o}n_1(r)dz$ that is found from Appendix B. The field at the final observation plane, after propagation through the random medium, the accumulation of N_z-1 phase screens are implemented using the Fast Fourier

Transform (FFT) using the following product

$$U(r_{N_z}) = \mathscr{Q}_1\left[\frac{m_{N_z-1}-1}{m_{N_z-1}\Delta z}, r_{N_z}\right]\left(\prod_{j=2}^{N_z-1}\mathscr{T}[z_j, z_{j+1}]\mathscr{F}_2^{-1}\left[f_{j+1}, \frac{r_{j+1}}{m_j}\right]\right.$$
$$\left.\times\mathscr{Q}_2\left[-\frac{\Delta z}{m_j}, f_j\right]\mathscr{F}_2[r_j, f_j]\right)\mathscr{Q}_1\left[\frac{1-m_1}{\Delta z}, r_1\right]\mathscr{T}[z_1, z_2]U(r_1). \tag{5.5}$$

The final beam profile, after an arbitrary number of partial propagation steps through the random medium, can easily be modeled through various strengths of scattering and turbulence. This is due to the tuning of the phase distortion strength in both turbid and turbulent media depending on the propagation distance. Multiple partial propagation steps are key to modeling strong phase perturbations as one phase screen will not be accurate. This is due to sampling errors as the phase distortion size becomes comparable to the grid pixel pitch. For more discussion of sampling constrains the reader is turned to Chapter 9 of Schmidt [88].

5.1.1 Verification of Gaussian Beam Simulations

To verify the simulations for the weak turbulence regime the well accepted theoretical predictions for a Gaussian beam's MCF, spot size, scintillation, and intensity are compared. The weak turbulence regime is defined here as satisfying the weak scintillation condition where $\sigma_R^2 < 0.1$ such that the Rytov approximation is considered valid. Analytic methods using the EHFP have been seen to generalize to the strong turbulence regime, which is not always true for fourth order statistics [50], [187]. Figure 5.2(a-c) shows a qualitative illustration of the laser beam intensity pattern after propagating through vac-

uum (Fig. 5.2(a)), 1 random realization of weak turbulence (Fig. 5.2(b)), and 500 random realizations of weak turbulence (Fig. 5.2(c)). The x-axis and y-axis show a cross section through the center of the intensity pattern. After averaging over 500 realizations of turbulence, the average intensity takes on a similar form of the intensity through vacuum, however the effective beam size is slightly larger. The next set of metrics quantify other properties of beam after propagation through turbulence. Figure 5.3(a-d) shows results of comparing the numerical beam metrics to simulated values for a Gaussian beam. Each of the following plots are done with a $w_0 = 7$ cm Gaussian beam over distance of 2 km with a wavelength of 632.8 nm through turbulence with a refractive index PSD following a Kolmogorov power law. More simulation parameters for the Gaussian beam verification are given in Table 5.1.

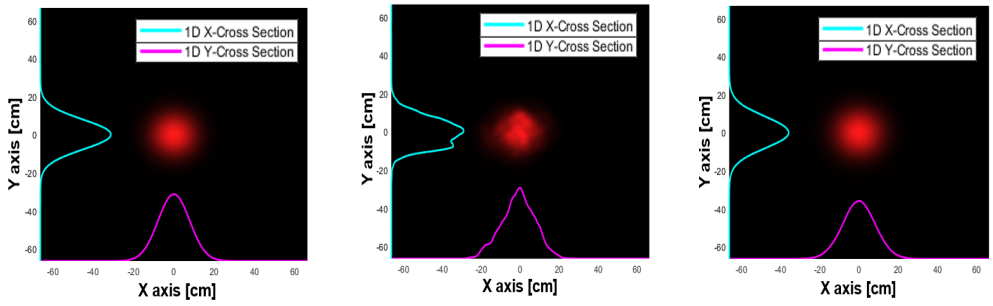

(a) (b) (c)

Figure 5.2: (a) Theoretical Gaussian beam intensity profile with X and Y cross sections. (b) Single realization of weak turbulence for a Gaussian beam intensity profile with X and Y cross sections. (c) Average intensity of a Gaussian beam over 500 realizations with X and Y profiles.

The metrics of choice for verification are average intensity, scintillation, spot size, MCF, and beam wander as they encapsulate various properties of the distorted beam profile. Each metric contains the long-term average over 500 random realizations, which is then compared to theory for verification. All simulation parameters for this section are

provided in Table 5.1 including: propagation distance, grid size, turbulence parameters, and beam properties. Figure 5.3(a) shows the average intensity, a single realization of the intensity, and theoretical profile which are in good agreement for a Rytov number of 0.1. Equation E.10 is used for comparison where the theoretical long-term spot size determines the average intensity profile. For statistical metrics throughout this work, single realizations are known as short-term average and more distortions are generally seen.

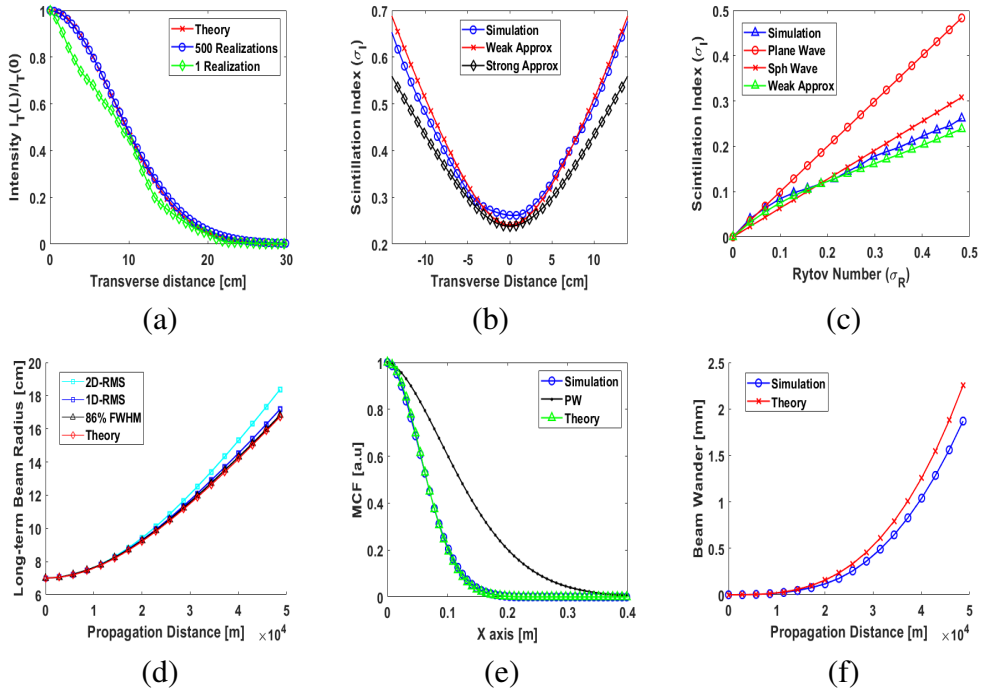

Figure 5.3: (a) Gaussian beam average intensity. (b) Gaussian beam transverse scintillation profile. (c) Gaussian beam scintillation as a function of Rytov number. (d) Spot size as a function of propagation distance. (e) Gaussian beam MCF at the final propagation step. (f) Beam wander for a Gaussian beam as a function of propagation distance.

The second metric is the scintillation profile (shown in Fig. 5.3(b)), which is also in good agreement with the theoretical result within the weak turbulence predicted by equation E.12, but due to the random nature of the fluctuations there is a slight difference. The scintillation is also compared as a function of varying Rytov number in Fig. 5.3(c),

which is in good agreement with the Gaussian beam result. The plane wave and spherical wave scintillation curves are also shown for comparison of the difference between the three forms of wave profiles. The Gaussian beam scintillation is seen to contain a different fundamental shape due to the beam wandering about its propagation axis that is not seen for a spherical or plane wave.

Figure 5.3(d) shows the long-term spot size as a function of propagation distance for a 2D and 1D profile. The 1D profile is calculated by using a cross section of the 2D intensity profile to calculate the $1/e^2$ point. The 1D profile fits the theoretical expression better as a 2D calculation renders more effects of the beam profile tails leading to an effectively larger spot size. In the strong turbulence regime the spot size saturates as the beam becomes a speckle field [188].

Figure 5.3(e) shows the beam MCF in comparison to that of a plane wave and Gaussian-beam theory. As these simulations use a sub-harmonic phase screen routine, the MCF is seen to be in good agreement with the theory for short and large transverse scale sizes. Typical MCF calculations are immensely sensitive to edge effects of numerical Fourier transforms that can be removed using a window function on each propagation step. The MCF's $1/e$ point is the SCR that is clearly defined for a Gaussian beam. As decorrelation occurs a Gaussian beam MCF contains a reduced SCR as coherence is lost. For OAM beams it has been found that the SCR is not a good metric for comparison due to more complex shapes of OAM beam MCFs. The last metric is the beam wander that follows the beam centroid in Fig. 5.1(f) which is in good agreement with theory.

Results for each metric are in good agreement with the theory for Gaussian beam propagation. As these results generalize the validity of our turbulent phase screen simula-

tions within the weak regime a cascade of multiple phase screens can be used to simulate the effects of strong turbulence, which will be used explicitly in Chapter 7 [189].

Parameter	Notation	Value
Number of realizations	N_r	500
Grid Size		1 [m] x 1 [m]
Grid Samples	N_g	512 x 512
Grid Spacing	δ	2 [mm]
Propagation Distance	L	2 [km]
Number of Propagation Steps	N_z	9
Propagation Spacing	Δz	222 [m]
Wavelength	λ	632.8 [nm]
Structure Parameter	C_n^2	3.3×10^{-18} [$m^{-2/3}$]
Rytov Number	σ_R^2	$0 - 0.23$
Fried Parameter	r_0	$\infty - 2.68$ [cm]
Initial Spot Size	w_0	7 [cm]

Table 5.1: Simulation parameters used for Gaussian beam verification simulations

5.2 OAM Propagation through a Turbulent Medium

To study OAM beam propagation through a three-dimensional random medium, the phase screen approximation is used [67]. The simulations validated in Section 5.1.1 are used to study the effects of the random turbulent phase shifts that are known to degrade a beam's spatial coherence. Simulations in this section are done within the weak and moderate turbulence regimes as strong turbulence can fully degrade an OAM based system following the parameters in Table 5.2. An OAM beam contains various degrees of freedom such as beam profile, mode number l, and spot size. Changing these inital conditions can be quantified using a number of beam metrics such as MCF, OAM spectrum, on-axis intensity, on-axis scintillation, spot size, and divergence. Numerical methods to calculate these beam metrics are discussed in Appendix F along with their analytic expressions

predicted by turbulence theory [50].

This section presents results of OAM beam propagation compared to Gaussian beams to understand if there are inherent differences upon propagation and which beam metrics are most important for OAM propagation. The simulations are then adapted for time-domain turbulence to briefly explore the effects of partial coherence on the OAM spectrum.

5.2.1 OAM Spectrum Spreading

OAM spectrum spreading is the most important metric to quantify throughout this work both analytically and computationally. To understand how different beam parameters affect OAM mode spreading, the following variables are studied: turbulence strength, beam shape, source coherence, beam size, and OAM mode. The OAM spectrum is calculated using the numerical method in Section E.1.

The first effect studied is the turbulence strength that strongly affects mode spreading as previously seen in many OAM based studies [130], [190]. Theoretical predictions using a Kolmogorov refractive index PSD are used for comparison to show the effects of beam size in comparison to the Fried parameter $2w_0/r_0$ as shown in Fig. 5.4 independent of inner and outer scale effects. The second variable is the initial beam shape that dictates the scale sizes of turbulence that the beam interacts with. Figure 5.4(a-d) summarizes the effects of propagation distance, OAM mode, and beam profile shape. Figure 5.4(a) is an LG beam with $l = 6$ that propagates over 2 km of weak turbulence where significant mode spreading occurs as the total Rytov number across the propagation path reaches 0.1. It

Parameter	Notation	Value
Number of realizations	N_r	500
Grid Size		1 [m] x 1 [m]
Grid Samples	N_g	512 x 512
Grid Spacing	δ	2 [mm]
Propagation Distance	L	2 [km]
Number of Propagation Steps	N_z	9
Propagation Spacing	Δz	222 [m]
Wavelength	λ	632.8 [nm]
Structure Parameter	C_n^2	5×10^{-16} [$m^{-2/3}$]
Rytov Number	σ_R^2	$0 - 0.1$
Fried Parameter	r_0	$\infty - 1$ [cm]
Radial wave number (Bessel \BG beam)	k_r	150
Radial index (LG beam)	p	0
OAM orders	l	0-20
Initial LG & BG spot size	w_0	1.5 [cm]
Gaussian spot sizes	-	1.5 - 6.8 [cm]

Table 5.2: Simulation parameters used for all OAM based simulations without time-correlated turbulence.

can be seen that even in a weak turbulence regime the OAM spectrum quickly degrades into a uniform distribution.

Figure 5.4(b) shows the amount of OAM power received at a 2 km distance for varying OAM orders of different beam profiles which are a Gaussian, LG, BG, and Bessel beam through weak turbulence ($\sigma_R^2 = 0.1$). The BG beam shows to retain slightly more OAM information than its counter parts due to its divergence. The Gaussian beam appears to retain the most OAM information with increasing initial spot size following $\sqrt{|l|+1}$ since its divergence and spot size are always generally smaller since in this case, the second order beam moment is not normalized in a similar manner across all beams. Figures 5.4(c-d) summarize the OAM power in the central OAM mode as a function of propagation distance and OAM mode for a LG and BG beam respectively. The heat map is the OAM mode where yellow is closer to an undisturbed beam and green is a significant loss

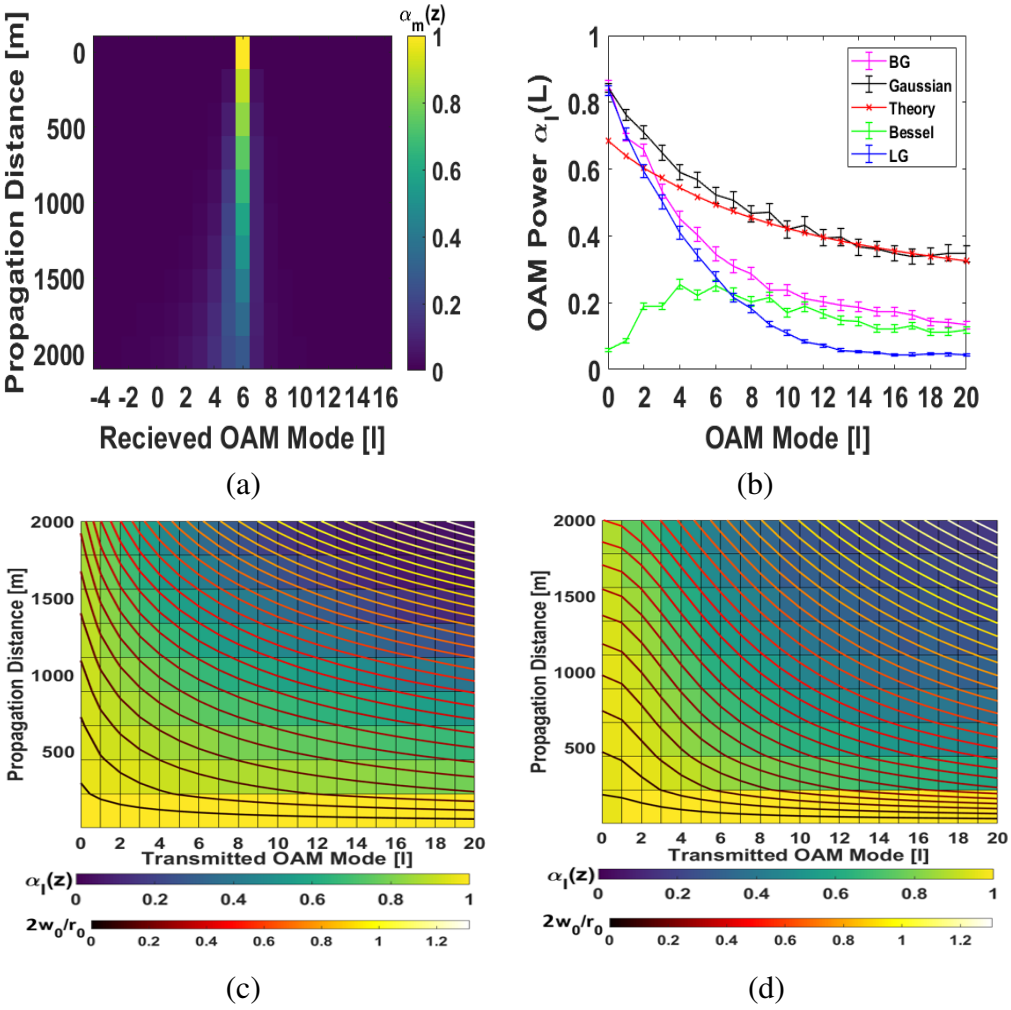

Figure 5.4: (a) Mode spreading as a function of propagation distance for an LG beam with $l = 6$. (b) Mode spreading as a function of beam profile and OAM mode through weak turbulence at the final propagation distance of 2 km. (c) OAM mode spreading from the incident mode power for LG beams as a function of propagation distance and initial OAM mode. (d) OAM mode spreading from the incident mode power for BG beams as a function of propagation distance and initial OAM mode. The contours on (c) and (d) represent the ratio $2w_0/r_0$.

of OAM information. The contours represent the ratio $2w_0/r_0$ as $2w_0/r_0 \to 1$ more OAM spreading occurs as the beam size reaches the Fried parameter scale. It can be seen that the LG beam loses OAM information much faster across all propagation distances, but each shows that higher order modes (which have a larger spot size) are more perturbed by the turbulence.

The last parameter varied is the initial beam size as shown in Figs. 5.5(a-b). For a moderate turbulence scenario the OAM power in the transmitted mode $\alpha_l(L)$ is varied as a function of beam size and OAM mode to see the effects of a changing beam size. The contours in this case represent the normalized on-axis Strehl ratio to quantify the image quality of the beam. Figure 5.5(a) is the simulation of LG modes with their initial spot size normalized by $\sqrt{|l|+1}$. It can be seen that as a function of l each beam performs the same even for the Strehl ratio meaning that OAM mode spreading, if the second order spot size is the same, is independent of OAM mode. The Strehl ratio shows that the spatial power spectrum of the beam also spreads out more significantly meaning the beam itself is more affected by the turbulence if the beam size is not normalized. Otherwise if the second order spot size is not normalized as shown in Fig. 5.5(b) higher order modes are more susceptible to turbulence induced mode spreading.

A significant take away of these turbulence simulations are the various beam parameters, specifically spot size and OAM mode, lead to more significant OAM mode spreading. Theoretically this can be seen in equation 4.4 where the modulus square of the radial beam profile scales the OAM power. As the radial beam extent increases a larger area of the phase perturbation is imparted on the beam leading to more OAM mode spreading than a beam with smaller radial extent. This interaction leads to more cumulative phase distortions. It is equivalent to thinking of the beam profile as a 2D spatial filter of the turbulence present. Which is also similar to thinking of a telescope aperture limiting the turbulence strengths, but since the beam is smaller than the aperture for these simulations the beam size is the limiting factor. As OAM mode changes, the power in the transmitted OAM is seen to decrease with increasing OAM mode. This is due to the

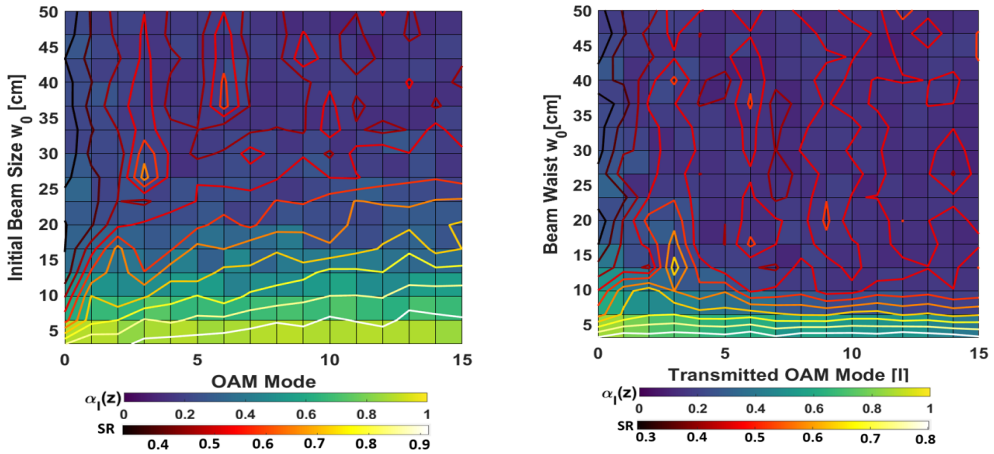

(a) (b)

Figure 5.5: (a) OAM mode spreading from the incident mode power for LG beams as a function of initial spot size and OAM mode with the second order spot size normalized by $\sqrt{|l|+1}$. (b) OAM mode spreading from the incident mode power for LG beams as a function of initial spot size and OAM mode without a normalization of the spot size (i.e. the spot size increases as a function of $\sqrt{|l|+1}$.) The contours represent the Strehl ratio.

change in beam size not the OAM mode. This is supported in Fig. 5.4(a-b) where a LG and BG beam with $l = 1$ and $l = 2$ are propagated and the initial spot size is normalized by $\sqrt{|l|+1}$ such that the initial beam size is the same. The OAM spectrum in each case is seen to be about the same, but the difference between the curves is the shape of the radial beam profile. An OAM beam whose spot size is kept a minimum and its radial extent the shortest will retain the most OAM information as it propagates. Beams with higher radial or OAM number are inherently larger leading to more susceptible to the effects of turbulent phase distortions.

It is also important to note that this change in OAM spectrum occurs when the turbulence strength reaches the beam diameter using the metric $2w_0/r_0$. This can be seen in Figs. 5.4(c-d) where the OAM spectrum loses its most information once the contour lines of $2w_0/r_0$ reaches unity. This ratio can either be reached when turbulence is strong

or over a longer propagation distance when optical wavelength is kept consistent as the loss of coherence will be affected the same due to the linear dependence of distance and turbulence strength in the Fried parameter.

5.2.1.1 Effects of Inner and Outer Scale

The previous simulations of the OAM spectrum varied beam parameters and the effective turbulence strength by using a long path length. Another parameter of interest are the perturbations by varying the turbulence scale sizes present. This is done by changing the inner and outer scale that limit the extent of the inertial subrange. Figure 5.6(a-b) shows the power in the transmitted OAM mode as a function of inner and outer scale averaged over 500 random realizations of turbulence. The simulation grid contains the same parameters as described in Table 5.1 except: C_n^2 is fixed at $1.45 \times 10^{-15}\mathrm{m}^{-2/3}$, $L = 500$, $\sigma_R^2 = 0.02$, $r_0 = 2.94$ cm, LG beam with $l = 2$, and $w_0 = 5$ cm.

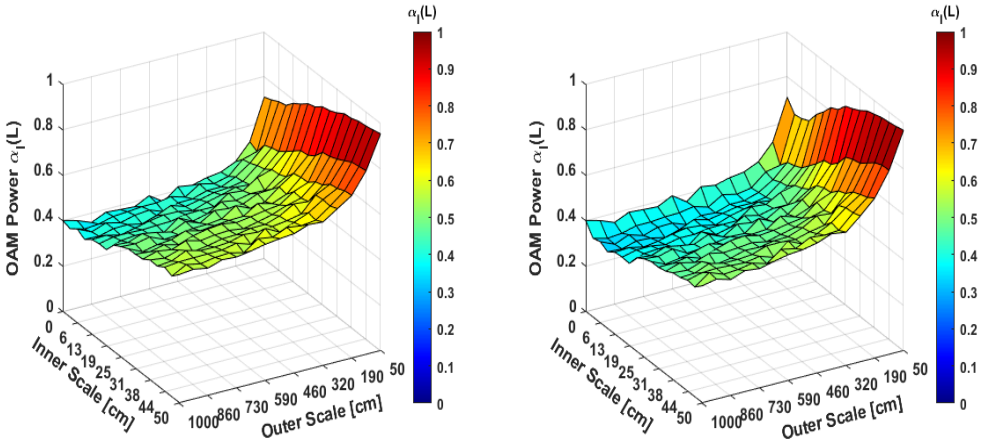

Figure 5.6: OAM mode spreading, $\alpha_l(L)$, as a function of inner and outer scale for turbulence with refractive index fluctuations following the (a) MVK PSD and (b) MA spectrum. The incident beam is an LG beam with $l = 2$ and $w_0 = 5$ cm.

Figure 5.6(a) is of turbulence following the MVK PSD in equation 2.19. As the inner scale decreases at a fixed outer scale, the power in the central OAM mode decreases. The same effect occurs as the outer scale increases for a fixed inner scale. The key point is that as the difference between inner and outer scale becomes smaller, the OAM mode power maintains the most power. The dependence of OAM mode spreading on refractive index scales sizes is due to the rate at which energy is dissipated that dictates the phase perturbation sizes. Energy is dissipated from large eddies to smaller eddies creating a continuum of eddy sizes between the outer and inner scale. If the the difference between outer and inner scale is small, no significant refractive index fluctuations are created due to no energy being transferred even if the strength of the perturbations is large (C_n^2). As the inertial subrange begins to increase (larger difference between inner and outer scale) energy begins to dissipate leaving stronger refractive index perturbations, therefore, stronger phase perturbations creating OAM mode spreading. A ratio of the inner and outer scale L_0/l_0 can quantify this dependence of mode spreading on the eddy sizes. As $L_0/l_0 > 1$ increases there will be an increase in mode spreading whereas when $L_0/l_0 \sim 1$ there will not be significant mode spreading.

Depending on the inner scale dependence of the PSD, the results can lead to significant changes in the refractive index fluctuations. This can be seen in Fig. 5.6(b) for turbulence following the MA spectrum in equation 2.20. The OAM power decreases in the same manner with inner and outer scale as the MVK results, but the rate at which OAM power decreases is different. As inner scale decreases, the overall gradient of the surface in Fig. 5.6(b) decreases quicker than Fig. 5.6(a). This is due to the different PSD shape where the MA spectrum depends on a polynomial as a function of inner scale com-

pared to the constant coefficient MVK PSD. This result is important to take into account when dealing with more complicated turbulence statistics because the size of the inertial subrange can also influence mode spreading besides the turbulence strength.

5.2.2 OAM Beam Size and Divergence Analysis

The next metric of interest can be used to determine the aperture size in an OAM based sensing system. Due to phase perturbations causing beam wander that moves the beam centroid, the long-term averaged beam size can increase leading to the beam missing the detector aperture. This spreading of the beam size also leads to an increased divergence as power is spread through larger areas in space. Knowing how large an aperture is, is key to quantifying the OAM spectrum as an aperture truncating the beam can lead to significant mode spreading [178]. The beam must stay smaller than the detector aperture or the center of the beam must be in sight of the aperture at all times otherwise the measured OAM spectrum will not be accurate. Figure 5.7(a-b) summarize the effects of initial OAM mode and beam profile and its effects of beam size and divergence respectively.

The simulations show that the turbulence induced beam size is not as significant as first thought for the beam sizes tested over a long propagation distance. The divergence is more prevalent depending on the initial beam size. The LG beam is seen to retain its similar divergence that depends on the mode order, whereas BG beams follow a similar divergence to a Gaussian beam. This divergence is what is attributed to the BG beam retaining more OAM information in section 5.2.1. This is important for sensing systems

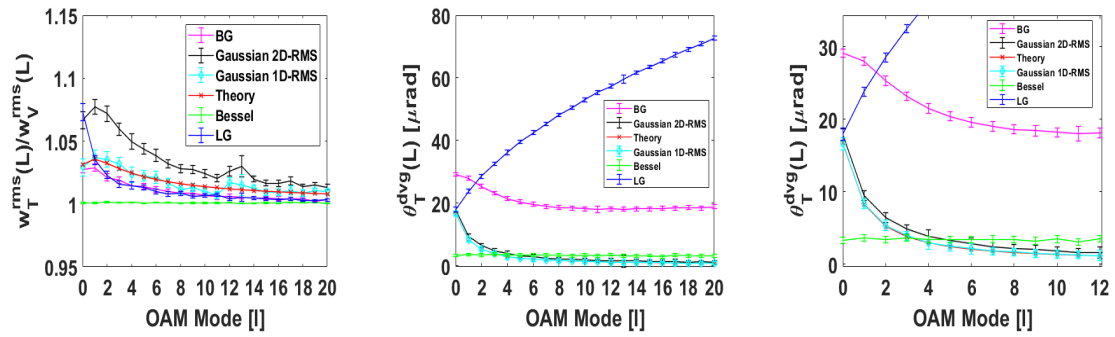

Figure 5.7: (a) Spot size at the final propagation distance of 2 km as a function of OAM mode normalized by the vacuum value of the spot size. (b) Divergence at the final propagation distance as a function of OAM mode. (c) Zoomed in view from plot (b) highlighting the differences in beam divergence.

that may work over a longer distance where divergence will start playing a role even for a well collimated transmitted beam. Experiments in this work will not have to consider the effects of significant beam spreading due to turbulent effects.

5.2.3 OAM Beam Intensity and Scintillation Analysis

The last metric is the turbulence induced intensity fluctuations. This is of interest as a few recent works have quantified OAM beams using on-axis intensity as defined for a Gaussian beam [191], [192]. Defining "on-axis" for an OAM beam in this work means measurement along the main annulus of any OAM beam [186]. The turbulence induced on-axis losses and scintillation are shown in Fig. 5.8.

The scintillation and on-axis intensity losses for the LG beam are consistent across all OAM modes. This is due to the LG beam symmetry across all OAM modes upon propagation, which is not shared for the BG beam due to the change in divergence that follows a Gaussian beam and dependence on the radial wavenumber k_r. A similar trend

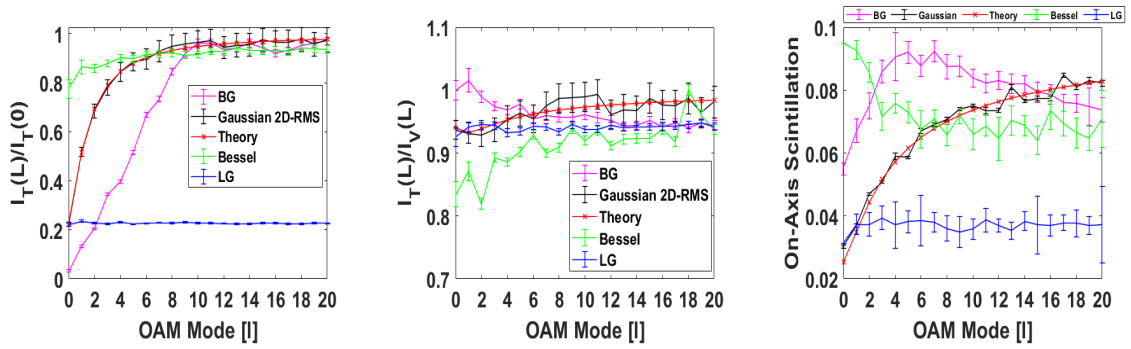

(a) (b) (c)

Figure 5.8: (a) On-axis intensity losses as a function of OAM mode at the final propagation distance normalized to the initial on-axis intensity. (b) On-axis intensity losses as a function of OAM mode normalized to the vacuum intensity loss to remove free-space diffractive losses. (c) On-axis scintillation as a function of OAM mode at the final propagation step for various beam profiles.

is seen for the on-axis scintillation which is not seen to increase for OAM beams in comparison to BG, Bessel, or Gaussian beams. This is due to the symmetry across the annuli of each OAM beam that maintains the same shape for each OAM mode order. Although each beam does contain a different divergence, which is known to affect scintillation, the annulus diverges at a similar rate respective to the original size.

These results show OAM beams do provide scintillation and intensity benefits, but only when the beam divergence and spot size are matched to the propagation distances in question. Otherwise the OAM beam will be affected by turbulence in a similar manner to a Gaussian beam. It is also shown that higher order OAM modes do not necessarily have outstanding benefits to lower order OAM modes in terms of intensity or scintillation effects within weak Kolmogorov power-law turbulence. Our results for strong scintillation show higher order modes, with an initial spot size of 2 cm, had a 25% less on-axis scintillation index for a Kolmogorov power-law spectrum [193]. When the initial beam size was changed to 12 cm, the scintillation appeared to be similar across each OAM mode.

It is important to note that the beams here are fairly compared by being normalized with respect to their own vacuum propagation which brings divergence and spot size symmetry into question when comparing OAM beams to Gaussian beams. If the sensing modality or communication application in question takes into account shaping the beam size and divergence according to their distances benefits of LG beams may be seen over a Gaussian beam due to the symmetrical divergence.

5.2.4 Impact of a Partially Coherent Laser Source

In relation to intensity and scintillation, it is known that partially coherent beams can minimize the amount of scintillation that can induce errors within optical measurements [194]–[196]. A specific case of a partially coherent beam with OAM is the I_m Bessel beam that has been experimentally seen to reduce scintillation [140]. Using the coherent mode representation of the MCF (CSD in coherence theory), the I_m Bessel beam can be simulated using a modified split-step method to include temporally correlated turbulence discussed in Appendix B and Ferlic *et al.* [183]. This simulation method can vary the transmitter cycling rate f_T and detector exposure time f_D to see the effects of partial coherence ξ on the OAM spectrum as well as intensity and scintillation. Simulation parameters are described in Table 5.3 for each of the simulations in this section.

Parameter	Notation	Value
Temporal Duration	N_t	250, 500 [ms]
Detector Cycling Rate	f_D	50 - 3500 [Hz]
Transmitter Cycling Rate	f_T	50 - 3500 [Hz]
Time Step	dt	$1/f_D$ [s]
Grid Size		1 x 1 [m^2]
Grid Sample	N_g	512 x 512
Grid Spacing	δ	2 [mm]
Propagation Distance	L	2 [km]
Number of Propagation Steps	N_z	9
Propagation Spacing	Δz	222 [m]
Wavelength	λ	632.8 [nm]
OAM Orders	l	0-20
Initial Spot Size	w_0	5 [cm]
Coherence Parameter	ξ	0.01, 0.5, 0.9
Number of Eigenmodes	N_p	16
Structure Parameter	C_n^2	4.2×10^{-16} [$m^{-2/3}$]
Rytov Number	σ_R^2	$0 - 0.1$
Fried Parameter	r_0	$\infty - 1$ [cm]
Memory Parameter	α	0.99
Wind Vector	(v_x, v_y)	$(\sqrt{3}, 0)$ [m/s]

Table 5.3: Simulation parameters used for all partially coherent OAM beam simulations presented in this paper containing time-correlated turbulence.

5.2.4.1 OAM Spectrum Spreading

The main results of the simulation is understanding how the added temporal sampling rates play a part in perturbing the OAM spectrum. It is known for Gaussian-Schell sources the OAM spectrum coherence is reduced leading to little or no OAM information [137], [197]. The results here are quite in contrast as the I_m Bessel beam's well defined OAM state effectively decouples the OAM information from the source coherence. The propagation of an I_m Bessel beam, detailed in Appendix D, relies on a DMD to rotate through the series of basis modes to arrive at the correct MCF. The detector exposure time changes the amount of temporal averaging that can change the measured MCF and

thus the detector OAM mode power. Figure 5.9(a-f) summarizes the effects of transmitter and detector cycling rates on the detected OAM spectra for various coherence parameters.

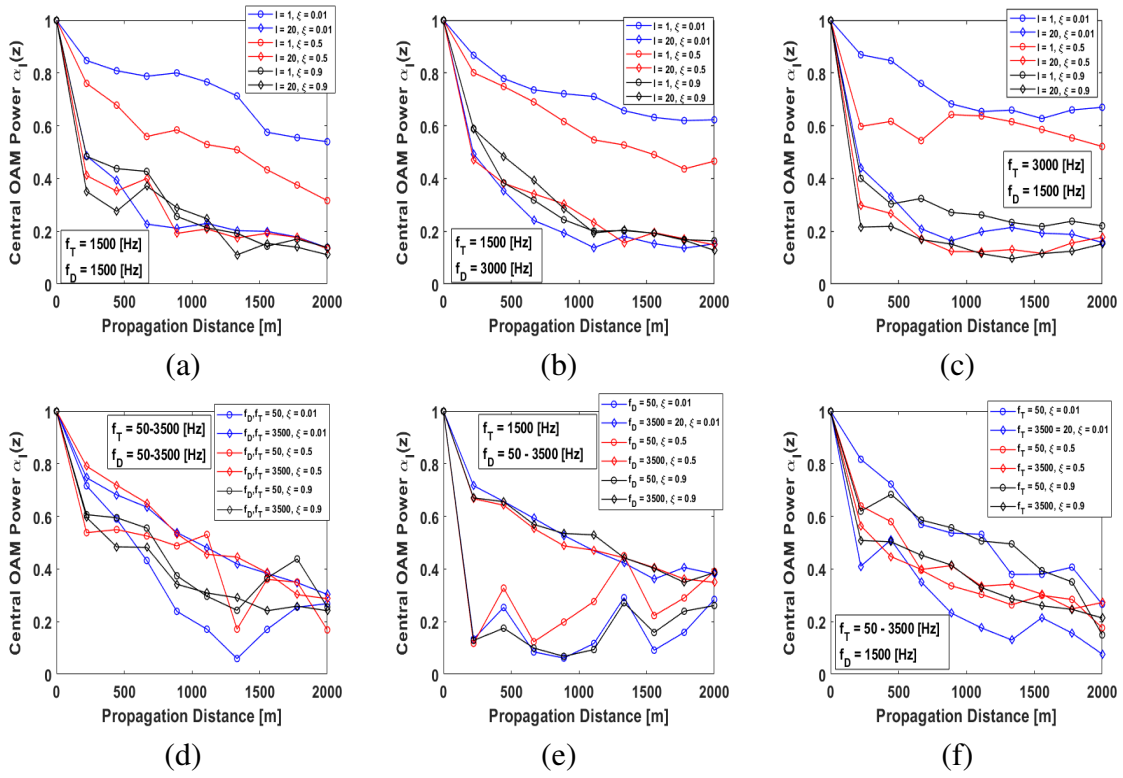

Figure 5.9: OAM mode spreading as a function of propagation distance for (a) matched transmitter and receiver, (b) faster detector speed, (c) faster transmitter speed, (d) matched transmitter and receiver, (e) fixed transmitter speed, (f) fixed detector speed and varying transmitter speed.

Figure 5.9(a-c) show the OAM mode spreading as a function of propagation distance z for different OAM modes ($l = 1$ and $l = 20$) for fixed cases of transmitter and receiver rate. In each case, the larger OAM mode loses more OAM power compared to the smaller OAM mode. The results in Fig, 5.9(b) show that a faster detector rate increases the amount of OAM mode power due to more temporal averaging compared to the cases with a shorter detector exposure time. With a short exposure time, a lucky image of the OAM spectrum could be obtained with higher mode power, albeit not consistently.

In Fig. 5.9(d-f) the transmitter and detector rates are varied along with the coherence parameter with a fixed OAM mode of $l = 5$. For the cases in Fig.5.9(d) and 5.9(f) show no significant difference in retained OAM information. However, the case of a faster detector rate in Fig. 5.9(e) shows that more OAM power can be retained as a function of propagation distance.

For beams with less coherence, the OAM information is seen to decrease mainly due to higher order LG_l^p modes being introduced, which leads to a larger beam size and thus more OAM spreading as the area of interaction with the turbulence increases. The general trend is that the transmitter cycling speed does not strongly affect the detector OAM spectrum compared to the detector exposure time. Effects of OAM mode play a similar role as discussed in Section 5.2.1 due to the increase in beam size.

Using a transmitter with a faster sampling rate will drastically improve the long-term averaging affects to measure higher transmitted OAM mode power. This was experimentally seen in an experiment by Funes *et al.* [198] where a significant long-term average ($>$ 30 minutes) produced a clearer OAM spectrum, although not for the I_m Bessel beam explicitly. For an OAM based sensing modality the detector sampling rate will have to be taken into account in a practical setup depending on if short-term of long-term statistics are of interest.

5.2.4.2 Intensity and Scintillation

As expected the source coherence strongly affects the intensity and scintillation. As the beam's coherence decreases the intensity losses increase and the scintillation also

increases. The scintillation increases because the reduced spatial coherence also increases the baseline scintillation created from simply switching between beam shapes quickly [183]. This means for a practical implementation the scintillation that is to be reduced by turbulence must be compared to the scintillation by switching beams. Depending on the application this may be a beneficial effect, but for OAM sensing the added scintillation and intensity losses do not add any significant benefits for a sensing modality.

5.2.5 Summary: Simulations of a Turbulent Medium

The simulation foundation developed in this section provides key information on understanding which propagation degrees of freedom are most important being turbulence strength, beam profile, source coherence, beam size, and OAM mode. The two most influential degrees of freedom are turbulence strength and beam profile which generalizes the effects on beam size and OAM mode. Developing and verifying these simulations also provide a basis for the rest of the experimental and simulation work in Section 5.3 and Chapter 7. By understanding which variables affect OAM mode spreading a few practical lessons are learned when OAM is used in a practical setup:

- OAM beam divergence reliant on the initial wavefront shape plays a key role in OAM spectrum degradation.
- OAM spreading is dependent on the beam size not the initial OAM mode order. Motivates the use $2w_0/r_0$.
- A partially coherent source is not significantly beneficial for an active OAM remote sensing modality due to its minimal benefits and added experimental complexity.

- Turbulence induced beam spreading is not a significant issue for the turbulence strengths and distances simulated in this work.

- Detector sampling frequency will play a role in gathering short or long term statistics depending on the OAM information of interest.

- Difference between the inner and outer scale (using the ratio L_0/l_0), changing the size of the inertial subrange, plays a role in creating mode spreading. A ratio of $L_0/l_0 > 1$ indicates when this impacts OAM mode spreading.

5.3 OAM Propagation through a Turbid Medium

The second medium of concern is a turbid medium that can also perturb a beam's coherence significantly in specific circumstances. A difficulty with modeling a turbid medium is developing a similar method of beam propagation that focuses on coherent effects like turbulence, but also can deal with higher angle scattered light. The benefits of the WOS over other simulation routines is that it provides the inherent ability to model coherent effects of laser beam propagation, which are typically limited to smaller scales using finite-element methods [199]–[201] or not inherently taken into account using traditional Monte Carlo ray tracing routines [202], [203], but trials at including coherence to Monte Carlo techniques have been made [204]–[207]. There has also been discrete particle models used to simulate the effects of a turbid medium [115], [185], [208]. Models have also been developed to simulate the far-field diffraction pattern from a volume containing particulate matter with an OAM beam incident on it, but loss of coherence upon propagation was not the focus of this method [209], [210].

The turbid medium simulations are done using the same split-step method with the main difference being the phase power spectrum derived in chapter 3. Using WOS in a turbid medium inherently limits the validity of the results to the small-angle approximation of the RTE. The light scattered in a WOS falls within the simulations predefined field of view (FOV) and light scattered at high angles, such as backscatter, is not modeled. Depending on the particle sizes, large FOVs cannot be modeled due to grid size limitations that lead to discretization errors. It is also noted that turbid medium simulations contain an additive intensity factor that represents the incoherent scattered radiation when in the multiple scattering regime from various places within the medium, which is not accounted for in a WOS [210], [211]. This additive factor is allowed as incoherent light has lost its ability to spatially interfere with the forward scattered and ballistic light [117], [118], [212].

5.3.1 OAM Spectrum Spreading through a Turbid Medium

Within a turbid medium, OAM mode spreading is dictated again by the refractive index inhomogeneities that are dependent on the optical depth and particle sizes present. The main difference is that the scattering strength breaks the RGD approximation where the phase function takes on the role of the refractive index power spectrum. The phase function calculations from Mie theory can be used (Appendix B.2) for prediction of the phase correlations to construct random turbid phase screens. These phase screens can then be used to study beam propagation in large scale environments. An important factor is understanding when the phase function can change shape due to the structure of the

incident field. The phase function is seen to change in a few particle environment when the full electromagnetic field of the beam profile must be simulated [28], [209]. For an environment containing many particles, the phase function of an OAM beam is seen to be similar to that predicted of Mie Theory [210], [213]. This finding parallels the RGD approximation for a continuous medium that requires a large enough volume to statistically represent the particle scattering [59]. The simulations in this section briefly explore the effects of a turbid medium on the following variables that are known to affect OAM beam propagation: particle size, optical depth, OAM order, and beam size. The grid and beam parameters used for all turbid medium simulations are provided in Table 5.4.

Parameter	Notation	Value
Number of realizations	N_r	100
Grid Size		5 [mm] x 5 [mm]
Grid Samples	N_g	512 x 512
Grid Spacing	δ	9.8 [μm]
Propagation Distance	L	5 [cm]
Number of Propagation Steps	N_z	30
Propagation Spacing	Δz	0.1 [cm]
Wavelength	λ	532 [nm]
Optical Depth	$\sigma_{ext}L$	0 - 20
Particle Size	2a	0.01 [μm] - 800 [μm]
Initial Spot Size	w_0	98 [μm] - 1.22 [mm]
OAM Mode	l	0 - 15

Table 5.4: Simulation parameters used for all turbid medium simulations.

The first form of verification of WOS through turbid media is of the single scattering regime. Figure 5.10(a) shows the 2D far-field intensity distribution over 100 realizations for a simulation of an LG beam with $l = 2$ ($w_0 = 0.3$ mm) after propagating over 5 cm containing 50 μm particles of refractive index $n_p = 1.59$ and $n_{water} = 1.33$. The far-field intensity is calculated using the Fraunhofer approximation ($|\mathscr{F}_2\{U(r,\phi,z)\}|^2$) [91].

In Fig. 5.10(b), at an optical depth of 0.5, the minimums of the far-field pattern correspond to scattering angles of 0.7° and 1.3°. These points agree with the Mie theory phase function shown as the red plot in Fig. 5.10. The simulated data within the single scattering regime does not reach the minimums exactly due to significant randomization of the scattered light that blurs the data. With this verification that the phase screens contain the correct correlation properties OAM beam propagation can be done.

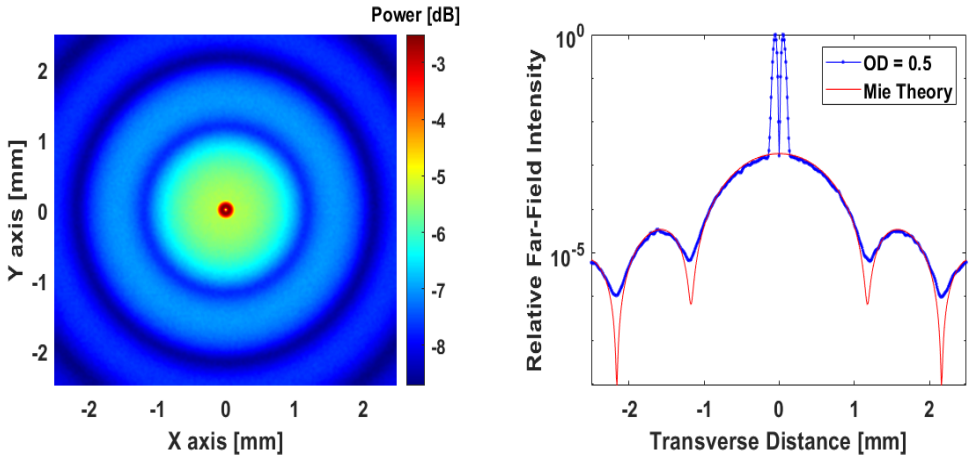

Figure 5.10: (a) Log scale of the 2D far-field intensity distribution of an incident Gaussian beam. (b) 1D cross section of the 2D far-field intensity distribution normalized to the maximum point.

The first simulation to determine how a turbid medium affects OAM beam propagation varies the particle size. The MCF and OAM spectrum are calculated to quantify how scattering affcets an OAM beam. The MCF is the second quantity used to determine the validity of the turbid medium model described in Section 4.3. The simulated MCF can be compared to the functions from Section 3.6. This comparison is done as a function of particle size in Fig. 5.11(a). The green curve represents the vacuum MCF in the presence of no perturbations, the open circles are simulated values, and closed crosses, asterisks,

and stars are theoretical MCF using equations 3.9 and 3.24. For various particle sizes at a fixed optical depth, the theoretical and simulated values of the MCF for an LG beam with $l = 2$ are in good agreement. The values around the axis are seen to lose correlation, but maintain their spatial structure especially in the case of the 600 μm particles. This is unlike a turbulent MCF where the MCF shape is quickly lost. The MCF of a turbid medium is similar in nature to Gaussian phase fluctuations as they both contain a diffuse halo around the origin [91]. Using a logarithmic x-axis the largest change are the values close to the axis, which become more decorrelated as particle size increases.

Figure 5.11(b) shows the OAM spectrum spreading for an LG beam with $l = 2$ as a function of particle size at a fixed optical depth over 100 random realizations of phase screens. The x-axis of the bar chart is the detected OAM mode, the y-axis is the particle size in microns, and the z-axis is the amount of power retained ($\alpha_l(L)$) in each OAM at the final propagation distance L with an optical depth of 4. Results show that as particle size increases the OAM spectrum becomes more perturbed as expected for larger particles from other models [185]. This loss of coherence is due to larger particles containing more forward scattered light that interferes with the ballistic light leading to loss of coherence therefore creating OAM spreading. This is also explained by the particle size limiting the sizes of phase perturbations present similar to the inner and outer scale of turbulent phase perturbations. The WSF of a turbid medium can be considered similar to a low-pass filter that begins to introduce higher frequency phase distortions as the particle size begins to increase. Another effect of particle size is the particle size distribution of the medium that can dictate changes within the medium's MTF such as a larger forward scatter component due to the presence of larger particles.

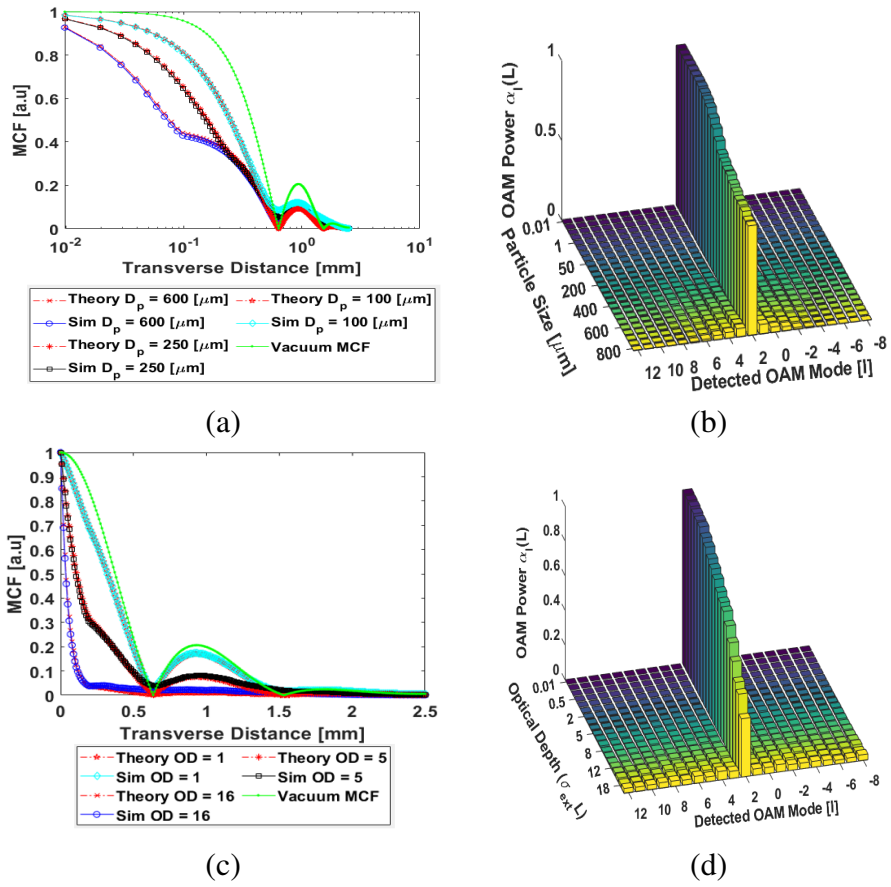

Figure 5.11: (a) MCF of an LG beam with $l = 2$ for various particle sizes at a fixed optical depth of 4. (b) Mode spreading of an LG beam with $l = 2$ for varying particle sizes at a fixed optical depth of 4. (c) MCF of an LG beam with $l = 2$ for varying optical depth for a single particle diameter of 200 μm. (d) Mode spreading of an LG beam with $l = 2$ for varying optical depth at a fixed particle diameter of 200 μm.

The next variable that is varied is the optical depth while beam size, OAM mode, and particle size (set to 200 μm) are fixed. Figure 5.11(c) contains three MCFs of an LG beam with $l = 2$ through three optical depths. As the optical depth increases, the correlation around the axis decreases. The shape of the MCF also starts to blur due to strong scattering effects leaving a speckle field. As the MCF shape changes, the OAM spectrum is also expected to change. When the optical depth reaches the multiple scattering regime ($\sigma_{sca} z > 12$), noticeable mode spreading begins to occur. In these WOSs, the ballistic

field is easily decoupled from incoherent higher angle scattering. Figure 5.11(d) accounts for these intensity losses by normalizing the OAM spectrum using equation 4.3. If the optical receiver, in a practical experiment, does not contain enough sensitivity these effects will not be measurable and scattering will be seen to induce little mode spreading effects.

The particle size also dictates the amount of mode spreading even when fixed, this is due to the optical depth and phase function amplitude dictating the turbid medium phase correlation function. The phase correlation is scaled linearly with optical depth whereas the phase function amplitude varies in a more complicated manner. For large particles, the phase function can be approximated as an Airy disk scaled as $1/(ka)^2$ that is similar to the Mie theory phase function scaled by $1/(k^2 C_{sca})$ [96].

For the study of turbulence it was seen that the beam size compared to the atmospheric coherence length $2w_0/r_0$ strongly dictates mode spreading. A turbid medium also contains a coherence length on the order of the particle diameter. Since the beam size affects the MCF shape and how much of the beam interacts with the medium, the OAM spectrum is expected to change depending on the scattering strength. In the following plots an LG beam with $l = 2$ is transmitted through a path length of $L = 5$ cm containing a turbid medium. Figure 5.12(a) is a surface plot where the colorbar represents the power within the central OAM mode $\alpha_2(L)$ at the final propagation step, the x-axis is the beam size, and the y-axis is the particle diameter. A clear trend is seen where as the particle size increases the amount of OAM power reduces across all beam sizes. As particle size reaches the beam size OAM mode spreading becomes more severe. A larger beam, in this case of random medium, seems to maintain more OAM power in the transmitted mode than a smaller beam.

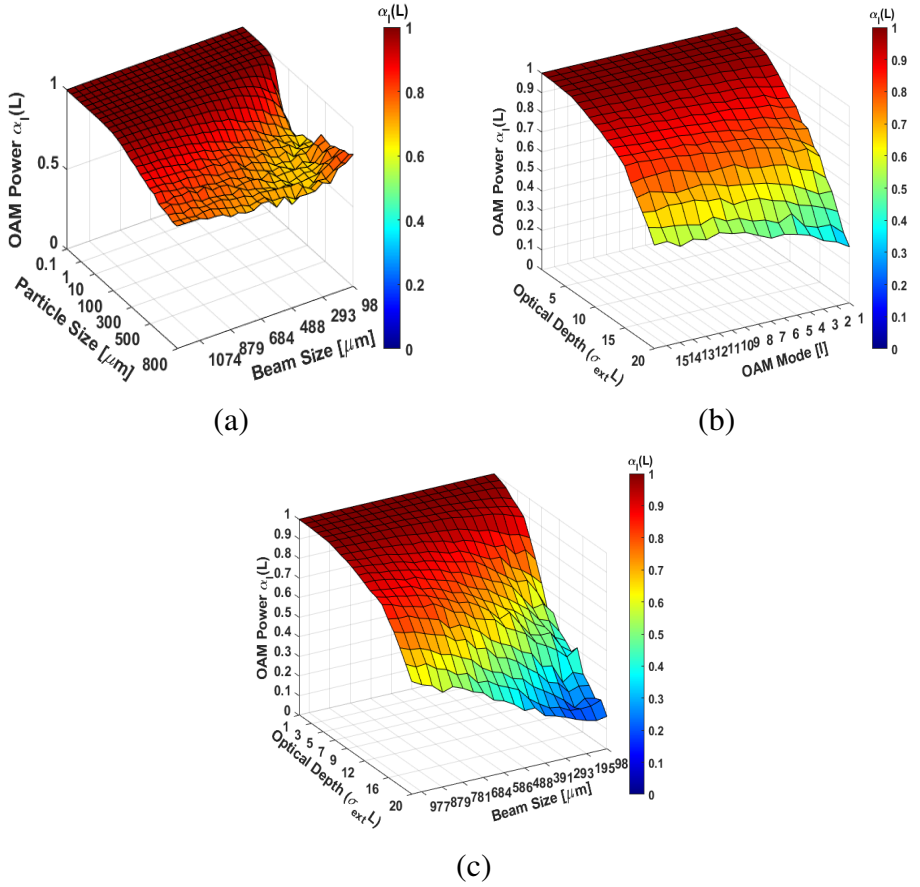

Figure 5.12: (a) MCF for an LG beam with $l = 2$ for a fixed particle size, optical depth of 4, and varying initial beam size. (b) Mode spreading as a function of initial beam size and particle diameter for a fixed optical depth and OAM mode $l = 2$. (c) Mode spreading as a function of initial beam size and optical depth with a fixed OAM mode $l = 2$. (d) Mode spreading with varying optical depth and OAM mode for a fixed beam size.

In the case of a fixed particle diameter of 200 μm and fixed beam size effects of a varying OAM mode can be studied. As determined for a turbulent medium, varying the OAM mode without normalization of $\sqrt{(|l|+1)}$ will result in the same effects as if the beam size were increased. Figure 5.12(b) plots the OAM spectrum power $\alpha_2(L)$ (color-bar) as a function of particle size (y-axis) and incident OAM mode (x-axis). The results show that a higher order OAM beam retains a bit more OAM power in the transmitted mode similar to the previous results in Fig. 5.12(a). This is thought to be due to the

phase perturbations length scales and MTF shape which contains a cutoff frequency of a/λ [101]. This cut off frequency limits the high frequency phase perturbations that typically perturb larger beams more than low frequency components. A smaller beam is more susceptible to beam wander as the beam of interest becomes misaligned with the basis function origin leading to mode spreading. This is also compared to focusing a laser through a volume of scattering particles where the light afterwards is strongly perturbed due to the interaction with a few particles compared to an unfocused beam interacting with many particles which averages out single scattering effects [210], [213].

The last variable studied is the optical depth as a function of beam size for a fixed LG beam with $l = 2$ and a particle size of 200 μm. Figure 5.12(c) shows this case where the x-axis is the beam size in millimeters and the y-axis is the optical depth. The heatmap color represents the OAM spectrum power $\alpha_l(L)$ with $l = 2$. The trend shows that smaller beams are more susceptible to mode spreading as a function of optical depth compared to larger beams. The ratio w_0/a can be used to describe when the effects of particle size will play the greatest role. This is due to the same reason as in Fig. 5.12(b) where a smaller beam is more affected by an individual phase perturbation unlike a larger beam that averages over many perturbations. The most mode spreading is seen for optical depths greater than 12, which in practice are not necessarily going to be reached due to power losses if not enough optical power is used with a small FOV system and finite noise floor detectors. Therefore, if a low sensitivity detector or not enough optical power is used OAM mode spreading may not be seen experimentally. OAM mode spreading may also not been seen if the particle size is too small. In the cases of experimentation in this work, this is believed to be why the effects of mode spreading in a turbid medium are

not measured. Other studies have seen particle scattering to affect the mode spectrum but direct comparison to these results is difficult due to each measurement using a different experimental apparatus.

5.3.2 Summary: OAM Beam Propagation through a Turbid Medium

Modeling a turbid medium using WOS's provided great insight to how particulate matter perturbs the OAM spectrum while maintaining numerical efficiency. Results of this work say similar results to work by Viola *et al.* [185] which are that larger particles created more OAM mode spreading than smaller particles at a fixed optical depth. It is not clear how much their beam size affected results as simulation results were over long distances using an initial sub-micron beam which would be most likely highly divergent over meter propagation lengths even when well collimated. Important information to draw upon from this section is as follows for later experiments:

- Larger particles are seen to create forms of OAM spreading compared to smaller particles for a fixed OD.
- Beam size plays a similar role to turbulence, but smaller beams are perturbed more than larger beams in a turbid medium. When $w_0/a > 1$ the phase perturbations due to particles will create mode spreading, when $w_0/a < 1$ the effects on mode spreading will be less.
- If a particle distribution contains mostly small particles a laser wavefront will not be as greatly perturb except for slight blurring effects as with larger particles. a/λ plays a role in determining the spacial cutoff frequencies to create blurring effects.

- An increasing OAM mode order affects the amount mode spreading due to an increase in beam size changing the ratio w_0/a.

- Optical depths of 0 - 20 (transition between single scattering and multiple scattering) do not produce significant mode spreading even for a large particle of 200 μm for various beam sizes leading to the result that mode spreading will be difficult to measure.

Chapter 6: Initial Active OAM Sensing Experiments

As a first trial to understand the fundamentals of experimental OAM spectrum measurements, two experiments using different OAM spectrum measurement techniques are implemented. The first method, using a wavefront folding interferometer [214], was deemed appealing due to its simple experimental setup by placing the OAM measurement complexity into a single image without needing custom optics like a mode sorter. The second experiment is a standard mode projection experiment through turbid water. Mode projection contains a more involved transmitter and receiver as compared to the interferometer, but no interference is needed leading to less stringent optical stability conditions. The results, lessons learned, and comparison to the literature are provided for each experiment.

6.1 Experiment #1: Wavefront Folding Interferometer

The first method uses a wavefront folding interferometer (WFI) [214], Fig. 6.1, to measure the effects of lab generated turbulence. The goal is to determine the sensitivity to turbulence and if a WFI would be an effective way to measure the OAM spectrum due to its minimal optical components and ability to measure the OAM spectrum in a single image. It is known that turbulence can wash out the interference pattern if averaged over a

long period, if data is acquired using short exposure time an average OAM spectrum can be obtained. It is expected that more mode spreading will occur for a stronger turbulence strength.

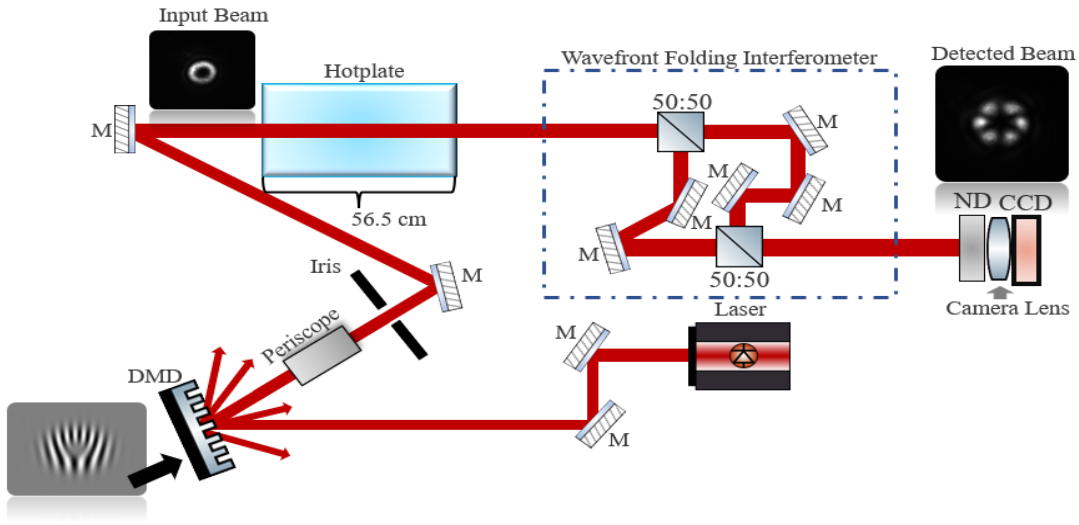

Figure 6.1: Experimental setup using a WFI to measure the turbulent distortions as the beam propagates over the hotplate. M: mirror, DMD: deformable micromirror device, 50:50: beamsplitter, ND: neutral density filters, CCD: charged coupled device.

At first glance this is the same way OAM superpositions are created that result in petal shaped beams using a modified Mach-Zehnder interferometer. But the petals are also related to a quantity called the angular coherence function (ACF). The ACF is derived from the coherent mode representation of the beam's MCF using OAM modes [155], [163]

$$\Gamma_2(r_1,\phi_1,r_2,\phi_2) = \langle U^*(r_1,\phi_1)U(r_2,\phi_2)\rangle = \sum_{l=-\infty}^{\infty}\sum_{p=0}^{\infty}\sum_{p'=0}^{\infty}\lambda_{lpp'}\Psi_l^{*p}(r_1,\phi_1,z)\Psi_l^{p'}(r_2,\phi_2,z), \tag{6.1}$$

where $\lambda_{lpp'}$ are the eigenvalues following from $\langle c_{lp}^* c_{l'p'}\rangle = \lambda_{lpp'}\delta_{ll'}$ assuming that $l = l'$ and $\delta_{ll'}$ is the Kronecker-delta function. Upon integration over the radial coordinates of

equation 6.1 the ACF is defined as

$$\Gamma_{ACF}(\Delta\phi) = \frac{1}{2\pi} \sum_{l=-\infty}^{\infty} S_l e^{-il\Delta\phi}. \tag{6.2}$$

and the angular Wiener-Khinchin theorem can be applied to obtain the OAM spectrum

$$S_l = \int_{-\pi}^{\pi} \Gamma_{ACF}(\Delta\phi) e^{il\Delta\phi} d(\Delta\phi). \tag{6.3}$$

A more physical interpretation of the above equations can be thought of as an angular equivalent to spatial coherence. Typically a beam's spatial coherence can be measured using two slits and quantifying the contrast between the peaks and valleys within the interference pattern, but here the angular information is being quantified instead. If two angular splits were placed in the beam path, the resulting interference pattern would depend on the angular coherence between the two beams which depends on the OAM spectrum. As the spatial coherence, or angular coherence, of the beam decreases, the OAM spectrum begins to spread into higher order modes. This is one reason why a well defined OAM state is typically recreated using a fully coherent laser.

The measurement procedure in Fig. 6.1 starts with a He-Ne laser with a wavelength of 632.8 nm that is directed towards a DMD displaying a type 2 forked grating [135], [136] to generate an LG beam. The DMD generates 2 orders of diffraction patterns where a spatial filter is needed to pick one of the four main lobes. The filtered beam is then passed over a hot plate that generates convective turbulence. The WFI sits across the optical bench to receive the beam. The output of the WFI can be used to measure the

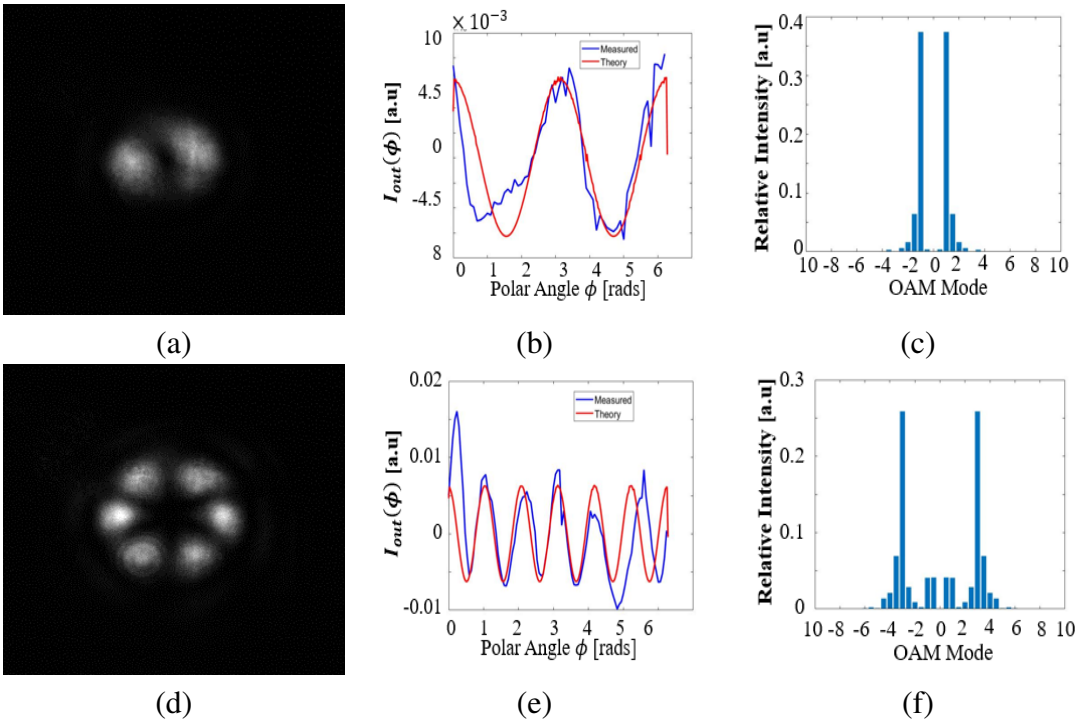

Figure 6.2: Image of the interference pattern using an LG beam with $l = 1$ (a), azimuth intensity $I_{out}(\phi)$ (b), and OAM spectrum (c). Image of the interference pattern using an LG beam with $l = 3$ (d), azimuth intensity $I_{out}(\phi)$ (e), and OAM spectrum (f).

OAM spectrum as the intensity distribution of the WFI is directly proportional to the ACF upon integration over the radial coordinate ($I_{out}(\phi)$). Upon recording an intensity pattern using the CCD camera in Fig. 6.1, the OAM spectrum can be recovered using [155]

$$S_l = \int_{-\pi}^{\pi} W(2\phi) e^{il2\phi} d(2\phi) = \frac{1}{\tau \cos(\delta)} \int_{-\pi}^{\pi} \left(I_{out}(\phi) - \frac{1}{2\pi} \right) \cos(l2\phi) d\phi, \tag{6.4}$$

where τ is related to temporal coherence and $\cos(\delta)$ is related to the path length difference. The azimuth intensity is then Fourier transformed and the OAM spectrum is found. Note that the OAM spectrum in this case is two sided compared to previous definitions in chapter 4. This does not change the results as now modal power is split between the incident mode and its conjugate instead, but the same information is retained. Figure 6.2

shows the resultant interferogram, azimuth intensity $I_{out}(\phi)$, and measured OAM spectrum for OAM modes $l = 1$ (Figs. 6.2(a-c)) and $l = 3$ (Figs. 6.2(d-f)). Even within the presence of no turbulence the OAM spectrum is rather noisy. This is due to imperfections across the intensity image, although it looks decent the small asymmetries translate to severe perturbations of $I_{out}(\phi)$ and thus to OAM spectrum.

6.1.1 Impact of Turbulence Strength

By changing the heat setting of the hot plate two different values of the refractive index structure parameter (C_n^2) can be reached. These values were measured as 93° C and 220° C using resistive temperature detectors [215]. At two temperature settings of $93°C$ and $220°C$ the C_n^2 was measured to be $7.4 \times 10^{-13}\text{m}^{-2/3}$ and $2.2 \times 10^{-11}\text{m}^{-2/3}$ respectively. The corresponding Rytov numbers for each value of C_n^2 are 1.4×10^{-3} and 4.6×10^{-5}. The Fried parameters of each turbulence strength are then 2.36 cm and 18.05 cm. The inner scale was estimated to be $4 - 8$ cm [216]. Results of the average OAM spectra for an LG beam with $l = 3$ are shown in Figs. 6.3(a-f). The top row (Figs. 6.3(a-c)) are for the weaker value C_n^2 and the bottom row (Figs. 6.3(d-f)) are for the stronger value of C_n^2. Each image of the interference pattern and azimuth intensity are a single picture whereas the OAM spectra are averaged over 500 image acquisitions.

The resulting OAM spectra followed the trend as expected that the OAM spectrum spreads further for higher values of C_n^2 at a fixed propagation distance. More measurements are made for $l = 1, 2, 4, 5$ and the same results are achieved and show that higher order beams are more perturbed by the turbulence, but it is not clear due to the noisy

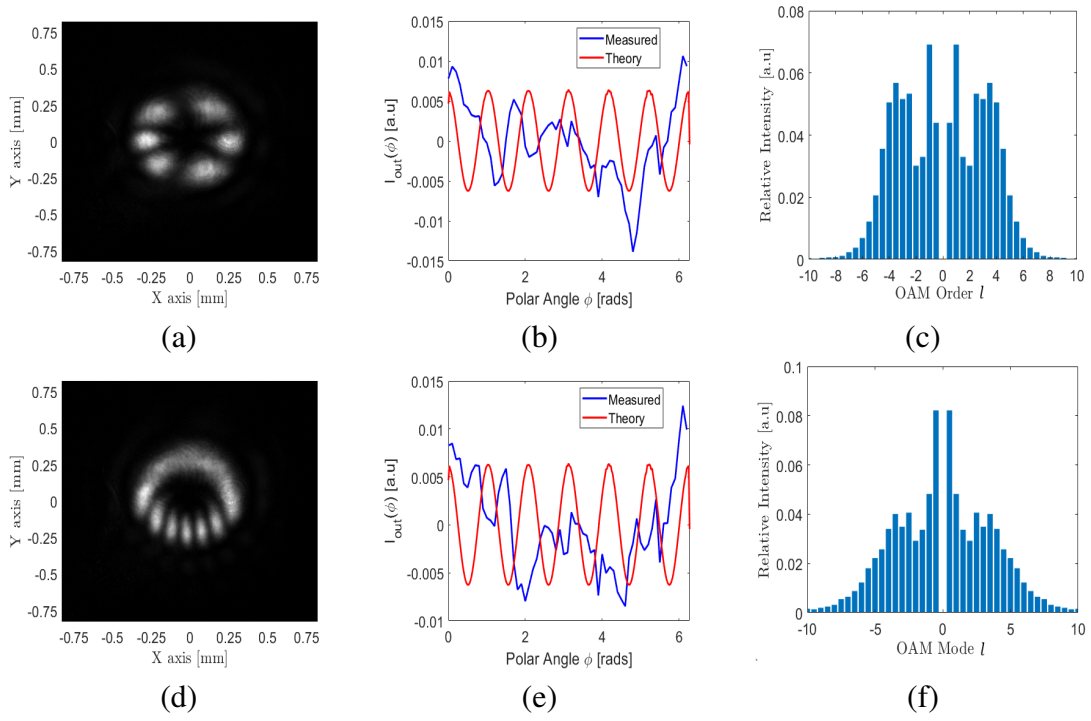

Figure 6.3: Single realization of the interference pattern for an LG beam with $l = 3$ at the first C_n^2 value of $7.4 \times 10^{-13}\mathrm{m}^{-2/3}$ (a), azimuth intensity of the same realization (b), and averaged OAM spectrum for 500 image realizations (c). Single realization of the interference pattern for an LG beam with $l = 3$ at the second C_n^2 value of $2.2 \times 10^{-11}\mathrm{m}^{-2/3}$ (a), azimuth intensity of the same realization (b), and averaged OAM spectrum for 500 image realizations (c).

images. The resultant OAM spectra measurements did result from a simplified data processing technique, but this does not makeup for difficult alignment and stability of the interferometer. The next experiment is using a traditional Mach-Zehnder interferometer using a reference beam to measure the phase to study more about how the OAM spectrum is affected by turbulence.

In comparison to other measurement techniques the WFI would be ideal for lab measurements, but not a technique for practical measurements. To measure OAM spreading wavefront sensing devices, such as Shack-Hartmann sensors, that do not rely on interferometry would be more beneficial. Within this experiment it can be deemed that a more

ingenious image acquisition technique would be better than trying to simplify it with the optical setup.

6.1.2 WFI Compared to a Traditional Interferometer

Alongside the modified Mach-Zehnder interferometer, a traditional Mach-Zehnder interferometer is setup. This uses a reference laser that directly measures the optical phase rather than using the ACF. Upon imaging the interferogram, the optical phase can be measured and decomposed into a series of OAM modes [217]. The OAM decomposition provides a much better view of the OAM spectrum compared to the WFI due to the inconsistencies within the WFI intensity images that accumulate upon integration over the radial coordinate leading to OAM spectrum noise. A resultant intensity image and phase profile using the Mach-Zehnder interferometer are shown in Fig. 6.4 for an LG beam with $l = 1$ along with detection of the singularity points.

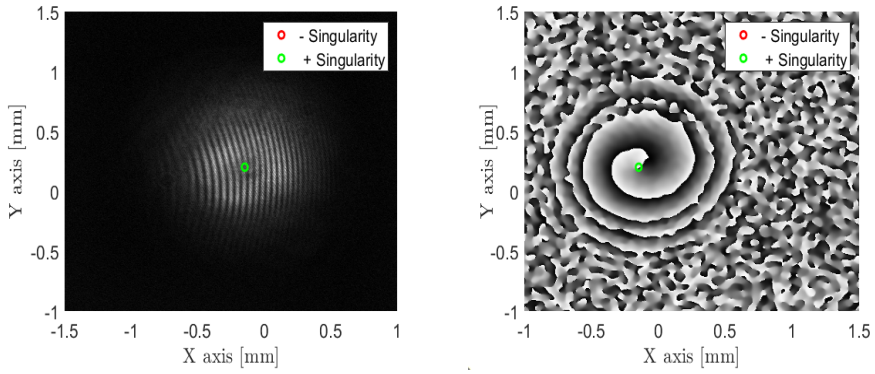

Figure 6.4: (a) Interferogram of a LG beam with $l = 1$ and the Gaussian reference beam with the phase singularity location marked. (b) Measured optical phase of the LG beam with the location of the single phase singularity marked.

For each turbulence strength the optical phase is measured and then decomposed

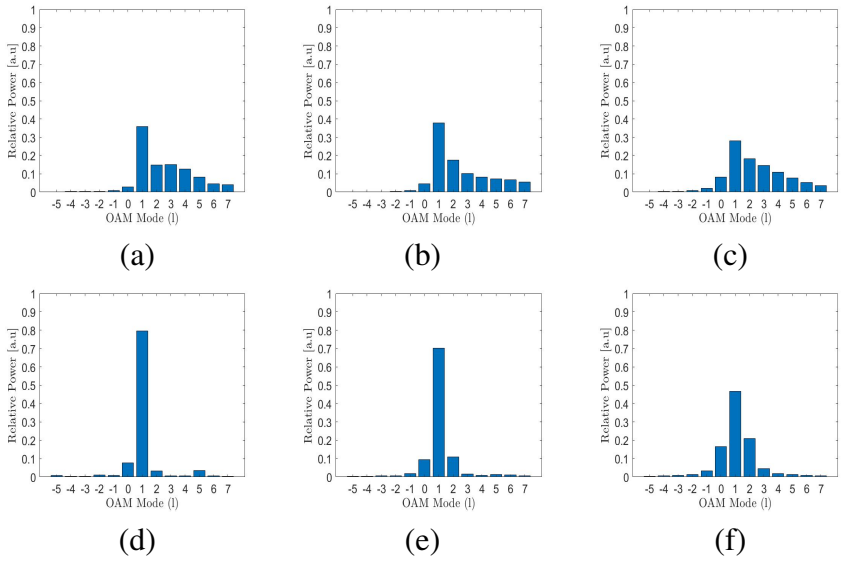

Figure 6.5: OAM spectra for clear air (a), $C_n^2 = 7.4 \times 10^{-13}\mathrm{m}^{-2/3}$ (b), and $C_n^2 = 2.2 \times 10^{-11}\mathrm{m}^{-2/3}$ (c) without singularity tracking. OAM spectra for clear air (a), $C_n^2 = 7.4 \times 10^{-13}\mathrm{m}^{-2/3}$ (b), and $C_n^2 = 2.2 \times 10^{-11}\mathrm{m}^{-2/3}$ (c) with singularity tracking. Each OAM spectrum is for an incident LG with $l = 1$.

into OAM modes to find the OAM spectrum. A set of 500 images are taken at each turbulence strength whose respective OAM spectra are then averaged to obtain the results in Fig. 6.5(a-f). The first row of results in Fig. 6.5(a-c) show the optical phase being decomposed when the singularity points are misaligned leading to the effect of a tilt aberration. Upon correction of this tilt using singularity tracking the resultant OAM spectrum appears more intact and mode spreading is clearly seen as turbulence strength increases (Fig. 6.5(d-f)). The singularity tracking performed best for $l = 1$ as there is only one single singularity present at almost all times since the turbulence is weak. For higher order modes the singularities begin to split from one singularity into multiple. This leads to the creation of negative and positive charged singularities that are exhibited from the effects of stronger phase perturbations.

In comparison to the WFI, the OAM spectra results contain less noise due to the

use of singularity tracking that effectively removes first-order tilt which cannot be performed in the WFI data. Besides comparison to the WFI, the traditional interferometer data shows, that even with rather weak turbulence, experimentally measuring the OAM spectrum is challenging. This leads to the motivation of a method that can contain a measurement metric proportional to the OAM mode spreading that requires less effort to process as compared to images.

6.1.3 Summary of Mach-Zehnder Interferometer

Both of these interferometers provided valuable insight that interferometry is not an effective way to develop an active OAM sensing modality. This is due to difficult alignment procedures, being extremely sensitive during post-processing which led to significant noise in the final images, and the requirement of image processing. Three observations made are:

- Less optical stability conditions are deemed more important than simplified data processing.
- The modified interferometer is only applicable for experimental setups that can be significantly isolated from the outside environment.
- Drawback of needing a camera to capture a picture of the beam for post-processing.

Along with goals of this work to simplify the optical receiver, the removal of image processing is a key component of simplifying the OAM detection method. This leads us to look at other techniques to see what may be more effective at developing an active OAM sensing modality.

6.2 Experiment #2: Mode Projection

The second OAM method that is tested is mode projection [218]. In contrast to the previous method, modal projection is a more robust measurement scheme as it does not require interference. In contrast to section 6.1, this experiment was performed to measure the OAM spectrum spreading by a turbid medium instead of a turbulent one. Initially it is thought that a turbid medium will lead to mode spreading as shown in previous results in the literature [11]. The goal is to determine if mode spreading occurs as a function of optical depth by increasing the amount of scattering agent. If mode spreading does have a dependence on OD, mode spreading could be used as an active sensing modality through turbid mediums. The turbid medium is created by using Equate® antacid that consists of a mixture of roughly 50 % Magnesium Hydroxide ($Mg(OH)_2$) and Aluminium Hydroxide ($Al(OH)_3$) [219]. Equate® is used as it approximately simulates the VSF effects of a true oceanic/water environment as measured by Petzold [63].

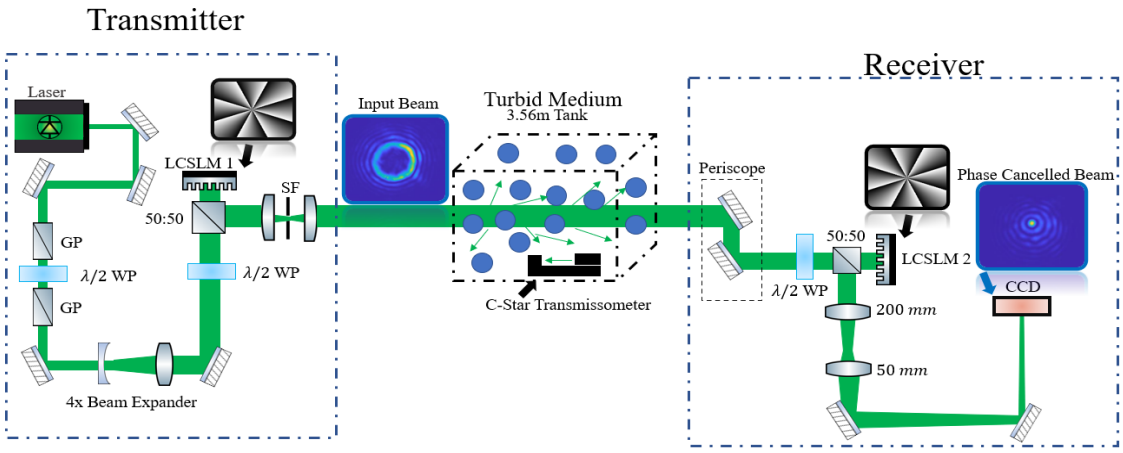

Figure 6.6: Mode projection experimental setup through turbid water. GP: Glan polarizer, WP: waveplate, LCSLM: liquid crystal spatial light modulator, SF: spatial filter, CCD: Charged coupled device

Experimentally the setup is quite different as the setup is separated into a transmitter, that creates the OAM beam, and a receiver that performs the mode projection illustrated in Fig. 6.6. The transmitted laser wavelength is changed to 532 nm to minimize the absorptive effects upon propagation through water. The laser is expanded and illuminates an LCSLM that displays a spiral phase hologram that creates a beam with a HyGG form. The beam is spatially filtered and then transmitted into the turbid environment, which is a 3.56 m propagation path that is then filled with water containing different amounts of Equate®. The particle sizes present range from a couple of nanometers to a few microns [220]–[222]. Although the particles are immersed in water, the effects of scattering are no different than atmospheric aerosols. The main differences are the shape of the particle distribution and the relative ODs. The receiver, in Fig. 6.6, consists of a second LCSLM that can cycle through various conjugate spiral phase holograms to measure the OAM spectrum. After reflecting off the second LCSLM, the beam passes through a 200 mm focal length lens that performs the phase cancellation. At the lens focus the inner product in equation 4.2 is implemented. Since the spot size at the focus of this lens is small a second 50 mm focal length lens is used to magnify the focus of the first lens. The magnified focus is then detected using a CCD camera. The on-axis light of the magnified focus is then selected in post-processing to obtain the OAM spectrum of the measured beam.

Figure 6.7 shows the various mode projection images and the respective measured OAM spectrum in water and water with a nonzero OD for an HyGG beam with $l = 8$. The first row in Fig. 6.7(a-c) are in air when the receiver is set to a phase hologram with the case $\{8,-7\}$, $\{8,-8\}$, and $\{8,-9\}$. When the transmitter and receiver OAM modes are matched ($\{8,-8\}$) the vortex shape becomes a point. A virtual pinhole mask is then

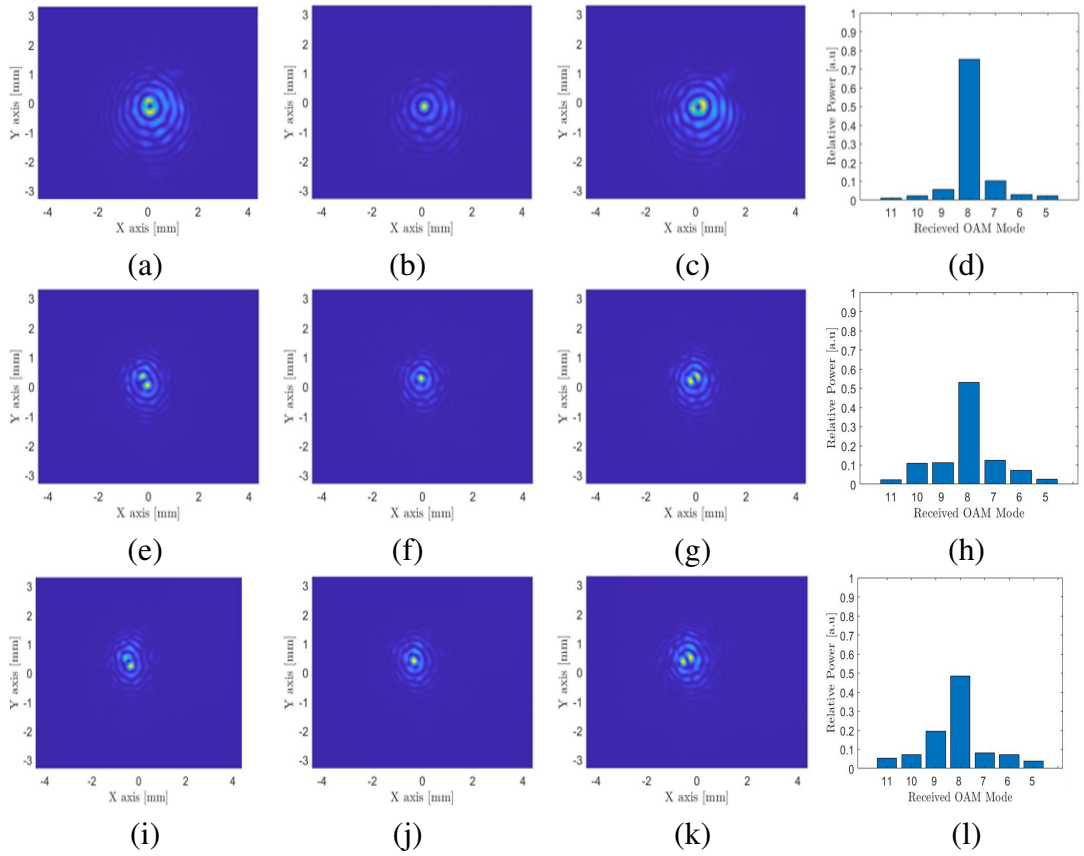

Figure 6.7: Cancellation images for $\{8,-7\}$, $\{8,-8\}$, and $\{8,-9\}$(a-c) and the OAM spectrum (d) through air. Cancellation images for $\{8,-7\}$, $\{8,-8\}$, and $\{8,-9\}$(e-g) and the OAM spectrum (h) through clear water. Cancellation images for $\{8,-7\}$, $\{8,-8\}$, and $\{8,-9\}$(i-k) and the OAM spectrum (l) through water with an OD of 9.8.

placed on the intensity image to select the power within this point. The respective air OAM spectrum in Fig.6.7(d), normalized as equation 4.3, shows that the OAM mode is in a pure state. When the setup is placed through water and realigned, the phase cancelled images contain a small astigmatism as shown in Figs. 6.7(e-g) and leads to a bit of mode spreading in Fig.6.7(h). The astigmatism becomes the baseline OAM spectrum for the rest of the measurement as OD is varied. At an OD of 9.8 the phase cancellation images and OAM spectrum in Figs.6.7(i-l) are seen to be the same as the baseline water case. The images are slightly moved as the beam centroid does move around slightly due to the

presence of the particulate matter. The next part of the experiment is to vary the OD and measure if the OAM spectrum changes for various incident OAM modes $l = 0, 1, 2, 3, 4, 8$.

6.2.1 Impact of Turbidity

Figure 6.8(a-d) summarizes the results for an incident beam $l = 8$. The heat map in Fig.6.8(a) shows the OAM spectrum as a function of OD and received mode. The OD is along the y-axis, the received OAM mode is along the x-axis, and the heat map shows the received OAM power α_l. As the OD increases the OAM spectrum is seen to retain its shape even into the multiple scattering regime. The OAM spectrum is seen to slightly decrease at an OD of 14.2 due to the background signal increasing as the detector dynamic range reaches the noise floor. Figures 6.8(b-d) show selected slices of Fig. 6.8(a) to emphasize a slight change in shape. As compared to similar results through turbulence [198], the OAM spectrum in these results does not vary significantly. For other modes transmitted through the medium, $l = 1, 2, 3, 4, 8$, similar results of their OAM spectra were obtained. This shows that there is not a strong influence of incident OAM mode and thus beam size as increasing OAM mode increases the beam size. These results at the

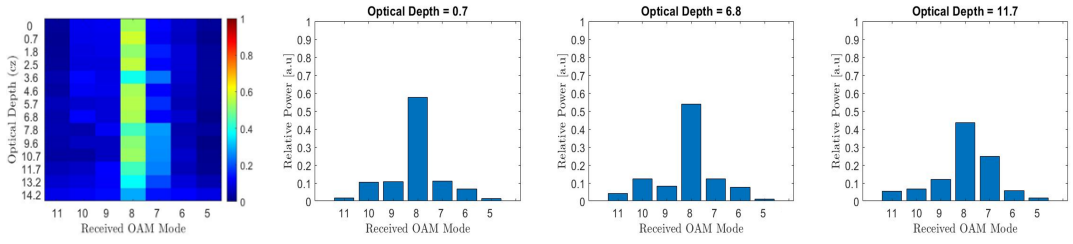

Figure 6.8: (a) Heat map of the OAM mode spectrum as a function of OD for $l = 8$. (b) OAM spectrum at an OD of 0.7 for $l = 8$. (c) OAM spectrum at an OD of 6.8 for $l = 8$. (d) OAM spectrum at an OD of 6.8 for $l = 11.7$.

time were unexpected as a turbid medium was considered a random medium where the refractive index inhomogeneities would cause significant enough phase perturbations to induce mode spreading. This is possibly due to not a significantly large forward scattering component collected by the detector. This is either due to the small field of view or a relatively weak forward scatter component of the Equate® (Maalox) phase function compared (see Fig. 2.2) to a medium containing large particles. As no mode spreading is measured it can be inferred that the phase variance may not be large enough to induce significant phase perturbations on the non-scattered light. The phase variance in a turbid medium is affected by both the OD and particle size that determine the medium's MTF.

Another reason no mode spreading is seen is because the setup contains a small FOV that is on the order of 0.01°. This small FOV should not play a large role in affecting the OAM spectrum as the main beam is not apertured. The reason why the FOV may cause an issue is that the phase perturbations are due to the interference of near-forward scattered light and the ballistic light, which may be limited if too much forward scattered light is blocked from the optical system. A counter argument to this point is forward scattered light will fall into the SAA leading to the light that contributes to the phase distortion as always present in the main beam. Thus this leaves the reason for no perturbations being seen due to the strength of the phase variance and size of the WSF being limited by the particle sizes present in the medium.

The second verification of the experiment is by comparing the attenuated OAM mode power to Beer's law that predicts the power attenuation of ballistic light. Figure 6.9(a) shows the power within the matched case $\{l, -l\}$ across all OAM modes transmitted. "Matched case" refers to the transmitted OAM mode being equal to the mode

that the detector is tuned to measure, the notation $\{l_1, l_2\}$ is used to denote these cases where l_1 is the transmitted OAM mode and l_2 is the received OAM mode. Each matched case follows Beer's law well up to the final OD where the detector noise floor is reached. Next, all modes except the transmitted mode power is summed together and compared to Beer's law in Fig. 6.9(b). As multiple scattering occurs, the power starts to increase in other modes due to the sensing of background light. Figure 6.9(b) begins to deviate slightly upon the onset of multiple scattering as background light is detected in modes other than the transmitted mode. Figure 6.9(c) shows that around an OD of 12 multiple scattering begins as the total beam power deviates from Beer's law. This is as expected for the total beam power as more diffuse light is collected.

The results presented as a function of OD for various OAM modes show that for the propagation geometry experimented with, the OAM spectrum does not vary significantly with changing OD. This result was unexpected at the time as other experiments in the literature showed that mode spreading occurred in a turbid or diffusive medium [11], [47], [223]. This discussion is presented in the next section.

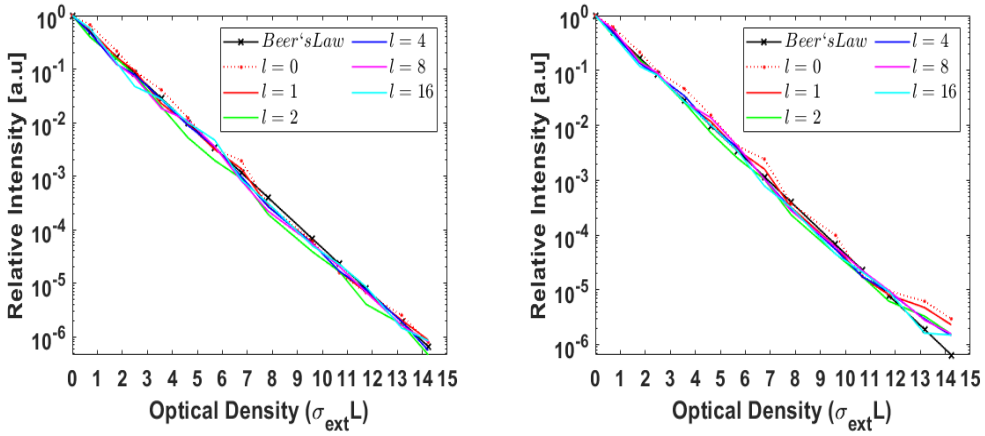

(a) (b)

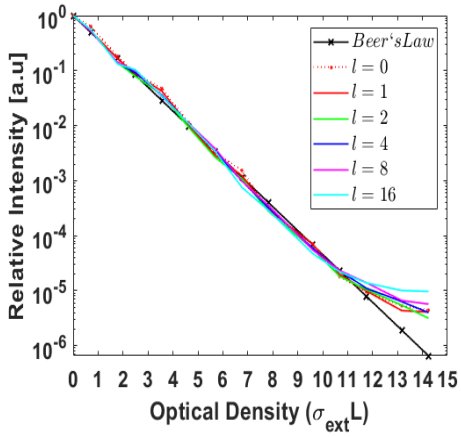

(c)

Figure 6.9: (a) Power attenuation compared to Beer's law for the mode power $\{8, -8\}$. (b) Power attenuation for the power in all other modes except $\{8, -8\}$. (c) Total power attenuation across the entire beam with no pinhole present.

6.2.2 Comparison to the Literature

Previous studies have shown that the total power attenuation of OAM beams follow the slope of Beer's law similar to a Gaussian beam [11], [99], [210], [224]. These studies did not take into account the power attenuation of each OAM mode. Zhang *et al.*[11] showed that the power in the $\{l, -l\}$ case attenuated faster after an OD of ~ 6 due to the loss of mode purity from multiple scattering. Instead of recording images of the phase

cancellation, the power in the phase cancellation spot was measured using a single-mode fiber. Another work by Viola *et al.* explored the effects of particle size on OAM propagation through particulate matter with an emphasis on studying the ballistic scattering component [185].

In this work, the transition from ballistic to multiple scattering is seen around an OD of ~ 12 similar to previous studies for both the mode power in the $\{l, -l\}$ case and total beam power [99], [210], [224]. Along with the power attenuation of the modes following Beer's law, the mode purity in general remains resilient in our experiment as the OAM spectrum retains its shape for increasing OD. In relation to Viola's work our results are similar showing little to no mode spreading over a 3 meter propagation distance through water containing different levels of Equate®. On the other hand Zhang *et al.*'s [11] results are different possibly due to size of the scattering volume, beam size, detector FOV, propagation distance, data processing method, and single mode fiber aperture size. Zhang *et al.* used a 2 mm glass cuvette compared to our 3.56 m tank and Viola's 3 - 20 m distances. With there being multiple parameters playing a role it is hard to determine exactly which one is the limiting factor.

Originally the difference in results was Zhang *et al.*'s experiment using a small fixed single mode fiber aperture compared to this works larger and dynamic aperture. It is possible using such a small aperture could return incorrect results or if the data averaging was not over a long enough period [198], [225]. Another explanation is that the spectrum was normalized when the detector noisefloor was reached which would include incorrect OAM power measurements for modes other than the mode of interest. This is because the OAM spectra recovered in Zhang *et al.*'s Figures 5(a-d) still maintains a 10 - 20 dB

difference between nearest modes at OD's in the multiple scattering regime. But these results can also be supported by their interferograms that show an almost completely distorted wavefront. Without knowing the full details of data collection this explanation could be nullified.

Incidentally upon further investigation of ballistic light and OAM, Viola *et al.* [185] performed an experiment with water containing Equate® (same as Zhang *et al.*) and corn starch showing OAM spreading depending on particle size. Viola *et al.* observed a strong change in the OAM spectrum of light that travelled up to 20 meters. It is unclear how large the beam was, but it will have to be a well collimated beam on the order of a couple of millimeters to centimeters to travel that distance. For the Equate® scenario Viola *et al.* predicted and saw little to no mode spreading over a 3 meter propagation path similar to our work and simulations, but for larger particles a larger disturbance was seen. Since the scattering agents in all three experiments were the same, it still leaves the reasons previously mentioned as an explanation as it is known that a diffuse phase distortion does cause mode spreading [47].

A turbid medium within the diffuse approximation does lend to using a Gaussian phase PSD, but by the time this approximation is reached the ballistic attenuation is large [66], [73]. This loss of the ballistic component may hide the effects of how the OAM spectrum spreads on the ballistic component of light leaving only an OAM spectrum of diffuse light that will be similar to a uniform distribution. This is key to point out as scattering by particles and a rough surface share similar phase statistics but different normalization dependencies. This supports the claim that scattering by small particles does not impart enough forward scattering to interfere with the ballistic component that

carries the main beam with OAM.

6.2.3 Summary

Within the results and literature comparison of our turbid medium study, the propagation of an OAM beam is significantly different compared to propagation in a turbulent medium. In a turbulent medium less variables were at play to create a phase distortion as turbulent eddies are almost always greater than the wavelength of the incident laser. Our experiment, Zhang *et al.* [11] and Viola *et al.* [185] showed interesting results regarding measurement of the OAM spectrum through a turbid medium with different experimental apparatuses. The following worthwhile takeaways of this experiment are:

- Using a camera instead of a pinhole limits the OD that could be reached in a turbid medium due to the sensitivity of the camera.
- For mode projection measurements detector FOV plays a large role in how the optical receiver interprets the environment as a small FOV rejects significant amounts of scattered light.
- In the propagation and receiver geometries of interest little to no significant mode spreading is seen for various OAM modes.
- Experimental results see that smaller particles do not affect the mode spectrum significantly as compared to simulations in this work.

With the lessons learned from these two experiments and beam simulations, the next chapter will synthesize the information to determine a more practical way to sense

the environment with some benefits that have not been seen in the literature to the best of the authors knowledge.

Chapter 7: Optical Heterodyne Detection of Orthogonal OAM Modes (OHDOOM)

The previous chapters have provided context of how an active OAM sensing modality extracts information using mode spreading along with the difficulties to measure OAM experimentally. With the motivation to simplify the OAM detection setup and data acquisition procedure a possibly more practical OAM sensing modality can be developed. Using relevant literature, experimental experience, and simulated results, the introduction of a new method to approach active OAM sensing is introduced in this chapter to reach these goals.

7.1 Concept of OHDOOM

In chapters 4 - 6 it is made apparent that active OAM sensing, based on mode spreading, uses complex apparatuses that lead to experimental difficulty. This led to the ideas of how to simplify the optical receiver to detect mode spreading without loss of environmental information. Various OAM detection schemes were considered all with the intention to simplify the optical setup as discussed in Chapter 4. Within the literature a technique developed by Yang *et al.* [226] and experimentally implemented by

Zhang *et al.* [12], [13] showed that optical phase distortions can be mitigated or completely removed from an OAM SDM communications link using heterodyne detection. The technique presented by Zhang *et al.* [12] uses a co-propagating signal beam as a local oscillator to remove optical phase distortions from the optical signal that has propagated through the channel. The heterodyne technique is then modified by utilizing the orthogonality among OAM modes to detect when the optical phase is distorted due to misalignment of the beam on the detector aperture [227]. Each technique accomplishes a unique goal, but neither provides evidence of the strength of the phase distortions caused by the channel. OHDOOM is similar to a method called synthetic array heterodyne detection [228]–[231], but our method does not use a local oscillator and can be used over long propagation paths.

Using the combination of OAM and heterodyne detection, a technique called optical heterodyne detection of orthogonal OAM modes (OHDOOM) is developed with the intention to simplify the optical receiver and data acquisition process while maintaining information about the environment using mode spreading. A single beatnote, produced via heterodyne detection, provides a simple modality to detect the presence of environmental characteristics, such as turbulence, that cause optical phase distortions. The mode spreading information is retained as OHDOOM is equivalent to an optical projection measurement that measures a single component of the OAM spectrum. Using two beams that create a temporal interference pattern, OHDOOM inherently leverages the benefits of AC-coupled detection, without the need of a pulsed or amplitude modulated laser source, to reject DC light sources such as multiply-scattered light or background noise sources. In contrast to mode projection where the receiver is varied to measure the OAM spectrum,

the transmitted OAM modes can be changed to obtain information about the channel. This allows the receiver to be a static device that can passively measure OAM mode spreading without requiring multiple measurements. With this being said, this chapter discusses the theoretical operating principle of OHDOOM with it being verified experimentally along with developing a model to predict the beatnote behavior in turbulent and turbid media.

7.2 Operational Principle

The receiver detects a coherent superposition of two beams with optical frequencies f_1 and f_2, called the "dual probe beam (DPB)", created at the transmitter. Using a square-law photodetector, the two beams in the DPB are mixed to create a beatnote with an electrical frequency $f_b = f_2 - f_1$, which will become the indicator of OAM mode spreading. The optical receiver contains a telescope, pinhole, and photodetector. Without an LCSLM, the setup is the equivalent mode projection setup to measure the power within the 0^{th} order OAM mode. To measure more information about the environment the DPB OAM values, l_1 and l_2, can be changed at the transmitter. Depending on the OAM mode structure of the incident beam, the photodetector signal has four different situations of the beatnote illustrated in Fig. 7.1. The cases depend on if the DPB is in a matched condition ($l_1 = l_2$) or a mismatched condition ($l_1 \neq l_2$). When the DPB is in the matched condition a beatnote is always observed (Fig. 7.1(a-b)), but as the optical distortion strength increases the beatnote power will decrease (Fig. 7.1(c)). For the unmatched case of the DPB (Fig. 7.1(d-e)) there is no beatnote signal as the beams are orthogonal, but as the optical distortion strength increases mode spreading occurs driving power into the 0^{th} order mode

creating a beatnote (Fig. 7.1(f)).

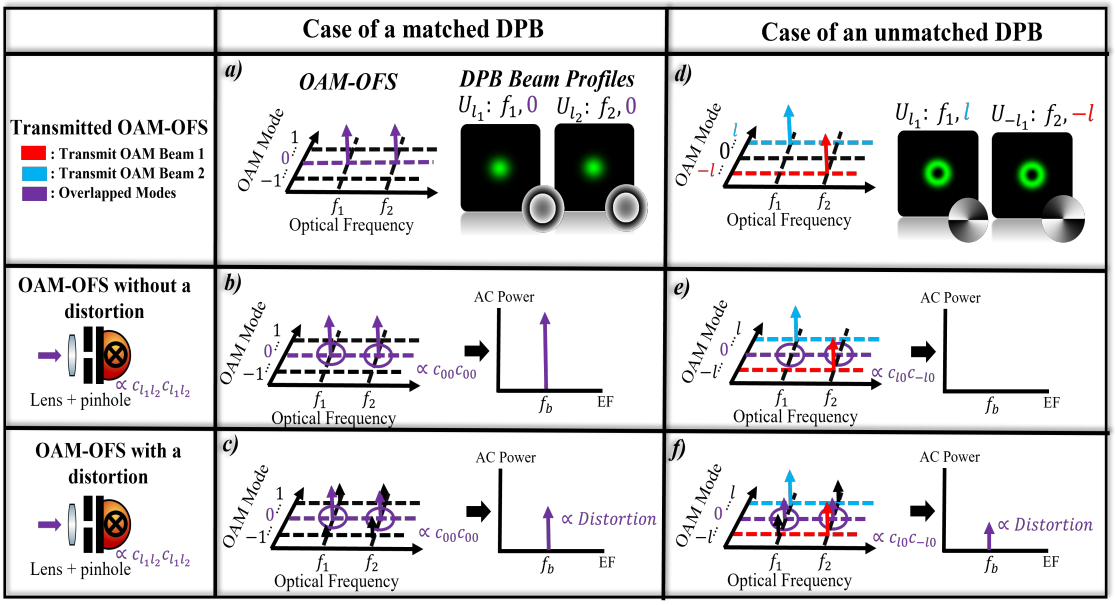

Figure 7.1: Illustration of beatnote response when the DPB is in the matched case with the (a) transmitted respective beam profiles and phase distribution, (b) beatnote response without a phase distortion and corresponding OAM-OFS, and (c) beatnote response with a phase distortion and corresponding OAM-OFS. Beatnote response when the DPB is in the mismatched case, (d) transmitted OAM-OFS and respective beam profiles and phase distribution, (e) beatnote response without a phase distortion and corresponding OAM-OFS, (f) beatnote response with a phase distortion and corresponding OAM-OFS.

Before discussing the matched and mismatched condition, the formalism to predict the beatnote must be discussed. To quantitatively understand how the beatnote depends on the initial structure of the DPB fields each beam's field profile can be written as

$$E_j(r,\phi,z,t) = U_j(r,z)e^{i2\pi f_j t}e^{il_j\phi}, \tag{7.1}$$

where $j = 1,2$ represents the first and second beam that makeup the DPB, $U_j(r,z)$ is a radial complex amplitude, f_j is the optical frequency, and l_j is the OAM order. Upon detection of the DPB at a photodetector, the photocurrent ($\mathscr{I}(t)$) is proportional to the

optical intensity, $I(r,\phi,z,t) = |E_1 + E_2|^2$, given by

$$\begin{aligned}\mathscr{I}(t) &= \mathscr{R}\iint W(r,\phi) I(r,\phi,z,t)\, r dr d\phi \\ &= \mathscr{R}\int_0^{2\pi}\int_0^{D_d/2} (|E_1|^2 + |E_2|^2 + E_1 E_2^* + E_1^* E_2)\, r dr d\phi\,, \end{aligned} \tag{7.2}$$

where $\mathscr{R}$ is the detector responsivity, $W(r,\phi)$ is a circular photodetector aperture function with diameter D_d, and E_j are the DPB fields described by equation 7.1. To simplify the photodetector aperture function, the aperture is assumed to be larger than the beam, thus limiting the integration bounds.

The optical intensity contains two components: first, the sum of the intensities of each optical field, $|E_1|^2 + |E_2|^2$, and the interference of the two fields, $E_1 E_2^* + E_1^* E_2$, which are proportional to the DC ($\mathscr{I}_{DC}$) and AC ($\mathscr{I}_{AC}$) photocurrents respectively. As the photocurrent contains an AC component, the average electrical power of the beatnote can be defined as

$$\langle P_{BN} \rangle = G^2 R \langle \mathscr{I}^2(t) \rangle, \tag{7.3}$$

where R is the load resistor of the detector, and G is the detector gain.

To understand how OAM orthogonality, i.e. mode spreading, affects the DPB upon detection, it is appropriate to use a modal expansion of the incident fields $E_{l_j}(r,\phi,z,t)$ since the photocurrent and beatnote strength rely on DPB spatial distributions. Using the decomposition from equation 4.1

$$E(r,\phi,z,t) = \sum_{n=-\infty}^{\infty} c_n(z)\Psi_n(r,\phi)e^{i2\pi ft}, \tag{7.4}$$

where $c_n(z)$ are the weights of each OAM eigenfunction $\Psi_n(r,\phi)$ of the beam. If each field in equation 7.2 is expanded using equation 7.4, the AC photocurrent can be rewritten as

$$\mathscr{I}_{AC}(z,t) = 2\mathscr{R}\sum_{n=-\infty}^{\infty}|c_{n1}(z)||c_{n2}(z)|\cos(2\pi f_b t - (\angle c_{n1}(z) - \angle c_{n2}(z))), \tag{7.5}$$

where c_{n1} represents OAM coefficients of the first beam, c_{n2} represents the OAM coefficients of the second beam, and $\angle$ represents the phase angle of each OAM coefficient. The full derivation of equation 7.5 along with the DC photocurrent is given in Appendix F. The weights, $c_{nj}(z)$, can be found using the inner product from equation 4.2.

The beatnote is measured using a mode projection of the 0^{th} order OAM mode with a pinhole at the focus of a lens. Upon selection of the 0^{th} order OAM mode, the truncation of the OAM spectrum leaves equation 7.5 simplified as

$$\mathscr{I}_{AC}(t) = 2\mathscr{R}|c_{01}||c_{02}|\cos(2\pi f_b t - (\angle c_{02} - \angle c_{01})). \tag{7.6}$$

The beatnote amplitude is now directly proportional to the coupling of the 0^{th} OAM coefficient of each beam's OAM mode to the 0^{th} OAM mode. The AC photocurrent's electrical signal power, in terms of the each beam's 0^{th} order OAM coefficient, follows from equations 7.3 and 7.6 as

$$\langle P_{BN}\rangle = 2R(\mathscr{R}G)^2\langle|c_{01}|^2|c_{02}|^2\rangle. \tag{7.7}$$

The value of $|c_{0j}|^2$ is the fraction of energy in the 0^{th} OAM mode of the j^{th} beam of the DPB.

The combinations using the OAM-optical frequency spectrum (OAM-OFS) are illustrated in Figs. 7.1(a-f) where each beam of the DPB contains their own OAM mode, l_1 and l_2. If the two beams contain an equal OAM charge, this is considered as the "matched case $\{l,l\}$", otherwise different OAM charges are called the "mismatched case $\{l_1,l_2\}$", each of which are described in Figs. 7.1(a-c) and 7.1(d-f), respectively. The same notation as Section 6.2 is used, however, l_1 and l_2 represent the OAM within the first and second beam of the DPB rather than the transmitted and detected OAM mode.

7.2.1 OHDOOM with a matched DPB

First, if the DPB is matched and the phase is not distorted, a beatnote is created by the beams carrying the same OAM mode (as shown in Fig. 7.1(b) where $l_1 = l_2 = 0$). Otherwise, if the DPB is matched and the phase is distorted, the beatnote is proportional to the channel-induced loss of the transmitted OAM mode when a pinhole is present (as shown in Fig. 7.1(c)).

For a matched DPB, $\{l_1,l_1\} = \{0,0\}$, the AC photocurrent, using equation 7.2, at the focus of the lens after the pinhole is

$$\begin{aligned} \mathscr{I}_{AC}(t) &= 2\mathscr{R}A(t)\int_0^{2\pi}\int_0^{D_p/2}|\mathscr{F}_2\{U_1\}|^2\, r dr d\phi \\ &= 2\mathscr{R}|c_{01}|^2\cos(2\pi f_b t), \end{aligned} \tag{7.8}$$

where $A(t) = \cos(2\pi f_b t)$ is the time dependent amplitude modulation, D_p is the pinhole

diameter that limits the integration bounds, and $\mathscr{F}_2$ represents a two-dimensional Fourier transform. It is assumed that $c_{01} = c_{02}$. The photocurrent contains a DC offset determined by

$$\mathscr{I}_{DC} = 2\mathscr{R}\int_0^{2\pi}\int_0^{D/2} |\mathscr{F}_2\{U_1\}|^2 r dr d\phi = 2\mathscr{R}|c_{01}|^2. \tag{7.9}$$

The beatnote power for the matched case is then $\langle P_{BN}\rangle = 2R(\mathscr{R}G)^2\langle |c_{01}|^2|c_{02}|^2\rangle$.

The second case of the matched case beatnote signal is when an optical phase distortion is present in the channel as illustrated in Fig. 7.1(c). Assuming the optical phase distortion can be written as a thin phase screen, the field after propagation through the channel is

$$E_o(r,\phi,z,t) = U(r,z)e^{i\theta(r,\phi,z)}e^{i2\pi ft}e^{il\phi}, \tag{7.10}$$

where E_o denotes the field after propagation through the optical channel, and $\theta(r,\phi,z)$ is a phase perturbation that creates mode spreading. Using equation 7.9 it can be seen that there will always be a beatnote as long as there is power within the 0^{th} OAM mode, which decreases as the optical phase perturbation strength increases.

For OHDOOM without a pinhole it is worthy to note that due to the conjugation, $E_{1o}E_{2o}^*$ following from equation 7.2, and $e^{i\theta(r,\phi,z)}$ being a unitary operator, the phase perturbations effectively cancel, since $E_{1o}E_{2o}^* = E_1 e^{i\theta(r,\phi,z)}e^{-i\theta(r,\phi,z)}E_2^* = E_1E_2^*$ where E_1 and E_2 are from equation 7.1. The cancellation of the phase distortion preserves the orthogonality of the OAM modes and leaves the final heterodyne signal unperturbed. This effect is the centerpiece of the work by Yang *et al.* [226] and experimentally used

by Zhang *et al.* [12], [13], [227]. For communication applications the elimination of the phase perturbations is advantageous, but this also removes any information about the environment for our measurement purposes as will be demonstrated in Section 7.3.1

7.2.2 OHDOOM with a mismatched DPB

The mismatched DPB case changes the input OAM-OFS, illustrated in Fig. 7.1(d), to equal but opposite OAM modes. When the beam profiles contain unequal OAM $\{l_1, l_2\}$, the AC photocurrent becomes

$$\mathscr{I}_{AC}(t) = 2\mathscr{R}\int_0^{2\pi}\int_0^{D_p/2}\mathscr{F}_2\{U_1\}\mathscr{F}_2\{U_2\}A(\phi,t)\,rdrd\phi, \tag{7.11}$$

$$= 2\mathscr{R}|c_{01}||c_{02}|\cos(2\pi f_b t - (\angle c_{02} - \angle c_{01})), \tag{7.12}$$

where $A(\phi,t) = \cos(2\pi f_b t + (l_2 - l_1)\phi)$ is the mismatched amplitude modulation. If equal and opposite OAM modes are used, whom share the same radial intensity distribution and divergence, the beatnote amplitude in equation 7.12 is the product of DPB's beam magnitudes. By rearranging terms, with $l_1 = -l_2$, the time-dependent amplitude becomes

$$A(\phi,t) = \cos\left(2\pi f_b\left(t + \frac{l_1}{\pi f_b}\phi\right)\right). \tag{7.13}$$

By inspection of equation 7.12, the time-dependent amplitude rotates at an angular frequency $l_1/\pi f_b$ producing no sinusoidal varying amplitude modulation. Using the modal description (equation 7.12), the beam contains no overlapping OAM coefficient at the 0^{th} OAM mode ($c_{01} = c_{02} = 0$) leading to no detectable beatnote. The rotating phase term

is removed due to the pinhole only detecting on-axis light that contains a constant phase shift that does not depend on space in equation 7.12.

The same cannot be said for the case with optical distortions in the channel that cause mode spreading. Mode spreading creates a beatnote power, described by equation 7.3, that is proportional to the amount of coupling of the two transmitted modes into the 0^{th} OAM mode (purple arrows) in Fig. 7.1(f). Depending on the nature of the optical phase distortion, the coefficients $|c_{l_jn}|^2$ can be predicted to determine the beatnote signal. Reversely, the beatnote signal can be used to infer the strength of the optical phase distortion.

7.3 OHDOOM Experimental Results

Three sets of experiments are performed to verify the functionality of OHDOOM. The first experiment in Section 7.3.1 verifies the beatnote behavior upon truncation by an aperture and phase only distortion without a pinhole. The second and third experiments in Section 7.3.2 and 7.3.3 measure the beatnote power through a turbulent and turbid medium respectively.

7.3.1 Experiment #1: Verification of the Beatnote Behavior

The first results are quantifying the beatnote behavior in the presence of OAM mode spreading. The experimental setup is illustrated in Fig. 7.2 where two objects are used to perturb the OAM spectrum, the first being an aperture and the second is a phase-only object simulated as a rough surface.

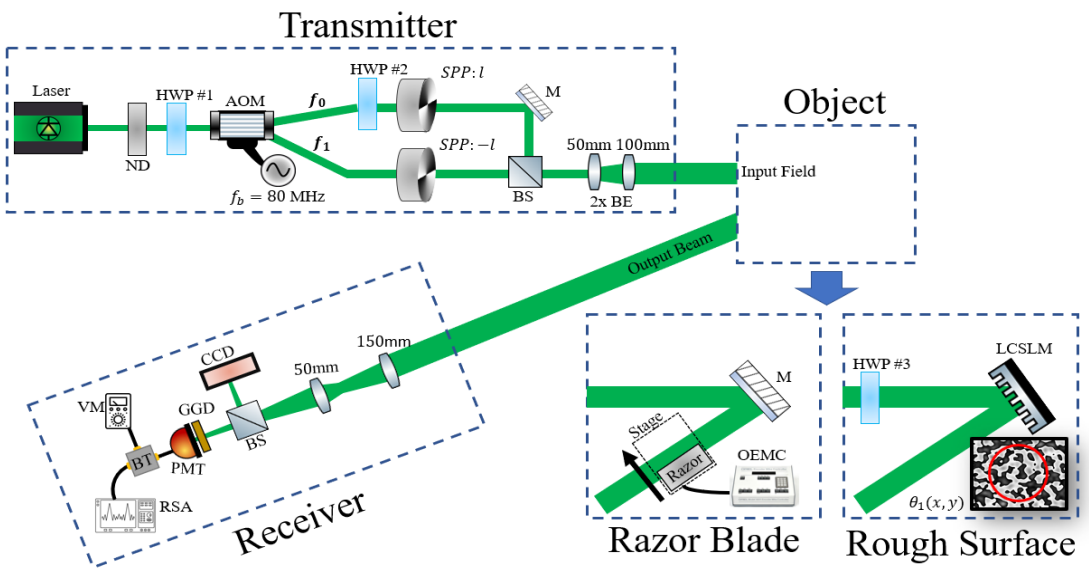

Figure 7.2: Experimental setup to verify the beatnote behavior in the presence of mode spreading that can be predicted from an aperture blocking (razor blade) the beam and the presence of a known rough surface distortion. ND: neutral density filter, AOM: acousto-optic modulator, HWP: half-waveplate, SPP: spiral phase plate, BS: 50/50 beam splitter, BE: beam expander, M: mirror, PMT: photomultipler tube, CCD: charged coupled device, VM: volt-meter, BT: Bias-T, GGD: Ground Glass Diffuser, and RSA: real-time spectrum analyzer..

The DPB is generated using a laser source at a wavelength of 532 nm that is then directed onto half waveplate (HWP) #1 to align the laser polarization to the linear input state required by the acousto-optic modulator (AOM). Upon interaction with the AOM, driven at a frequency $f_b = 80$ MHz to satisfy the Bragg condition, a 1^{st}-order diffracted mode is created at optical frequency $f_2 = f_1 - f_b$. The 0^{th}-order mode is unaffected by the OAM and remains at optical frequency f_1. The two beams diverge from the AOM and are steered into separate paths and encoded using SPPs as shown in Fig. 7.2 tuned to contain equal optical power. For the mismatched case, the SPP charges are equal since the extra mirror in the top arm of the interferometer, shown in Fig. 7.2, conjugates the OAM charge of the SPP. The SPP charges can be changed such that higher or lower order OAM beams

can be transmitted into the optical channel to obtain further channel characteristics. One arm of the transmit interferometer contains a HWP to meet the heterodyne polarization matching condition. The two beams are coherently combined at the transmitter beam splitter creating the DPB signal. The DPB is then sent through a 2x beam expander and collimator into the propagation channel.

Upon detection of the photodetector photocurrent using a load resistance, R, on the output of the photomultipler, the DC and AC components are separated using a Bias-T. The voltmeter in Fig. 7.2 measures the average DC voltage as

$$\langle V_{DC} \rangle = \langle \mathscr{I}_{DC} \rangle R. \tag{7.14}$$

The AC component of the photocurrent is then terminated into a spectrum analyzer with input impedance Z that measures the power in dBm, therefore, the AC voltage signal is an RMS measurement. It can be found directly from the power measurement as

$$V_{AC}^{rms} = \left(\frac{Z}{1000} 10^{-\frac{\langle P_{BN} \rangle}{10}} \right)^{1/2}. \tag{7.15}$$

The propagation channel contains a razor blade that is translated in front of the beam using a programmable translation stage. By blocking the beam with an aperture, mode spreading can be created in a predictable fashion as the beam diffracts around the edge [153]. Diffraction around the razor edges creates a predictable phase and amplitude distribution of OAM modes that is seen as the beatnote is measured as a function of beam blockage seen in Fig. 7.3(a-f).

The results are shown for the AC and DC photocurrent. The matched case AC signal when the DPB OAM modes are $\{0,0\}$, monotonically decreases as a function of slit displacement. For the mismatched case $\{1,0\}$ in Fig. 7.3(b), the signal produces a peak when the beam is half covered by the razor blade. When the OAM is increased on one of the beams to $\{2,0\}$ in Fig. 7.3(c), two peaks show up and a minimum appears that occurs at a quarter, three quarters, and half slit displacement, respectively. The DC signal for the matched case $\{0,0\}$ (see Fig. 7.3(d)) decreases as a function of slit width similar to the AC signal in Fig. 7.3(a). In Fig. 7.3(d) the beam one (green), beam two (magenta), and total power (red) of the DPB curves are directly one top of one another since each beam attenuate the same. This same trend of DC beatnote attenuation occurs for the mismatched cases as well due to the loss of power.

The apparent difference between the AC and DC photocurrent voltages as a function of slit displacement is due to diffraction around the razor blade. The diffractive effects change the phase and amplitude of the OAM coefficients in equation 7.5. This result cannot be explained by measuring only the power in each OAM mode, i.e. mode projection, since phase information within the sum in equation 7.5 is lost. The pinhole truncates equation 7.5 to one mode and the phase component would have to be measured separately to obtain the correct beatnote response as predicted by equation 7.5. Depending on the nature of the optical distortion a phase only distortion can be measured using the power of the OAM modes, while an amplitude only distortion, or truncation of the beam, can be measured by both the beatnote and power of each OAM mode. Using this experimental knowledge, the experiment will shift to how the system responds to varying strength phase only perturbation.

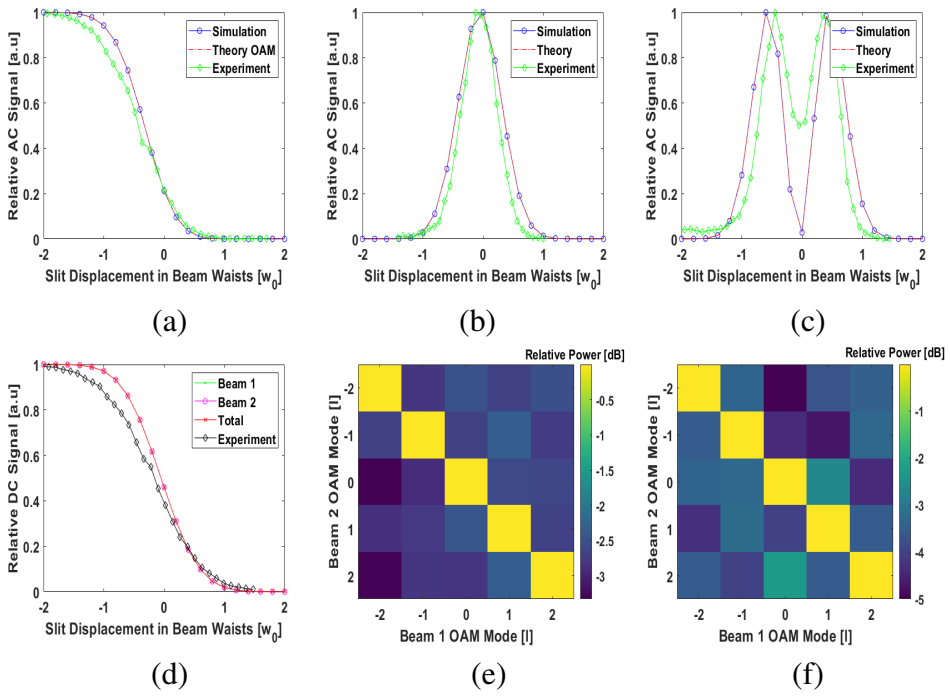

Figure 7.3: (a) Matched case AC signal when the DPB OAM modes are $\{0,0\}$ followed by the mismatched case (b) $\{1,0\}$, and (c) $\{2,0\}$. (d) DC signal for the matched case $\{0,0\}$. (e) Experimental beatnote response for a phase only distortion mimicking a rough surface for various cases of the matched and mismatched conditions. (f) Simulated beatnote response for a phase only distortion mimicking a rough surface for various cases of the matched and mismatched conditions.

An example of the beatnote signal without a pinhole for a single realization of a phase only distortion that mimics a rough surface is shown in Figs. 7.3(e-f) measured in dB. The object indicating rough surface is used in the same experimental configuration illustrated in Fig. 7.2. Figure 7.3(e) are the experimental results showing that the beatnote is minimized for all mismatched cases due to the phase perturbations being cancelled out upon being mixed at the photodetector. The beatnote signal for each matched case is roughly three orders of magnitude greater than each mismatched case signal. Figure 7.3(f) shows the same effect produced in WOSs. If the photodetector does not have a pinhole in front all information about the environment will be removed as shown by Zhang *et*

al.[12].

7.3.2 Experiment #2: Verification of Sensing Turbulence

To test OHDOOM's sensitivity to a turbulent distortion, represented by a phase only modulation, the experimental setup in Fig. 7.4 is used. With the inclusion of the pinhole, the optical receiver takes the form shown in Fig.7.4 which is much simpler than that of the modal projection setup in Fig. 6.6. The experimental results show that when one OAM mode is detected, the beatnote signal becomes proportional to the strength of the phase distortion.

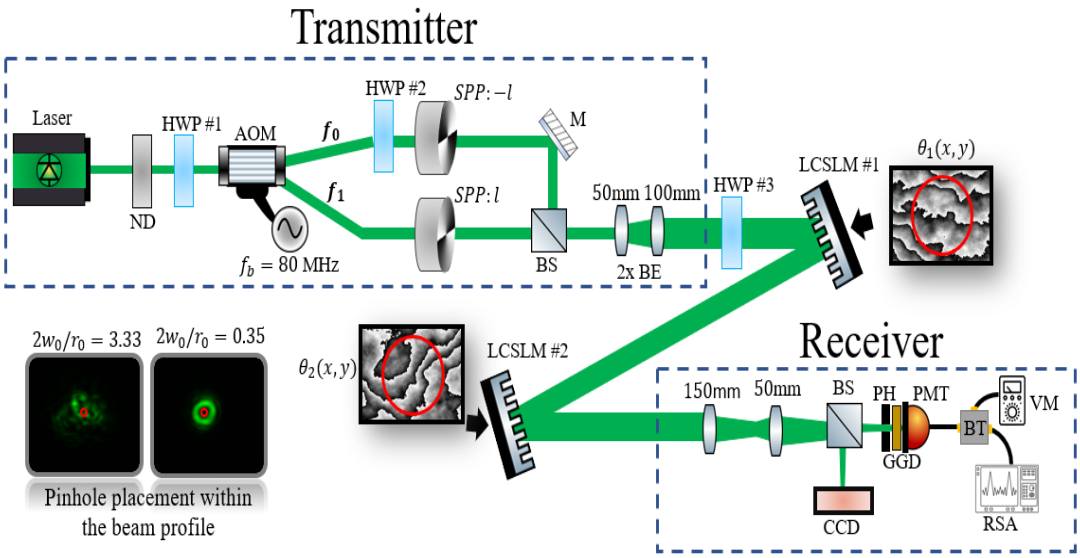

Figure 7.4: Experimental setup to test OHDOOM centered around a transmitter to generate the DPB signal and a receiver to detect the 0^{th} order OAM beatnote. Each SLM displays a turbulent phase map generated from the WOS routine. The two beam profiles on the left show where the pinhole is placed relative to the beam size for two different turbulence strengths. ND: neutral density filter, AOM: acousto-optic modulator, HWP: half-waveplate, SPP: spiral phase plate, BS: 50/50 beam splitter, BE: beam expander, M: mirror, SLM: spatial light modulator, PH: pinhole, PMT: photomultipler tube, CCD: charged coupled device, VM: voltmeter, BT: Bias-T, GGD: ground glass diffuser, and RSA: real-time spectrum analyzer.

In this experiment, the propagation channel contains optical turbulence that is emulated using two LCSLMs displaying turbulent phase screens. Care is taken to display phase screens whose phase distributions do not contain features smaller than the LCSLM's pixel spacing, which could induce sampling errors. Using a single phase screen to model strong optical turbulence will be subject to these sampling errors, therefore, a two phase screen model is implemented. A two phase screen model is used so that stronger turbulence strengths can be realized without being subjected to LCSLM digitization errors. The turbulence strength of the full channel is characterized by a single value of r_0, which is used to determine the effective Fried parameter, r_0^{eff}, of each of the phase screens on LCSLM #1 and #2 based on an optimization routine using the target r_0 and the Rytov variance $\sigma_R^2 = 2.91 r_0^{-5/3} k^{-5/6} L^{5/6}$ discussed in chapter 9 of Schmidt [88].

In each plot of Figure 7.5, the red curve marks the theoretical result calculated from the analytic prediction for substituting the OAM coefficient power predicted by equation 7.16 in the average beatnote power in equation 7.7. The amount of average power in the n^{th} OAM mode of the j^{th} beam is given by

$$\begin{aligned}\langle |c_{nj}|^2 \rangle = &\int_0^{\infty}\int_0^{2\pi} |U_j(\rho,z)|^2 \rho d\rho \exp(i\Delta_{nl_j}\phi) \\ &\times \exp\left(-3.44\left(\frac{2w_0}{r_0}\right)^{5/3}\left|\rho \sin\left(\frac{\phi}{2}\right)\right|^{5/3}\right) d\phi, \end{aligned} \tag{7.16}$$

where the turbulent plane wave structure function from equation 3.28 is substituted into equation 4.4, $\rho = 2r/w_0$ is the normalized transverse distance, $\Delta_{nl_j} = l_j - n$ is the distance away from the central OAM mode l_j of the j^{th} beam, and $U_j(\rho,z)$ is the radial amplitude of the HyGG modes from equation C.6 as the experimental beams are created with spiral

phase plates. Alongside the theoretical results, the black curve is simulated data using a modified version of WOS code and blue is the experimental result. Figure 7.5(a) shows the result when the DPB is in the matched case $\{0,0\}$ and the beatnote signal monotonically decreases as turbulence strength increases. As r_0 reaches the beam diameter, the signal drops off significantly due to the mode power of the Gaussian mode spreading to higher order OAM modes. A similar effect occurs for the mismatched cases $\{-2,2\}$, $\{-4,4\}$, $\{-8,8\}$ in the following figures. For $\{-2,2\}$, the beatnote increases power as turbulence strength increases, which is also the case for $\{-4,4\}$ and $\{-8,8\}$. The difference is that the peak of the beatnote shifts to higher $2w_0/r_0$ since a stronger turbulence strength is needed to create more mode spreading to sense a signal at the 0^{th} order mode. Approximating the turbulence response curves as a Gaussian, the maximum value can be found by fitting the experimental and simulated data to a Gaussian and finding which turbulence strength this occurs as plotted in Fig. 7.5(e).

Another benefit of the OHDOOM method is that it can use the benefits of an AC coupled signal compared to traditional OAM spectrum measurements. The AC signal is compared to the DC signal in Fig. 7.5(f) showing the noise floor of the AC signal to be slightly lower. This plot also shows that the AC coupled information is similar to the DC coupled signal meaning mode spreading information is not lost by AC coupling the signal. The AC coupling also provides the benefit of being able to measure the phase of the beatnote referenced to the unused port of the transmitter beamsplitter in Fig. 7.4. This was not explored in this setup due to the transmissive nature of the geometry, non-time correlated turbulence approach in simulation, and the beatnote phase being proportional to a difference of OAM coefficients which does not provide obvious information. The

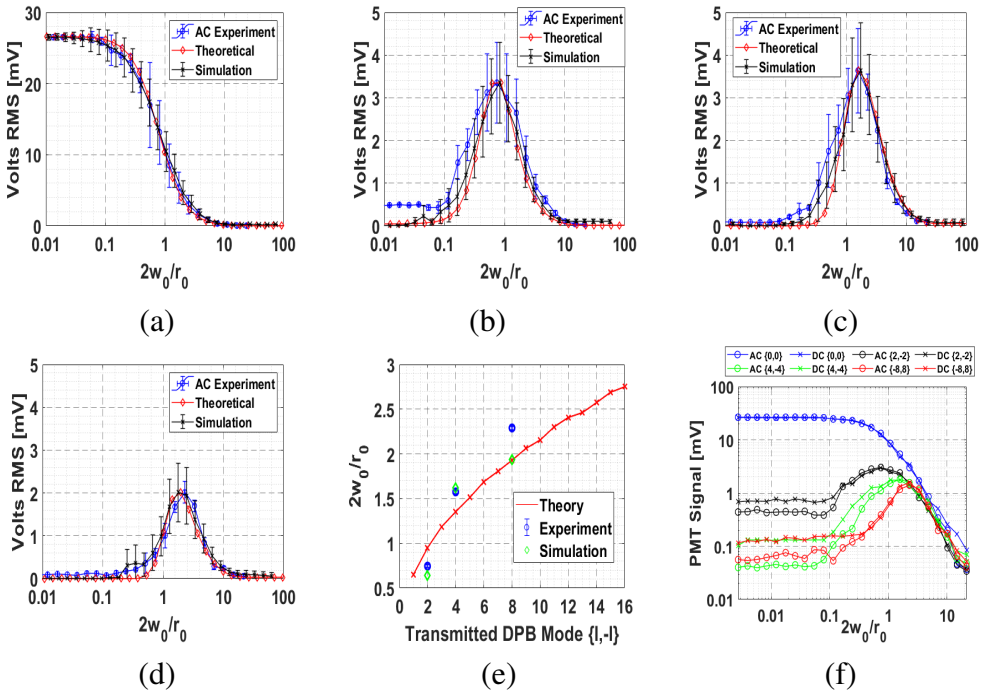

Figure 7.5: Turbulence strength response for the matched DPB case with $\{0,0\}$ (a), mismatched DPB case with $\{2,-2\}$ (b), mismatched DPB case with $\{4,-4\}$ (c), and mismatched DPB case with $\{8,-8\}(d)$. Note the change in vertical scale of (a) compared to (b-d). (e) Transmitted DPB mode against $2w_0/r_0$, where the beatnote signal is predicted to be at a maximum for experiment and compared to theory from equations 7.3 and 7.6. (f) DC and AC coupled signals as a function of $2w_0/r_0$ as measured by the voltmeter and RSA respectively.

average beatnote phase would also result in a constant value once averaged over independent realizations of turbulence leading to no gain in information. OHDOOM thus can be used to measure the strength of an optical distortion of a phase only distortion such as turbulence. It is also key to note that this measurement is AC coupled in the sense of the optical signal varying in time not the detector signal, which is similar to the HOBBIT method that creates an AC coupled signal but the optical signal is a DC measurement [162], [232].

7.3.3 Experiment #3: OHDOOM Turbid Medium Results

The next set of experiments using OHDOOM are within a turbid medium with solutions containing various particle sizes. The experimental setup is shown in Fig. 7.6 where the LCSLMs are replaced with a glass water cell to create the turbid medium. The same receiver setup is used from the previous experiments. Before testing, the full-angle FOV is measured to be 0.03° half angle. The FOV limits the amount of higher angle scattered light and only allows in near-forward scattered and ballistic light that falls within the paraxial approximation, this becomes important for a turbid medium as the transition between the ballistic and multi-scatter regime depends on FOV.

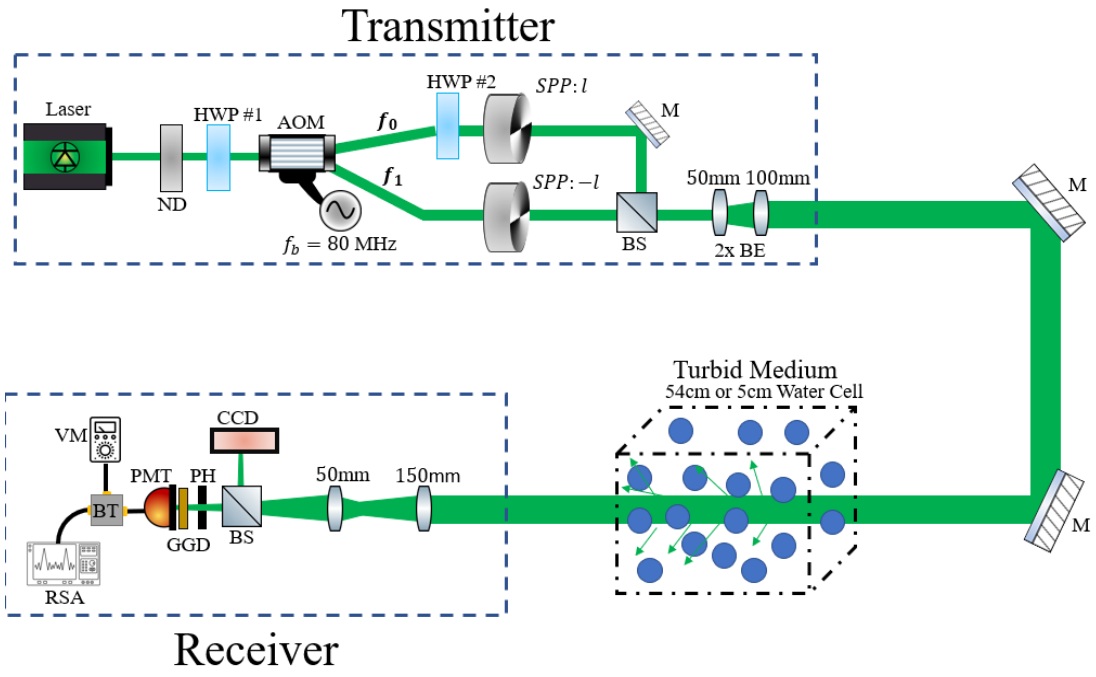

Figure 7.6: Experimental setup to test OHDOOM through a turbid medium. ND: neutral density filter, AOM: acousto-optic modulator, HWP: half-waveplate, SPP: spiral phase plate, BS: 50/50 beam splitter, BE: beam expander, M: mirror, PH: pinhole, PMT: photo-multipler tube, CCD: charged coupled device, VM: volt-meter, BT: Bias-T, GGD: ground glass diffuser, and RSA: real-time spectrum analyzer.

The experiments performed measure the beatnote response as a function of increasing optical depth using Equate®, $Mg(OH)_2$, and various sizes of microspheres to act as the turbid medium. The first set of experiments were performed through a 54 cm and 5 cm path length. The varying lengths were used to determine if an increase in particle density within the 5 cm path would create more mode spreading. The DC signal and AC signal are calculated using the same method as discussed in Section 7.3.1 equations 7.14 and 7.15.

For the first set of experiments using water containing Equate® and $Mg(OH)_2$ (see Figures 7.7(a-d)), the matched case $\{0,0\}$ and unmatched case $\{2,-2\}$ AC (stars) and DC (triangles) photocurrent are measured as a function of optical depth. The matched case DC signal begins to deviate from the slope of Beer's law upon the onset of multiple scattering. Whereas the AC signal follows the same slope as Beer's law until the detector noise floor is reached. For the 5 cm path length using Equate®, for both the matched and mismatched case in Figure 7.7(b), similar results to the 54 cm path length are obtained. The constant offset between the matched and mismatched case shows that there is no significant mode spreading. If an increase of power was transferred to the 0^{th} order mode, the attenuation curve would show a decrease in slope, otherwise, a decrease in modal power would increase the slope compared to Beer's law. The path length difference is also assumed negligible due to the laser beam being relatively large and well collimated removing any significant effects of a parabolic wavefront.

The AC data does not deviate from the slope of Beer's law compared to the DC results at the onset of multiple scattering as the interference induced amplitude modulation rejects incoherent forward scattered light [233]. This benefit is of significant importance

as changes in the beatnote will be due to the loss of forward scatter coherence rather than the collection of just scattered light alone.

OHDOOM measurements through water containing Equate® were motivated by the results of the study by Zhang *et al.* [11] and Ferlic *et al.* [218]. The results of the two experiments differed as the first experiment saw mode spreading over a 2 mm path length at an optical depth of 6 using Equate®, while the second saw no mode spreading over a 3 m path length reaching optical depths of 14. Nonetheless, OHDOOM results are performed with a similar receiver apparatus to Ferlic *et al.* [218], but with a more sensitive detector. The OHDOOM results support the same results as Ferlic *et al.* [218] due to no significant mode spreading as optical depth increases. This is because the OHDOOM attenuation curves do not change slope as a function of optical depth. This means it is likely that Equate® does not induce significant phase distortions to create mode spreading. As a result, a small FOV detector geometry may not be sensitive to OAM mode spreading from small particles. Note that the propagation and scattering geometry are different in the OHDOOM setup as compared to Section 6.2.1, but the results are the same.

OAM mode spreading is determined to not been seen for three reasons: (1) limitations of the optical receiver, (2) high enough optical depth was not reached to create a large phase variance, or (3) small particles do not produce enough forward scattering effects to create mode spreading.

The next set of experiments were done to address the question if a medium, with known sizes of small particles, will induce mode spreading. The following particle diameters were tested: 930 nm, 600 nm, 300 nm, and 50 μm. For these experiments, WOSs of

a turbid medium can be used to predict the beatnote at varying optical depths as the particle characteristics are known. The results are summarized in Figs. 7.8(a-d) and 7.9(a-d) for the matched case $\{0,0\}$ and mismatched case $\{2,-2\}$.

In Figures 7.8(a-b), the plots are as follows: green stars represent the experimental AC data, black triangles represent the experimental DC data, red dashed line represents Beer's law, blue squares represent the simulated DC data, and magenta asterisks represent the simulated AC data. The plot labels are used in both the matched and mismatched cases in Figs. 7.8 and 7.9.

The results in Figs 7.8(a-b) for the 930 nm diameter particles appear similar to the Equate® and $Mg(OH)_2$ for the matched and mismatched cases. The simulated data for the AC and DC signals also follow the same trends as the experimental data. The same results occur for the 600 nm diameter particles in Figs. 7.8(c-d).

In Figs. 7.9(a-b) the matched and mismatched case for 300 nm diameter particles are shown alongside simulated results for the DC and AC signals. The results follow the same trend as the previously used microspheres. There is a slight deviation between the simulated DC signal and experimental DC signal as the simulation predicted more power upon multiple scattering. Otherwise, the experimental and simulated data agree well for the matched and mismatched cases. The last particle diameter tested was 50 μm (seen in Figs. 7.9(c-d)), however the optical depth reached did not indicate the onset of multiple scattering. For the optical depth that is reached, the matched and mismatched case did not show significant mode spreading. However, the signal variance did increase compared to previous results.

The main result is that OHDOOM appears to be insensitive to the phase distortions

created by small particle scattering. It is thought that significant forward scattering will presumably create a change in beatnote power when larger particles are present. If more mode spreading occurs a noticeable fluctuation to the AC beatnote could be measured using a short exposure rather than a long exposure. If the optical depth is held constant and the particle size is seen to change then the AC signal is proposed to increase due to mode spreading. This result is as expected given the simulations in Chapter 5 of OAM beams through a turbid medium. In the case of simulation showing OAM mode spreading as a function of particle size (Fig. 5.8(b)), particles with diameters < 50 μm were shown not to produce significant mode spreading. This result is also supported by previous work on OAM and ballistic light by Viola *et al.* [185] and MCF work by Bissonnette [101].

As these experiments indicate small particles do not produce mode spreading, limitations of the optical receiver cannot be dismissed. The unmatched case AC and DC data contain an offset at an optical depth of zero from leakage light that is still in the 0^{th} mode due to imperfections of the SPPs and the diffraction limit [160]. This issue can be addressed by optimizing the OHDOOM receiver. The second issue of not reaching high enough optical depths can be addressed by using more optical power that will increase signal to noise to within multiple scattering. Both of these sensitivity limitations of the optical receiver prompt further experimentation.

The results for the turbid water case using microspheres in comparison to simulation shows a slight difference between the AC and DC component for the matched case. For the first three particle sizes, the DC case is seen to diverge upon the start of multiple scattering due to the collection of incoherent forward scattered light from different distances along the propagation path. The AC signal is seen to attenuate following Beer's law

past this multi-scatter transition until the detector noisefloor is reached. If mode spreading were to occur, this AC signal would follow a different slope other than Beer's law. If mode spreading becomes large, the slope will be less than Beer's law. If significant mode spreading occurs the beatnote response slope would be greater than Beer's law as seen in Zhang *et al.*'s work [11].

The results for a turbid medium offer significant insight to practical applications. As Equate® and $Mg(OH)_2$ have been used to simulate water conditions similar to those of Petzold [63], the results are relevant to real oceanic conditions. As OHDOOM is seen to only lose signal power due to intensity losses and not the loss of forward coherence, this infers that turbulence can be sensed through turbid oceanic or atmospheric conditions. The same can not be said when the diameter of particulate matter reaches hundreds of microns and their size distributions are not widely variable as these particles can increase OAM mode spreading. For the mismatched case, there is a beatnote as this is residual power that could not be reduced further due to alignment and a practical setup as seen similarly in other OAM measurement devices[160].

7.4 Summary of OHDOOM

As stated in the introduction of this thesis, the goal was to develop an active OAM sensing modality to measure environmental perturbations. A method to compare the results of a turbid medium is done by comparing the matched case AC signal to the unmatched case AC signal. Figure 7.10(a-c) shows this beatnote ratio for a turbulent medium (Fig. 7.10(a)) and turbid medium (Figs. 7.10(b-c)).

The turbulent medium results in Fig. 7.10(a) shows an increase in the beatnote ratio as the mode spreading in the matched and unmatched cases become equal. When this matched case to unmatched case ratio is greater than 1, the mode spreading of the mismatched case is greater than that of the matched case. This occurs due to not enough averaging over enough random realizations. In Fig. 7.10(b), the ratio does not increase, as in the turbulent case, as scattering strength increases leading to the conclusion that no significant mode spreading occurs.

This chapter has addressed this goal along with simplifications to the optical receiver to measure OAM mode spreading. OHDOOM is a newly proposed method to sense OAM mode spreading using an AC coupled signal using the benefits of heterodyne detection. Verification and testing of OHDOOM were done with three separate experiments, two of which were through a simulated turbulent medium and a turbid medium. The following conclusions can be made about the OHDOOM system:

- OHDOOM provides a simpler optical receiver setup by placing complexity in the transmitter with the benefits of an AC coupled signal.
- The presence of a pinhole in the optical receiver makes the heterodyne based beatnote sensitive to optical phase perturbations.
- Preliminary results show the signal is sensitive to phase distortions such as optical turbulence.
- In the presence of specific forms of turbid media, the OHDOOM signal is not strongly affected by particulate matter except power losses that follow Beer's law.

- Allows for the sensing of turbulence in the presence of a turbid medium that contains particles comparable to the wavelength.

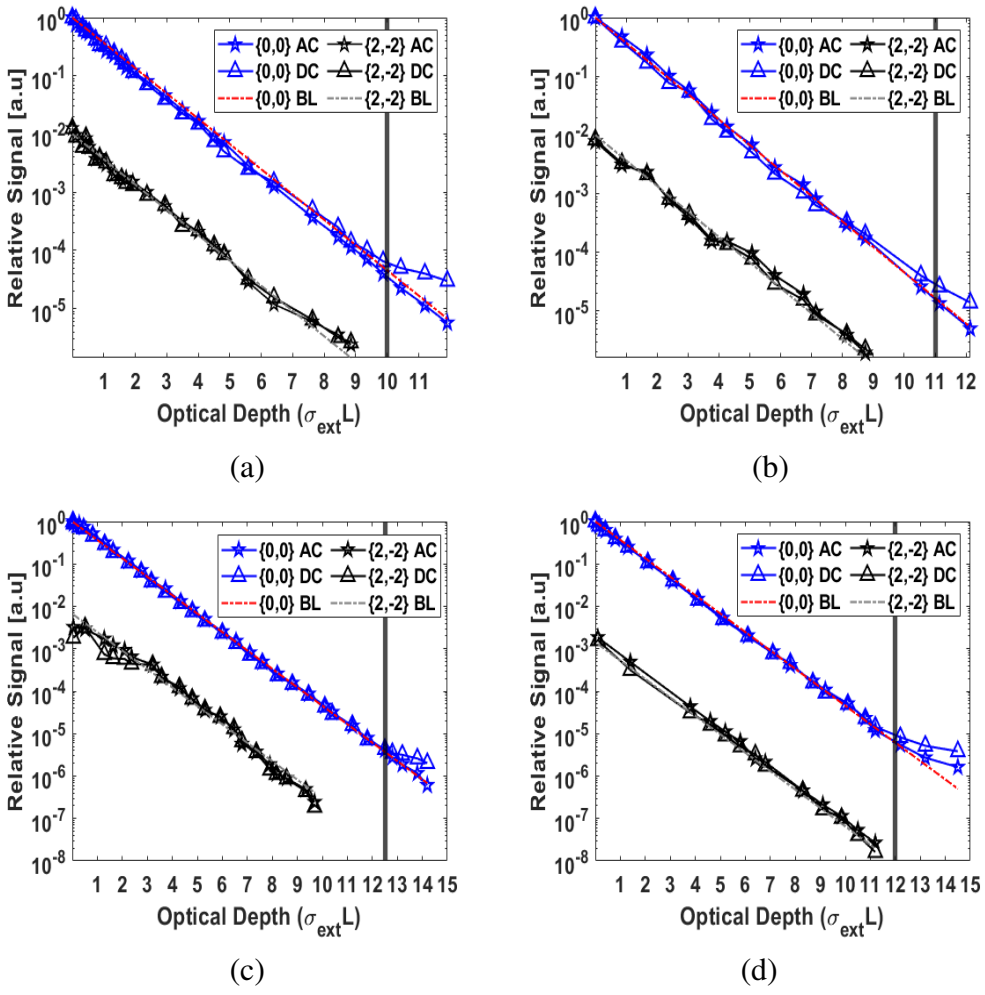

Figure 7.7: Experimental results of the beatnote for the matched and mismatched case through a 54 cm (a) and 5 cm (b) path length using Equate®. Experimental results of the beatnote for the matched and mismatched case through a 54 cm (c) and 5 cm (d) path length using $Mg(OH)_2$. Where Beer's law (BL) is plotted alongside experimental data showing the comparison of their slopes.

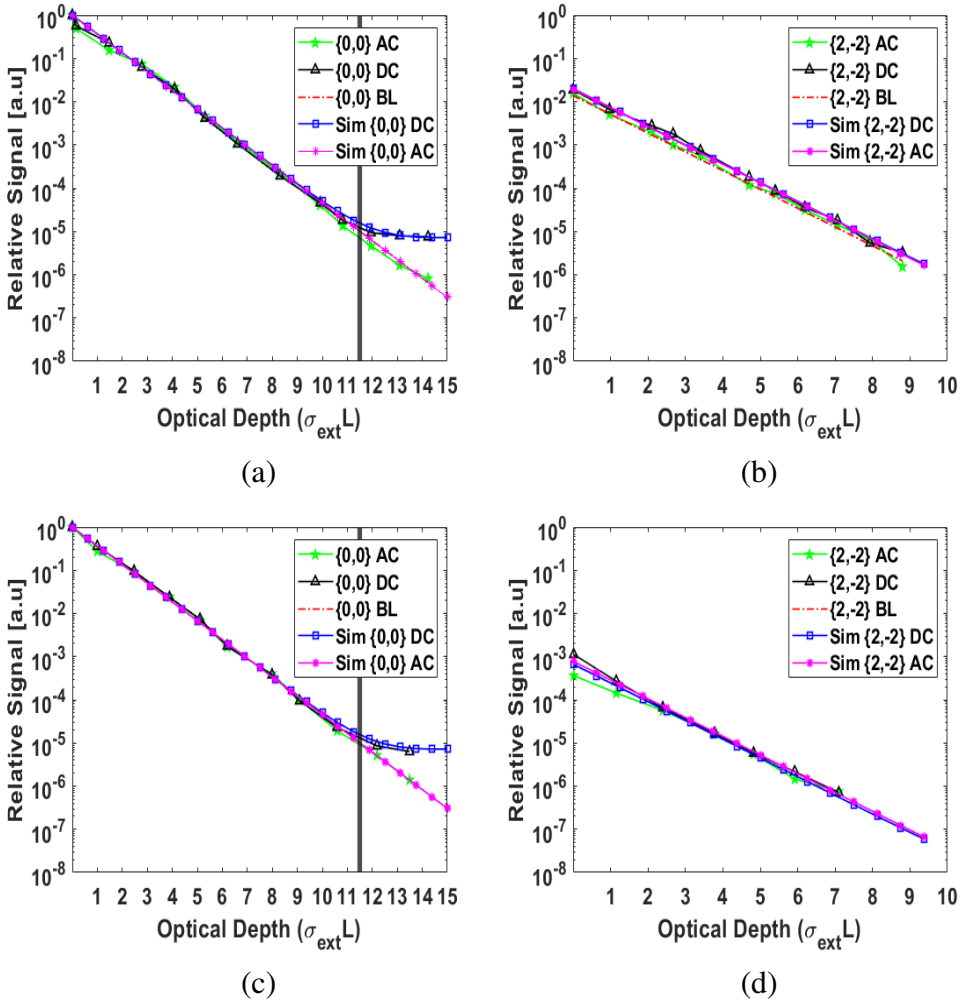

Figure 7.8: Experimental and simulated data for the matched (a) and unmatched (b) case in a 5 cm path length for 930 nm diameter particles. Experimental and simulated data for the matched (c) and unmatched (d) case in a 5 cm path length for 600 nm diameter particles. The theoretical Beer's law curve is plotted alongside both simulated and experimental data showing the comparison of their slopes.

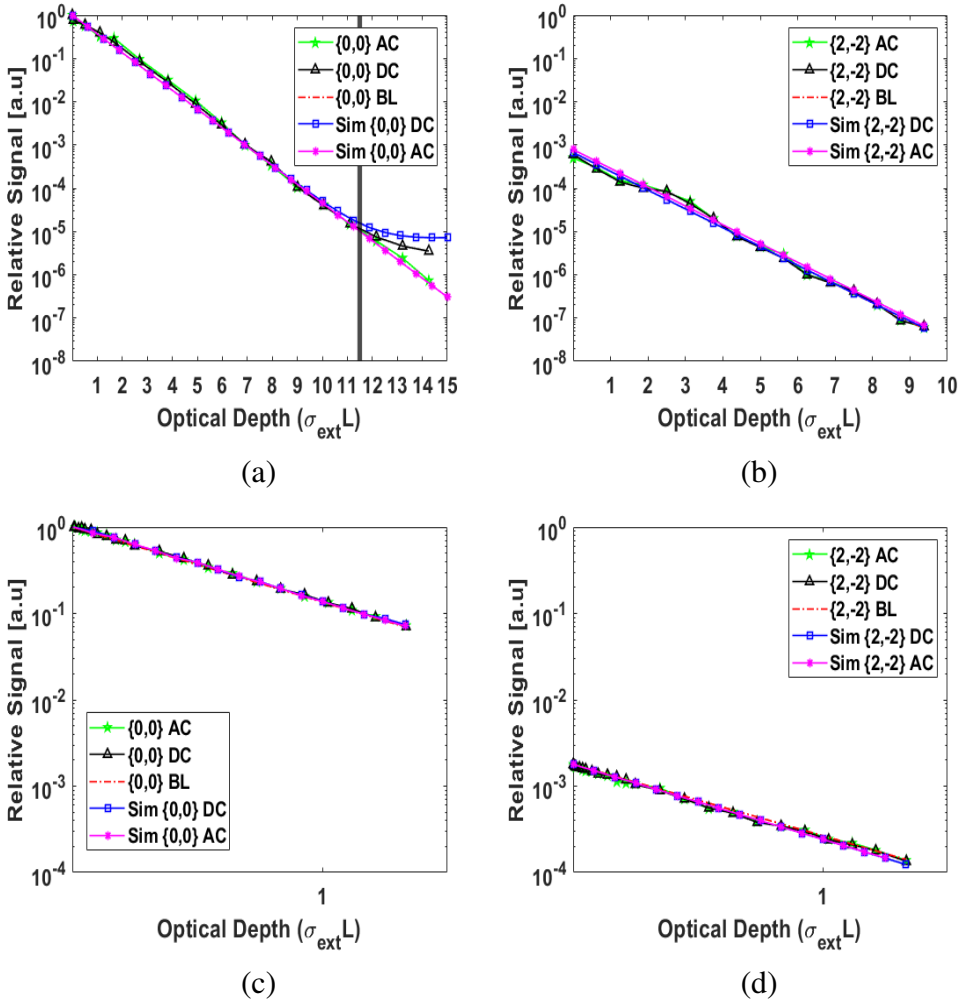

Figure 7.9: Experimental and simulated data for the matched (a) and unmatched (b) case in a 5 cm path length for 300 nm diameter particles. Experimental and simulated data for the matched (c) and unmatched (d) case in a 5 cm path length for 50 μm diameter particles. The theoretical Beer's law curve is plotted alongside both simulated and experimental data showing the comparison of their slopes.

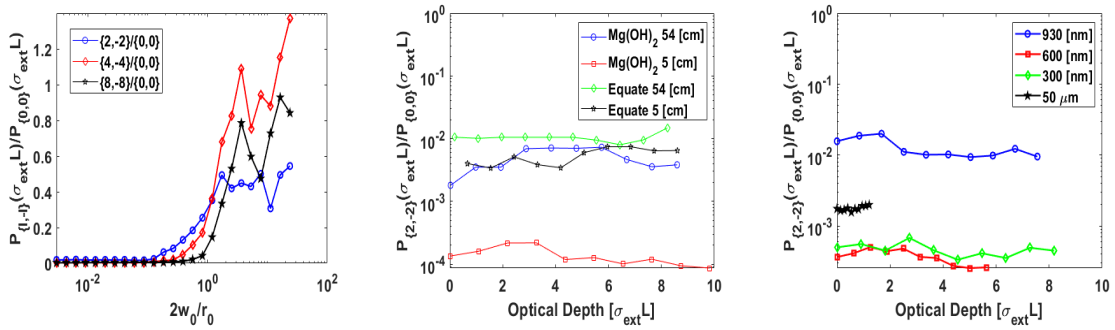

(a) (b) (c)

Figure 7.10: (a) Matched case to unmatched case ratio as a function of $2w_0/r_0$ for three mismatched cases $\{2,-2\}$, $\{4,-4\}$, and $\{8,-8\}$. (b) Scattering agent Equate® and $Mg(OH)_2$. (c) Microsphere beatnote response ratio as a function of optical depth using diameters 930 nm, 600 nm, and 300 nm.

Chapter 8: Conclusions

8.1 Summary of Findings

This research has led to the development of a new active OAM based sensing modality that responds to turbulent and turbid media in significantly different manners. This conclusion was reached based on the theoretical foundation in Chapters 2-4, simulations performed in chapter 5 and experiments in chapter 6. Chapters 2 and 3 provide a literature review and mathematical background of laser propagation through a random medium with a highlight on the similarities between turbulent and turbid media. Comparisons of each environment are made through the use of their phase correlation function supported with simulations. Chapter 4 discusses the phenomena of OAM, applications, and the physical mechanisms of OAM mode spreading in both turbulent and turbid media. A literature review was performed providing context of OAM based sensing modalities and the motivation of this dissertation to develop a more practical OAM based sensing modality. Using simulation results and comparison to experimental data help further the development of an active OAM sensing modality. Chapter 5 provides a set of simulations with the results summarized as follows:

- OAM beam performance through a turbulent environment strongly depends on the

beam size and divergence that are dependent on OAM order rather than OAM order alone. This infers that a strategically chosen divergence and spot size can reduce turbulence induced mode spreading across varying turbulence strengths. This is supported as $2w_0/r_0 > 1$, mode spreading becomes significant and quickly forces the OAM spectrum to a uniform distribution. Thus, the size of the input beam limits the applicability of using the OAM spectrum for sensing.

- Effects of the inner and outer scale play a role in OAM mode spreading along with the turbulence strength. As inner scale decreases mode spreading increases. The same occurs for increasing outer scale. When the inner and outer scales are equal no significant mode spreading is observed $L_0/l_0 \sim 1$. Introduction of the ratio L_0/l_0 provides regions where scale sizes become important.

- A partially coherent source, with an MCF containing intrinsic OAM, is seen to not strongly affect OAM spectrum spreading, but rather the intensity and scintillation upon propagation through temporally varying turbulence.

- OAM propagation through turbid media appears to be significantly different due to the phase correlation function that is dictated by a turbid medium's optical depth, particle size, and particle size distribution. The shape of the phase correlation function appears to strongly affect the dependence of OAM spreading as the input beam size changes.

- Depending on the beam metric chosen, how it is calculated, and compared, OAM beams can be seen to propagate in a similar manner as Gaussian beams. If the

chosen metric is measured in a different manner results can be significantly skewed.

- Ratio of beam size to particle size (w_0/a) plays a larger role in mode spreading than just a/λ alone.

Chapter 6 presents initial trials at developing an OAM based sensing modality using a folding wavefront interferometer and optical modal decomposition. These results led to the development of the OHDOOM sensing method to simplify the optical receiver without losing significant information about the OAM mode spreading. Experiments showed that OHDOOM is significantly sensitive to turbulence scales on the order of the beam size, but is insensitive to mode spreading by small particles. Simulations and theory are able to verify the OHDOOM signal response to each type of random media. The insensitivity to particulate matter is believed to be due to the use of small particles whose MTF does not significantly bandlimit the DPB. Experimental results can be summarized as follows

- Folding wavefront interferometry proves to be useful for a laboratory environment, but its sensitivity and need for image processing does not lend well to a practical setup outside of the lab.

- Modal decomposition is a useful method for quantifying the full OAM spectrum, but its receiver setup requiring a LCSLM leads to a complicated and impractical optical receiver.

- OHDOOM provides a number of benefits: simplification of the optical receiver without a loss of mode spreading information, ability to implement AC coupled detection, lower detector noisefloor, and background light rejection.

- The OHDOOM sensing method is seen to be sensitive to turbulence, but not to a "realistic" scattering environment meaning phase distortions due to scattering can be neglected. This assumes the particle sizes present do not have large diameters $\sim$ 50 μm.

- OAM beam propagation through a turbid medium may not necessarily be robust due to the beam shape, but rather due to the phase statistics of the medium.

8.2 Practicality of OAM for Imaging and Communications

As the discussion of this dissertation centered on OAM applications for sensing, the results can be directly discussed in the context of imaging or communications. Free-space OAM SDM communications is clearly affected by mode spreading that can lead to channel errors. SDM communications is plausible and has already been demonstrated experimentally as long as the alphabet of OAM modes are chosen with enough modal separation so mode spreading effects can be reduced [130]. Our simulations, in weak turbulence following a Kolmogorov power-law, showed LG beams had similar on-axis intensity and scintillation losses. This infers that some turbulent effects are the same across all modes, but when strong turbulence is present this may change according to our work [193]. In reality turbulence will not be as consistent as simulated which leads to most simulation results to be tentative until proven experimentally. In applications containing scattering, when particle size and optical depth are small, OAM based communications is definitely plausible and effective [234]. Although these results are explicitly for water, the atmospheric aerosol case will be similar except with varying particle distribu-

tion still containing a significant amount of small particles [101], [235]. This leads to the assumption that OAM based communications through fog is still significantly plausible and less mode spreading will occur than an atmosphere limited by turbulence.

Active OAM based imaging applications are not as clear since imaging can take on many forms as to how the information is extracted from the beam. If a scene is illuminated with, the results will be similar to a Gaussian beam. However, if the beam is comparable to the object size as in the case of phase microscopy an OAM beam can act as an enhanced edge detector [25]. For applications in a macroscopic environment these effects aren't as clear. When OAM is applied as a filtering modality, imaging applications can be enhanced such as its use as a spatial filter [22]–[24] or coherence filter [48], [49], [119]. None of these applications use OAM as an "active" imaging method where the object is illuminated by OAM.

8.3 Future Work

Within the development of this work various results were found that were not originally expected leading to much of the work on OHDOOM. There are still many questions left unanswered with further paths of research to be traversed from this work. A couple of areas of research and questions that can be developed further to understand OAM based sensing are as follows: further development of OAM based propagation metrics, more experimental work using OHDOOM, verification of the forward scatter model on the MTF of an optical system and OAM propagation, OAM based sensing into strong turbulence and multiple scattering, and effects of varied statistical assumptions such as time-varying

turbulence.

Metrics concerning OAM can explore the effects of turbulence inner scale, outer scale, and anisotropy on the OAM spectrum and scintillation. Strong phase perturbations are also of interest to better understand limitations of remote sensing due to complete loss of wavefront coherence leaving the sensing modality inoperable. This region of a coherent OAM spectrum depends on the size of the beam dictating the region of interaction with the environment. Being able to discern if this is the upper limit of active OAM sensing would be of great interest as it can help provide if OAM has to be applied in another manner to the remote sensing problem such as measuring rotational Doppler shifts or using OSP. Within this context, temporally evolving turbulence in a real environment will demonstrate very different effects than most OAM based studies performed, cited, and preluded to in this work.

8.3.1 Extensions of OHDOOM

The new sensing modality presented in this work called OHDOOM has only been tested in a fashion to confirm its ability to sense a random medium. The results showing it is sensitive to a turbulent medium is only the starting point to understand more about the ability of this OAM sensing modality. For starters it is suggested that a turbid medium does not affect the OAM spectrum significantly, but larger particle sizes were not tested in this work and only hypothesised to create more mode spreading based on simulated results. Confirmation of this mode spreading must be done before confirming that OHDOOM is insensitive to a turbid medium.

Transitioning OHDOOM into a backscatter geometry is also a future direction of concern. Within this setup a local oscillator could be used to measure true phase information of the beatnote. Other phenomena can be studied as well that may depend on the OAM of the incident laser such as scattering from objects in the medium, effects of enhanced backscattering, or rotational Doppler effects [46]. The rotational Doppler effect might be possible to see in environments with rotating particles due to strong flow, vortices, or turbulence.

Other studies of interest are focusing on combining the coherent effects of particle scattering and turbulence to see how the two phenomena combined affect the beatnote experimentally. This would be practical in cases underwater where turbulence forms in the presence of particles or in the atmosphere when boundary levels turbulence is created among boundary layer clouds. In Fig. 8.1 two examples of turbulence combined with scattering are shown. Figure 8.1(a) shows a simulated case that if the beam interacts with a single realization of turbulence and turbid media containing 50 μm particles. Perturbations of the attenuation curve from Beer's law show changes in mode spreading introduced by the turbulence and not the particles. Figure 8.1(b) is the same turbulence strength and particle size, but averaged over 20 independent realizations.

Another question of OHDOOM is how the AC coupled signal changes in a turbid or turbulent medium compared to an amplitude modulated laser. The beatnote of OHDOOM depends on the ability of the interference produced by the DPB. As forward coherence is lost this interference pattern will lose its temporal and spatial coherence reducing its visibility, therefore reducing the beatnote signal. This is in contrast to an amplitude modulated laser whose signal decreases with intensity losses and increased bandwidth due to

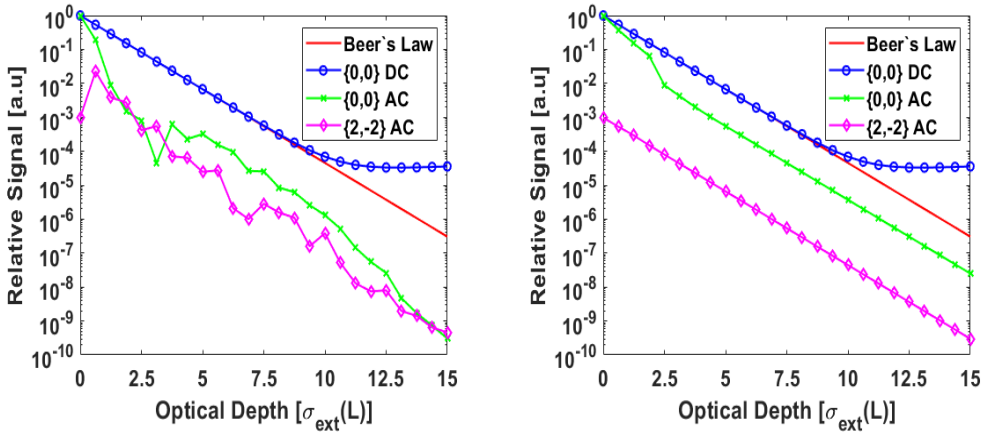

Figure 8.1: (a) Single realization of simulated beatnote signal containing turbulence and a turbid medium containing 50 μm diameters particles. (b) Simulated beatnote signal averaged over 20 realizations with turbulence along the entire turbid medium propagation length.

scattered light. What are the effects of a turbid medium on an amplitude modulated laser compared to a temporal interference modulated laser or if both modulations are combined? The latter is thought to have its signal reduced by the loss of both temporal and spatial coherence, but further experimentation will provide the answer.

The last future test of OHDOOM will be to quantify the effects of temporally correlated turbulence in an atmospheric, oceanic, or controlled laboratory environment. The fluctuations of the beatnote power, beatnote phase, integration time, and possible Doppler effects will all become factors in analyzing the receiver signal.

8.3.2 Further Exploration of Forward Scatter Coherence

Specific research can also continue looking into how the coherence of forward scattered light changes through a turbid medium. Being able to verify the theoretical and simulated MTF of the turbid medium WOSs presented in this work would help move for-

ward the understanding of how a laser beam carrying OAM propagates through a turbid medium. This includes how the OAM spectrum of a laser beam close to the particle size is affected as this would concern how the output electric field is changed. This case cannot easily be modeled using WOSs as it is assumed the phase function does not change. This raises the question if the MTF is affected by the change in the phase function behavior or are phase perturbations a change in phase function or are they decoupled events.

Within the theory of a turbid medium being able to define a quantity similar to the Fried parameter would also be of great interest that can be related to image formation instead of only the optical depth. As the Fried parameter scale dictates how well an image can be formed, a turbid medium does not contain a similar pattern as larger attenuation lengths do not always translate to the same effect depending on the medium of interest such as fog compared to water. The optical density in fog allows for longer propagation distances than water, but the loss of forward scatter coherence occurs in a similar manner. The answer to this question is not obvious.

Using OAM mode spreading, another concern is if the OAM spectrum perturbations can be mapped back to the phase variance. The issue is that the phase variance depends on both the magnitude of the phase function and the optical depth. If another metric can be used to decouple the two a unique phase variance can be determined similar to the ratio $2w_0/r_0$ to determine a unique Fried parameter. But this uniqueness is broken when inner scale, outer scale, and anisotropy are introduced to the random medium. Instead the Rytov number could be the nondimensional metric of interest as it does not depend on the beam size, but rather only on the turbulence strength present.

8.4 Conclusions

This experimental and simulation work on active OAM sensing modalities helps push forward the practicality of OAM based sensing. Experimental effort led to the development of OHDOOM, which provides an optical receiver with less hardware than previous experiments. OHDOOM also leverages the benefits of an inherently AC coupled signal to reject any low frequency noise sources. Future work will evolve both OHDOOM and simulation methods of OAM beams through random media.

Appendix A: Calculation of Large Particle VSF

The phase function (or VSF) of large particles described by equation 2.15 is calculated directly from Mie theory for spherical particles. $S(\theta,\varphi,\xi)$ are the amplitude scattering coefficients for the far-field distribution of scattered light [54], [55]. For more information on their physical derivation the reader is directed to Van De Hulst [54], Bohren and Huffman [55], or Deirmendjian [235], [236].

The scattering amplitudes, independent of the azimuthal angle, are given as

$$\begin{aligned} S_1(\theta) &= \sum_{n=0}^{Nc} \frac{2n+1}{n(n+1)}(a_n\pi_n(\theta)+b_n\tau_n(\theta)) \\ S_2(\theta) &= \sum_{n=0}^{Nc} \frac{2n+1}{n(n+1)}(a_n\tau_n(\theta)+b_n\pi_n(\theta)). \end{aligned} \tag{A.1}$$

The scattering amplitudes are used in a matrix representation to denote the amplitude of the various polarization components depending on the incident wave. For example if the laser is horizontally polarized to the scattering plane S_1 is used, otherwise, a vertically polarized laser will use S_2.

The Mie coefficients a_n and b_n weigh each angular function $\tau(\theta)$ and $\pi(\theta)$ that

carry the angular dependence and are defined as

$$\begin{aligned} \pi_n(\cos(\theta)) &= \frac{P_n^1(\cos(\theta))}{\sin(\theta)} \\ \tau_n(\cos(\theta)) &= \frac{dP_n^1(\cos(\theta))}{d\theta} \\ P_n^m(\cos(\theta)) &= (1-\cos^2(\theta))^{m/2}\frac{d^m P_n(\cos(\theta))}{d(\cos(\theta))^m} \end{aligned} \tag{A.2}$$

where $P_n^m(\cos(\theta))$ are the associated Legendre polynomials. For this series $m = 1$ as the boundary conditions call for higher order polynomials to vanish. The functions can then be implemented using their recursion relationships for computational efficiency as

$$\begin{aligned} \pi_0(\cos(\theta)) &= 0 \\ \pi_1(\cos(\theta)) &= 1 \\ \pi_n(\cos(\theta)) &= \frac{2n-1}{n-2}\cos(\theta)\pi_{n-1}(\cos(\theta)) - \frac{n}{n-1}\pi_{n-2}(\cos(\theta)) \\ \tau_0(\cos(\theta)) &= 0 \\ \tau_1(\cos(\theta)) &= \cos(\theta) \\ \tau_n(\cos(\theta)) &= n\cos(\theta)\pi_n(\cos(\theta)) - (n+1)\pi_{n-1}(\cos(\theta)). \end{aligned} \tag{A.3}$$

The Mie scattering coefficients a_n and b_n are defined as

$$\begin{aligned} a_n &= \frac{m\psi_n(mx)\psi_n^{'}(x) - \psi_n(x)\psi_n^{'}(mx)}{m\psi_n(mx)\xi_n^{'}(x) - \xi_n(x)\psi_n^{'}(mx)} \\ b_n &= \frac{\psi_n(mx)\psi_n^{'}(x) - m\psi_n(x)\psi_n^{'}(mx)}{\psi_n(mx)\xi_n^{'}(x) - m\xi_n(x)\psi_n^{'}(mx)} \end{aligned} \tag{A.4}$$

where $\psi_n(\rho)$ and $\xi_n(\rho)$ are Riccatti-Bessel functions defined as

$$\begin{aligned} \psi_n(\rho) &= \rho\, j_n(\rho) \\ \xi_n(\rho) &= \rho h_n^1(\rho) = \rho[j_n(\rho) + i y_n(\rho)] \end{aligned} \tag{A.5}$$

where $h_n^1(\rho)$ are spherical Hankel functions, and $j_n(\rho)$ and $y_n(\rho)$ are written using Bessel functions of the first and second kind

$$\begin{aligned} j_n(\rho) &= \left(\frac{\pi}{2\rho}\right)^{1/2} J_{n+1/2}(\rho) \\ y_n(\rho) &= \left(\frac{\pi}{2\rho}\right)^{1/2} Y_{n+1/2}(\rho). \end{aligned} \tag{A.6}$$

The computation of the Mie coefficients is easier with the addition of the logarithmic derivative [237]. The logarithmic derivative of $\psi_n(mx)$ is defined as

$$\begin{aligned} \frac{d[ln(\psi_n(mx)]}{d(mx)} &= \frac{\psi_n^{'}(mx)}{\psi_n(mx)} \\ D_n(mx) = -\frac{n}{mx} + \frac{j_{n-1}(mx)}{j_n(mx)} &= -\frac{n}{mx} + \frac{1}{\frac{n}{mx} - D_{n-1}(mx)} \\ D_0(mx) = \frac{j_{-1}(mx)}{j_0(mx)} &= \cot(mx). \end{aligned} \tag{A.7}$$

The Mie coefficients can then be rewritten as

$$\begin{aligned} a_n &= \frac{\left[\frac{D_n(mx)}{m} + \frac{n}{x}\right] \Re\{\zeta_n(x)\} - \Re\{\zeta_{n-1}(x)\}}{\left[\frac{D_n(mx)}{m} + \frac{n}{x}\right] \zeta_n(x) - \zeta_{n-1}(x)} \\ b_n &= \frac{\left[mD_n(mx) + \frac{n}{x}\right] \zeta_n(x) - \zeta_{n-1}(x)}{\left[mD_n(mx) + \frac{n}{x}\right] \Re\{\zeta_n(x)\} - \Re\{\zeta_{n-1}(x)\}} \end{aligned} \tag{A.8}$$

where $\zeta(x)$ can be found from the recursion relations

$$\begin{aligned}\zeta_n(x) &= \frac{2n-1}{x}\zeta_{n-1}(x) - \zeta_{n-2}(x) \\ \zeta_{-1}(x) &= \cos(x) - i\sin(x) \\ \zeta_0(x) &= \sin(x) + i\cos(x).\end{aligned} \tag{A.9}$$

Using the forward recursive techniques to compute $D_n(mx)$ from equation A.7 induces numerical errors which can be fixed using a downward recursive method [60], [237]

$$D_{n-1}(mx) = \frac{n}{mx} - \frac{1}{D_n(mx) + \frac{n}{mx}}. \tag{A.10}$$

The verification and further use of generating VSFs is detailed in previous work [60].

Upon calculating of the Mie coefficients, other useful quantities can be defined as well which are used in the text. Such as the scattering and extinction cross sections

$$C_{sca} = \frac{2\pi}{k^2}\sum_{n=1}^{N_c}(2n+1)(|a_n|^2+|b_n|^2) \tag{A.11}$$

$$C_{ext} = \frac{2\pi}{k^2}\sum_{n=1}^{N_c}(2n+1)\Re\{a_n+b_n\}. \tag{A.12}$$

From the scattering and extinction cross sections the scattering and extinction coefficients of the particle can be defined as $\sigma_{sca} = NC_{sca}$ and $\sigma_{ext} = NC_{ext}$ as discussed in Section 2.3 in equation 2.9 where N is the number density in particles per cubic meter.

For more practical calculations a turbid medium is generally polydisperse and the number density is an integral over the particle diameter distribution as

$$N = \int_0^\infty n(a)da. \tag{A.13}$$

Using the particle distribution all previously defined quantities can be represented as a weighted average across the particle distribution. The unpolarized phase function of a polydisperse system becomes

$$\sigma_{V_{pd}}(\theta,\varphi) = \frac{\int_0^\infty \left(|S_1(\theta,\varphi,a)|^2 + |S_2(\theta,\varphi,a)|^2\right) n(a)da}{2k^2 \int_0^\infty C_{sca}(a)n(a)da}. \tag{A.14}$$

Using this particle distribution the scattering coefficients are redefined as

$$C_{sca_{pd}} = \int_0^\infty C_{sca}(a)n(a)da \tag{A.15}$$

$$C_{ext_{pd}} = \int_0^\infty C_{ext}(a)n(a)da \tag{A.16}$$

Appendix B: Numerical Generation of two-dimensional Phase Screens

Under the assumption that a turbulent medium contains phase and amplitude distortions, the phase distortions contribute a larger distortion to the incident beam. This allows the distortion to be modeled as a single phase only distortion $\exp(i\theta_{rnd}(x,y))$, which does not account for non-isoplanatic effects [238], [239]. Assuming the optical phase is Fourier transformable, the phase can be written as a 2D Fourier transform in terms of the sampling variables p,q and Fourier indices n,m as [240]

$$\theta_{rnd}(q\Delta x, p\Delta y) = \sum_{n=-\infty}^{\infty}\sum_{m=-\infty}^{\infty} \tilde{c}(n\Delta\kappa_x, m\Delta\kappa_y) e^{i\left(q\Delta x[n\Delta\kappa_x]+p\Delta y[m\Delta\kappa_y]\right)}, \tag{B.1}$$

where the spatial domain grid spacing are Δx and Δy and the wavenumber grid spacing are $\Delta_{\kappa_x} = 2\pi/Ndx$ and $\Delta_{\kappa_y} = 2\pi/Ndy$. The Fourier coefficients are defined as

$$\tilde{c} = (a+ib)\sqrt{\Delta\kappa_x\Delta\kappa_y\Phi_{n,2}(n\Delta\kappa_x, m\Delta\kappa_y)}, \tag{B.2}$$

where a and b are normal Gaussian random variables and $\Phi_S(n\Delta\kappa_x, m\Delta\kappa_y)$ is the phase power spectrum. Using the phase power spectrum and the random number matrices that

are a and b, a single spatial phase realization of the random medium can be found as

$$\theta_{rnd}(p\Delta x, q\Delta y) = N^2 \mathscr{F}_2^{-1}\{\tilde{c}\}. \tag{B.3}$$

Depending on the medium in question the phase power spectrum will take on different forms.

B.1 Turbulent Phase Screen

Within a turbulent medium with refractive index variations much larger than the wavelength, the phase power spectrum is directly proportional to the refractive index power spectrum as [71]

$$\Phi_S(n\Delta\kappa_x, m\Delta\kappa_y) = 2\pi k^2 dz \Phi_n(n\Delta\kappa_x, m\Delta\kappa_y), \tag{B.4}$$

where the refractive index power spectrum follows a power-law $\kappa^{-11/3}$ as shown in Section 2.3.3. The numerical issue with this form of spectra are the singularity that exist at $\kappa = 0$ [59], [238], [240]. To deal with this issue numerically this Fourier component is typically set to zero and approximated by introducing sub-harmonics. Sub-harmonics are an artificial method to add in low frequency components that are removed when the singularity at $\kappa = 0$ is set to zero. By setting this singularity to zero a significant portion of low frequency components are not sampled properly leading to an incorrect representation of refractive index fluctuations. An example of a turbulent phase screen produced using this method is shown in Fig. B.1(a) showing the phase shifts as a function of grid

coordinate.

There are various methods to add in low frequency components to improve phase screen accuracy [238], [240], [241], but the method chosen in this work is a randomized spectral sampling technique introduced by Paulson *et al.* [242]. This technique leverages the benefits of randomized grid sampling to improve the phase screen statistics to include low frequency inherently in the inverse Fourier transform in equation B.3. This is done by adding a random shift factor in the x and y directions as $\delta\kappa_x$ and $\delta\kappa_y$, bounded between $\pm\Delta\kappa_x/2$ and $\pm\Delta\kappa_y/2$, to equation B.1 as

$$\theta_{rnd}(q\Delta x, p\Delta y) = \sum_{n=-\infty}^{\infty}\sum_{m=-\infty}^{\infty} \tilde{c}(n\Delta + \delta\kappa_x\kappa_x, m\Delta\kappa_y + \delta\kappa_y) e^{i\left(q\Delta x[n\Delta\kappa_x+\delta\kappa_x]+p\Delta y[m\Delta\kappa_y+\delta\kappa_y]\right)}. \tag{B.5}$$

The sub-harmonics spatial frequency coordinates are randomized for each individual sub-harmonic frequency. The low frequency grid is divided into nine sub harmonics which adds a low frequency component to the phase as

$$\theta_{sh}(q\Delta x, p\Delta y, j) = 3^{2j}\sum_{n=-1}^{1}\sum_{m=-1}^{2}\sum_{j=1}^{N_s}\tilde{c}\left(\frac{n\Delta\kappa_x+\delta\kappa_x}{3^j}, \frac{m\Delta\kappa_y+\delta\kappa_x}{3^j}\right) e^{i\left[q\Delta x\frac{n\Delta\kappa_x+\delta\kappa_x}{3^j}+p\Delta y\frac{n\Delta\kappa_y+\delta\kappa_y}{3^j}\right]}, \tag{B.6}$$

where N_s is the number of sub-harmonic grids, for all uses in this paper $N_s = 9$. For the center grid when $n = m = 0$ the normalization is $N_s + 1$ rather than the index j. Each for the $\delta\kappa_x$ and $\delta\kappa_y$ are different random numbers for each sub-harmonic draw.

B.2 Turbid Phase Screen

The process for generating a turbid phase screen is much simpler than that of a turbulence screen since the phase power spectra do not contain a singularity at $\kappa = 0$. Power-law sectrum's, even bounded models such as MVK or MAS, contain a continuum of spatial wavenumbers compared to turbid media spectra that resemble Gaussian power spectra. A turbid medium contains strict bandlimits on the spatial frequencies present that depend on the particle diameters present in the medium.

A bandlimit leaves no need for sub-harmonic routines for the phase screen. The phase power spectrum is proportional to the scattering phase function. Physical interpretation of the phase PSD can be made apparent as the phase function or VSF is also the far-field distribution of the scattered field. This creates a relationship between the scattering wave-vector as defied by Tatarski [71] and Ishimaru [72] and the spatial wavenumber

$$|\boldsymbol{\kappa}| = |\vec{k} - \vec{k_m}| = 2k \sin\left(\frac{\theta}{2}\right) = \kappa = (\kappa_x^2 + \kappa_y^2)^{1/2}. \tag{B.7}$$

From studies looking at patterns in particle scattering, the magnitude of the scattering wave vector is the length scale of the scattering effects where the product of the scattering inhomogeneity size ($|\boldsymbol{\kappa}|$) results in a useful treatment of patterns in scattering [243], [244]. Depending on the grid size and number of points, the size of the spatial frequencies will be limited and a non-physical result may be obtained as many spatial frequencies will be under sampled. Depending on computational power this will strongly limit the simulation domain size, but beams on the centimeter scale can still be simulated with relative ease.

An example of a turbid phase screen in Fig. B.1(b) shows the phase shifts of a medium containing 50 μm diameter particles. Notice the grid size is significantly smaller than the turbulent medium due to the scale size of the phase shifts being comparable to the particle diameter.

For particles with a small forward scattering component of the phase function, a significant amount of scattered light will diverge quickly off the numerical grid. This leads to errors if no absorbing boundaries are added as light scattered light becomes reintroduced to the numerical grid by the periodic structure of the discrete Fourier transform. This is done by using a super-Gaussian window that leaves$\sim$ 95% of the simulation grid usable. Quickly diverging light can also be more accurately modeled using an expanding grid which is discussed in Schmidt [88] and Fleck *et al.* [89], [90]. The benefit of using this expanding grid is to keep the quickly diverging light within a useful computational domain. For atmospheric propagation with larger distortion scale sizes, the effects of this expanding grid are less noticeable. But for smaller phase distortions care must be taken to choose the appropriate parameters such that the expanding grid does not ruin correlation statistics. Much of this sampling concern is discussed in Chapter 9 of Schmidt [88].

For a turbid medium there is also a large attenuation factor that follows Beer's law due to higher angle scattering and absorption. This is modeled by multiplying each phase screen by an attenuation factor proportional to the amount of light that is scattered outside the numerical grid.

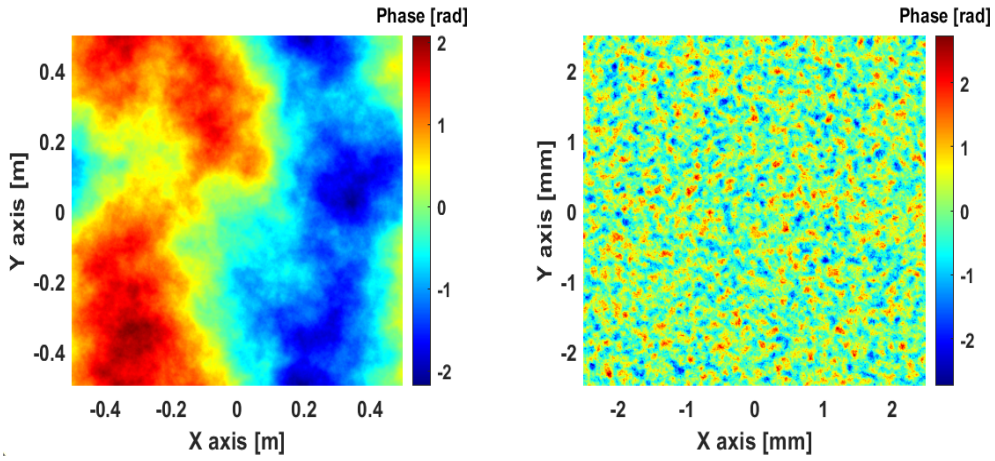

(a) (b)

Figure B.1: (a) Example of a turbulent phase screen generated using the randomized spectral sampling method. (b) Example of a turbid medium phase screen without the addition of sub-harmonics for a medium containing 50 μm diameter particles.

B.3 Generation of Temporally-Correlated Turbulence

For time-correlated turbulence, the phase is modeled in the spatial frequency domain as a first-order auto-regressive (AR) process [245]–[247]. The AR method takes a single phase screen realization in spatial frequency, $\mathscr{F}_2\left[\theta_{t-1}(x,y)\right]$, at the previous time step $t-1$ and adds another phase screen realization, $\mathscr{F}_2\left[\theta_D(x,y)\right]$, that are linearly related using a complex scaling parameter, α, as described by equation B.9

$$\theta_t(x,y) = \Re\left[\mathscr{F}_2^{-1}\left(\alpha\mathscr{F}_2[\theta_{t-1}(x,y)] + \sqrt{1-|\alpha|^2}\mathscr{F}_2[\theta_D(x,y)]\right)\right], \tag{B.8}$$

where $x = q\Delta x$ and $y = p\Delta y$. The scaling parameter α encodes how much atmospheric phase is "remembered" from the previous time step for each spatial frequency component. The newly added phase perturbations, $\theta_D(x,y)$, represents atmospheric "boiling", which is the temporal evolution of the eddy turnover rate [245]. Atmospheric boiling is the tem-

poral dependence of length scale changes within the eddy size distribution being blown across the detector aperture by the mean wind speed [248]. The coefficient α is defined as

$$\alpha = |\alpha| \exp(-iT(\kappa_x v_x + \kappa_y v_y)), \tag{B.9}$$

where $v_{x,y}$ is the wind velocity along the x, y direction, $\kappa_{x,y}$ is the spatial frequency component along the x, y direction, and T is the receiver sampling period. This coefficient provides a linear phase ramp in the frequency domain depending on the wind speed and direction, which equates to a shift of the numerical grid in real-space. The magnitude, $|\alpha|$, is fixed between 0 and 1. When $|\alpha|$ is 0, the turbulence is uncorrelated as in a traditional WOS approach. When $|\alpha|$ is 1, the turbulence represents pure frozen flow.

The injected phase is scaled by $\beta = \sqrt{1 - |\alpha|^2}$ in the frequency domain so that the power in the time series is conserved. Each phase screen is generated using a Fourier transform based sampling routine, which undersamples low frequency components. An AR based method does help to improve low frequency sampling across a number of temporal steps, but to improve each phase screen low frequency sub-harmonics are added. Each sub-harmonic is individually scaled by the same value of β to conserve power. To initialize the AR process at $t = 0$, a random phase screen is generated using the regular phase screen generation process.

Appendix C: Beam Profile Expressions

The electric field, or wavefunction, that describes the spatial distribution of the optical wavefront in this work is referred to as the beam profile. The formal electric field contains a temporal dependence

$$E(r,\phi,z,t) = U(r,\phi,z)e^{i2\pi ft}, \tag{C.1}$$

which is omitted when considering the beam profiles in this work unless otherwise mentioned especially in Chapter 7. The beam profiles used or referenced to in this work are as follows.

C.1 Gaussian Beam

A standard laser beam profile that is a solution to the wave equation is the Gaussian mode given as

$$U(r,z) = A_0 \exp\left(-\frac{r^2}{w^2(z)}\right)\exp\left(i\left[kz - \frac{kr^2}{2R(z)} + i\zeta(z)\right]\right), \tag{C.2}$$

where $w(z) = w_0[1+(z/z_R)^2]^{1/2}$ is the diffraction limited beam waist, $R(z) = z\left[1+(z_R/z)^2\right]$ is the radius of curvature, $z_R = \pi w_0^2/\lambda$ is the Rayleigh length, $\zeta = \tan^{-1}(z/z_R)$ is the Gouy

phase, w_0 is the initial $1/e^2$ beam waist, $r = (x^2+y^2)^{1/2}$ and $\phi = \tan^{-1}(y/x)$ are the radial coordinates, and A_0 is a constant amplitude factor [1].

C.2 Laguerre-Gaussian (LG) Beam

LG beams are idealized OAM beams that are a solution to the wave equation. They are commonly used to model OAM beam interactions due to their simple propagation properties for analytic and simulation treatment. The LG beam profile in terms of regular Gaussian parameters is

$$\begin{aligned} U(r,\phi,z) = A_0 \left(\tfrac{\sqrt{2}r}{w(z)}\right)^{|l|} L_p^{|l|}\left(\tfrac{2r^2}{w^2(z)}\right) \exp\left(-\tfrac{r^2}{w^2(z)}\right) \exp(il\phi) \\ \times \exp\left(i\left(kz - \tfrac{kr^2}{2R(z)}\right)\right) \exp\left(i(2p+|l|+1)\zeta(z)\right), \end{aligned} \tag{C.3}$$

where $L_p^{|l|}$ are the associated Laguerre polynomials, p is the radial index, and l is the OAM index [1].

C.3 Bessel Beam

A unique solution to the wave equation is the Bessel beam whose profile is diffractionless upon propagation [129] meaning the beam does not expand in free-space. This property cannot be replicated perfectly in reality as the beam would require infinite energy, but the profile can still be studied when it is passed through a finite aperture and allowed to diffract. Depending on the radial wavenumber k_r a region of little diffraction

can be observed using the beam profile [249]–[251]

$$U(r,\phi,z) = A_0 J_l(k_r r)\exp(ik_z z)\exp(il\phi), \tag{C.4}$$

where k_r is the radial wavenumber where $k = (k_r^2 + k_z^2)^{1/2}$ and $J_l(k_r r)$ is the l^{th} order Bessel function of the first kind. When working with this profile in simulation a circular aperture is always applied before propagation.

C.4 Bessel-Gaussian (BG) Beam

The BG beam is the finite version of the ideal Bessel beam that propagates with more of a Gaussian beam nature depending on the radial wavenumber. The BG profile is given as [130]

$$\begin{aligned} U(r,\phi,z) = A_0 J_l\left(\frac{k_r r}{1+i\frac{z}{z_R}}\right)\exp\left(iz\left(k_z - \frac{k_r^2}{2k_z}\right) - i\zeta(z)\right) \\ \times \exp(il\phi)\exp\left(-\frac{r^2}{w^2(z)}\right)\exp\left(-\frac{ik_z}{2R(z)}\left(r^2 + \frac{k_r^2 z_R}{k_z^2}\right)\right). \end{aligned} \tag{C.5}$$

If $k_r = 0$ a Gaussian beam profile is returned as given in equation C.1.

C.5 Hypergeometric Gaussian (HyGG) Beam

When a Gaussian beam propagates through a diffractive optical element such as a spiral phase plate (SPP), the resultant beam contains OAM but contains a more complex

radial beam profile. The profile after the SPP is given as [128], [252]

$$U(r,\phi,z) = \frac{(-i)^{n+1}}{4\sqrt{\pi}} \left(\frac{kw_0^2}{zq^2}\right) \left(\frac{kw_0 r}{\sqrt{2}qz}\right) \left(I_{\frac{n-1}{2}}(\nu) - I_{\frac{n+1}{2}}(\nu)\right) \exp\left(-\frac{r^2}{w^2(z)} + i\left[\frac{kr^2}{2R(z)} + l\phi\right]\right), \tag{C.6}$$

where $q = (1 - ikw_0^2/z)^{1/2}$, $I_n(\nu)$ are modified Bessel functions of the first kind, and $\nu = 1/2(kw_0 r/\sqrt{2}qz)^2$.

Appendix D: I_m Bessel Beam MCF

The I_m-Bessel beam, originally introduced by Ponomarenko, is a partially coherent beam with an MCF that carries a separable azimuthal phase component [138]. The coherence properties are isotropic in the sense that coherence properties of the beam do not depend on the relative orientation of the transverse points. A beam of this nature can be expanded into an incoherent summation of coherent basis modes known as the coherent mode representation (CMR). Consequently, partially coherent beams of this form are highly stable upon propagation. The I_m Bessel beam's MCF, or cross spectral density (CSD) in coherence theory, is

$$W(r_1, r_2, \omega) = \langle U^*(r_1, \omega) U(r_2, \omega) \rangle = \sum_{p=0}^{N_e} \lambda_{lp}(\omega) \psi_{lp}^*(r_1, \omega) \psi_{lp}(r_2, \omega), \tag{D.1}$$

where r_1 and r_2 are spatial coordinates, U represent the electric field of the beam, $\omega = 2\pi/\lambda$, ψ_{lp} are the eigenmodes, N_e is the number of eigenmodes, and λ_{lp} are the eigenvalues. Each eigenmode will be generated at the same optical frequency ω, which will be inferred. The eigenmodes to describe the IBB are the LG modes described by equation C.3.

Using the LG modes as the eigenmodes, the eigenvalues of equation D.1 are found

to be [138]

$$\lambda_{lp} = \frac{p!\,\xi^p}{(p+l)!}, \tag{D.2}$$

where ξ defines the coherence of the beam and is limited between $0 < \xi < 1$. When $\xi \sim 1$ the beam is considered to be incoherent and the eigenvalue distribution broadens. When $\xi \sim 0$, the beam is fully coherent and is described by the LG expression in equation C.3. The analytical form of an IBB source's CSD is found by substituting equation C.3 into D.1, taking the form

$$W(r_1, r_2) = \frac{\xi^{-l/2}}{1-\xi} e^{-\frac{(1+\xi)(r_1^2+r_2^2)}{(1-\xi)w^2(z)}} e^{-il(\phi_1-\phi_2)} I_m\left(\frac{4\sqrt{\xi}r_1 r_2}{(1-\xi)w^2(z)}\right), \tag{D.3}$$

where I_m is a modified Bessel function of the first kind.

The average intensity, $I(r,z)$, or spectral density, of the beam can be found by setting the observation points to be the same, $r_1 = r_2 = r$ and $\phi_1 = \phi_2 = \phi$, to obtain

$$I(r,z) = \frac{\xi^{-l/2}}{1-\xi} e^{-\frac{2(1+\xi)r^2}{(1-\xi)w^2(z)}} I_m\left(\frac{4\sqrt{\xi}r^2}{(1-\xi)w^2(z)}\right). \tag{D.4}$$

D.1 Propagation of the I_m Bessel Beam

Using the coherent mode representation (CMR), defined in equation D.1, of a partially coherent beam, the beam propagation can be easily adopted to the split-step method. The only difference to coherent beam propagation is an exposure time must be introduced to average over a set of realizations of the partially coherent beam. This breaks the typical use of the split-step method that simulates independent spatial realizations of the random

process. Depending on the exposure time, the realizations of turbulence present may not be independent. Simulation of this form of turbulence is discussed in Appendix B.

To generate the average intensity of the I_m Bessel beam, the simulation procedure could be performed where the CSD itself is propagated. However the simulation goal is to replicate the experimental implementation of the IBB discussed by Chen *et al.* [139]. In summary the simulation procedure is as follows:

1. Calculate the eigenvalue distribution given the eigenmode index p, a set number of eigenmodes N_p, OAM value l, and coherence value ξ.

2. Weight each eigenvalue following, $P(\lambda_{lp}) = \frac{\lambda_{lp}}{\sum_{j=0}^{N_p} \lambda_{lj}}$, where $P(\lambda_{lp})$ is the probability that the p^{th} eigenmode is drawn and transmitted.

3. Take the beam profile from equation C.3 for the p^{th} eigenmode with OAM value l, propagate the beam using coherent beam propagation from Appendix E, and then temporally average the beam metrics (such as intensity) to obtain the average intensity given by equation D.4.

For larger values of ξ the number of iterations must be increased to reduce the ripples due to the finite number of modes. N_p is set to 16 modes due to limitations of experimental equipment to generate higher order modes due to the large apertures needed for higher order LG beams. As ξ increases, the point of maximum intensity tends to get closer to the origin, whereas for lower values of ξ the mean intensity converges to that of an LG beam with indices l and $p = 0$. The next section will discuss the simulation procedures with the inclusion of atmospheric turbulence using phase screens.

Appendix E: Beam Metrics used in Chapter 5

For the simulations throughout this work the beam metrics of interest are generally simple to discuss theoretically, but to computationally find them is not as straight forward at times. Each metric in this section is quickly explained with its numerical implementation discussed. All functions are assumed to be written in terms of the Cartesian coordinates x and y to adapt to a square grid.

E.1 OAM Spectrum

Given a complex beam profile on a numerical grid $U(x_q, y_p, z)$ the OAM spectrum is most easily found by computing each inner product from equation 4.2 individually. For more explicit forms of calculating the OAM spectrum performing an azimuth integral over the grid space and taking a 1D Fourier transform [178].

The inner product from equation 4.2 is turned into two discrete sums over the entire grid space as

$$c_l(z) = \frac{1}{N_g^2} \sum_{q=1}^{N_g} \sum_{p=1}^{N_g} U(x_q, y_p y, z) \Psi_l^*(x_q, y_p, z). \tag{E.1}$$

For the analytic form of the OAM spectrum spreading used for comparison to the

simulations the equation is [175]

$$|c_{ln}|^2 = \int_0^{\infty} |U(r,z)|^2 \int_0^{2\pi} e^{i\Delta_{ln}\phi} e^{\left(-3.44\left(\frac{2w_0}{r_0}\right)^{5/3}\left|\rho\sin\left(\frac{\phi}{2}\right)\right|^{5/3}\right)} r dr d\phi, \tag{E.2}$$

where $\Delta_{ln} = l - n$ is the distance away from the central OAM mode l of the incident beam, and $\rho = 2r/w_0$ is the normalized radial coordinate.

E.2 Spot Size

The beam spot size, also called the $1/e^2$ point, can be defined as the diameter located at the centroid of the beam where 86% of the intensity falls. Using the mean value of r will generally over estimate the beam spot size due to its sensitivity at the wings of a band-limited beam profile. This is important for only comparing to analytical theory for the Gaussian beam case. To make sure this is not an issue the spot size is calculated using a 1D cross section of the 2D beam profile as all beams in this work are assumed rotationally symmetric. The 1D cross section is then set equal to the $1/e^2$ point and a zero crossing algorithm is used to find the points of intersection.

For OAM beams and comparison of their spot sizes, the RMS radius (w_{rms}) is calculated instead since a $1/e^2$ is not an obvious value for non-Gaussian beams. For the vacuum case, the RMS radius is equal to the $1/e^2$ point. The RMS radius is defined as

$$
\begin{aligned}
w_{rms}(z) &= \sqrt{2\frac{\int_{-\infty}^{\infty}\int_{-\infty}^{\infty}(x^2+y^2)I(x,y,z)dxdy}{\int_{-\infty}^{\infty}\int_{-\infty}^{\infty}I(x,y,z)dxdy}} \\
&= \sqrt{2\frac{\sum_{q=1}^{N_g}\sum_{p=1}^{N_g}\left[x_q^2+y_p)^2\right]I(x_q,y_p,z)}{\sum_{q=1}^{N_g}\sum_{p=1}^{N_g}I(x_q,y_p,z)}}
\end{aligned}
\tag{E.3}
$$

where $I(x_q,y_p,z) = |U(x_q,y_p,z)|^2$ is proportional to the beam intensity.

Within weak turbulence the analytic form of the long-term spot size used for comparison to the simulations for a collimated beam is

$$
w_{LT}(z) = w(z)\sqrt{1+T}, \tag{E.4}
$$

where T is related to the turbulence statistics by

$$
T \;=\; 4\pi^2k^2L\int_0^L\int_0^{\infty}\kappa\Phi_n(\kappa)\left(1-\exp\left(-\Lambda L\kappa^2\left(1-\frac{z}{L}\right)^2\right)\right)d\kappa dz, \tag{E.5}
$$

where $\Lambda = 2z/kw^2(z)$ is the real part of the Gaussian beam propagation parameter.

E.3 Divergence

The divergence angle for propagation far from the initial starting point is approximated as

$$
\theta^{dvg}(z) = 2\tan^{-1}\left(\frac{w_{rms}(z)-w_{rms}(0)}{z}\right), \tag{E.6}
$$

but for long propagation distances the argument of the above inverse tangent can be used. The spot size theoretically used is calculated from equation E.5.

E.4 Mutual Coherence Function

As the MCF is the autocorrelation function of the 2D matricies which can be efficiently calculated using the FFT as

$$\begin{aligned}\Gamma_2(x_1,y_1,x_2,y_2,z) =& \frac{1}{N_g^2}\sum_{q_1=1}^{N_g}\sum_{p_1=1}^{N_g}\sum_{q_2=1}^{N_g}\sum_{p_2=1}^{N_g} U(x_{q_1},y_{p_1},z)U^*(x_{q_2},y_{p_2},z) \\ =& \frac{1}{N_g^2}\mathscr{F}_2^{-1}\left[\mathscr{F}_2\{U(x_q,y_p,z)\}\mathscr{F}_2\{U^*(x_q,y_p,z)\}\right],\end{aligned} \tag{E.7}$$

and the complex degree of coherence as

$$\mu(x_1,y_1,x_2,y_2,z) = \frac{\Gamma_2(x_1,y_1,x_2,y_2,z)}{[\Gamma_2(x_1,y_1,x_1,y_1z)\Gamma_2(x_2,y_2,x_2,y_2,z)]^{1/2}}, \tag{E.8}$$

For a system containing turbulence the specific form of a Gaussian beam MCF is expressed as (see Ch. 6 Eq. 35 [50])

$$\begin{aligned}\Gamma_2(\mathbf{r}_1,\mathbf{r}_2,L) =\ & \Gamma_0(\mathbf{r}_1,\mathbf{r}_2,L)\exp\Bigg[-4\pi^2k^2L\int_0^L\int_0^\infty \kappa\Phi_n(\kappa) \\ & \times\left(1-\exp\left(-\Lambda L\kappa^2\left(1-\frac{z}{L}\right)^2\right)\right) \\ & \times J_0\left(\left|\left(1-\overline{\Theta}\frac{z}{L}\right)\mathbf{p}-2i\Lambda\frac{z}{L}\mathbf{r}\right|\kappa\right)\Bigg]d\kappa dz,\end{aligned} \tag{E.9}$$

where $\Gamma_0(\mathbf{r}_1,\mathbf{r}_2,L)$ is the Gaussian free-space MCF, $\Lambda = 2z/kw^2(z)$, $\overline{\Theta} = 1-\Theta$, $\Theta = 1-z/R(z)$ is the complex part of the Gaussian propagation parameter, and $\mathbf{p} = \mathbf{r}_1 - \mathbf{r}_2$.

This can also be done by using just the free-space MCF with the product of the spherical wave MCF [50].

E.5 Spatial Coherence Radius (SCR)

The SCR is defined as the $1/e$ point of the beam autocorrelation function. For a Gaussian beam the autocorrelation function is also of Gaussian form. Autocorrelation functions carrying OAM do not contain a Gaussian form but rather a hypergeometric nature. The $1/e$ point for a non-Gaussian function is not intuitively obvious which lends as a non-useful metric for comparing OAM and Gaussian beams.

For a Gaussian beam the SCR is calculated by taking a 1D cross section of a rotationally symmetric autocorrelation function then finding the zero crossings where the autocorrelation is equal to $1/e$ point. This is similar to finding the $1/e^2$ spot size.

E.6 On-axis Intensity

A Gaussian beam contains intensity directly on the center of the optical axis, but OAM beams have an intensity null leaving the term "on-axis" up for debate. For an OAM beam "on-axis" is defined as the center annulus along the main vortex ring. To measure the on-axis intensity of an OAM beam a circular mask is created that covers the center of the annulus of the main beam. This mask is multiplied to the intensity pattern and then summed over to find the average on-axis intensity. For beams that travel through turbulence, the on-axis intensity is found by multiplying an annular mask created from propagating the beam through vacuum the same distance. This is so that the intensity

losses by divergence are accounted for but not those by turbulence.

The long-term or mean intensity of a Gaussian beam after propagation through turbulence is found to be

$$\Gamma_2(\mathbf{r},\mathbf{r},L) = \langle I(\mathbf{r},L)\rangle = \frac{w_0^2}{w^2(z)}\exp\left(-\frac{2r^2}{w_{LT}^2(z)}\right). \tag{E.10}$$

E.7 On-axis Scintillation

The on-axis scintillation is calculated using the same masks found from finding the on-axis intensity. Before the mask is multiplied the scintillation defined as

$$\sigma_I^2(x_q,y_p,z) = \frac{\langle I^2(x_q,y_p,z)\rangle - \langle I(x_q,y_p,z)\rangle^2}{\langle I(x_q,y_p,z)\rangle^2}, \tag{E.11}$$

is calculated and then the mask is multiplied to this 2D scintillation profile and averaged over the amount of non-zero points within the mask.

Within a turbulent enviornment the scintillation can be predicted from the fourth order beam moment or the intensity autocorrelation function. If the initial beam waist is not within either limiting beam case of a plane wave or spherical wave, the scintillation across the beam profile, assuming isotropic Kolmogorov turbulence for an untracked beam centroid [50], is given by

$$\begin{aligned}\sigma_I^2(r,z) \;=\; & 3.86\,\sigma_R^2\,\Re\left(i^{5/6}\,{}_2F_1\left(\frac{-5}{6},\frac{11}{6};\frac{17}{6};\overline{\Theta}+i\Lambda\right)\right.\\ & \left.-2.64\,\sigma_R^2\,\Lambda^{5/6}\,{}_1F_1\left(\frac{-5}{6};1;2\frac{r^2}{w^2(z)}\right)\right),\end{aligned} \tag{E.12}$$

where ${}_2F_1(a,b,c,d)$ and ${}_1F_1(a,b,c)$ are confluent hypergeometric functions.

E.8 Near-Field Beam Wander

Due to turbulence perturbations the beam centroid moves about its propagation axis. If the beam centroid is tracked its average radial distance from the beam axis can be determined. Theoretically, notation from Belmonte [188], this movement is predicted as

$$\langle \beta^2 \rangle = 2.42 C_n^2 L^3 w_0^{-1/3} \ {}_2F_1\left(\frac{1}{3}, 1; 4; 1 - |\Theta_0|\right), \tag{E.13}$$

where $\Theta = 1 - z/R(z)$ is the complex part of the Gaussian propagation parameter.

Numerical calculate involves finding the standard deviation along the x and y directions from $\beta_x^2 = \langle x^2 \rangle - \langle x \rangle^2$ which are the first and second order moments of the spatial coordinates. Then the total beam wander is found as $\beta^2 = \beta_x^2 + \beta_y^2$.

Appendix F: Derivation of Equation 7.5

In Chapter 7, the beatnote photocurrent is said to be proportional to the OAM coefficients in equation 7.4. The derivation is done using the orthogonality of the OAM basis functions from the modal decomposition discussed in Section 4.1. Starting with the general form of the OAM basis functions

$$\Psi_{l,p}(r,\phi,z,t) = A_p(r,z)e^{il\phi}e^{-i2\pi ft}, \tag{F.1}$$

where p is the radial mode index, $A_p(r,z)$ is a complex amplitude distribution formed from an arbitrary radial basis set, f is the optical frequency, and the fields are normalized such that $\int_0^{2\pi}\int_0^{\infty}|\Psi_{l,p}(r,\phi,z,t)|^2\, rdrd\phi = 1$. The radial basis functions can either be Bessel, Laguerre, or hypergeometric functions as discussed in Appendix C. The basis functions, $\Psi_{l,p}(r,\phi,z,t)$, satisfy the orthogonality relationship

$$\int_0^{2\pi}\int_0^{\infty}\Psi_{l_1,p}(r,\phi,z,t)\Psi^*_{l_2,p}(r,\phi,z,t)\, rdrd\phi = D_{l_1l_2,p}(z)\delta_{l_1l_2}, \tag{F.2}$$

where l_1 and l_2 are azimuthal indices, $\delta_{l_1l_2}$ is the Kronecker delta function, and $D_{l_1l_2,p}(z)$ are non-zero functions of the propagation distance z. Starting from the DPB superposition

$(S(r,\phi,t))$, the fields can be expanded using the OAM modal decomposition

$$\begin{aligned} S(r,\phi,t) &= E_{l_1}(r,\phi,z,t) + E_{l_2}(r,\phi,z,t) \\ &= \sum_{p=0}^{\infty}\sum_{n=-\infty}^{\infty} a_{l_1+n,p}\Psi_{l_1+n,p}(r,\phi,z,t) + \sum_{q=0}^{\infty}\sum_{m=-\infty}^{\infty} b_{l_2+m,q}\Psi_{l_2+m,q}(r,\phi,z,t), \end{aligned} \tag{F.3}$$

where a_{l_1} and b_{l_2} are the OAM coefficients of beam 1 and beam 2 respectively with initial OAM modes l_1 and l_2, n and n' are OAM indices of each beam, and p and q are the radial indices. The intensity of the DPB is then proportional to

$$\begin{aligned} S(r,\phi,z,t) &= |E_{l_1}(r,\phi,z,t) + E_{l_2}(r,\phi,z,t)|^2 \\ &= |E_{l_1}(r,\phi,z)|^2 + |E_{l_2}(r,\phi,z)|^2 + E_{l_1}(r,\phi,z)E^*_{l_2}(r,\phi,z)e^{-i2\pi(f_2-f_1)} \\ &\quad + E^*_{l_1}(r,\phi,z)E_{l_2}(r,\phi,z)e^{i2\pi(f_2-f_1)} \\ &= \left|\sum_{p=0}^{\infty}\sum_{n=-\infty}^{\infty} a_{l_1+n,p}A_p(r,z)e^{i(l_1+n)\phi}\right|^2 + \left|\sum_{q=0}^{\infty}\sum_{=-\infty}^{\infty} b_{l_2+m,q}A_q(r,z)e^{i(l_2+m)\phi}\right|^2 + \\ &\sum_{p=0}^{\infty}\sum_{n=-\infty}^{\infty} a^*_{l_1+n,p}A^*_p(r,z)e^{-i(l_1+n)\phi}\sum_{q=0}^{\infty}\sum_{m=-\infty}^{\infty} b_{l_2+m,q}A_q(r,z)e^{i(l_2+m)\phi}e^{-i2\pi(f_2-f_1)} + \\ &\sum_{p=0}^{\infty}\sum_{n=-\infty}^{\infty} a_{l_1+n,p}A_p(r,z)e^{i(l_1+n)\phi}\sum_{q=0}^{\infty}\sum_{m=-\infty}^{\infty} b^*_{l_2+m,q}A^*_q(r,z)e^{-i(l_2+m)\phi}e^{i2\pi(f_2-f_1)}. \end{aligned} \tag{F.4}$$

Upon detection of the intensity in F.4, the photocurrent is $\mathscr{I} = \mathscr{R}\iint |S(r,\phi,z,t)|^2 r dr d\phi$. The DC photocurrent ($\mathscr{I}_{DC}$) is proportional to the magnitude of the field amplitudes and the AC photocurrent ($\mathscr{I}_{AC}$) is due to the wave mixing. Using equation F.4, and simplifi-

cation of the summations, the photocurrent becomes

$$\begin{aligned}
\mathscr{I}(z,t) &= \mathscr{I}_{DC}(z) + \mathscr{I}_{AC}(z,t) = \mathscr{R}\iint S_{DC}(r,\phi,z)rdrd\phi + \mathscr{R}\iint S_{AC}(r,\phi,z,t)rdrd\phi \\
S_{DC}(r,\phi,z) &= \left|\sum_{p=0}^{\infty}\sum_{n=-\infty}^{\infty} a_{l_1+n,p}A_p(r,z)\right|^2 + \left|\sum_{q=0}^{\infty}\sum_{=-\infty}^{\infty} b_{l_2+m,q}A_q(r,z)\right|^2 \\
S_{AC}(r,\phi,z,t) &= \sum_{p=0}^{\infty}\sum_{n=-\infty}^{\infty} a^*_{l_1+n,p}A^*_p(r,z)e^{-i(l_1+n)\phi}\sum_{q=0}^{\infty}\sum_{m=-\infty}^{\infty} b_{l_2+m,q}A_q(r,z)e^{i(l_2+m)\phi}e^{-i2\pi(f_2-f_1)} \\
&\quad + \sum_{p=0}^{\infty}\sum_{n=-\infty}^{\infty} a_{l_1+n,p}A_p(r,z)e^{i(l_1+n)\phi}\sum_{q=0}^{\infty}\sum_{m=-\infty}^{\infty} b^*_{l_2+m,q}A^*_q(r,z)e^{-i(l_2+m)\phi}e^{i2\pi(f_2-f_1)}.
\end{aligned} \tag{F.5}$$

Simplification of the radial amplitudes terms can be done using $\sum_{p=0}^{\infty}A_p(r,z)A^*_p(r',z) = E(z)\delta(r,r')$ and the orthogonality condition in equation F.2 resulting in the DC photocurrent

$$\begin{aligned}
\mathscr{I}_{DC}(z) &= \int_0^{\infty}\int_0^{2\pi}\left(\left|\sum_{p=0}^{\infty}\sum_{n=-\infty}^{\infty} a_{l_1+n,p}A_p(r,z)\right|^2 + \left|\sum_{q=0}^{\infty}\sum_{=-\infty}^{\infty} b_{l_2+m,q}A_q(r,z)\right|^2\right)rdrd\phi \\
&= \sum_{n=-\infty}^{\infty}|a_{l_1+n}|^2 + \sum_{m=-\infty}^{\infty}|b_{l_2+m}|^2,
\end{aligned} \tag{F.6}$$

where power is conserved as $\sum_{n=-\infty}^{\infty}|a_{l_1+n}|^2=1$. This DC component is directly proportional to the total power in the OAM spectrum. The AC photocurrent becomes

$$\begin{aligned}\mathscr{I}_{AC}(z,t) &= \int_0^{\infty}\int_0^{2\pi}\Bigg(\sum_{p,q=0}^{\infty}\sum_{n,m=-\infty}^{\infty} a^*_{l_1+n,p}b_{l_2+m,q}A_q(r,z)A^*_p(r,z)e^{i(l_2-l_1+m-n)\phi}e^{-i2\pi(f_2-f_1)} \\ &\quad + \sum_{p,q=0}^{\infty}\sum_{n,m=-\infty}^{\infty} a_{l_1+n,p}b^*_{l_2+m,q}A^*_q(r,z)A_p(r,z)e^{i(l_1-l_2+n-m)\phi}e^{i2\pi(f_2-f_1)}\Bigg) r dr d\phi \\ &= \sum_{m=-\infty}^{\infty} a^*_m b_m e^{-i2\pi\Delta f} + a_m b^*_m e^{i2\pi\Delta f},\end{aligned} \tag{F.7}$$

where the integration over the detector surface limits the summations to modes $m=n$ and $\Delta f = f_2 - f_1$. As the OAM coefficients themselves are complex the substitutions $a_m = \alpha_m e^{i\gamma_m}$ and $b_m = \beta_m e^{i\delta}$ can be made where α_m and β_m are real numbers. The AC photocurrent written in terms of the OAM coefficients (reintroduced the z dependence of the OAM coefficients) is then

$$\begin{aligned}\mathscr{I}_{AC}(z,t) &= \sum_{m=-\infty}^{\infty} \alpha_m(z)\beta_m(z)e^{-i(\gamma_m-\delta_m)}e^{-i2\pi\Delta f} + \alpha_m(z)\beta_m(z)e^{i(\gamma_m-\delta_m)}e^{i2\pi\Delta f} \\ &= 2\sum_{m=-\infty}^{\infty} \alpha_m(z)\beta_m(z)\cos(2\pi\Delta f - [\gamma_m - \delta_m]).\end{aligned} \tag{F.8}$$

This final result states that the AC photocurrent is dependent on the correlation of the OAM coefficient phase across all OAM modes of each beam in the DPB. This equation is the basis of the beatnote used in OHDOOM to detect phase distortions once the summation in equation F.8 is truncated.

Bibliography

[1] C. C. Davis, *Lasers and Electro-optics: Fundamentals and Engineering*, 2nd ed. Cambridge: Cambridge University Press, 2014.

[2] M. R. Dennis, K. O'Holleran, and M. J. Padgett, "Chapter 5 singular optics: Optical vortices and polarization singularities," in *Progress in Optics*, E. Wolf, Ed., vol. 53, Elsevier, Jan. 1, 2009.

[3] G. J. Gbur, *Singular Optics*, 1st edition. Boca Raton: CRC Press, Nov. 9, 2016, 563 pp.

[4] L. Allen, M. W. Beijersbergen, R. J. C. Spreeuw, and J. P. Woerdman, "Orbital angular momentum of light and the transformation of laguerre-gaussian laser modes," *Physical Review A*, vol. 45, no. 11, Jun. 1, 1992.

[5] J. H. Poynting, "XV. on the transfer of energy in the electromagnetic field," *Philosophical Transactions of the Royal Society of London*, vol. 175, 1884.

[6] J. H. Poynting, "The wave motion of a revolving shaft, and a suggestion as to the angular momentum in a beam of circularly polarised light," *Proceedings of the Royal Society of London. Series A, Containing Papers of a Mathematical and Physical Character*, vol. 82, no. 557, Jul. 31, 1909.

[7] R. A. Beth, "Mechanical detection and measurement of the angular momentum of light," *Physical Review*, vol. 50, no. 2, Jul. 15, 1936.

[8] C. G. Darwin, "Notes on the theory of radiation," *Proceedings of the Royal Society of London. Series A, Containing Papers of a Mathematical and Physical Character*, vol. 136, no. 829, May 2, 1932.

[9] J. M. Vaughan and D. V. Willetts, "Interference properties of a light beam having a helical wave surface," *Optics Communications*, vol. 30, no. 3, Sep. 1, 1979.

[10] V. Y. Bazhenov, M. S. Soskin, and M. V. Vasnetsov, "Screw dislocations in light wavefronts," *Journal of Modern Optics*, Mar. 1, 2007.

[11] R. Zhang, L. Li, Z. Zhao, *et al.*, "Coherent optical wireless communication link employing orbital angular momentum multiplexing in a ballistic and diffusive scattering medium," *Optics Letters*, vol. 44, no. 3, Feb. 1, 2019.

[12] R. Zhang, N. Hu, K. Zou, *et al.*, "Experimental demonstration of crosstalk reduction to achieve turbulence-resilient multiple-OAM-beam free-space optical communications using pilot tones to mix beams at the receiver," in *2020 Conference on Lasers and Electro-Optics (CLEO)*.

[13] R. Zhang, N. Hu, H. Zhou, *et al.*, "Turbulence-resilient pilot-assisted self-coherent free-space optical communications using automatic optoelectronic mixing of many modes," *Nature Photonics*, vol. 15, no. 10, Oct. 2021.

[14] Y. Ren, H. Huang, G. Xie, *et al.*, "Atmospheric turbulence effects on the performance of a free space optical link employing orbital angular momentum multiplexing," *Optics Letters*, vol. 38, no. 20, Oct. 15, 2013.

[15] A. E. Willner, H. Huang, Y. Yan, *et al.*, "Optical communications using orbital angular momentum beams," *Advances in Optics and Photonics*, vol. 7, no. 1, Mar. 31, 2015.

[16] H. He, M. E. J. Friese, N. R. Heckenberg, and H. Rubinsztein-Dunlop, "Direct observation of transfer of angular momentum to absorptive particles from a laser beam with a phase singularity," *Physical Review Letters*, vol. 75, no. 5, Jul. 31, 1995.

[17] Y. Yang, Y. Ren, M. Chen, Y. Arita, and C. Rosales-Guzmán, "Optical trapping with structured light: A review," *Advanced Photonics*, vol. 3, May 17, 2021.

[18] E. Karimi and R. W. Boyd, "Classical entanglement?" *Science*, Dec. 4, 2015.

[19] B. Ndagano, B. Perez-Garcia, F. S. Roux, *et al.*, "Characterizing quantum channels with non-separable states of classical light," *Nature Physics*, vol. 13, no. 4, Apr. 2017.

[20] B. Ndagano, I. Nape, M. A. Cox, C. Rosales-Guzman, and A. Forbes, "Creation and detection of vector vortex modes for classical and quantum communication," *Journal of Lightwave Technology*, vol. 36, no. 2, Jan. 15, 2018.

[21] A. Jantzi, W. Jemison, D. Illig, and L. Mullen, "Spatial and temporal domain filtering for underwater lidar," *JOSA A*, vol. 38, no. 10, Oct. 1, 2021.

[22] G. A. Swartzlander, "Peering into darkness with a vortex spatial filter," *Optics Letters*, vol. 26, no. 8, Apr. 15, 2001.

[23] G. A. Swartzlander and R. I. Hernandez-Aranda, "Optical rankine vortex and anomalous circulation of light," *Physical Review Letters*, vol. 99, no. 16, Oct. 19, 2007.

[24] W. Sun, Y. Hu, D. G. MacDonnell, C. Weimer, and R. R. Baize, "Technique to separate lidar signal and sunlight," *Optics Express*, vol. 24, no. 12, Jun. 13, 2016.

[25] S. Fürhapter, A. Jesacher, S. Bernet, and M. Ritsch-Marte, "Spiral phase contrast imaging in microscopy," *Optics Express*, vol. 13, no. 3, Feb. 7, 2005.

[26] B. Cochenour, L. Rodgers, A. Laux, *et al.*, "The detection of objects in a turbid underwater medium using orbital angular momentum (OAM)," in *Ocean Sensing and Monitoring IX*, vol. 10186, International Society for Optics and Photonics, May 22, 2017.

[27] A. Alley, A. Laux, L. Mullen, and B. Cochenour, "An optical vortex transmissometer," in *Ocean Sensing and Monitoring X*, vol. 10631, International Society for Optics and Photonics, May 25, 2018.

[28] C. Weimer, Y. Hu, J. T. Applegate, M. Lieber, W. Sun, and D. MacDonnell, "Lidars utilizing vortex laser beams," in *Ocean Sensing and Monitoring X*, vol. 10631, International Society for Optics and Photonics, May 25, 2018.

[29] D. J. Sanchez, D. W. Oesch, and O. R. Reynolds, "The creation of photonic orbital angular momentum by molecular clouds," in *Imaging and Applied Optics (2013), paper PTu3F.3*, Optical Society of America, Jun. 23, 2013.

[30] G. Xie, H. Song, Z. Zhao, *et al.*, "Using a complex optical orbital-angular-momentum spectrum to measure object parameters," *Optics Letters*, vol. 42, no. 21, Nov. 1, 2017.

[31] N. Cvijetic, G. Milione, E. Ip, and T. Wang, "Detecting lateral motion using light's orbital angular momentum," *Scientific Reports*, vol. 5, no. 1, Oct. 23, 2015.

[32] M. P. J. Lavery, F. C. Speirits, S. M. Barnett, and M. J. Padgett, "Detection of a spinning object using light's orbital angular momentum," *Science*, vol. 341, no. 6145, Aug. 2, 2013.

[33] M. P. J. Lavery, S. M. Barnett, F. C. Speirits, and M. J. Padgett, "Observation of the rotational doppler shift of a white-light, orbital-angular-momentum-carrying beam backscattered from a rotating body," *Optica*, vol. 1, no. 1, Jul. 22, 2014.

[34] D. J. Sanchez and D. W. Oesch, "Orbital angular momentum in optical waves propagating through distributed turbulence," *Optics Express*, vol. 19, no. 24, Nov. 21, 2011.

[35] D. J. Sanchez and D. W. Oesch, "Localization of angular momentum in optical waves propagating through turbulence," *Optics Express*, vol. 19, no. 25, Dec. 5, 2011.

[36] D. J. Sanchez and D. W. Oesch, "Hiding the phase: The filling of the slope discrepancy hilbert space," in *Unconventional Imaging and Wavefront Sensing 2012*, vol. 8520, International Society for Optics and Photonics, Oct. 15, 2012.

[37] G. Gbur and R. K. Tyson, "Vortex beam propagation through atmospheric turbulence and topological charge conservation," *Journal of the Optical Society of America A*, vol. 25, no. 1, Jan. 1, 2008.

[38] A. Dipankar, R. Marchiano, and P. Sagaut, "Trajectory of an optical vortex in atmospheric turbulence," *Physical Review E*, vol. 80, no. 4, Oct. 28, 2009.

[39] Y. Gu, "Statistics of optical vortex wander on propagation through atmospheric turbulence," *Journal of the Optical Society of America A*, vol. 30, no. 4, Apr. 1, 2013.

[40] S. Qiu, T. Liu, Y. Ren, *et al.*, "Detection of spinning objects at oblique light incidence using the optical rotational doppler effect," *Optics Express*, vol. 27, no. 17, Aug. 19, 2019.

[41] W. Zhang, J. Gao, D. Zhang, *et al.*, "Free-space remote sensing of rotation at the photon-counting level," *Physical Review Applied*, vol. 10, no. 4, Oct. 4, 2018.

[42] H. Zhou, D. Fu, J. Dong, P. Zhang, and X. Zhang, "Theoretical analysis and experimental verification on optical rotational doppler effect," *Optics Express*, vol. 24, no. 9, May 2, 2016.

[43] H.-L. Zhou, D.-Z. Fu, J.-J. Dong, *et al.*, "Orbital angular momentum complex spectrum analyzer for vortex light based on the rotational doppler effect," *Light: Science & Applications*, vol. 6, no. 4, Apr. 2017.

[44] S. Qiu, T. Liu, Z. Li, *et al.*, "Influence of lateral misalignment on the optical rotational doppler effect," *Applied Optics*, vol. 58, no. 10, Apr. 1, 2019.

[45] Z. Zhang, L. Cen, J. Zhang, J. Hu, F. Wang, and Y. Zhao, "Rotation velocity detection with orbital angular momentum light spot completely deviated out of the rotation center," *Optics Express*, vol. 28, no. 5, Mar. 2, 2020.

[46] A. Ryabtsev, S. Pouya, A. Safaripour, M. Koochesfahani, and M. Dantus, "Fluid flow vorticity measurement using laser beams with orbital angular momentum," *Optics Express*, vol. 24, no. 11, May 30, 2016.

[47] X. Su, N. Hu, A. Minoofar, *et al.*, "Modal purity and LG coupling of an OAM beam reflected by a rough surface for NLoS THz links," in *2021 IEEE International Conference on Communications Workshops (ICC Workshops)*, Jun. 2021.

[48] A. Jantzi, W. Jemison, A. Laux, L. Mullen, and B. Cochenour, "Enhanced underwater ranging using an optical vortex," *Optics Express*, vol. 26, no. 3, Feb. 5, 2018.

[49] A. Jantzi, W. Jemison, D. Illig, and L. Mullen, "Axicons for improved lidar performance," in *Ocean Sensing and Monitoring XII*, vol. 11420, International Society for Optics and Photonics, Apr. 22, 2020.

[50] Larry C. Andrews and Ronald L. Phillips, *Laser Beam Propagation through Random Media*, 2nd ed. Bellingham, Washington: SPIE, 2005.

[51] R. F. Lutomirski and H. T. Yura, "Wave structure function and mutual coherence function of an optical wave in a turbulent atmosphere," *JOSA*, vol. 61, no. 4, Apr. 1, 1971.

[52] J. A. Ogilvy, *Theory of Wave Scattering From Random Rough Surfaces,* 1st edition. Bristol, England ; Philadelphia: CRC Press, Jan. 1, 1991, 292 pp.

[53] C. D. Mobley, *Light and water : Radiative Transfer in Natural Waters*. Academic Press, 1994, 592 pp.

[54] Van De Hulst, H.C., *Absorption and Scattering of Light by Small Particles*. New York: Dover Publications, 1957.

[55] D. R. Bohren C.F.; Huffman, *Absorption and Scattering of Light by Small Particles*. New York: John Wiley & Sons, 1983.

[56] H. Kaushal, V. K. Jain, and S. Kar, "FSO system modules and design issues," in *Free Space Optical Communication*, ser. Optical Networks, H. Kaushal, V. Jain, and S. Kar, Eds., New Delhi: Springer India, 2017.

[57] L. S. Dolin and V. A. Savel'ev, "Theory of the propagation of a narrow light beam in a stratified scattering medium," *Radiophysics and Quantum Electronics*, vol. 22, no. 11, Nov. 1, 1979.

[58] E. P. Zege, A. P. Ivanov, and I. L. Katsev, *Image Transfer Through a Scattering Medium*, 1st ed. Berlin, Heidelberg: Springer-Verlag, 1991, 346 pp.

[59] J. D. Rogers, A. J. Radosevich, J. Yi, and V. Backman, "Modeling light scattering in tissue as continuous random media using a versatile refractive index correlation function," *IEEE Journal of Selected Topics in Quantum Electronics*, vol. 20, no. 2, Mar. 2014.

[60] Nathaniel A. Ferlic, "Forward scattering meter for visibility measurements," Masters, University of Maryland, College Park, 2019, 160 pp.

[61] R. F. Lutomirski, "Atmospheric degradation of electrooptical system performance," *Applied Optics*, vol. 17, no. 24, Dec. 15, 1978.

[62] B. M. Cochenour, "Experimental measurements of temporal dispersion for underwater laser communications and imaging," Ph.D. dissertation, Jan. 1, 2013.

[63] T. J. Petzold, "Volume scattering functions for selected ocean waters," Oct. 1, 1972.

[64] G. C. Mooradian, M. Geller, L. B. Stotts, D. H. Stephens, and R. A. Krautwald, "Blue-green pulsed propagation through fog," *Applied Optics*, vol. 18, no. 4, Feb. 15, 1979.

[65] H. T. Yura and S. G. Hanson, "Effects of receiver optics contamination on the performance of laser velocimeter systems," *JOSA A*, vol. 13, no. 9, Sep. 1, 1996.

[66] M. Xu, "Scattering-phase theorem: Anomalous diffraction by forward-peaked scattering media," *Optics Express*, vol. 19, no. 22, Oct. 24, 2011.

[67] I. G. Yakushkin, "Intensity fluctuations during small-angle scattering of wave fields (review)," 1985.

[68] Joseph W. Goodman, *Statistical Optics*, 1st ed. New York: Wiley, Aug. 14, 2000, 550 pp.

[69] A. Kolmogorov, "The local structure of turbulence in incompressible viscous fluid for very large reynolds' numbers," *Akademiia Nauk SSSR Doklady*, vol. 30, Jan. 1, 1941.

[70] R. J. Hill and S. F. Clifford, "Modified spectrum of atmospheric temperature fluctuations and its application to optical propagation," *JOSA*, vol. 68, no. 7, Jul. 1, 1978.

[71] V. I. Tatarski, *Wave Propagation in a Turbulent Medium*, Reissue edition, trans. by R. A. Silverman. Mineola, New York: Dover Publications, Dec. 14, 2016, 304 pp.

[72] A. Ishimaru, *Wave Propagation and Scattering in Random Media*, 2 vols. Piscataway, New Jersey: IEEE Press, 1978.

[73] Z. Wang, H. Ding, and G. Popescu, "Scattering-phase theorem," *Optics Letters*, vol. 36, no. 7, Apr. 1, 2011.

[74] R. F. Lutomirski and H. T. Yura, "Propagation of a finite optical beam in an inhomogeneous medium," *Applied Optics*, vol. 10, no. 7, Jul. 1, 1971.

[75] R. F. Lutomirski and H. T. Yura, "Modulation-transfer function and phase-structure function of an optical wave in a turbulent medium," *JOSA*, vol. 59, no. 8, Aug. 1, 1969.

[76] S. Chandrasekhar, *Radiative Transfer*. New York: Dover Publications, Jan. 1, 1960, 416 pp.

[77] D. Arnush, "Underwater light-beam propagation in the small-angle-scattering approximation," *JOSA*, vol. 62, no. 9, Sep. 1, 1972.

[78] L. S. Dolin, "Propagation of a narrow beam of light in a medium with strongly anisotropic scattering," *Soviet Radiophysics*, vol. 9, no. 1, Jan. 1, 1966.

[79] A. Zardecki, S. A. W. Gerstl, and J. F. Embury, "Multiple scattering effects in spatial frequency filtering," *Applied Optics*, vol. 23, no. 22, Nov. 15, 1984.

[80] R. L. Fante, "Mutual coherence function and frequency spectrum of a laser beam propagating through atmospheric turbulence," *Journal of the Optical Society of America*, vol. 64, no. 5, May 1, 1974.

[81] A. Ishimaru, "Correlation functions of a wave in a random distribution of stationary and moving scatterers," *Radio Science*, vol. 10, no. 1, Jan. 1975.

[82] R. L. Fante and J. L. Poirier, "Mutual coherence function of a finite optical beam in a turbulent medium," *Applied Optics*, vol. 12, no. 10, Oct. 1, 1973.

[83] V. I. Tatarskii, *The Effects of the Turbulent Atmosphere on Wave Propagation*. Springfield, VA: Jerusalem: Israel Program for Scientific Translations, 1971.

[84] H. T. Yura, "Mutual coherence function of a finite cross section optical beam propagating in a turbulent medium," *Applied Optics*, vol. 11, no. 6, Jun. 1, 1972.

[85] H. T. Yura and S. G. Hanson, "Second-order statistics for wave propagation through complex optical systems," *JOSA A*, vol. 6, no. 4, Apr. 1, 1989.

[86] H. T. Yura, "Propagation of finite cross-section laser beams in sea water," *Applied Optics*, vol. 12, no. 1, Jan. 1, 1973.

[87] H. T. Yura, "Optical propagation through a turbulent medium," *JOSA*, vol. 59, no. 1, Jan. 1, 1969.

[88] J. D. Schmidt, *Numerical Simulation of Optical Wave Propagation with Examples in MATLAB*. 1000 20th Street, Bellingham, WA 98227-0010 USA: SPIE, Jul. 12, 2010.

[89] J. A. Fleck, J. R. Morris, and M. D. Feit, "Time-dependent propagation of high energy laser beams through the atmosphere," *Applied physics*, vol. 10, no. 2, Jun. 1, 1976.

[90] J. A. Fleck, J. R. Morris, and M. D. Feit, "Time-dependent propagation of high-energy laser beams through the atmosphere: II," *Applied physics*, vol. 14, no. 1, Sep. 1, 1977.

[91] J.W. Goodman, *Introduction to Fourier Opticis*, 4th ed. New York: W.H. Freeman, May 1, 2017, 554 pp.

[92] Leonard Mandel and Emil Wolf, *Optical Coherence and Quantum Optics*. New York: Cambridge University Press, 1995, 1166 pp.

[93] D. L. Fried, "Optical resolution through a randomly inhomogeneous medium for very long and very short exposures," *JOSA*, vol. 56, no. 10, Oct. 1, 1966.

[94] D. Fried, "Optical heterodyne detection of an atmospherically distorted signal wave front," *Proceedings of the IEEE*, vol. 55, no. 1, Jan. 1967.

[95] R. J. Noll, "Zernike polynomials and atmospheric turbulence*," *JOSA*, vol. 66, no. 3, Mar. 1, 1976.

[96] D. A. d. Wolf, "Coherence of a light beam through an optically dense turbid layer," *Applied Optics*, vol. 17, no. 8, Apr. 15, 1978.

[97] A. Ishimaru, "Limitation on image resolution imposed by a random medium," *Applied Optics*, vol. 17, no. 3, Feb. 1, 1978.

[98] W. H. Wells, "Loss of resolution in water as a result of multiple small-angle scattering," *JOSA*, vol. 59, no. 6, Jun. 1, 1969.

[99] B. Cochenour, L. Mullen, and J. Muth, "A modulated pulse laser for underwater detection, ranging, imaging, and communications," in *Ocean Sensing and Monitoring IV*, vol. 8372, International Society for Optics and Photonics, Jun. 11, 2012.

[100] P. E. Andersen, L. Thrane, H. T. Yura, A. Tycho, and T. M. Jørgensen, "Optical coherence tomography: Advanced modeling," in *Handbook of Coherent Domain Optical Methods: Biomedical Diagnostics, Environmental and Material Science*, V. V. Tuchin, Ed., New York, NY: Springer US, 2004.

[101] L. R. Bissonnette, "Imaging through fog and rain," *Optical Engineering*, vol. 31, no. 5, May 1992.

[102] B. Ben-Dor, P. Bruscaglioni, A. D. Devir, P. Donelli, and A. Ismaelli, "Cloud, fog, and aerosol effect on the MTF of optical systems," in *Optics in Atmospheric Propagation and Adaptive Systems*, vol. 2580, SPIE, Dec. 15, 1995.

[103] B. Ben-Dor, A. D. Devir, and G. Shaviv, "Atmospheric scattering effect on spatial resolution of imaging systems: Experimental," in *10th Meeting on Optical Engineering in Israel*, vol. 3110, SPIE, Sep. 22, 1997.

[104] M. E. Hanafy, M. C. Roggemann, and D. O. Guney, "Detailed effects of scattering and absorption by haze and aerosols in the atmosphere on the average point spread function of an imaging system," *Journal of the Optical Society of America. A, Optics, Image Science, and Vision*, vol. 31, no. 6, Jun. 1, 2014.

[105] Y. Kuga and A. Ishimaru, "Modulation transfer function and image transmission through randomly distributed spherical particles," *Journal of the Optical Society of America A*, vol. 2, no. 12, Dec. 1, 1985.

[106] I. Dror, A. Sandrov, and N. S. Kopeika, "Experimental investigation of the influence of the relative position of the scattering layer on image quality: The shower curtain effect," *Applied Optics*, vol. 37, no. 27, Sep. 20, 1998.

[107] L. Thrane, H. T. Yura, and P. E. Andersen, "Analysis of optical coherence tomography systems based on the extended huygens–fresnel principle," *JOSA A*, vol. 17, no. 3, Mar. 1, 2000.

[108] D. Sadot and N. S. Kopeika, "Effects of practical aerosol forward scatter of infrared and visible light on atmospheric coherence diameter," *Optical Engineering*, vol. 34, no. 1, Jan. 1995.

[109] B. B. Dor, A. D. Devir, G. Shaviv, P. Bruscaglioni, P. Donelli, and A. Ismaelli, "Atmospheric scattering effect on spatial resolution of imaging systems," *JOSA A*, vol. 14, no. 6, Jun. 1, 1997.

[110] K. K. Benke and B. H. McKellar, "Modulation transfer function of photographic emulsion: The small-angle approximation in radiative transfer theory," *Applied Optics*, vol. 29, no. 1, Jan. 1, 1990.

[111] P. Donelli, P. Bruscaglioni, A. Ismaelli, and G. Zaccanti, "Experimental validation of a monte carlo procedure for the evaluation of the effect of a turbid medium on the point spread function of an optical system," *Journal of Modern Optics*, vol. 38, no. 11, Nov. 1, 1991.

[112] D. Sadot and N. S. Kopeika, "Imaging through the atmosphere: Practical instrumentation-based theory and verification of aerosol modulation transfer function," *JOSA A*, vol. 10, no. 1, Jan. 1, 1993.

[113] I. Dror and N. S. Kopeika, "Experimental comparison of turbulence modulation transfer function and aerosol modulation transfer function through the open atmosphere," *JOSA A*, vol. 12, no. 5, May 1, 1995.

[114] H. T. Yura, L. Thrane, and P. E. Andersen, "Closed-form solution for the wigner phase-space distribution function for diffuse reflection and small-angle scattering in a random medium," *JOSA A*, vol. 17, no. 12, Dec. 1, 2000.

[115] Y. Feng, R. K. Wang, and J. B. Elder, "Theoretical model of optical coherence tomography for system optimization and characterization," *JOSA A*, vol. 20, no. 9, Sep. 1, 2003.

[116] B. Rose, H. Imam, S. G. Hanson, and H. T. Yura, "Effects of target structure on the performance of laser time-of-flight velocimeter systems," *Applied Optics*, vol. 36, no. 2, Jan. 10, 1997.

[117] M. Nairat and D. Voelz, "Approach for incorporating aerosol scattering in wave optics propagation simulation," in *2013 IEEE Aerospace Conference*, Mar. 2013.

[118] M. Nairat and D. Voelz, "Propagation of rotational field correlation through atmospheric turbulence," *Optics Letters*, vol. 39, no. 7, Apr. 1, 2014.

[119] A. Jantzi, W. Jemison, and L. Mullen, "Determining the spatial phase distribution of light scattered by turbid water," in *Ocean Sensing and Monitoring XIII*, vol. 11752, SPIE, Apr. 12, 2021.

[120] L. G. Henyey and J. L. Greenstein, "Diffuse radiation in the galaxy.," *The Astrophysical Journal*, vol. 93, Jan. 1, 1941.

[121] J. P. Bos, M. C. Roggemann, and V. S. R. Gudimetla, "Anisotropic non-kolmogorov turbulence phase screens with variable orientation," *Applied Optics*, vol. 54, no. 8, Mar. 10, 2015.

[122] C. Tamm and C. O. Weiss, "Bistability and optical switching of spatial patterns in a laser," *JOSA B*, vol. 7, no. 6, Jun. 1, 1990.

[123] M.W. Beijersbergen, R.P.C Coerwinkel, M. Kristensen, and J.P. Woerdman, "Helical-wavefront laser beams produced with a spiral phaseplate," *Optics Communcations*, vol. 112, 1994.

[124] Bazhenov, V. Yu., Soskin, Marat S.S, and Vasnetsov, M.V; "Screw dislocations in light wavefronts," *Journal of Modern Optics*, vol. 39, no. 5, 1992.

[125] E. Karimi, B. Piccirillo, E. Nagali, L. Marrucci, and E. Santamato, "Efficient generation and sorting of orbital angular momentum eigenmodes of light by thermally tuned q-plates," *Applied Physics Letters*, vol. 94, no. 23, Jun. 8, 2009.

[126] J. C. Maxwell, "VIII. a dynamical theory of the electromagnetic field," *Philosophical Transactions of the Royal Society of London*, vol. 155, Jan. 1, 1865.

[127] M. Charnotskii, "Transverse linear and orbital angular momenta of beam waves and propagation in random media," *Journal of Optics*, vol. 20, no. 2, Dec. 2017.

[128] V. V. Kotlyar and A. A. Kovalev, "Family of hypergeometric laser beams," *JOSA A*, vol. 25, no. 1, Jan. 1, 2008.

[129] J. Durnin, J. J. Miceli, and J. H. Eberly, "Diffraction-free beams," *Physical Review Letters*, vol. 58, no. 15, Apr. 13, 1987.

[130] T. Doster and A. T. Watnik, "Laguerre–gauss and bessel–gauss beams propagation through turbulence: Analysis of channel efficiency," *Applied Optics*, vol. 55, no. 36, Dec. 20, 2016.

[131] J. C. Gutiérrez-Vega, M. D. Iturbe-Castillo, and S. Chávez-Cerda, "Alternative formulation for invariant optical fields: Mathieu beams," *Optics Letters*, vol. 25, no. 20, Oct. 15, 2000.

[132] N. R. Heckenberg, R. McDuff, C. P. Smith, and A. G. White, "Generation of optical phase singularities by computer-generated holograms," *Optics Letters*, vol. 17, no. 3, Feb. 1, 1992.

[133] N. Matsumoto, T. Ando, T. Inoue, Y. Ohtake, N. Fukuchi, and T. Hara, "Generation of high-quality higher-order laguerre-gaussian beams using liquid-crystal-on-silicon spatial light modulators," *JOSA A*, vol. 25, no. 7, Jul. 1, 2008.

[134] S. Scholes, R. Kara, J. Pinnell, V. Rodríguez-Fajardo, and A. Forbes, "Structured light with digital micromirror devices: A guide to best practice," *Optical Engineering*, vol. 59, no. 4, Nov. 2019.

[135] V. Arrizón, G. Méndez, and D. Sánchez-de-La-Llave, "Accurate encoding of arbitrary complex fields with amplitude-only liquid crystal spatial light modulators," *Optics Express*, vol. 13, no. 20, Oct. 3, 2005.

[136] V. Arrizón, U. Ruiz, R. Carrada, and L. A. González, "Pixelated phase computer holograms for the accurate encoding of scalar complex fields," *JOSA A*, vol. 24, no. 11, Nov. 1, 2007.

[137] C. Zhao, F. Wang, Y. Dong, Y. Han, and Y. Cai, "Effect of spatial coherence on determining the topological charge of a vortex beam," *Applied Physics Letters*, vol. 101, no. 26, Dec. 24, 2012.

[138] S. A. Ponomarenko, "A class of partially coherent beams carrying optical vortices," *Journal of the Optical Society of America A*, vol. 18, no. 1, Jan. 1, 2001.

[139] X. Chen, J. Li, S. M. H. Rafsanjani, and O. Korotkova, "Synthesis of im-bessel correlated beams via coherent modes," *Optics Letters*, vol. 43, no. 15, Aug. 1, 2018.

[140] J. Li, X. Chen, S. McDuffie, M. A. M. Najjar, S. M. H. Rafsanjani, and O. Korotkova, "Mitigation of atmospheric turbulence with random light carrying OAM," *Optics Communications*, vol. 446, Sep. 1, 2019.

[141] M. Padgett, J. Arlt, N. Simpson, and L. Allen, "An experiment to observe the intensity and phase structure of laguerre–gaussian laser modes," *American Journal of Physics*, vol. 64, no. 1, Jan. 1, 1996.

[142] C.-S. Guo, S.-J. Yue, and G.-X. Wei, "Measuring the orbital angular momentum of optical vortices using a multipinhole plate," *Applied Physics Letters*, vol. 94, no. 23, Jun. 8, 2009.

[143] J. M. Hickmann, E. J. S. Fonseca, W. C. Soares, and S. Chávez-Cerda, "Unveiling a truncated optical lattice associated with a triangular aperture using light's orbital angular momentum," *Physical Review Letters*, vol. 105, no. 5, Jul. 29, 2010.

[144] J. Leach, M. J. Padgett, S. M. Barnett, S. Franke-Arnold, and J. Courtial, "Measuring the orbital angular momentum of a single photon," *Physical Review Letters*, vol. 88, no. 25, Jun. 5, 2002.

[145] J. Leach, J. Courtial, K. Skeldon, S. M. Barnett, S. Franke-Arnold, and M. J. Padgett, "Interferometric methods to measure orbital and spin, or the total angular momentum of a single photon," *Physical Review Letters*, vol. 92, no. 1, Jan. 5, 2004.

[146] T. Kaiser, D. Flamm, S. Schröter, and M. Duparré, "Complete modal decomposition for optical fibers using CGH-based correlation filters," *Optics Express*, vol. 17, no. 11, May 25, 2009.

[147] J. Pinnell, I. Nape, B. Sephton, M. A. Cox, V. Rodríguez-Fajardo, and A. Forbes, "Modal analysis of structured light with spatial light modulators: A practical tutorial," *JOSA A*, vol. 37, no. 11, Nov. 1, 2020.

[148] J. Pinnell, V. Rodríguez-Fajardo, and A. Forbes, "Quantitative orbital angular momentum measurement of perfect vortex beams," *Optics Letters*, vol. 44, no. 11, Jun. 1, 2019.

[149] C. Schulze, A. Dudley, D. Flamm, M. Duparré, and A. Forbes, "Measurement of the orbital angular momentum density of light by modal decomposition," *New Journal of Physics*, vol. 15, no. 7, Jul. 10, 2013.

[150] D. Flamm, D. Naidoo, C. Schulze, A. Forbes, and M. Duparré, "Mode analysis with a spatial light modulator as a correlation filter," *Optics Letters*, vol. 37, no. 13, Jul. 1, 2012.

[151] J. Du, R. Zhang, Z. Zhao, *et al.*, "Single-pixel identification of 2-dimensional objects by using complex laguerre–gaussian spectrum containing both azimuthal and radial modal indices," *Optics Communications*, vol. 481, Feb. 15, 2021.

[152] S. Zhao, S. Chen, X. Wang, *et al.*, "Measuring the complex spectrum of orbital angular momentum and radial index with a single-pixel detector," *Optics Letters*, vol. 45, no. 21, Nov. 1, 2020.

[153] G. Gibson, J. Courtial, M. J. Padgett, *et al.*, "Free-space information transfer using light beams carrying orbital angular momentum," *Optics Express*, vol. 12, no. 22, Nov. 1, 2004.

[154] Martin P. J. Lavery, David Roberston, Mehul Malik, *et al.*, "The efficient sorting of light's orbital angular momentum for optical communications," presented at the Proc.SPIE, vol. 8542, Nov. 19, 2012.

[155] G. Kulkarni, R. Sahu, O. S. Magaña-Loaiza, R. W. Boyd, and A. K. Jha, "Single-shot measurement of the orbital-angular-momentum spectrum of light," *Nature Communications*, vol. 8, no. 1, Oct. 20, 2017.

[156] M. P. J. Lavery, D. J. Robertson, A. Sponselli, *et al.*, "Efficient measurement of an optical orbital-angular-momentum spectrum comprising more than 50 states," *New Journal of Physics*, vol. 15, no. 1, Jan. 2013.

[157] G. C. G. Berkhout, M. P. J. Lavery, J. Courtial, M. W. Beijersbergen, and M. J. Padgett, "Efficient sorting of orbital angular momentum states of light," *Physical Review Letters*, vol. 105, no. 15, Oct. 4, 2010.

[158] G. C. G. Berkhout, M. P. J. Lavery, M. J. Padgett, and M. W. Beijersbergen, "Measuring orbital angular momentum superpositions of light by mode transformation," *Optics Letters*, vol. 36, no. 10, May 15, 2011.

[159] M. P. J. Lavery, G. C. G. Berkhout, J. Courtial, and M. J. Padgett, "Measurement of the light orbital angular momentum spectrum using an optical geometric transformation," *Journal of Optics*, vol. 13, no. 6, Apr. 2011.

[160] B. Rodenburg, M. P. J. Lavery, M. Malik, *et al.*, "Influence of atmospheric turbulence on states of light carrying orbital angular momentum," *Optics Letters*, vol. 37, no. 17, Sep. 1, 2012.

[161] M. P. J. Lavery, D. J. Robertson, G. C. G. Berkhout, G. D. Love, M. J. Padgett, and J. Courtial, "Refractive elements for the measurement of the orbital angular momentum of a single photon," *Optics Express*, vol. 20, no. 3, Jan. 30, 2012.

[162] W. Li, K. S. Morgan, Y. Li, *et al.*, "Rapidly tunable orbital angular momentum (OAM) system for higher order bessel beams integrated in time (HOBBIT)," *Optics Express*, vol. 27, no. 4, Feb. 18, 2019.

[163] A. Jha, G. S. Agarwal, and R. Boyd, "Partial angular coherence and the angular schmidt spectrum of entangled two-photon fields," *Phys. Rev. A*, vol. 84, Dec. 27, 2011.

[164] J. E. Cisternas, J. I. Espinoza, and J. A. Anguita, "Machine learning identification of multiple-state OAM superpositions detected with spatial mode sensors," in *Laser Communication and Propagation through the Atmosphere and Oceans X*, vol. 11834, SPIE, Aug. 1, 2021.

[165] S. Wei, S. K. Earl, X.-C. Yuan, S. S. Kou, and J. Lin, "Active sorting of orbital angular momentum states of light with cascaded tunable resonators," *arXiv:1704.01703 [physics]*, Apr. 6, 2017.

[166] N. K. Fontaine, R. Ryf, H. Chen, D. T. Neilson, K. Kim, and J. Carpenter, "Laguerre-gaussian mode sorter," *Nature Communications*, vol. 10, no. 1, Apr. 26, 2019.

[167] P. Bierdz, M. Kwon, C. Roncaioli, and H. Deng, "High fidelity detection of the orbital angular momentum of light by time mapping," *New Journal of Physics*, vol. 15, no. 11, Nov. 2013.

[168] M. Krenn, R. Fickler, M. Fink, *et al.*, "Communication with spatially modulated light through turbulent air across vienna," *New Journal of Physics*, vol. 16, no. 11, Nov. 11, 2014.

[169] O. A Schmidt, C. Schulze, D. Flamm, *et al.*, "Real-time determination of laser beam quality by modal decomposition," *Optics express*, vol. 19, Mar. 1, 2011.

[170] A. A. Kovalev, V. V. Kotlyar, A. P. Porfirev, and D. S. Kalinkina, "Measuring the orbital angular momentum of light beams by using a single intensity distribution," *Journal of Physics: Conference Series*, vol. 1400, Nov. 2019.

[171] J. Delpiano, G. L. Funes, J. E. Cisternas, S. Galaz, and J. A. Anguita, "Deep learning for image-based classification of OAM modes in laser beams propagating through convective turbulence," in *Laser Communication and Propagation through the Atmosphere and Oceans VIII*, vol. 11133, SPIE, Sep. 6, 2019.

[172] H. Laabs, B. Eppich, and H. Weber, "Modal decomposition of partially coherent beams using the ambiguity function," *JOSA A*, vol. 19, no. 3, Mar. 1, 2002.

[173] S. Sharifi, Y. M. Banadaki, G. Veronis, and J. P. Dowling, "Towards classification of experimental laguerre–gaussian modes using convolutional neural networks," *Optical Engineering*, vol. 59, no. 7, Jul. 2020.

[174] A. Volyar, M. Bretsko, Y. Akimova, and Y. Egorov, "Measurement of the vortex and orbital angular momentum spectra with a single cylindrical lens," *Applied Optics*, vol. 58, no. 21, Jul. 20, 2019.

[175] C. Paterson, "Atmospheric turbulence and orbital angular momentum of single photons for optical communication," *Physical Review Letters*, vol. 94, no. 15, Apr. 18, 2005.

[176] A. Klug, I. Nape, and A. Forbes, "The orbital angular momentum of a turbulent atmosphere and its impact on propagating structured light fields," *New Journal of Physics*, 2021.

[177] S. Franke-Arnold, S. M. Barnett, E. Yao, J. Leach, J. Courtial, and M. Padgett, "Uncertainty principle for angular position and angular momentum," *New Journal of Physics*, vol. 6, Aug. 2004.

[178] N. A. Ferlic, C. O'Donnell, M. v. Iersel, and C. C. Davis, "The azimuthal spectrum of common transmittance functions and random media," in *Laser Communication and Propagation through the Atmosphere and Oceans X*, vol. 11834, SPIE, Aug. 4, 2021.

[179] K. Dai, J. K. Miller, and E. G. Johnson, "Real-time OAM cross-correlator based on a single-pixel detector HOBBIT system," *Optics Express*, vol. 28, no. 26, Dec. 21, 2020.

[180] G. A. Tyler and R. W. Boyd, "Influence of atmospheric turbulence on the propagation of quantum states of light carrying orbital angular momentum," *Optics Letters*, vol. 34, no. 2, Jan. 15, 2009.

[181] Y. Zhu, L. Zhang, Z. Hu, and Y. Zhang, "Effects of non-kolmogorov turbulence on the spiral spectrum of hypergeometric-gaussian laser beams," *Optics Express*, vol. 23, no. 7, Apr. 6, 2015.

[182] J. Zeng, X. Liu, C. Zhao, *et al.*, "Spiral spectrum of a laguerre-gaussian beam propagating in anisotropic non-kolmogorov turbulent atmosphere along horizontal path," *Optics Express*, vol. 27, no. 18, Sep. 2, 2019.

[183] N. A. Ferlic, M. v. Iersel, and C. C. Davis, "Simulation of im-bessel beam propagation through time-correlated atmospheric turbulence," in *Laser Communication and Propagation through the Atmosphere and Oceans X*, vol. 11834, SPIE, Aug. 4, 2021.

[184] M. J. Padgett, F. M. Miatto, M. P. J. Lavery, A. Zeilinger, and R. W. Boyd, "Divergence of an orbital-angular-momentum-carrying beam upon propagation," *New Journal of Physics*, vol. 17, no. 2, Feb. 2015.

[185] S. Viola, Z. Chen, A. M. Yao, *et al.*, "Degradation of light carrying orbital angular momentum by ballistic scattering," *Physical Review Research*, vol. 2, Jul. 17, 2020.

[186] N. A. Ferlic, M. v. Iersel, and C. C. Davis, "Weak turbulence effects on different beams carrying orbital angular momentum," *JOSA A*, vol. 38, no. 10, Oct. 1, 2021.

[187] E. Wijerathna, D. Voelz, A. Muschinski, and H. Zhan, "Spherical wave scintillation in atmospheric turbulence: A comparison of analytical models and simulation results," in *Imaging and Applied Optics 2019 (COSI, IS, MATH, pcAOP)*, Munich: OSA, 2019.

[188] A. Belmonte, "Feasibility study for the simulation of beam propagation: Consideration of coherent lidar performance," *Applied Optics*, vol. 39, no. 30, Oct. 20, 2000.

[189] H. Zhan, E. Wijerathna, and D. Voelz, "Is the formulation of the fried parameter accurate in the strong turbulent scattering regime?" *OSA Continuum*, vol. 3, no. 9, Sep. 15, 2020.

[190] J. A. Anguita, M. A. Neifeld, and B. V. Vasic, "Turbulence-induced channel crosstalk in an orbital angular momentum-multiplexed free-space optical link," *Applied Optics*, vol. 47, no. 13, May 1, 2008.

[191] W. Cheng, J. W. Haus, and Q. Zhan, "Propagation of vector vortex beams through a turbulent atmosphere," *Optics Express*, vol. 17, no. 20, Sep. 28, 2009.

[192] A. Saito, A. Tanabe, M. Kurihara, N. Hashimoto, and K. Ogawa, "Propagation properties of quantized laguerre-gaussian beams in atmospheric turbulence," in *Free-Space Laser Communication and Atmospheric Propagation XXVIII*, vol. 9739, International Society for Optics and Photonics, Mar. 15, 2016.

[193] N. A. Ferlic, M. v. Iersel, D. A. Paulson, and C. C. Davis, "Propagation of laguerre-gaussian and im-bessel beams through atmospheric turbulence: A computational study," in *Laser Communication and Propagation through the Atmosphere and Oceans IX*, vol. 11506, International Society for Optics and Photonics, Aug. 22, 2020.

[194] T. J. Schulz, "Optimal beams for propagation through random media," *Optics Letters*, vol. 30, no. 10, May 15, 2005.

[195] J. C. Ricklin and F. M. Davidson, "Atmospheric turbulence effects on a partially coherent gaussian beam: Implications for free-space laser communication," *JOSA A*, vol. 19, no. 9, Sep. 1, 2002.

[196] G. Gbur and E. Wolf, "Spreading of partially coherent beams in random media," *JOSA A*, vol. 19, no. 8, Aug. 1, 2002.

[197] D. M. Palacios, I. D. Maleev, A. S. Marathay, and G. A. Swartzlander, "Spatial correlation singularity of a vortex field," *Physical Review Letters*, vol. 92, no. 14, Apr. 9, 2004.

[198] G. Funes and J. Anguita, "On the cancellation of OAM beams propagating through convective turbulence," *Optics Letters*, vol. 42, no. 9, May 1, 2017.

[199] W. Sun, Y. Hu, C. Weimer, K. Ayers, R. R. Baize, and T. Lee, "A FDTD solution of scattering of laser beam with orbital angular momentum by dielectric particles: Far-field characteristics," *Journal of Quantitative Spectroscopy and Radiative Transfer*, vol. 188, Feb. 2017.

[200] W. Sun, Y. Hu, C. Weimer, *et al.*, "Does orbital angular momentum have effect on laser's scattering by molecular atmosphere?" *Journal of Quantitative Spectroscopy & Radiative Transfer*, vol. 220, Nov. 2018.

[201] P. J. M. Vanbrabant, J. Beeckman, K. Neyts, R. James, and F. A. Fernandez, "A finite element beam propagation method for simulation of liquid crystal devices," *Optics Express*, vol. 17, no. 13, Jun. 22, 2009.

[202] L. R. Bissonnette, "Multiscattering model for propagation of narrow light beams in aerosol media," *Applied Optics*, vol. 27, no. 12, Jun. 15, 1988.

[203] R. Leathers, T. Downes, C. Davis, and C. Mobley, "Monte carlo radiative transfer simulations for ocean optics: A practical guide," Sep. 1, 2004.

[204] J. Zhang, L. Kou, Y. Yang, F. He, and Z. Duan, "Monte-carlo-based optical wireless underwater channel modeling with oceanic turbulence," *Optics Communications*, vol. 475, Nov. 2020.

[205] M. Qiao and X. Yuan, "Realistic phase screen model for forward multiple-scattering media," *Optics Letters*, vol. 45, no. 4, Feb. 15, 2020.

[206] S. A. Prahl, D. D. Duncan, and D. G. Fischer, "Monte carlo propagation of spatial coherence," in *Biomedical Applications of Light Scattering III*, vol. 7187, SPIE, Feb. 24, 2009.

[207] S. A. Prahl, D. D. Duncan, and D. G. Fischer, "Stochastic huygens and partial coherence propagation through thin tissues," presented at the BiOS, A. P. Wax and V. Backman, Eds., San Francisco, California, Feb. 11, 2010.

[208] J. M. Schmitt and G. Kumar, "Optical scattering properties of soft tissue: A discrete particle model," *Applied Optics*, vol. 37, no. 13, May 1, 1998.

[209] A. W. Jantzi, M. G. Cockrell, L. K. Rumbaugh, and W. D. Jemison, "A mixed numeric and analytic method for investigating OAM beam scattering in turbid water," in *Cyber Sensing 2018*, vol. 10630, International Society for Optics and Photonics, May 3, 2018.

[210] A. W. Jantzi, M. G. Cockrell, L. K. Rumbaugh, and W. D. Jemison, "Mixed numerical and analytical method for investigating orbital angular momentum beam scattering in turbid water," *Optical Engineering*, vol. 58, no. 4, Apr. 2019.

[211] L. Wind and W. W. Szymanski, "Quantification of scattering corrections to the beer-lambert law for transmittance measurements in turbid media," *Measurement Science and Technology*, vol. 13, no. 3, Feb. 2002.

[212] V. V. Dudorov, M. A. Vorontsov, S. L. Lachinova, and S. Cunningham, "Numerical techniques for analysis of joint impact of atmospheric turbulence and aerosol scattering effects on imaging systems," in *Unconventional Imaging and Wavefront Sensing XII*, vol. 9982, SPIE, Sep. 20, 2016.

[213] N. A. Ferlic, A. Jantzi, A. E. Laux, L. J. Mullen, and B. M. Cochenour, "Volume scattering of particles by beams carrying orbital angular momentum," in *Ocean Sensing and Monitoring XII*, vol. 11420, International Society for Optics and Photonics, Apr. 22, 2020.

[214] M. Koivurova, H. Partanen, J. Lahyani, N. Cariou, and J. Turunen, "Scanning wavefront folding interferometers," *Optics Express*, vol. 27, no. 5, Mar. 4, 2019.

[215] M. v. Iersel, D. A. Paulson, C. Wu, *et al.*, "Measuring the turbulence profile in the lower atmospheric boundary layer," *Applied Optics*, vol. 58, no. 25, Sep. 1, 2019.

[216] A. Consortini, Y. Y. Sun, C. Innocenti, and Z. P. Li, "Measuring inner scale of atmospheric turbulence by angle of arrival and scintillation," *Optics Communications*, vol. 216, no. 1, Feb. 1, 2003.

[217] N. A. Ferlic, M. v. Iersel, and C. C. Davis, "Measurement of the orbital angular momentum spectrum of light through artificial turbulence by interferometry," in *Laser Communication and Propagation through the Atmosphere and Oceans IX*, vol. 11506, International Society for Optics and Photonics, Aug. 22, 2020.

[218] N. A. Ferlic, A. E. Laux, M. v. Iersel, C. C. Davis, L. J. Mullen, and B. M. Cochenour, "Measurement of the orbital angular momentum spectrum of light through turbid water using modal decomposition," in *Laser Communication and Propagation through the Atmosphere and Oceans IX*, vol. 11506, International Society for Optics and Photonics, Aug. 22, 2020.

[219] B. Cochenour, K. Morgan, K. Miller, E. Johnson, K. Dunn, and L. Mullen, "Propagation of modulated optical beams carrying orbital angular momentum in turbid water," *Applied Optics*, vol. 55, no. 31, Nov. 1, 2016.

[220] A. Pilarska, M. Lukosek, K. Siwińska-Stefańska, K. Pilarski, and T. Jesionowski, "Use of MgO to promote the oxyethylation reaction of lauryl alcohol," *Polish Journal of Chemical Technology*, vol. 16, Jun. 26, 2014.

[221] X. Lai, Y. Zheng, H. Ipsen, *et al.*, "Particle size determination in aluminum hydroxide suspensions using near-infrared transmittance spectroscopy," *Applied spectroscopy*, vol. 61, Dec. 1, 2007.

[222] X. Sun, M. Kong, O. Alkhazragi, *et al.*, "Non-line-of-sight methodology for high-speed wireless optical communication in highly turbid water," *Optics Communications*, vol. 461, Apr. 1, 2020.

[223] S. Viola, A. Yao, D. McKee, and M. P. J. Lavery, "Propagation dynamics of ballistic light carrying orbital angular momentum (conference presentation)," in *Complex Light and Optical Forces XIV*, vol. 11297, International Society for Optics and Photonics, Mar. 9, 2020.

[224] K. S. Morgan, E. G. Johnson, and B. M. Cochenour, "Attenuation of beams with orbital angular momentum for underwater communication systems," in *OCEANS 2015 - MTS/IEEE Washington*, Washington, DC: IEEE, Oct. 2015.

[225] H. Qassim, F. M. Miatto, J. P. Torres, M. J. Padgett, E. Karimi, and R. W. Boyd, "Limitations to the determination of a laguerre-gauss spectrum via projective, phase-flattening measurement," *JOSA B*, vol. 31, no. 6, Jun. 1, 2014.

[226] C. Yang, C. Xu, W. Ni, Y. Gan, J. Hou, and S. Chen, "Turbulence heterodyne coherent mitigation of orbital angular momentum multiplexing in a free space optical link by auxiliary light," *Optics Express*, vol. 25, no. 21, Oct. 16, 2017.

[227] R. Zhang, N. Hu, X. Su, *et al.*, "Alignment monitor for free-space optical links in the presence of turbulence using the beating of opposite-order orbital-angular-momentum beams on two different wavelengths," in *2020 Optical Fiber Communications Conference and Exhibition (OFC)*, Mar. 2020.

[228] S. J. Rehse and E. M. Strauss, "Synthetic array heterodyne detection: Developments within the caliope CO{sub 2} DIAL program," Los Alamos National Lab. (LANL), Los Alamos, NM (United States), LA-UR-95-2546; CONF-9507151-1, Sep. 1, 1995.

[229] C. E. M. Strauss, "Synthetic-array heterodyne detection: A single-element detector acts as an array," *Optics Letters*, vol. 19, no. 20, Oct. 15, 1994.

[230] C. E. M. Strauss and S. J. Rehse, "Rainbow heterodyne detection," in *Conference on Lasers and Electro-Optics (1996), paper CTuT4*, Optical Society of America, Jun. 2, 1996.

[231] B. J. Cooke, A. E. Galbraith, B. E. Laubscher, C. E. M. Strauss, N. L. Olivas, and A. C. Grubler, "Laser field imaging through fourier transform heterodyne," in *Laser Radar Technology and Applications IV*, vol. 3707, SPIE, May 28, 1999.

[232] R. J. Watkins, K. Dai, G. White, *et al.*, "Experimental probing of turbulence using a continuous spectrum of asymmetric OAM beams," *Optics Express*, vol. 28, no. 2, Jan. 20, 2020.

[233] L. Mullen, D. Alley, and B. Cochenour, "Investigation of the effect of scattering agent and scattering albedo on modulated light propagation in water," *Applied Optics*, vol. 50, no. 10, Apr. 1, 2011.

[234] K. Morgan, "A study on the dynamic manipulation of structured light using orbital angular momentum for wireless underwater links," *All Dissertations*, Aug. 1, 2020.

[235] D. Deirmendjian. "Electromagnetic scattering on spherical polydispersions." (1969), (visited on 07/30/2019).

[236] D. Deirmendjian, "Scattering and polarization properties of water clouds and hazes in the visible and infrared," *Applied Optics*, vol. 3, no. 2, Feb. 1, 1964.

[237] J. V. Dave, "Scattering of electromagnetic radiation by a large, absorbing sphere," *IBM Journal of Research and Development*, vol. 13, no. 3, May 1969.

[238] R. G. Lane, A. Glindemann, and J. C. Dainty, "Simulation of a kolmogorov phase screen," *Waves in Random Media*, vol. 2, no. 3, Jul. 1, 1992.

[239] F. Roddier, "V the effects of atmospheric turbulence in optical astronomy," in *Progress in Optics*, E. Wolf, Ed., vol. 19, Elsevier, Jan. 1, 1981.

[240] R. Frehlich, "Simulation of laser propagation in a turbulent atmosphere," *Applied Optics*, vol. 39, no. 3, Jan. 20, 2000.

[241] M. Charnotskii, "Comparison of four techniques for turbulent phase screens simulation," *Journal of the Optical Society of America. A, Optics, Image Science, and Vision*, vol. 37, no. 5, May 1, 2020.

[242] D. A. Paulson, C. Wu, and C. C. Davis, "Randomized spectral sampling for efficient simulation of laser propagation through optical turbulence," *Journal of the Optical Society of America B*, vol. 36, no. 11, Nov. 1, 2019.

[243] C. M. Sorensen and D. J. Fischbach, "Patterns in mie scattering," *Optics Communications*, vol. 173, no. 1, Jan. 1, 2000.

[244] M. J. Berg, C. M. Sorensen, and A. Chakrabarti, "Patterns in mie scattering: Evolution when normalized by the rayleigh cross section," *Applied Optics*, vol. 44, no. 34, Dec. 1, 2005.

[245] L. A. Poyneer, B. A. Macintosh, and J.-P. Véran, "Fourier transform wavefront control with adaptive prediction of the atmosphere," *JOSA A*, vol. 24, no. 9, Sep. 1, 2007.

[246] S. Srinath, L. A. Poyneer, A. R. Rudy, and S. M. Ammons, "Computationally efficient autoregressive method for generating phase screens with frozen flow and turbulence in optical simulations," *Optics Express*, vol. 23, no. 26, Dec. 28, 2015.

[247] G. Badura, C. Fernandez, and J. Stewart, "Wave optics simulator for lasers in time-evolving turbulence," in *Laser Radar Technology and Applications XXV*, vol. 11410, International Society for Optics and Photonics, Apr. 23, 2020.

[248] A. Berdja and J. Borgnino, "Modelling the optical turbulence boiling and its effect on finite-exposure differential image motion," *Monthly Notices of the Royal Astronomical Society*, vol. 378, no. 3, Jul. 1, 2007.

[249] K. Tanaka, M. Taguchi, and T. Tanaka, "Quasi-diffraction-free beams," *JOSA A*, vol. 18, no. 7, Jul. 1, 2001.

[250] N. Mphuthi, R. Botha, and A. Forbes, "Are bessel beams resilient to aberrations and turbulence?" *JOSA A*, vol. 35, no. 6, Jun. 1, 2018.

[251] J. Mendoza-Hernández, M. L. Arroyo-Carrasco, M. D. Iturbe-Castillo, and S. Chávez-Cerda, "Laguerre–gauss beams versus bessel beams showdown: Peer comparison," *Optics Letters*, vol. 40, no. 16, Aug. 15, 2015.

[252] V. V. Kotlyar, A. A. Kovalev, R. V. Skidanov, S. N. Khonina, and J. Turunen, "Generating hypergeometric laser beams with a diffractive optical element," *Applied Optics*, vol. 47, no. 32, Nov. 10, 2008.